

Geohazard Monitoring with Satellite Radar Observations: Applications to Earthquakes and Landslides

Chuang Song

**Thesis submitted for the degree of
Doctor of Philosophy**



School of Engineering, Newcastle University

August 2022

Abstract

Over the past few decades, satellite radar observations have developed into a powerful means of monitoring geohazards. What makes it distinguishable is that both transient and long-term deformation involved in geohazards are measurable in detail using the well-established interferometric synthetic aperture radar (InSAR) technique. However, recent and advanced applications encounter limitations due to the decorrelation problem of InSAR when observing large-gradient transient deformation and the lack of subsurface information. In addition, considering the large amount of InSAR observations and the widespread error sources, how to automatically and adaptively identify geohazard-related risk areas on a large spatial scale is also worthy of attention.

This thesis aims to address the above-mentioned challenges and thereby improve the application of satellite radar observations to two typical geohazards: earthquakes and landslides, which occur frequently around the world and are interrelated in the sense that landslides can be triggered by earthquakes. Firstly, this thesis overcomes the InSAR decorrelation problem by combining InSAR with image offset tracking techniques so that the complete coseismic deformation of the 2019 Mw 7.5 New Ireland earthquake can be recovered and modelled. Secondly, this thesis incorporates seismic noise measurements to invert subsurface information (e.g., landslide depth) that is hard to obtain with InSAR alone and such a solution was used to investigate a landslide in Bolivia. Finally, a novel InSAR-based automated landslide detection method was developed to detect earthquake accelerated landslides (EALs) following the 2016-2017 Central Italy earthquake sequence. These EALs responded to coseismic or post-seismic stress disturbances differently from extensively studied coseismic landslides and were typically activated with considerably accelerated ground displacement velocities compared to their pre-earthquake levels, without acute failures/collapse. This is the first time that an inventory of EALs against catastrophic coseismic landslides was established, which enables a systematic analysis of the spatiotemporal characteristics of EALs and a comprehensive understanding of the prolonged legacy effects of earthquakes on landslides.

These works in this thesis provide detailed solutions for monitoring geohazards of different spatial scales and magnitudes using satellite radar observations. Also, they open a new perspective for assessing long-term earthquake-induced landslide risks, which could have important implications for hazard management in seismically active areas.

Declaration

I declare that this thesis has been composed solely by myself and that it has not been submitted, in whole or in part, for any other degree qualification. I confirm that the work submitted is my own original study, except where work that has formed part of the jointly authored publications has been included. My contributions and those of the other co-authors to this work have been explicitly indicated below. I confirm that appropriate credit has been given within this thesis where reference has been made to the work of others.

The work presented in Chapter 3 has been published in *Remote Sensing* as “Coseismic slip distribution of the 2019 Mw 7.5 New Ireland earthquake from the integration of multiple remote sensing techniques” authored by Chuang Song, Chen Yu, Zhenhong Li, Yongsheng Li and Ruya Xiao (<https://doi.org/10.3390/rs11232767>). I am the first author with primary contributions including the processing of satellite data, the modelling and analysis of the results, and the writing of the original manuscript. The second and third authors are my supervisors who directed the data processing and edited the manuscript. The remaining authors provided suggestions on InSAR data processing.

The work presented in Chapter 4 has been published in *Landslides* as “Landslide geometry and activity in Villa de la Independencia (Bolivia) revealed by InSAR and seismic noise measurements” by Chuang Song, Chen Yu, Zhenhong Li, Veronica Pazzi, Matteo Del Soldato, Abel Cruz and Stefano Utili (<https://doi.org/10.1007/s10346-021-01659-9>). I am the first author with primary contributions in InSAR data processing, experimental methods, result analysis and manuscript writing. The second, third and last authors are my supervisors who designed the research structure and directed the result interpretation. The fourth and fifth authors processed seismic noise measurements. The sixth author provided rock/soil samples and borehole data of the landslide.

The work presented in Chapter 5 is a reformatted version of an article published in *Nature Communications* (<https://doi.org/10.1038/s41467-022-35035-5>). Its authors are Chuang Song, Chen Yu, Zhenhong Li, Stefano Utili, Paolo Frattini, Giovanni Crosta and Jianbing Peng. I am the first author who conducted all experiments and result analysis. The second, third and fourth authors are my supervisors who directed the research and refined the draft structure. The remaining authors prepared the lithological data and coordinated the data analysis.

Acknowledgements

I would like to express my great appreciation to my supervisors, Prof. Stefano Utili, Dr Chen Yu and Dr Nigel Penna. Their patient guidance and earnest teachings during my doctoral study give me a deeper understanding of scientific research and guide my continuous learning and improvement in the field of InSAR. I am also very grateful to my former supervisor Prof. Zhenhong Li. Without his guidance during my first two-year study, I would not find my research goals. He not only enlightened and funded my PhD study at Newcastle University, but also opened my horizons in the field of InSAR and geohazards. Special thanks to Chen for his detailed guidance in InSAR data processing, research problem discovery and scientific writing. I still clearly remember us working together to revise those journal drafts dozens of times. He also helps me a lot in life in addition to the contact at work.

Great thanks to Chinese Scholarship Council for granting me a studentship for my doctoral study. Part of my work is also funded by the UK Natural Environment Research Council (NERC) through the Centre for the Observation and Modelling of Earthquakes, Volcanoes and Tectonics (COMET), and the European Union's Horizon 2020 Marie Skłodowska-Curie Action Research and Innovation Staff Exchange (RISE) via the projects HERCULES and Geo-ramp.

I am grateful to all my colleagues who provided helpful suggestions on my research, particularly Ruya Xiao, Lifu Chen, Yongsheng Li, Jia Xu, Gauhar Meldebekova, Hui Luo, Marine Roger, Zheng Wang, Teng Li, Panpan Tang, Yuande Yang, Wen Xiao, Jin Xing, Peng Li and Bingqian Chen. I am also grateful to my friends, Jiaying Zhang, Qin Fu, Hao Yin and Ming Ni for their kind supports. Special thanks to Dr Shuai Wang and Dr Xie Hu for sharing their knowledge of earthquakes and landslides. Sincere thanks to Dr Veronica Pazzi and Dr Matteo Del Soldato for their suggestions on interpreting seismic noise observations. Thanks to Prof Giovanni Crosta and Dr Paolo Frattini for providing the geological data and historical deep-seated landslide inventory in Italy, and Dr Daniele Cheloni for sharing the active fault database in Central Italy.

I would like to acknowledge the providers of data used in this work. The Sentinel-1 and Sentinel-2 data are provided by the European Space Agency (ESA), and the ALOS-2 PALSAR-2 data is provided by the Japan Aerospace Exploration Agency (JAXA). The precipitation data is provided by the NASA/Goddard Space Flight Centre's Mesoscale Atmospheric Processes Laboratory and Precipitation Processing System (PPS). The seismicity data is provided by the

United States Geological Survey (USGS). The historical landslide inventory in Italy (IFFI) is provided by the Istituto Superiore per la Protezione e la Ricerca Ambientale (ISPRA).

My final great appreciation goes to my parents and my fiancée. I am very grateful to my parents for their unreserved love and support throughout my life. In the past two years, affected by the pandemic, I have not been able to go back home. I can imagine their thoughts and concerns, but they always encourage and support me with a positive attitude in our video chats, which gives me a steady stream of courage and motivation to carry forward. Sincere and great thanks go to my beloved fiancée Yu Zhong as well. Since we met and fell in love 6 years ago, we have moved forward hand in hand, closely depended on each other, and made progress together. I would like to accompany you to spend the rest of my life with the warm wind blowing and spring blooming.

Chuang Song

April 2022, Newcastle, UK

Contents

Abstract	i
Declaration	ii
Acknowledgements	iii
List of Figures	vii
List of Tables	ix
Chapter 1. Introduction	1
1.1 Background	1
1.2 Satellite radar observations	3
1.3 Earthquake study using satellite radar observations	5
1.4 Landslide study using satellite radar observations	6
1.5 Motivations, aims and objectives	8
1.6 Outline	9
Chapter 2. SAR and InSAR techniques	11
2.1 Principles of SAR and InSAR	11
2.1.1 <i>Principles of SAR</i>	11
2.1.2 <i>Principles of InSAR</i>	14
2.1.3 <i>Error sources of InSAR and countermeasures</i>	18
2.2 Procedures of InSAR processing	23
2.3 SAR pixel offset tracking	24
2.4 InSAR stacking technique	27
2.5 InSAR time series methods	28
2.5.1 <i>Persistent Scatterers InSAR (PSI)</i>	29
2.5.2 <i>Small Baseline Subset method (SBAS)</i>	30
2.5.3 <i>StaMPS</i>	31
Chapter 3. Combining multiple satellite observations to model the 2019 Mw 7.5 New Ireland earthquake	35
3.1 Introduction	35
3.2 Data and processing strategy	38
3.2.1 <i>Sentinel-1 data and interferometry</i>	38
3.2.2 <i>Sentinel-1 offset tracking</i>	39
3.2.3 <i>Sentinel-2 data and offset tracking</i>	40
3.2.4 <i>ALOS-2 data and interferometry</i>	42
3.2.5 <i>ALOS-2 offset tracking</i>	42
3.3 Geophysical modelling	43
3.3.1 <i>Inversion method</i>	43
3.3.2 <i>Weighting strategy</i>	44
3.4 Results	45
3.5 Discussion	49
3.6 Summary	51

Chapter 4. Combining InSAR and seismic noise measurements to monitor a landslide in Villa de la Independencia (Bolivia)	53
4.1 Introduction	53
4.2 Study area	55
4.3 Data and methodology	58
4.3.1 <i>InSAR</i>	58
4.3.2 <i>Determination of the sliding geometry</i>	60
4.3.3 <i>Seismic noise measurements and H/V technique</i>	62
4.4 Results	63
4.4.1 <i>Identification of the fractured sliding surfaces from InSAR</i>	64
4.4.2 <i>Sliding interface depth obtained from H/V measurements</i>	67
4.4.3 <i>Landslide volume estimation</i>	70
4.4.4 <i>Temporal evolution of the landslide</i>	71
4.5 Discussion	74
4.5.1 <i>Seasonal oscillations in InSAR time series</i>	74
4.5.2 <i>Instability of the landslide</i>	75
4.6 Summary	76
Chapter 5. Detection and characterisation of earthquake accelerated landslides in Central Italy with InSAR observations	78
5.1 Introduction	78
5.2 Study area and data	81
5.2.1 <i>Study area</i>	81
5.2.2 <i>InSAR time series</i>	82
5.2.3 <i>IFFI</i>	85
5.2.4 <i>Geo-environmental data</i>	86
5.3 Methods	86
5.3.1 <i>EAL detection method</i>	86
5.3.2 <i>Statistical analysis method</i>	90
5.4 Results	92
5.4.1 <i>Spatial distribution of EALs</i>	93
5.4.2 <i>Conditioning factors of EAL occurrence</i>	94
5.4.3 <i>Post-earthquake dynamics of EALs</i>	98
5.5 Discussion	102
5.6 Summary	104
Chapter 6. Conclusions	107
6.1 Contributions of this thesis	107
6.2 Future works	109
Appendix: List of publications	111
References	112

List of Figures

Figure 1.1 An overview of SAR satellites launched since the 1990s.....	4
Figure 2.1 Geometry of a side-looking satellite radar in (a) 3D view, (b) lateral view and (c) top view.	12
Figure 2.2 Geometry of SAR imaging.....	13
Figure 2.3 Diagram illustration of geometric distortions: foreshortening, shadow and layover.	14
Figure 2.4 Geometry of InSAR based on primary and secondary SAR acquisitions.....	15
Figure 2.5 Examples of (a) a coherence map, (b) a wrapped interferogram and (c) an unwrapped phase map.	16
Figure 2.6 Illustration of ascending- and descending-track InSAR geometries (schematic modified from Highland and Bobrowsky, 2008).....	17
Figure 2.7 Range offset tracking results of the 2016 Mw 7.8 New Zealand earthquake.	25
Figure 2.8 Azimuth offset tracking results of the 2016 Mw 7.8 New Zealand earthquake.	26
Figure 2.9 Cumulative displacements one year before the failure of the 2018 Baige landslide in the (a) range and (b) azimuth directions measured by SAR pixel offset tracking.	26
Figure 2.10 Application of InSAR stacking in investigating landslides in the Alps.....	28
Figure 3.1 Seismotectonic setting of the 2019 New Ireland earthquake.	36
Figure 3.2 Coseismic displacement maps of the 2019 New Ireland earthquake from Sentinel and ALOS-2 data.	40
Figure 3.3 Horizontal deformation of the 2019 New Ireland earthquake decomposed from Sentinel-1 offsets.	41
Figure 3.4 Determination of the smoothing factor and dip angle.....	44
Figure 3.5 Iterative weighting of S1-range, ALOS2-azimuth, S2-NS and S2-EW.....	45
Figure 3.6 Slip distribution on the fault plane from joint and individual inversions.	46
Figure 3.7 Results of checkerboard tests.	47
Figure 3.8 Coseismic satellite observations (left), predictions from slip models (middle) and residuals between them (right).	48
Figure 3.9 Static Coulomb failure stress changes due to the 2019 New Ireland earthquake. ..	50
Figure 4.1 Location, geological setting and field photos of Villa de la Independencia, Bolivia.	56
Figure 4.2 Acquisition dates and interferometric pairs of Sentinel-1 imagery in the (a) descending and (b) ascending tracks.	58
Figure 4.3 Workflow of time series InSAR processing with tropospheric delay correction....	60
Figure 4.4 Maps of InSAR deformation velocity and its standard deviation.	63
Figure 4.5 Observed and simulated LOS cumulative displacements in Independencia.	65
Figure 4.6 Determined sliding geometries of the three landslide sub-blocks.	66
Figure 4.7 A representative selection of H/V curves for the seismic noise measurements carried out in the three landslide sub-blocks (town centre, upper block, and east block).	68
Figure 4.8 Reconstructed z depth values for seismic noise acquisitions located in the town centre (asterisks in yellow), upper block (in purple) and east block (in green).	68
Figure 4.9 Distribution and profiles of z2 depths.	69

Figure 4.10 Estimation of the sliding surface depth of the entire landslide body.	70
Figure 4.11 InSAR-derived descending- and ascending-track Sentinel-1 time series of (a) town centre, (b) upper block and (c) east block, compared with precipitation data.	72
Figure 4.12 Time series InSAR-derived movements along the sliding surface and 30-day accumulated precipitation from GPM.	73
Figure 4.13 Relationship between InSAR time series and differential zenith tropospheric delays (dZTD) and 30-day accumulated precipitation analysed with wavelet tools.	75
Figure 5.1 Seismotectonic background of the study area and InSAR-derived velocity fields in the Line of Sight (LOS).	82
Figure 5.2 Sentinel-1 acquisition dates and generated interferograms in the (a) descending and (b) ascending tracks.	83
Figure 5.3 Correlation analyses between InSAR and GPS displacements along the LOS in the (a) descending track and (b) ascending track.	84
Figure 5.4 Workflow for EAL/non-EAL detection and information gain (IG) methods.	88
Figure 5.5 InSAR-detected EALs and IFFI documented landslides.	94
Figure 5.6 IG ranking of 15 collected LCFs and histograms of four prominent LCFs.	95
Figure 5.7 Distribution of EAL velocity, EAL density, EAL acceleration and coseismic landslides.	96
Figure 5.8 Distribution of slope angles, aspect angles of EALs and non-EALs.	98
Figure 5.9 Sliding velocity estimated every three months and the monthly precipitation of the six landslide cases.	99
Figure 5.10 Temporal evolution of EALs.	100
Figure 5.11 Seismic, lithological, and topographic statistics of earthquake-triggered landslides.	103

List of Tables

Table 3.1 Satellite data used in this chapter	39
Table 4.1 Properties of rock and soil samples whose locations are shown in Figure 4.1b.	57
Table 5.1 Landslide conditioning/triggering factors used in this study	91

Chapter 1. Introduction

1.1 Background

Geohazards refer to natural geological processes that can cause widespread damage to human life, economy, environment and landforms (McCall, 2012; Culshaw, 2018). They occur widely all over the world, representing solid Earth changes and in general characterised by the movement of Earth's surface. According to the difference in the triggering process, the environmental conditions, or the property of hazardous materials, geohazards can be classified into five groups: earthquake/volcano-related hazards, geomorphological/geotechnical hazards, hydrogeological hazards, coastal/marine hazards and artificial hazards (Culshaw, 2018). The first group of geohazards includes earthquakes, volcanoes and related geological phenomena (e.g., soil liquefaction). The second group of geohazards, including landslides, avalanches, rock toppling and permafrost-related hazards, originates at or near the Earth's surface (Marston et al., 2017), usually with vulnerable materials. The third group, hydrogeological hazards such as flooding, is associated with water occurrences, movements, and distributions (Trajkovic et al., 2016). The fourth group of geohazards occurs in coastal and marine environments, including tsunamis, coastal erosion and submarine landslides, etc. The fifth group of geohazards, such as land subsidence and mining-induced sinkholes, is mainly caused by human activity.

Among the five groups of geohazards, earthquakes and landslides are two relatively common types, which occur frequently on a global scale and result in ground movements in a transient period (seconds to days) or with long term (years) effects. The transient behaviour is typically a quick and strong response to energy release (e.g., coseismic ruptures and landslide failures), while the long-term behaviour is a relatively slow process that may last for many years (e.g., interseismic/postseismic deformation and motion of slow-moving landslides). The transient motion is usually catastrophic and fatal. For example, the coseismic motion of earthquakes worldwide (~2,200 fatal events) had caused a total of over 2.3 million casualties between 1900 and 2015 (Daniell et al., 2017), and global landslide failures had killed over 130,000 people between 2004 and 2016 (Petley, 2012; Lacroix et al., 2015; Froude and Petley, 2018). The long-term effect of earthquakes and landslides is continuously accumulating over time and can also cause major damage to infrastructures and may transform into fatal transient events (Lacroix et al., 2020).

To capture both the transient and long-term motions of earthquakes and landslides, a number of monitoring techniques have been developed. In terms of earthquake monitoring, one of the

typical traditional instruments is the seismograph which records the seismic wave propagation at a high sampling rate (Boore and Bommer, 2005; Mousavi et al., 2020). Geodetic observations such as the levelling and Global Navigation Satellite System (GNSS) can measure accurate surface motions and have been widely used in seismic studies (e.g., Segall and Davis, 1997; Vigny et al., 2005; Yamagiwa et al., 2015). In terms of landslide monitoring, there are generally three categories of techniques: geotechnical, geodetic and geophysical surveys. The geotechnical technique relies on in-situ sensors, such as inclinometers, extensometers and piezometers, to measure both surface and subsurface deformation of landslides (e.g., Crosta et al., 2014a). Geodetic observations include those from levelling, total stations and GNSS, in which GNSS is more commonly used (Gili et al., 2000) due to its continuity and accuracy (a few millimetres, Li et al., 2017). The geophysical surveys such as micro-seismic and direct current geoelectric monitoring are usually used to measure the geometrical and physical properties of landslides (e.g., Pazzi et al., 2017) instead of measuring deformation as the geotechnical and geodetic techniques.

Although the monitoring techniques mentioned above are capable of providing sensitive and effective observations, they are all point-based surveys that require the careful selection of proper locations of in-situ sensors and are labour-intensive and costly to install and maintain. Moreover, the point-based monitoring restricts the spatial coverage and resolution of investigation and may not fully characterise the deformation of earthquakes and landslides (Domingues et al., 2012; Scaioni et al., 2015). These drawbacks can be overcome by the use of remote sensing techniques including photogrammetry, laser scanning, and synthetic aperture radar (SAR), which provide surface-based remote measurements without the requirement of installing or maintaining in-situ sensors deep into the deforming and hazardous zones. The performance (e.g., spatial resolution and coverage) and applicable scenarios of remote sensing observations largely depend on the platform carrying the imaging sensors (Chen et al., 2016). For example, terrestrial or airborne photogrammetry, terrestrial or airborne laser scanning (TLS or ALS) and ground-based SAR (GBSAR) are limited by the platform sensing range and are more suitable to be utilized on a local or regional scale (up to hundreds of square kilometres, e.g., Glennie et al., 2014; Mezaal et al., 2018), despite its high spatial resolution (< 1 m, e.g., Haddad et al., 2012; Wang et al., 2018).

Compared with terrestrial and airborne remote sensing, spaceborne remote sensing, such as satellite optical and radar imaging, is more capable to apply over a large spatial scale (tens of thousands of square kilometres) owing to the global observation capabilities of satellites.

Satellite optical imaging has been proven to be efficient in characterising the transient behaviours of large earthquakes (e.g., Leprince et al., 2007) and landslides (e.g., Ghorbanzadeh et al., 2019), but it can hardly capture small ground movements (centimetre level or smaller) in long terms, even by Very High Resolution (VHR) satellites (Stumpf et al., 2014), let alone the high cost of VHR for long-term monitoring. Satellite radar imaging (or named spaceborne SAR), on the other hand, is able to measure both transient deformations (e.g., Pathier et al., 2006; Hamling et al., 2017) and long-term subtle ground displacements (e.g., Elliott et al., 2016; Handwerger et al., 2019) so that is superior in earthquake and landslide studies.

1.2 Satellite radar observations

The first satellite platform equipped with a SAR sensor is SeaSat (Jordan, 1980) which was launched by NASA Jet Propulsion Laboratory (JPL) in June 1978. It was designed for global oceanographic monitoring and only operated for 110 days, but it inspired pioneering scientists to explore the use of satellite radar observations in topographic mapping through interferometry (e.g., Gabriel et al., 1989; Li and Goldstein, 1990). In July 1991, European Space Agency (ESA) launched European Remote-Sensing Satellite-1 (ERS-1) to provide regular monitoring of land and ocean surfaces (Attema, 1991). Based on this satellite's SAR data, the powerful ability of spaceborne interferometric SAR (InSAR) in measuring surface deformation other than elevation was firstly revealed by the study of the Landers, California earthquake (Massonnet et al., 1993), which ushered in a new era of InSAR. The success of ERS-1 also promoted satellite radar observations to the forefront of Earth observation and since then more SAR satellites came into operation as shown in Figure 1.1.

As of 2021, at least ten SAR missions are in operation, but their applicability varies due to differences in revisit time, spatial resolution, swath width and sensor wavelength (often referred to as bands). SAR satellites with less revisit time, higher spatial resolution and larger swath width (e.g., Sentinel-1A/B and ALOS-2) are generally more conducive to large-area, multi-temporal and detailed deformation monitoring, while satellite radars in different bands (usually X, L- or C-bands) correspond to different advantageous application scenarios. X-band SAR (e.g., TerraSAR-X and COSMO-SkyMed) can provide high-resolution (≤ 1 m) images but operates at a short wavelength of about 3.1 cm, which has little penetration of vegetation and will cause strong decorrelation in vegetated areas (Sica et al., 2020). Therefore, it is more suitable for urban or ice/snow monitoring (e.g., Bonano et al., 2013; Berg et al., 2015) without dense vegetation cover. L-band SAR (e.g., ALOS-1/2), on the other hand, has a much longer wavelength (about 23.5 cm), enabling great penetration into vegetation, and its phase quality in

vegetated areas degrades much less than X-band SAR (Schlögel et al., 2015). But the spatial resolution of L-band SAR is usually lower than X-band SAR (Aoki et al., 2021) and its phase measurements tend to be less sensitive to small surface deformation (Wempen and McCarter, 2017). The wavelength of C-band (about 5.6 cm) is between L-band and X-band, and thus C-band SAR (e.g., Envisat and Sentinel-1A/B) is a good compromise for deformation monitoring in both urban and natural environment conditions (e.g., Osmanoğlu et al., 2011; Intrieri et al., 2018) despite the lack of sub-metre resolution.

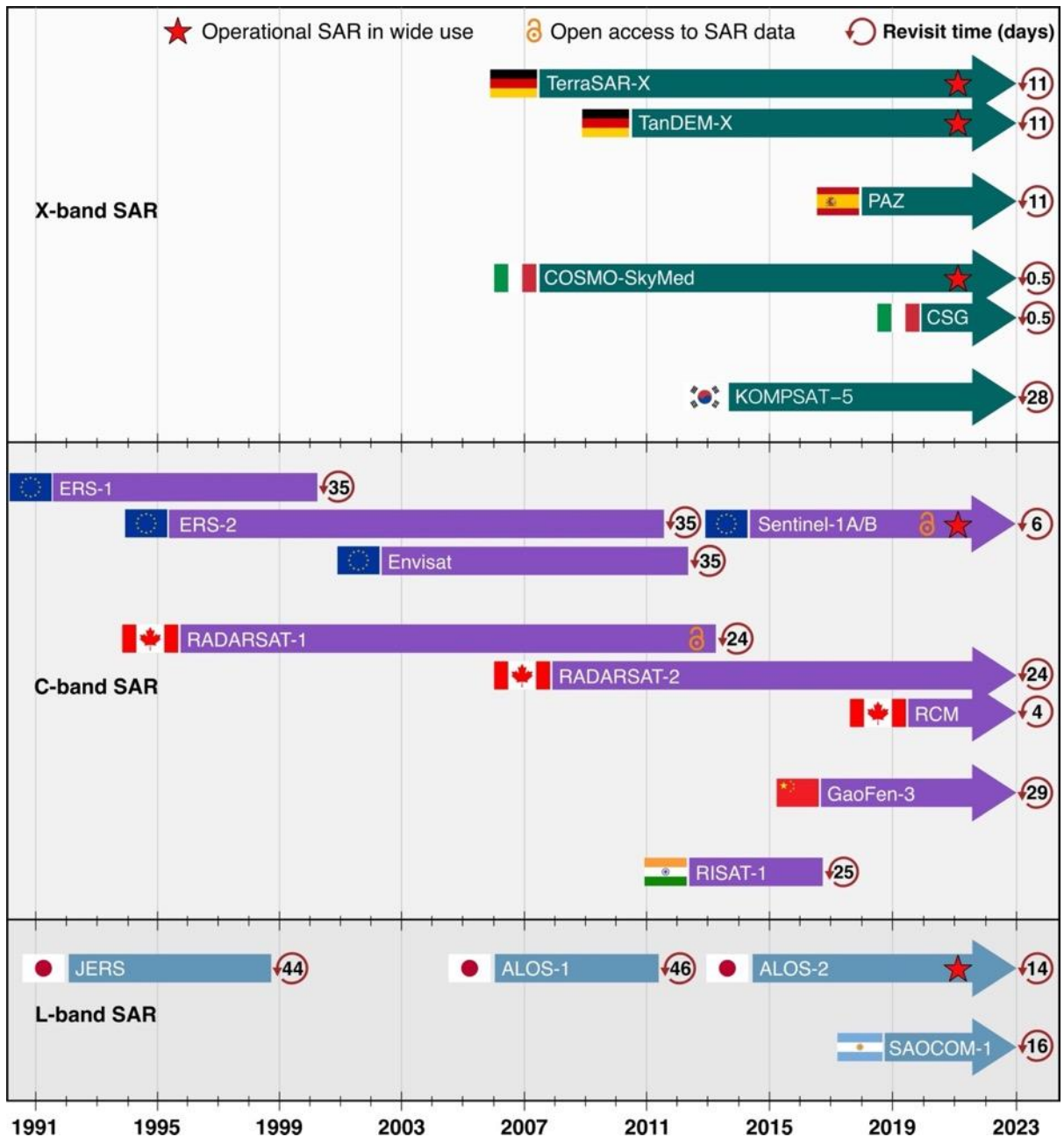


Figure 1.1 An overview of SAR satellites launched since the 1990s. The red stars indicate operational SAR missions that are widely used due to their global coverage capability and better data accessibility than other missions. Note that the short revisit time of some SAR missions (e.g., COSMO-SkyMed) is achieved through a constellation of multiple satellites. Future SAR missions such as NASA-ISRO SAR

Mission (NISAR, L- and S-bands) that will be launched in 2023 are not included here. The figure was updated from Yu (2019).

Among all the operational SAR satellite missions shown in Figure 1.1, Sentinel-1 is the only one capable of systematic global coverage every 6 or 12 days and providing open-access data. It is also the first SAR mission specifically designed for large-area (250 km wide) deformation monitoring, benefiting from the operation mode of Terrain Observation with Progressive Scans (Torres et al., 2012). Sentinel-1 performs C-band SAR imaging with a constellation of two satellites, Sentinel-1A and Sentinel-1B, running on the same orbital plane. Since the launch of the first satellite in April 2014, Sentinel-1 products have been widely applied to earthquake (e.g., Hamling et al., 2017; Bacques et al., 2020) and landslide studies (e.g., Dai et al., 2016; Carlà et al., 2019) due to the advantages of global coverage, regular acquisition, and open access. These advantages also prompted the use of Sentinel-1 as the main source of satellite radar observations in this thesis.

1.3 Earthquake study using satellite radar observations

Earthquakes result from the sudden release of energy in the Earth's crust and cause the transient shaking and displacing of the Earth's surface. The first application of satellite radar observations in the earthquake study can be traced back to the 1992 Landers, California earthquake. It was Massonnet et al. (1993) who first mapped the high-resolution coseismic displacement field with the differential InSAR technique based on ERS-1 images. This study was phenomenal and featured on the cover of *Nature* as it opened a new horizon for the earthquake study. Since then, researchers have imaged the coseismic deformation distribution of over 130 earthquakes (Funning and Garcia, 2018), such as the 1994 Northridge, U.S. earthquake (Massonnet et al., 1996), the 1999 Hector Mine, U.S. earthquake (Fialko et al., 2001), the 2003 Bam, Iran earthquake (Funning et al., 2005), the 2008 Wenchuan, China earthquake (Feng et al., 2010), the 2011 Tohoku, Japan earthquake (Wang et al., 2012), the 2016 Kaikoura, New Zealand earthquake (Xu et al., 2018) and the 2019 Ridgecrest, U.S. earthquake (Goldberg et al., 2020). Thanks to the systematic global coverage of Sentinel-1 data, the number of earthquakes studied using InSAR is increasing by 20–30 per year (Biggs and Wright, 2020). The short revisit time (6 days at minimum) of Sentinel-1 also highly improved the temporal resolution of InSAR and is beneficial in distinguishing between coseismic and early postseismic deformation (Sreejith et al., 2016), or the deformation of mainshocks and aftershocks.

Although InSAR is a powerful tool for coseismic monitoring, its phase measurements may significantly suffer from decorrelation under heavy vegetation, especially for X- and C-band satellite SAR as introduced in Section 1.2, which limits its use in tropical regions. For areas with large transient deformation, such as the epicentral areas of large earthquakes, the decorrelation problem will also occur (Socquet et al., 2019), along with serious unwrapping difficulties. In addition, InSAR can only measure the coseismic displacement in the Line of Sight (LOS), incapable of mapping 2D/3D deformation fields without assumption or combination with other sources of measurements. Therefore, to overcome the above shortcomings, it is reasonable to combine multiple satellite radar observations such as L-band SAR (e.g., ALOS-2) interferometric phases that are feasible over vegetated areas, and SAR pixel offsets that provide unambiguous deformation measurements regardless of the magnitude of the displacement gradient (Michel et al., 1999; Wang and Jónsson, 2015). Optical satellite image offsets can also be complementary to InSAR due to the direct estimation of displacement fields in the horizontal direction (north and east) (Leprince et al., 2007). Currently, the use of multiple-band InSAR phases (e.g., Wang et al., 2017), SAR pixel offsets (e.g., Elliott et al., 2007) and optical satellite image offsets (e.g., Milliner et al., 2016) in earthquake study is mature, but the proper combination of all these measurements for joint earthquake modelling still needs to be explored. The major concerns are the availability of multiple satellite observations, the difference in observation accuracy and an efficient weighting strategy. In this thesis (Chapter 3), I explore the potential solution of these concerns by investigating a large earthquake in New Ireland, Papua New Guinea.

1.4 Landslide study using satellite radar observations

Landslides are defined as a type of mass wasting on the ground surface that could behave as transient failures or long-term slow sliding. They can be triggered by earthquakes (Keefer, 2002), rainfalls (Guzzetti et al., 2007), snowmelt (Naudet et al., 2008), volcanism (de Vita et al., 2006) and anthropogenic activities (Lacroix et al., 2019). These triggers could activate dormant landslides, accelerate slow-moving landslides, and ultimately lead them to a catastrophic failure that is fatal to surrounding residents.

Since the operation of the ERS-1 mission in 1991, landslide studies using satellite radar observations began to rise and develop vigorously. Scanvic et al. (1993) presented the first application of spaceborne InSAR in monitoring landslide motion by use of ERS-1 data, followed by a series of pioneering landslide studies (e.g., Carnec et al., 1996; Fruneau et al., 1996) aiming at the retrieval of small-scale surface displacements. These studies all used the

conventional differential InSAR technique, but this technique is difficult to trace the small-scale landslide movements in long term due to the rising decorrelation issue over time (Agram and Simons, 2015) and the inevitable atmospheric disturb problem for small deformation (centimetre level) monitoring (Jolivet et al., 2014). To address these issues, Ferretti et al. (2001) proposed a time series InSAR method, i.e., Permanent Scatterers (PS) InSAR, and successfully applied it to measure the movement of a landslide in Ancona, Italy for more than five years. Berardino et al. (2002) developed another classic time series InSAR method, Small Baseline Subset (SBAS), which, together with PS InSAR greatly promotes the prosperity of using satellite radar observations to monitor landslides in long term (e.g., Hilley et al., 2004; Farina et al., 2006; Tomás et al., 2014; Dai et al., 2016; Zhang et al., 2020).

Although satellite radar observations perform well in recording long-term surface deformation of landslides, they fail to directly reveal the subsurface information (e.g., landslide depth). Researchers have to rely on strong assumptions such as spatially uniform landslide rheology and a priori vertical variation of velocity to retrieve the depth of landslides (e.g., Booth et al., 2013; Delbridge et al., 2016). However, these assumptions likely do not apply to compound landslides with spatially variable or unknown rheology (Booth et al., 2013). Another strategy to unravel the subsurface structure of landslides is to combine surface deformation from InSAR with measurements from geotechnical sensors (e.g., boreholes, Crosta et al., 2014a) or field surveys (Crippa et al., 2020), but the low spatial density of these measurements could be a limitation. The depth of landslides may also be obtained from geophysical techniques such as seismic noise measurement that is easy to deploy with high spatial density (Pazzi et al., 2017). Therefore, in this thesis (Chapter 4), I combine satellite radar and dense seismic observations to reveal both the long-term surface movement and subsurface characteristics of a landslide.

In addition to monitoring landslides locally as described above, satellite radar observations can also be used to document landslides on a regional (Bonì et al., 2020), provincial (Rosi et al., 2018), or even national scale (Dehls et al., 2019). The availability of Sentinel-1 data and the development of the time series InSAR technique have greatly improved the detectability of landslides (Raspini et al., 2019). However, there are still some challenges in automatically detecting very slow-moving landslides (a few centimetres per year or less). First, most detection methods employ an empirical InSAR velocity threshold (e.g., 2 mm/yr in Lu et al., 2019; 10 mm/yr in Zhang et al., 2020) to define moving InSAR pixels, which may lack versatility, especially in the absence of prior knowledge of the background deformation level. Second, the threshold-based detection method ignores the spatial correlation and clustering effects among

pixels inside a landslide and is susceptible to noisy pixels. Third, the landslide signal shows the characteristics of high frequency but small scales (Huang et al., 2018), and it is often difficult to separate localised subtle landslide motion from ambient noise such as atmospheric disturbances (Dong et al., 2019). To address these challenges, I developed a new InSAR-based landslide detection method (see Chapter 5), which enables the separation of localised landslide signals, the adaptive identification of moving pixels without velocity threshold constraints, and the automated clustering of identified moving pixels into landslide bodies.

1.5 Motivations, aims and objectives

Geohazards that may occur in a transient period or long term seriously threaten human lives and properties. This thesis aims to study two typical geohazards: earthquakes and landslides, which can cause transient displacing or long-term slow sliding of the ground surface. Earthquakes and landslides occur frequently on a global scale and are interrelated in the sense that landslides can be triggered by earthquakes. To understand their behaviours and assess their risks, this thesis applied satellite radar observations capable of measuring both the transient and long-term deformation to study the coseismic slips of earthquakes and the dynamic of slow-moving landslides.

As introduced in Sections 1.3 and 1.4, satellite radar observations have been widely used in earthquake and landslide monitoring through the InSAR technique, with the advantages of large coverages, high temporal resolutions and long-term operations. However, they also encounter some challenges, such as (1) the decorrelation problem of InSAR when observing large transient deformation (such as caused by large earthquakes); (2) the lack of subsurface information when observing the long-term ground deformation; and (3) how to automatically identify deforming areas after capturing the deformation field. This thesis aims to address these challenges by (1) combining InSAR with other remote sensing techniques to fully capture large transient deformation; (2) combining InSAR and seismic noise measurement to capture both the long-term surface deformation and subsurface information; and (3) developing a new adaptive and automatic deforming area detection method based on long-term InSAR measurements.

The specific objectives are as follows:

Objective 1. To fully capture large transient deformation by combining multiple satellite observations.

InSAR, SAR pixel offset tracking and the optical image offset tracking measurements will be combined to investigate the large transient deformation caused by an earthquake (Mw 7.5) that occurred in New Ireland, Papua New Guinea in 2019. Such a combination can overcome the poor performance of only using InSAR when observing large-gradient displacements. An iterative weighting strategy will also be developed for joint earthquake modelling.

Objective 2. To capture both the long-term surface deformation and subsurface information by combining InSAR and geophysical measurements.

InSAR time series will be used to capture the long-term surface deformation of a landslide in Villa de la Independencia, Bolivia. Seismic noise measurements will be used to determine the depth of the sliding surface. Combining InSAR and seismic noise measurements will enable the identification of the 3D sliding geometry and the dynamic heterogeneity within the landslide.

Objective 3. To automatically identify landslide risk areas after capturing long-term deformation by InSAR.

A new InSAR-based automated deforming area detection method will be developed and it will be used to identify landslide risk areas after capturing long-term deformation. This method will adaptively identify moving pixels on InSAR velocity maps without threshold constraint and automatically cluster moving pixels into intact landslide bodies. By applying the method to detect post-earthquake landslides in Central Italy after 2016, an inventory of earthquake accelerated landslides (EALs) in this area will be established for the first time, based on which the spatial clustering features and sliding dynamics of these EALs will be quantified.

1.6 Outline

Chapter 2 provides an overview of SAR/InSAR principles, the SAR pixel offset tracking, InSAR stacking and time series InSAR methods.

Chapter 3 describes the combination of multiple satellite observations to capture large transient deformation caused by an earthquake. L-band interferometry phases, SAR range/azimuth offsets and optical image offsets were combined to map the coseismic deformation field of the 2019 New Ireland, Papua New Guinea earthquake, and a proper weighting strategy was developed to model the fault slips of the earthquake.

Chapter 4 describes the combination of InSAR and geophysical measurements to capture both surface deformation and subsurface information of a landslide in Villa de la Independencia,

Bolivia. A new InSAR-based geometric inversion method was proposed to determine the geometry of the sliding planes and seismic noise measurements were used to estimate the sliding depth. The evolution of the landslide over time and its dynamic response to precipitation were also analysed.

Chapter 5 develops a new InSAR-based automated deforming area detection method. By applying it to detect landslide risk areas in Central Italy after the 2016-2017 earthquake sequence, an inventory of earthquake accelerated landslides (EALs) was established. Based on the EAL inventory, the prominent conditioning factors of postseismic landslide acceleration, the postseismic dynamics of EALs and the difference in seismic response between EALs and coseismic landslides were revealed.

Chapter 6 summarises the major findings and contributions of this thesis.

Chapter 2. SAR and InSAR techniques

2.1 Principles of SAR and InSAR

2.1.1 Principles of SAR

Radar, standing for radio detection and ranging, is an active sensing technique (or instrument) that uses electromagnetic pulses in the radio or microwaves domain to detect distant objects and measure their distance to the radar sensor (Skolnik, 1962). The emitted pulses will be reflected by the detected objects in the radar's LOS and their two-way travel time (t) will be measured to determine the range (r) between the objects and the radar (Hanssen, 2001) as shown in Equation (2.1).

$$r = \frac{ct}{2} \quad (2.1)$$

where, c is the speed of light. The direction of r is along the LOS, also referred to as the slant range direction. The resolution in the slant range (δr) represents the minimum distance at which two object pixels (assuming A and B, Figure 2.1b) can be distinguished, depending on the pulse length (L_p).

$$\delta r = \frac{L_p}{2} = \frac{c\tau}{2} = \frac{c}{2B} \quad (2.2)$$

where, τ is the pulse duration in units of time, equal to $1/B$, and B is the frequency bandwidth of the transmitted pulse. According to Equation (2.2), high range resolution (small Δr) can be achieved by decreasing pulse duration (e.g., pulse compression) or increasing the bandwidth.

Azimuth direction is perpendicular to the range direction and parallel to the flight path of the radar platform (see Figure 2.1a). In the azimuth direction, the angular spread of the radar beam (θ_a) is equal to $\theta_a = \lambda/L_a$ (Tomiyasu, 1978) where λ is the wavelength of the beam and L_a is the along-azimuth length of the radar antenna. As shown in Figure 2.1c, the minimum distance at which C and D can be distinguished in the azimuth direction, i.e., the azimuth resolution, is approximately equal to (Bamler and Hartl, 1998):

$$\delta a = r\theta_a = \frac{r\lambda}{L_a} \quad (2.3)$$

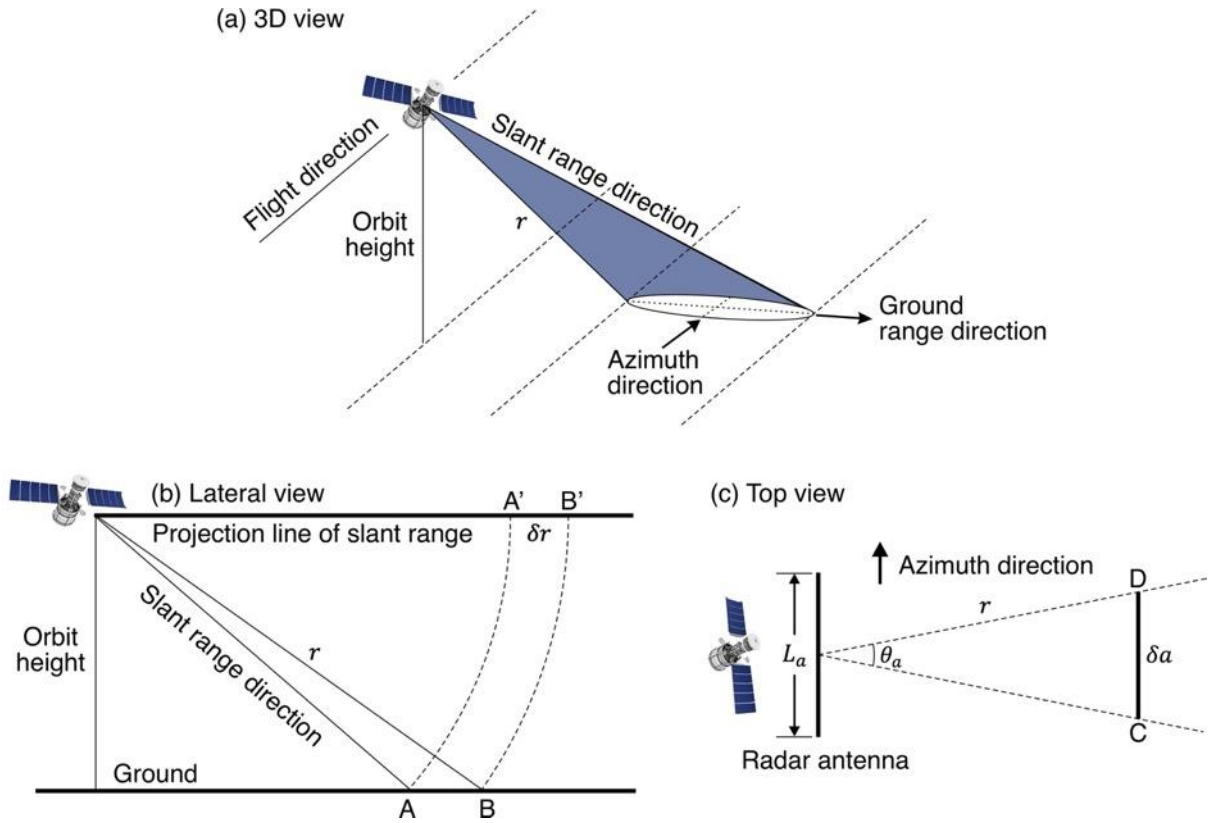


Figure 2.1 Geometry of a side-looking satellite radar in (a) 3D view, (b) lateral view and (c) top view. Flight direction, slant range direction, ground range direction and azimuth direction are indicated in (a). (b) shows the range resolution and (c) illustrates the azimuth resolution.

Equation (2.3) shows that the improvement of the azimuth resolution depends on the enlargement of L_a , but it is unattainable for a resolution of several metres by increasing the physical size of the radar antenna. For example, the wavelength and orbit height of Sentinel-1 are approximately 0.056 m and 693,000 m, so to achieve an azimuth resolution of 15 m, L_a needs to exceed 2,500 m which is impractical. Therefore, SAR was proposed to increase the virtual length of the antenna aperture (synthetic aperture size) by utilizing the Doppler effect of the pulse echo (Hovanessian, 1980). As shown in Figure 2.2a, with the constant motion of the radar, the equivalent length of the along-track beamwidth is $2\delta a$. Thus, the synthetic angular spread of the beam is equal to

$$\theta_a' = \frac{\lambda}{2\delta a} = \frac{L_a}{2r} \quad (2.4)$$

It determines the azimuth resolution of SAR:

$$\delta a' = r\theta_a' = \frac{L_a}{2} \quad (2.5)$$

This is the theoretical resolution obtainable, implying that a smaller antenna can achieve better azimuth resolution (Chan and Koo, 2008). But to produce an appropriate interference pattern between the dipoles of the antenna, the length of the antenna is generally not designed to be too small (e.g., 12.3 m for Sentinel-1, Torres et al., 2012).

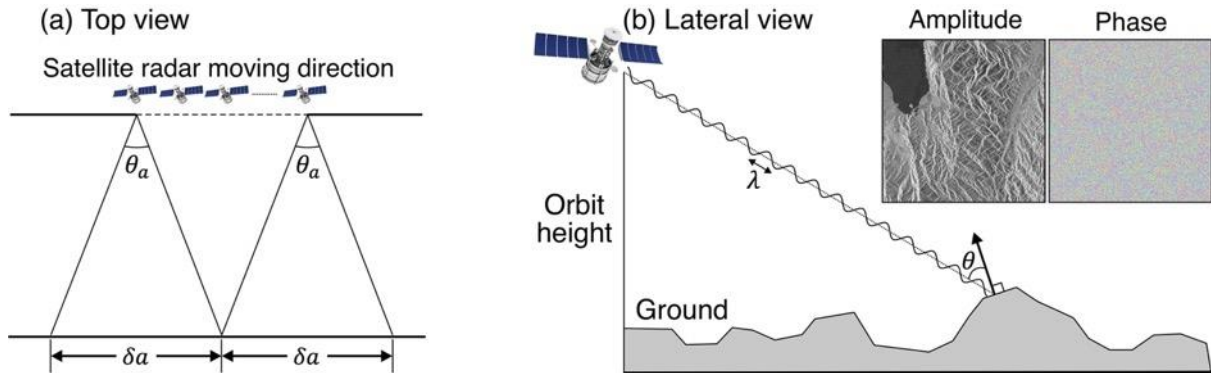


Figure 2.2 Geometry of SAR imaging. (a) Top view illustrating the constant motion of the radar. (b) Lateral view of SAR geometry. θ is the local incidence angle that is defined as the angle between the slant range direction and the normal direction of the ground surface. The SAR amplitude and phase are from the Sentinel-1 image acquired near the Lindu Lake in Central Sulawesi, Indonesia on 7 June 2018.

SAR measurements consist of two kinds of observations: amplitude and phase, as shown in Figure 2.2b. The amplitude (a) is the strength of the backscattered electromagnetic wave, which is related to the reflectivity of ground targets (Deledalle et al., 2011). The phase (φ) is the fraction of a single SAR wavelength, related to the distance between the radar antenna and the ground targets, and varies between $-\pi$ to π radians (Osmanoğlu et al., 2016). A pair of phase and amplitude forms a complex value ($z = ae^{\varphi}$) and each pixel on a SAR image will have such a value.

Due to the side-looking geometry of SAR (Figures 2.1 and 2.2b) and the terrain effect, the SAR measurements are inevitably affected by geometric distortions. As shown in Figure 2.3, the distance of pixels on a small slope facing the satellite radar will have a shorter distance in the SAR image (such as A'B') than the actual distance on the ground (such as AB), which is called the foreshortening effect. This effect requires the slope angle to be smaller than the local incidence angle (Colesanti and Wasowski, 2006), otherwise the layover effect, i.e., the top and bottom of the slope are reversed in the SAR image (such as DE and E'D' in Figure 2.3), will occur. In addition, steep slopes facing away from the satellite will be prevented from receiving SAR signals (Chen et al., 2018), resulting in the shadow effect (such as B'C' and D'F') in the SAR image. To deal with these geometric distortions, a digital elevation model (DEM) is usually used in SAR image formation processing to correct the foreshortening errors (Loew and

Mauser, 2007) and identify the layover and shadow areas for masking (Pairman and McNeill, 1997). Also, descending- and ascending-track SAR images, if available, can be used jointly to compensate for the geometric distortions caused by a single imaging geometry (Sansosti et al., 1999).

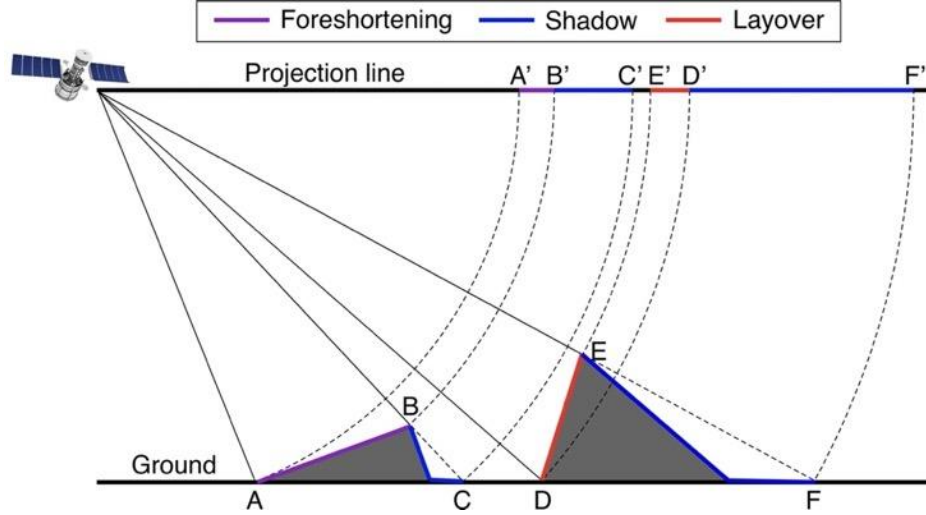


Figure 2.3 Diagram illustration of geometric distortions: foreshortening, shadow and layover.

2.1.2 Principles of InSAR

InSAR, representing interferometric SAR, measures the phase shifts between two repeat-pass SAR acquisitions (primary and secondary acquisitions as shown in Figure 2.4) using interferometry. The process of interferometry is complex multiplication of the SAR pixel values from the first and second acquisitions (assuming z_1 and z_2):

$$z_1 z_2^* = (a_1 e^{i\varphi_1})(a_2 e^{i\varphi_2})^* = a_1 a_2 e^{i(\varphi_1 - \varphi_2)} \quad (2.6)$$

The measured phase change $\Delta\varphi$ (i.e., $\varphi_1 - \varphi_2$) is wrapped between $-\pi$ to π radians and the map of $\Delta\varphi$ is called an interferogram. It is a sum of phases related to many factors such as topography, ground deformation and combined noise (e.g., from atmospheric delays and orbital errors), which can be expressed as:

$$\Delta\varphi = \varphi_{flat} + \varphi_{topo} + \varphi_{defor} + \varphi_{noise} \quad (2.7)$$

where, φ_{flat} is the flat earth phase due to the shape of the Earth; φ_{topo} is the topographic phase related to the topography of the ground surface; φ_{defor} is the phase related to the ground deformation, if any; φ_{noise} is the combined term of noise such as orbital errors, ionospheric and tropospheric delay errors. The flat earth phase (φ_{flat}), topographic phase (φ_{topo}) and ground deformation phase (φ_{defor}) are all related to the range difference ΔR between the two

passes of the SAR satellite. Considering the two-way travel of the SAR signal, ΔR can be converted to the phase of $4\pi/\lambda \cdot \Delta R$ (Bamler and Hartl, 1998).

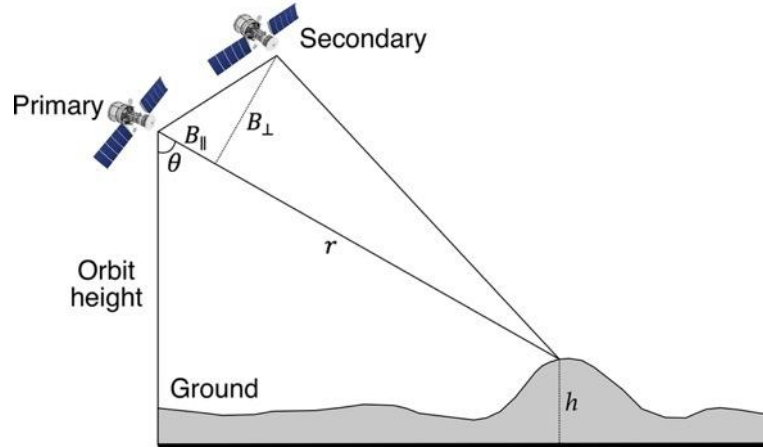


Figure 2.4 Geometry of InSAR based on primary and secondary SAR acquisitions.

The flat earth phase (φ_{flat}) can be estimated based on the SAR satellite orbits because it is proportional to the parallel baseline ($B_{||}$ shown in Figure 2.4) as follows (Pepe and Calò, 2017):

$$\varphi_{flat} = \frac{4\pi}{\lambda} \cdot B_{||} \quad (2.8)$$

The topographic phase (φ_{topo}) is related to the altitude of the ground targets and can be calculated given the terrain height (h) and the perpendicular baseline (B_{\perp} shown in Figure 2.4) (Hanssen, 2001):

$$\varphi_{topo} = -\frac{4\pi}{\lambda} \cdot \frac{B_{\perp}}{r \sin \theta} h \quad (2.9)$$

where, θ is the look angle as indicated in Figure 2.4.

The deformation phase (φ_{defor}) is measured in the LOS and determined by the ground displacement (d_{LOS}) between the primary and secondary SAR acquisitions:

$$\varphi_{defor} = \frac{4\pi}{\lambda} \cdot d_{LOS} \quad (2.10)$$

For the phase noise, in addition to the orbit determination and atmosphere delays, it can also be caused by the temporal change of ground scatterers or volume scattering (e.g., scattering from tree branches) (Dall, 2007). The temporal change of scatterers in watersheds or vegetation areas is usually very intense, resulting in strong phase noise in these areas. The effect of phase noise on InSAR phase measurements can be estimated by the local coherence, which is the cross-

correlation coefficient of the two repeat-pass SAR images estimated over a small moving spatial window (Ferretti et al., 2007) and is useful for generally assessing the InSAR phase quality. For two complex signals z_1 and z_2 , their complex coherence γ is defined as (Touzi et al., 1999):

$$\gamma = \frac{E(z_1 z_2^*)}{\sqrt{E(|z_1|^2)}\sqrt{E(|z_2|^2)}} \quad (2.11)$$

where, $E(x)$ represents the expected value of x . In practice, the maximum likelihood estimator of the coherence magnitude $|\hat{\gamma}|$, as the degree of the sample coherence, is more feasible to use than γ . $|\hat{\gamma}|$ can be estimated over a window of a few pixels in range and azimuth. Assuming that the total number of pixels in the window is N , then (Seymour and Cumming, 1994)

$$|\hat{\gamma}| = \frac{|\sum_{i=1}^N z_{1i} z_{2i}^*|}{\sqrt{\sum_{i=1}^N |z_{1i}|^2} \sqrt{\sum_{i=1}^N |z_{2i}|^2}} \quad (2.12)$$

According to Equation (2.12), each pixel in an interferogram will be assigned a coherence value (0 to 1). Figure 2.5a shows an example of a coherence map in the radar coordinate system, where the estimation window size is 7×7 (hence, $N = 49$). The primary and secondary SAR images for estimating the coherence were acquired on 20 and 26 May 2021, respectively, during which a large earthquake occurred in Maduo, Qinghai Province, China (Mw 7.4, 22 May 2021). In the middle of the map, the coherence is very low (< 0.3) due to the dramatic temporal change of ground scatterers caused by the earthquake.

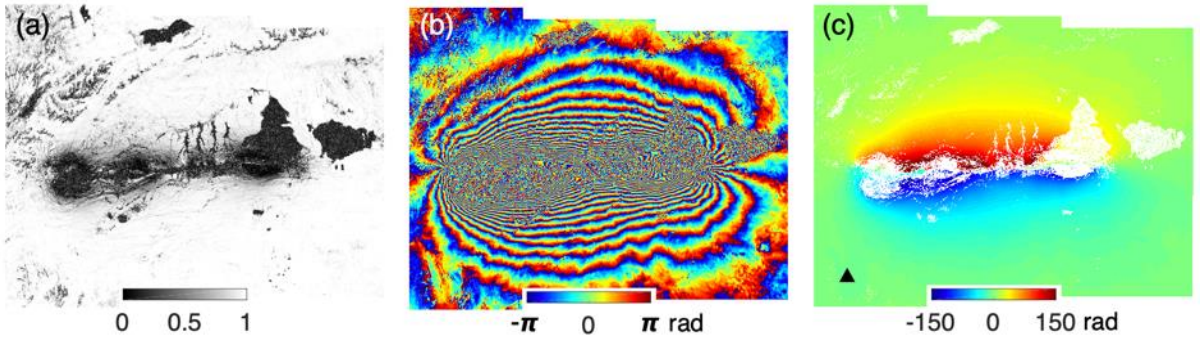


Figure 2.5 Examples of (a) a coherence map, (b) a wrapped interferogram and (c) an unwrapped phase map. The primary and secondary SAR images were acquired on 20 and 26 May 2021, respectively. Note that empty areas in (c) represent masked areas with low coherence (< 0.3).

Regardless of the coherence, the phase on an interferogram is always wrapped between $-\pi$ to π , so it is necessary to unwrap the interferogram to obtain continuous phase values. The process of phase unwrapping is an integral of the phase derivative with the initial condition of zero phase at the reference point (Tribolet, 1977), which determines that the InSAR phase

measurements are relative. After phase unwrapping, each phase value on the interferogram will add an integer multiple of 2π . Figures 2.5b and 2.5c show an example of the phase unwrapping, where Figure 2.5b is the wrapped phase of the interferogram as displayed by a repeating colour scale of $-\pi$ to π , whilst Figure 2.5c is the unwrapped phase without ambiguity (between -150 to 150 radians) relative to the reference point indicated by a black triangle. Note that the InSAR phase in this example is mainly due to the ground deformation because the first two terms in Equation (2.7) have been removed based on the known satellite orbit and DEM.

Another feature of InSAR phase measurement is that its direction is along the LOS. Therefore, when using InSAR to measure the ground deformation, the measured displacement is only a LOS projection component of the actual surface displacement. If the direction of the ground motion is nearly normal to the LOS direction, then its projection in the LOS will be negligibly small, leading to the unavailability of InSAR. Such defect in InSAR projection geometry can be improved by combining satellite radar observations from two different tracks: ascending and descending tracks. When the satellite travels from the south pole to the north pole, it is in the ascending track, while the opposite is in the descending track. Using both ascending- and descending-track InSAR will produce two projection components of the ground movement, as shown in Figure 2.6, which expands the terrain applicability of InSAR.

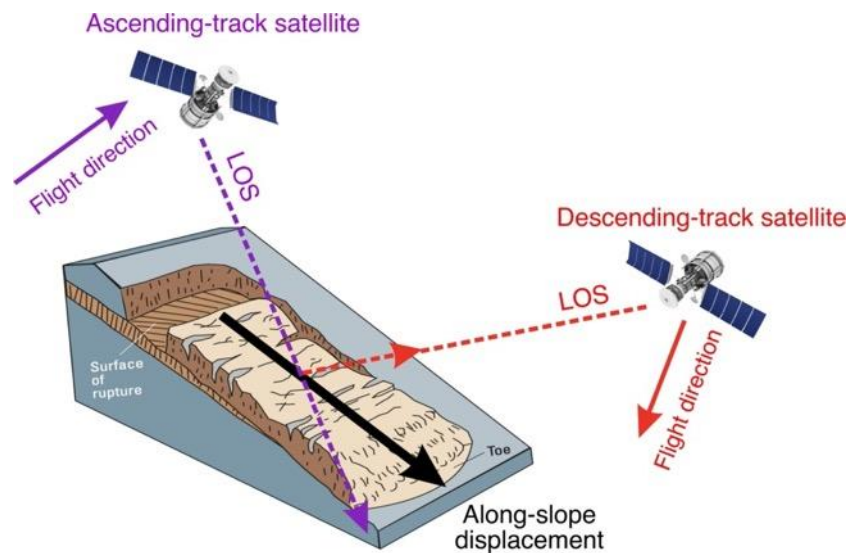


Figure 2.6 Illustration of ascending- and descending-track InSAR geometries (schematic modified from Highland and Bobrowsky, 2008). The black arrow indicates the actual ground movement of a hypothetical landslide. The red and purple arrows indicate the projection components in the descending and ascending LOS, respectively.

2.1.3 Error sources of InSAR and countermeasures

As pointed out in Section 2.1.2, the phase noise of InSAR is related to multiple error sources. In this section, the effect of six major error sources (i.e., orbital errors, DEM residual errors, ionospheric effect, tropospheric delays, decorrelation effect and unwrapping errors) on the InSAR phase measurement and the corresponding countermeasures to mitigate their effect will be introduced.

1. Orbital errors

Orbital errors refer to the errors in the SAR satellite state vectors, resulting in long-wavelength (> 50 km) phase disturbs on interferograms (Massonnet and Feigl, 1998). Their spatial pattern may bias the estimation of long-wavelength surface deformation (e.g, interseismic deformation and far-field coseismic deformation of large earthquakes) (Lohman and Simons, 2005). The conventional method of correcting the orbital errors is to estimate a linear or quadratic surface fitted to the InSAR phase (Massonnet and Feigl, 1998) or re-estimate baseline components (Kohlhase et al., 2003; Rosen et al., 2004). These methods are relatively simple but less accurate than consistently estimating surfaces fitted to the InSAR phase based on a network of interferograms (Biggs et al., 2007) or correcting satellite orbits in the time domain by small-baseline time series inversion (Pepe et al., 2011).

All these methods that treat long-wavelength interferometric phases as orbital errors have the risk of weakening the actual long-wavelength deformation signal (Fattahi and Amelung, 2014). A more reliable way to handle orbital errors is to use the precise orbital products, especially for the recent operational SAR satellite (e.g., Sentinel-1 and ALOS-2) with GNSS receivers on board. For example, the accuracy of Sentinel-1's precise orbital data is typically about 0.5 cm in 3D 1-sigma (Sentinel Online, 2021), which determines very small InSAR uncertainty caused by orbital errors (~ 0.2 mm/yr/100 km for velocity estimation, Fattahi and Amelung, 2014).

2. DEM residual errors

In the estimation of ground deformation, the topographic phase component (i.e., the second term of Equation 2.7) should be removed by using a DEM. As shown in Equation (2.9), the topographic phase is proportional to the perpendicular baseline and the terrain height, so errors in the DEM (Δh) will lead to the following residual errors $\Delta\varphi_{topo}$ in the interferometric phase.

$$\Delta\varphi_{topo} = -\frac{4\pi}{\lambda} \cdot \frac{B_{\perp}}{r\sin\theta} \Delta h \quad (2.13)$$

It is impractical to correct topographic residual errors based on a single interferogram, but with a set of interferograms, DEM errors can be estimated by the InSAR time series inversion. Equation (2.13) shows that the topographic residual errors are baseline-dependent and longer baseline separation between the two SAR acquisitions for interferometry will generate larger DEM residual phases on interferograms. Therefore, the phase due to the DEM errors can be minimised by selecting interferograms with small baselines to produce the InSAR time series. A group of small baseline interferograms also enable the estimation of DEM errors via the least-squares inversion in the interferogram domain that treats temporal low-pass components of the deformation signal and topographic artefacts as unknown parameters, and the InSAR phase on each interferogram as the observation vector (Berardino et al., 2002). After InSAR time series inversion, the obtained phase velocity history further allows the re-estimation of DEM errors via the least-squares inversion in the time domain that treats the phase velocity at each SAR acquisition as the observation vector. The re-estimation is independent of the interferogram network and more accurate in the case of retrieving complex time-variable deformation histories (Fattahi and Amelung, 2013).

3. Ionospheric effects

Microwaves emitted from satellite SAR are affected by the ionosphere during their propagation, resulting in ionospheric distortions in the InSAR phase measurements. The ionospheric distortions cause the group delay and phase advance on the SAR signal due to dispersive ionospheric propagation (Gomba et al., 2017). The magnitude of the distortions depends on the total electron content (TEC) experienced in the propagation of the SAR signal and is inversely proportional to the carrier frequency of the SAR, as shown in Equation (2.14) (Belcher, 2008).

$$\varphi_{iono} = \frac{4\pi K}{cf_0} \cdot TEC \quad (2.14)$$

where, φ_{iono} is the phase shift due to the ionospheric effects, K is a constant $40.28 \text{ m}^3/\text{s}^2$, c is the speed of light and f_0 is the carrier frequency. This equation indicates that L-band SAR systems with lower frequency such as ALOS-1/2 suffer greater ionospheric effects than C-band SAR systems such as Sentinel-1.

To mitigate the ionospheric effects on interferograms, especially for L-band interferometry, ionospheric differential TEC should be estimated precisely. GNSS systems can provide TEC estimates between GNSS satellites and ground receivers (Jakowski et al., 2011), but due to the limitation of spatial measurement density, they are not detailed enough to directly correct the ionospheric delay in SAR interferograms (Meyer, 2011). A more detailed and precise solution is to estimate the differential TEC from SAR data, such as the range split-spectrum method (Rosen et al., 2010), azimuth shift method (Raucoules and Michele, 2010) and Faraday rotation method (Meyer and Nicoll, 2008). Among these methods, the range split-spectrum method that takes advantages of the dispersive feature of the ionosphere and separates the ionospheric phase component from the nondispersive component (e.g., ground deformation related phase) in interferograms is the most applicable on a global scale (Gomba et al., 2016). Therefore, this method is recommended for correcting ionosphere-induced errors if observed in the interferograms, especially for L-band interferograms in polar and tropical areas or under ionospheric anomalies.

4. Tropospheric delays

Tropospheric delays occur during the propagation of satellite SAR microwaves in the troposphere, as a nondispersive component of the interferometric phase in contrast to dispersive ionospheric effects. They are usually expressed in the direction of the zenith, referred to as Zenith Tropospheric Delay (ZTD), and projected to the LOS when used in InSAR. ZTD is composed of two components: Zenith Hydrostatic Delay (ZHD) proportional to the surface pressure and Zenith Wet Delay (ZWD) generated by the tropospheric water vapour (Saastamoinen, 1972). The magnitude of ZTD is related to the temperature, pressure and water vapour content of the troposphere, which can be calculated by integrating the refractivity N between the surface height (h_0) and the top of the troposphere (h_{top}) (Askne and Nordius, 1987).

$$ZTD = 10^{-6} \int_{h_0}^{h_{top}} N dh = 10^{-6} \int_{h_0}^{h_{top}} (N_{hydr} + N_{wet}) dh \quad (2.15)$$

where, N_{hydr} and N_{wet} are the hydrostatic and wet components of the refractivity, respectively.

$$N_{hydr} = k_1 \frac{P}{T} \quad (2.16)$$

$$N_{wet} = k_2' \frac{e}{T} + k_3 \frac{e}{T^2} \quad (2.17)$$

where, P is the total atmospheric pressure, T is the temperature, e is the water vapour pressure, k_1 , k'_2 and k_3 are empirical constants: $k_1 = 77.6 \text{ K hPa}^{-1}$, $k'_2 = 23.3 \text{ K hPa}^{-1}$ and $k_3 = 3.75 \cdot 10^5 \text{ K}^2 \text{ hPa}^{-1}$, according to Smith and Weintraub (1953).

The tropospheric phase delay (φ_{tropo}) of SAR signals is converted from ZTD:

$$\varphi_{tropo} = -\frac{4\pi}{\lambda \cos\theta} ZTD \quad (2.18)$$

where, θ is the incidence angle as indicated in Figure 2.2b.

For InSAR, the tropospheric phase delay on the interferogram ($\Delta\varphi_{tropo}$) is the difference between φ_{tropo} at the primary and secondary SAR acquisition times. According to the physical origin of $\Delta\varphi_{tropo}$, its signal can be divided into two types: turbulent mixing and vertical stratification. The turbulent mixing results from turbulent processes in the troposphere and causes spatial heterogeneities in the refractivity (Hanssen, 2001). The vertical stratification results from different vertical refractivity profiles and is correlated with topography (Massonnet and Feigl, 1998). These two types of tropospheric effects can greatly contaminate the InSAR measurement of surface deformation, causing signals of up to 15-20 cm in the interferogram (Bekaert et al., 2015b), which highlights the necessity of InSAR tropospheric correction.

There are two categories of InSAR tropospheric correction methods: correction without and with external data. The tropospheric correction without external data is based on the interferogram itself and usually requires the assumption of a spatial frequency that is insensitive to deformation (Lin et al., 2010) or the functional relationship between the tropospheric phase and the topography. The assumed relationship for an individual interferogram could be a linear function (Wicks et al., 2002) or a power-law model (Bekaert et al., 2015a). For multi-temporal interferograms, tropospheric delays can be corrected in time series InSAR analysis by using spatiotemporal filters to extract signals with high spatial and low temporal correlation (Ferretti et al., 2001; Hooper et al., 2012). These methods depend on the empirical characteristics of InSAR tropospheric phases and may sometimes not be accurate enough due to the complexity of tropospheric variations (Xiao et al., 2021). On the other hand, the tropospheric correction with external data is independent of InSAR phases and is based on auxiliary tropospheric delay fields estimated from GNSS measurements (e.g., Onn and Zebker, 2006), spaceborne multi-spectral observations (e.g., from the Moderate Resolution Imaging Spectroradiometer (MODIS), Li et al., 2005), or numerical weather models (e.g., Jolivet et al., 2014). The quality

of the correction depends on the precision and availability of those auxiliary models that need to be interpolated in space and time to match the interferogram (Bekaert et al., 2015b).

5. Decorrelation effects

As introduced in Section 2.1.2, coherence (γ) is usually used to assess the phase quality of InSAR as a cross-correlation measurement. The magnitude of the coherence could be reduced due to various factors, which is called InSAR decorrelation. These factors are summarized into four decorrelation terms: spatial baseline decorrelation ($\gamma_{spatial}$), temporal decorrelation ($\gamma_{temporal}$), Doppler centroid decorrelation ($\gamma_{Doppler}$) and thermal decorrelation ($\gamma_{thermal}$) (Zebker and Villasenor, 1992).

$$\gamma = \gamma_{spatial} \cdot \gamma_{temporal} \cdot \gamma_{Doppler} \cdot \gamma_{thermal} \quad (2.19)$$

where, $\gamma_{spatial}$ is due to the spatial separation between the orbits of the primary and secondary SAR satellites, $\gamma_{temporal}$ is related to the temporal change of ground scatterers and $\gamma_{Doppler}$ is due to the difference in the attitude (e.g., yaw and pitch) of the primary and secondary SAR satellites. $\gamma_{thermal}$ is caused by the thermal noise of the satellite radar, which is usually neglected for InSAR (Osmanoğlu et al., 2016).

To suppress decorrelation effects on InSAR, it is better to generate interferograms from two SAR images with relatively small spatial baselines and a short time span (i.e., small temporal baselines). Long-wavelength SAR systems (e.g., L-band) are more suitable for use in vegetated areas due to the stronger resistance to temporal decorrelation than short to medium-wavelength SAR (e.g., X-band and C-band) benefiting from the greater penetration into vegetation. In addition, incoherent pixels that are greatly affected by decorrelation should be masked from interferograms to avoid their interference in the unwrapping and interpretation of InSAR phases.

6. Unwrapping errors

The process of InSAR phase unwrapping recovers the wrapped interferometric phase between $-\pi$ to π radians at each pixel to the unwrapped phase by adding integer multiples of 2π . Several mature phase unwrapping methods have been developed for decades, such as the branch-cut method (Goldstein et al., 1988; Zheng and Da, 2011) which follows a local path to unwrap pixels from a reference point and the minimum cost flow (MCF) method (Costantini, 1998) that finds a global optimisation of the misfit between the wrapped phase gradient and unwrapped gradient (Yu et al., 2019). However, inaccurate estimation of the 2π ambiguities (i.e.,

unwrapping errors) is still difficult to completely avoid due to the discontinuous phase noise in interferograms.

It is possible to detect and correct unwrapping errors after the process of phase unwrapping. The unwrapping errors that cause phase inconsistencies (or jumps) in the unwrapped phase map can sometimes be manually recognised and masked from interferograms (e.g., Jolivet et al., 2012), but a more efficient method is based on the phase closure of interferometric triplets (Biggs et al., 2007). The closure is expressed as follows:

$$\Delta\varphi_{closure} = \Delta\varphi_{12} + \Delta\varphi_{23} - \Delta\varphi_{13} \quad (2.20)$$

where, $\Delta\varphi_{12}$, $\Delta\varphi_{23}$ and $\Delta\varphi_{13}$ are three unwrapped InSAR phases generated from SAR acquisitions at t_1 , t_2 and t_3 . According to the magnitude of the phase closure, InSAR pixels with considerable unwrapping errors should be masked from interferograms. Their unwrapping errors can be further corrected by solving the integer ambiguity using the L1-norm regularized least-squares approximation if a redundant network of interferograms is available (Zhang et al., 2019b).

2.2 Procedures of InSAR processing

This section introduces the standard processing procedures of InSAR. Since this thesis aims at deformation monitoring rather than topographic mapping, the two-pass differential InSAR processing was performed by the GAMMA software (Wegmüller et al., 2016) after collecting primary and secondary SAR Single Look Complex (SLC) data. The specific procedures are as follows.

1. Co-registration. The primary and secondary SAR images must be firstly co-registered to within a small fraction of a pixel (Just and Bamler, 1994), which includes the modelling of the geometric difference between the two SAR images and the resampling of the secondary SAR image to follow the primary SAR geometry.
2. Geocoding. This step will register the SAR images in absolute geographic coordinates (Massonnet and Feigl, 1998) based on a DEM from the Shuttle Radar Topography Mission (SRTM) (Farr et al., 2007).
3. Interferometry following Equation (2.6). In this step, multi-looking that averages the pixel phase in range and azimuth can be used to suppress phase noise.

4. Flat-earth phase removal. This step requires precise orbital data as shown in Equation (2.8). The use of precise orbits can also mitigate orbital errors in generating interferograms.
5. Topographic phase removal. The topographic phase calculated from the DEM will be subtracted from the generated interferogram, which is the key step of differential InSAR.
6. Phase filtering and unwrapping. The interferogram will be filtered by the adaptive spectral filtering method (Goldstein and Werner, 1998) and unwrapped with the MCF method (Chen and Zebker, 2000). In the step of phase unwrapping, InSAR pixels with low coherence (e.g., < 0.3) could be masked to reduce unwrapping errors caused by the decorrelation effect.
7. Tropospheric delay correction. Generic Atmospheric Correction Online Service (GACOS) for InSAR (Yu et al., 2017; Yu et al., 2018b; Yu et al., 2018c) that provides high-resolution ZTD maps based on ECMWF weather models will be used to correct tropospheric delays on the unwrapped phase map.
8. Output of displacement maps. The corrected phase map in radian can be easily converted to a displacement map by multiplying by $\lambda/4\pi$. If strong ionospheric effects and unwrapping errors are observed in the displacement map, the corresponding countermeasures described in Section 2.1.3 can be further applied.

2.3 SAR pixel offset tracking

Pixel offsets refer to the difference in the position of a given ground point in two SAR images (Michel et al., 1999), which can be measured in both the LOS and azimuth directions using the SAR pixel offset tracking technique. This technique is advantageous over InSAR in providing unambiguous ground deformation measurements without the limitation of displacement gradient. The standard SAR pixel offset tracking method uses cross-correlation (Equation 2.21) between image windows of SAR amplitude to estimate range and azimuth offsets (Hu et al., 2014).

$$cc = \frac{\sum_{i=1}^N (p_i - \mu_p)(s_i - \mu_s)}{\sqrt{\sum_{i=1}^N (p_i - \mu_p)^2} \sqrt{\sum_{i=1}^N (s_i - \mu_s)^2}} \quad (2.21)$$

where, cc is the cross-correlation between two spatial windows in the primary and secondary SAR amplitude images, N is the number of pixels in the spatial windows (e.g., N is equal to 1024 for a 32×32 window), i is the pixel index in the windows, p_i and μ_p are the amplitude of the i th pixel and the average amplitude of all pixels in the primary SAR image window,

respectively, while s_i and μ_s are the i th and average amplitudes in the secondary SAR image window.

For each pixel, SAR offset tracking will firstly search for the maximum cross-correlation between moving windows of the co-registered primary and secondary SAR images and then calculate the corresponding pixel offset according to the location of the search windows in the two SAR images. The precision is around 1/10 of one single-look pixel (up to 1/20 given cross-correlation close to 1, Bamler and Eineder, 2005). For example, the pixel spacing of Sentinel-1 in the range direction is about 2.3 m, so the precision of offset tracking is about 0.2 m.

Figures 2.7 and 2.8 show the results of SAR pixel offset tracking for an Mw 7.8 earthquake that occurred in New Zealand on 13 November 2016. The primary and secondary Sentinel-1 images used were acquired on 5 September and 16 November 2016, respectively. Three-dimensional Global Positioning System (GPS) displacements from Hamling et al. (2017) were also collected and projected to the LOS direction for comparison. As shown in the blue rectangles in Figures 2.7a and 2.8a, large near-field deformation is completely retrieved in the range and azimuth direction. The average difference between GNSS and range offset measurements and its standard deviation (STD) are approximately 0.52 m and 0.36 m, respectively (Figure 2.7b). Since the pixel spacing of Sentinel-1 data in the azimuth direction is about 15 m, the theoretical precision of azimuth offsets is only about 1 m, which was validated in Figure 2.8b. In the near field, the performance of azimuth offset tracking is better. The inset of Figure 2.8a (with the same axes as Figure 2.8b) shows an average difference of 0.88 m and an STD difference of 0.5 m between the near-field GNSS and azimuth offset measurements.

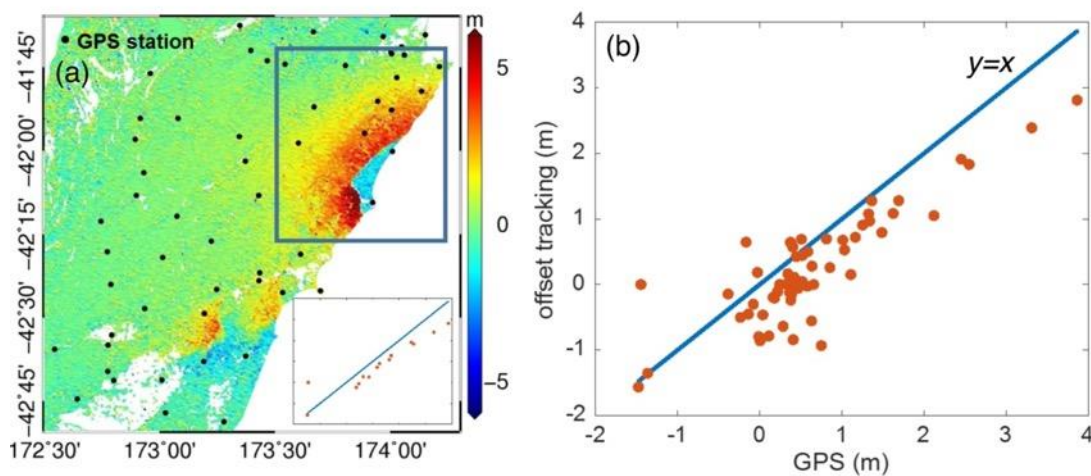


Figure 2.7 Range offset tracking results of the 2016 Mw 7.8 New Zealand earthquake. (a) Range offset displacement map, where the inset is the comparison result of GPS and range offset tracking in the near

field (blue rectangle). (b) Comparison between GPS and range offset tracking results with a correlation of 0.89, an average difference of 0.52 m and an STD difference of 0.36 m.

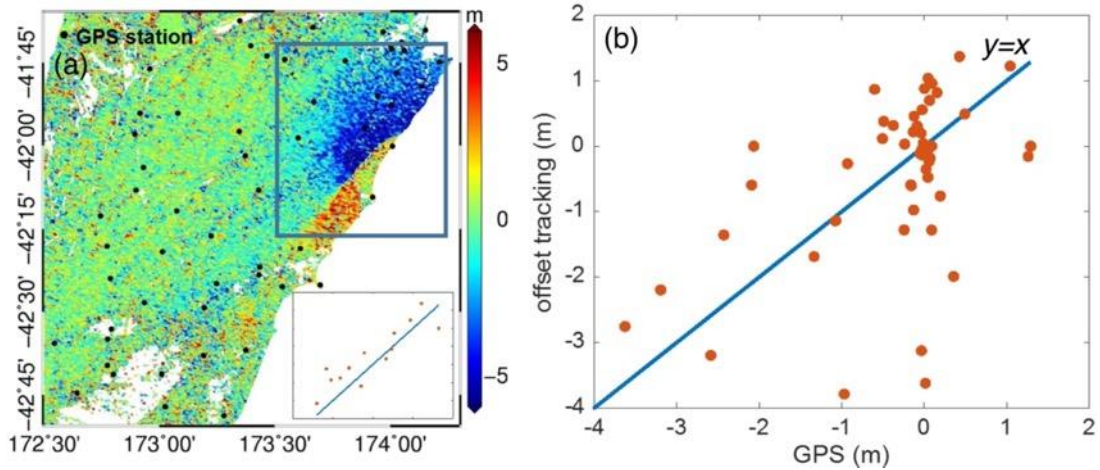


Figure 2.8 Azimuth offset tracking results of the 2016 Mw 7.8 New Zealand earthquake. (a) Azimuth offset displacement map. (b) Comparison between GPS and azimuth offset tracking results. Their correlation is 0.47, with an average difference of 1.14 m and an STD difference of 1.31 m. Near-field comparison is the inset of (a).

SAR pixel offset tracking is also powerful in retrieving the deformation of fast-moving landslides. On 11 October 2018, a large landslide occurred in Baige along the Jinsha River, China (Liu et al., 2020). The landslide without prior detection blocked the river and threatened the downstream hydropower stations. To figure out whether such a large landslide had obvious deformation before the main failure, its pre-failure displacements were estimated by SAR pixel offset tracking after collecting an ALOS-2 ascending-track image pair on 24 July 2017 and 23 July 2018. Offset tracking results (Figure 2.9) show that the accumulated deformation in the range and azimuth direction one year before the landslide failure reached 30 m and 10 m, respectively.

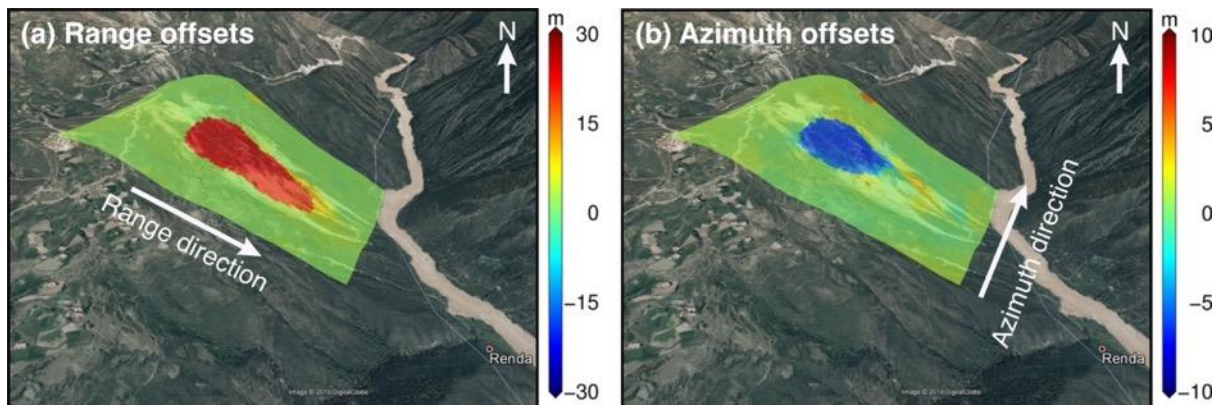


Figure 2.9 Cumulative displacements one year before the failure of the 2018 Baige landslide in the (a) range and (b) azimuth directions measured by SAR pixel offset tracking.

2.4 InSAR stacking technique

InSAR stacking is the simplest technique to estimate the linear velocity of ground deformation based on a network of unwrapped interferograms generated following Section 2.2. This technique assumes the ground deformation follows a linear model and averages a series of interferograms in time (see Equation 2.22), which can significantly reduce random phase noise (Wright et al., 2001).

$$V_{mean} = \frac{\sum_{i=1}^N \varphi_i \Delta t_i}{\sum_{i=1}^N \Delta t_i^2} \quad (2.22)$$

where, V_{mean} is the mean velocity estimated for any pixel in the image, N is the number of interferograms, i is the interferogram index, φ_i is the unwrapped phase of the pixel in the i th interferogram, Δt_i is the temporal baseline in days of the i th interferogram. This equation indicates that the individual interferometric phases are weighted by the time interval of interferometry.

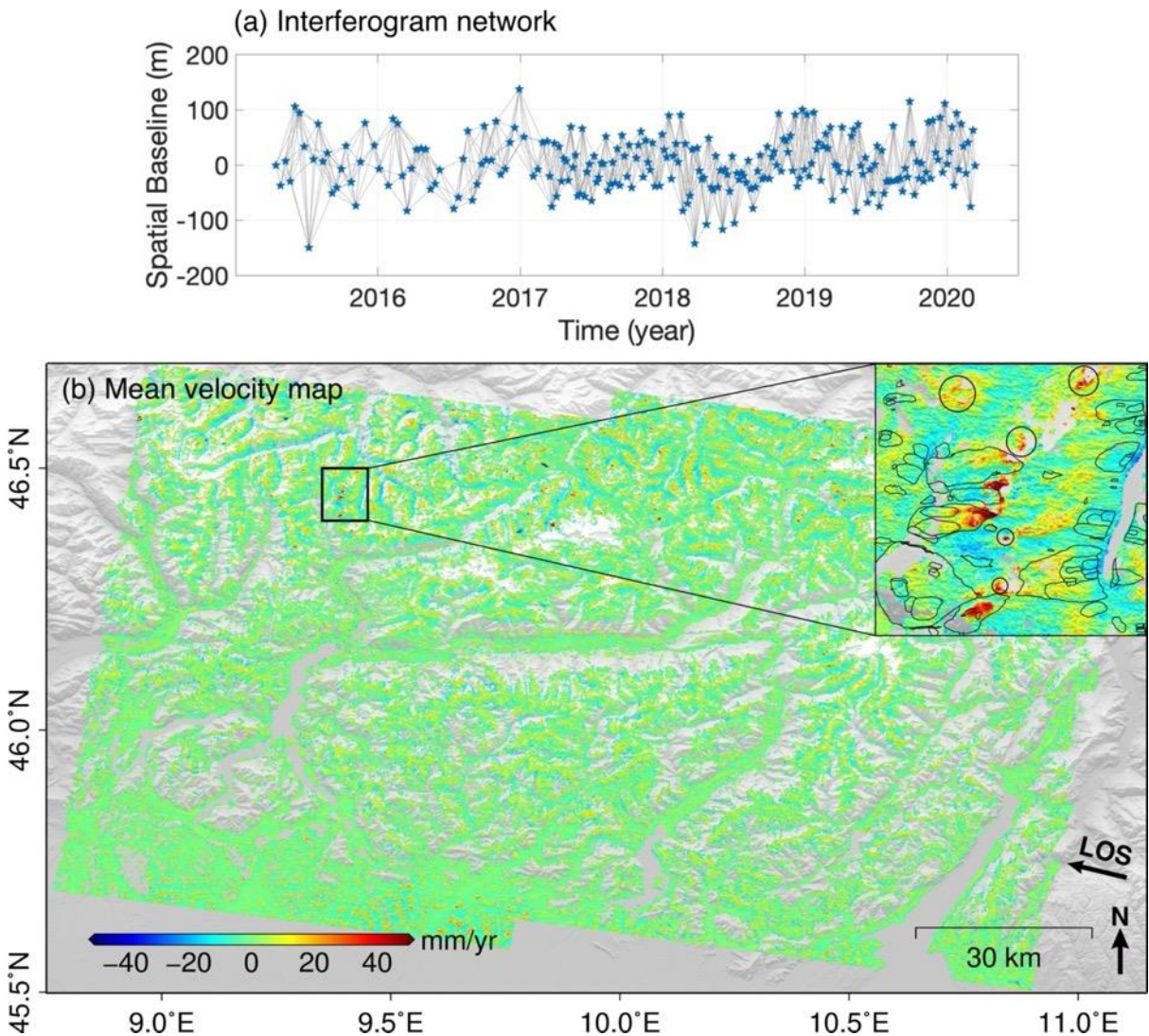


Figure 2.10 Application of InSAR stacking in investigating landslides in the Alps. (a) Sentinel-1 acquisitions (blue stars) and generated interferometric pairs (grey lines). Y-axis indicates the perpendicular baseline length (m) of these pairs. (b) Map of mean InSAR velocity in the LOS. The inset is a zoom-in view of the InSAR velocity, where black polygons are historical landslides recorded in the Italian national landslide inventory and black circles are potential new landslides detected.

An example of the application of the InSAR stacking method in investigating landslides in the Alps is shown in Figure 2.10. A total of 235 Sentinel-1 images in the descending track from 15 April 2015 to 13 March 2020 were collected and paired into 1137 interferograms (Figure 2.10a). Figure 2.10b shows the mean velocity derived from InSAR stacking applied to these interferograms. The velocity map enables the investigation of landslide activity in the study area. As shown in the zoom-in inset of Figure 2.10b, black polygons outline historical landslides recorded in the Italian national landslide inventory and their activities can be updated according to the average velocity of pixels inside the landslide bodies. Also, potential new landslides (black circles in the inset) with considerable velocity can be identified from the velocity map.

This example shows the feasibility of using InSAR stacking to perform a general survey of ground deformation over a large spatial scale due to the simplicity of computation (i.e., Equation 2.22). However, it only provides linear velocity estimates and lacks the temporal information on deformation. Such information is important to track the long-term development of deformation and can be obtained using InSAR time series methods.

2.5 InSAR time series methods

InSAR time series analysis is the advanced InSAR technique to retrieve Earth's surface deformation over time including mean velocity and displacement time series based on a network of multi-temporal interferograms. Some InSAR phase noise terms such as DEM and atmospheric residual errors are also mitigated by the time series inversion. Since 2000, many InSAR time series analysis methods have been developed, such as PSInSARTM (Ferretti et al., 2001), Small BAseline Subset (SBAS) (Berardino et al., 2002), Interferometric Point Target Analysis (IPTA) (Werner et al., 2003), Stanford Method for Persistent Scatterers (StaMPS) (Hooper et al., 2004; Hooper et al., 2007), Coherent Pixels Technique (CPT) (Blanco-Sánchez et al., 2008), SqueeSARTM (Ferretti et al., 2011) and Quasi Persistent Scatterers (QPS) (Perissin and Wang, 2012). All these methods follow the theory of two basic InSAR time series techniques: Persistent Scatterers InSAR (PSI) and SBAS.

2.5.1 Persistent Scatterers InSAR (PSI)

Persistent Scatterers (PS) refers to ground reflectors with strong backscatter properties and constant response to radar over time (Crosetto et al., 2016) and their dimension is smaller than the SAR resolution cell (Ferretti et al., 2001). Since PS can remain coherent over long time intervals without spatial baseline and temporal decorrelation, the interferogram network of PSI is allowed to include long-baseline interferograms based on a single primary SAR acquisition. This means all single SAR images are connected to the same primary SAR image to form interferograms used in PSI.

After generating a stack of single-primary interferograms, the next step of PSI is to select PS candidates (PSC) according to predefined criteria such as amplitude dispersion (Ferretti et al., 2001). The amplitude dispersion D_A of an InSAR pixel is equal to the ratio of the standard deviation (σ_A) to the mean value (μ_A) of its amplitude.

$$D_A = \sigma_A / \mu_A \quad (2.23)$$

InSAR pixels with a D_A of less than 0.25 are typically selected as PSC. They are rarely affected by decorrelation noise and their DEM errors and velocities can be computed by an iterative approximation algorithm starting from interferograms with small spatial and temporal baselines (Ferretti et al., 2001). After removing the estimated DEM errors and constant velocity terms from the interferometric phase of PSC, phase residuals are mainly contributed by atmospheric delays (defined as atmospheric phase screen, APS) and phase noise. By spatially smoothing the phase residuals, the phase noise could be filtered out and the APS is estimated for each PSC, considering the strong spatial correlation of APS. The APS on the sparse PSC grid is then interpolated on the uniform grid of the interferogram using Kriging interpolation.

After APS interpolation and removal from the interferograms, DEM errors and deformation velocity of InSAR pixels are estimated on a pixel-by-pixel basis by maximising the multi-interferogram coherence of each pixel (Colesanti et al., 2003). This is a non-linear inversion process, and the output coherence value indicates the accuracy of the estimation. Those pixels with high coherence (e.g., > 0.75) are thus selected as the PS that are characterized by high phase stability in time. Then, phase unwrapping on a grid of PS will be performed taking advantage of the estimated velocity and DEM error differences between neighbouring PS (Ferretti et al., 2000). Finally, based on the unwrapped phase both in space and time, the displacement time series for each PS with respect to a reference PS will be obtained.

In conclusion, PSI overcomes the spatial baseline and temporal decorrelation problems and can precisely retrieve long-term continuous deformation of PS by mitigating DEM errors and APS. However, the performance of PSI in non-urban areas is poor due to the low PS density and quality in vegetated or low-reflectivity areas (Crosetto et al., 2016), which limits its application in monitoring earthquakes or landslides that are prone to occur in complex natural environments. Such limitation of PSI highlights the usefulness of distributed scatterers (DS) that are composed of small random scatterers without one being dominant, because DS are widely distributed in natural environments such as bare soil, sparsely vegetated or desert lands (Dong et al., 2018).

2.5.2 Small Baseline Subset method (SBAS)

SBAS is the first typical DS method, which uses a multi-primary interferogram network with small baselines to target DS and analyse their temporal movements. In the process of generating interferograms, SAR images are co-registered to a single image and paired with multiple temporally adjacent images for interferometry (as shown in Figure 2.10a). The baselines of interferograms can be limited to less than 400 m in space and less than 1 year in time (Osmanoğlu et al., 2016) to minimise InSAR decorrelation. These multi-primary small baseline interferograms with flat-earth and topographic phases removed will be unwrapped to be used in SBAS (Berardino et al., 2002) and they mainly include deformation and atmospheric phase components in addition to phase noise.

Assuming that $N + 1$ co-registered SAR images form M differential interferograms, let $\phi^T = [\phi(t_1), \phi(t_2), \dots, \phi(t_N)]$ be the unknown phase vector of N images (not $N + 1$ due to the need of one reference image, $\phi(t_0) = 0$) and $\Delta\phi^T = [\Delta\phi_1, \Delta\phi_2, \dots, \Delta\phi_M]$ be the vector of the known unwrapped phase of M interferograms. Accordingly, the interferogram network can be expressed as:

$$\Delta\phi = A\phi \quad (2.24)$$

where, A is a $M \times N$ design matrix related to the network structure and it is in the form of Equation (2.25) if $\Delta\phi_1 = \phi(t_2) - \phi(t_1)$, $\Delta\phi_2 = \phi(t_3) - \phi(t_1)$ and $\Delta\phi_3 = \phi(t_2) - \phi(t_0)$.

If all the SAR acquisitions are grouped in a single small baseline subset (such as Figure 2.10a), then $M \geq N$ and the rank of A is N . Therefore, Equation (2.24) can be solved in the least-squares sense as Equation (2.26).

$$A = \begin{bmatrix} -1 & 1 & 0 & 0 & \dots \\ -1 & 0 & 1 & 0 & \dots \\ 0 & 1 & 0 & 0 & \dots \\ \dots & \dots & \dots & \dots & \dots \\ \dots & \dots & \dots & \dots & \dots \end{bmatrix} \quad (2.25)$$

$$\hat{\phi} = (A^T A)^{-1} A^T \Delta\phi \quad (2.26)$$

On the other hand, it is possible that SAR acquisitions are separated into different small baseline subset due to the existence of large baselines, resulting in a rank deficiency of A (Lanari et al., 2004). In such a case, Equation (2.24) should be converted to an observation equation that takes the mean phase velocity between temporally adjacent acquisitions as the input observations and solved via the single value decomposition (SVD) method (Berardino et al., 2002).

SBAS also accounts for the estimation of DEM residual errors by adding the topographic residual term Δh to Equation (2.24) according to Equation (2.13).

$$\Delta\phi = [A, A_{topo}] \begin{bmatrix} \phi \\ \Delta h \end{bmatrix} \quad (2.27)$$

wherein

$$A_{topo}^T = \left[\frac{-4\pi}{\lambda} \frac{B_{\perp 1}}{r \sin\theta}, \frac{-4\pi}{\lambda} \frac{B_{\perp 2}}{r \sin\theta}, \dots, \frac{-4\pi}{\lambda} \frac{B_{\perp M}}{r \sin\theta} \right] \quad (2.28)$$

where, $B_{\perp 1}, B_{\perp 2}, \dots, B_{\perp M}$ are the perpendicular baseline of the first, second to M th interferograms. The estimated $\hat{\phi}$ is a combination of deformation and APS components. To separate them, SBAS uses low-pass filtering performed in 2D space and high-pass filtering performed in time to extract the APS (Lanari et al., 2007) considering its high spatial and low temporal correlation (Ferretti et al., 2000), and finally obtains the deformation signals by subtracting the APS from $\hat{\phi}$.

2.5.3 StaMPS

StaMPS is an open-access InSAR time series software that was originally developed as a new PS method (Hooper et al., 2004) but also supports SBAS in its later version (Hooper, 2008).

1. PS mode

StaMPS redefines PS as scatterers with high phase stability in space and time. Amplitude dispersion proposed in PSI is also used for the initial selection of PSC in StaMPS, but its threshold (0.4) is set higher than that in PSI (0.25) to include more PSC for subsequent phase analysis. In the phase analysis, since the input interferograms have been flattened and topographically corrected, the wrapped phase $\varphi_{x,i}$ of the x th PSC in the i th interferogram can be expressed as (Hooper et al., 2007):

$$\varphi_{x,i} = W\{\phi_{D,x,i} + \phi_{A,x,i} + \Delta\phi_{O,x,i} + \Delta\phi_{\theta,x,i} + \phi_{N,x,i}\} \quad (2.29)$$

where, $W\{\cdot\}$ is the wrapping operator, $\phi_{D,x,i}$ is the phase change due to deformation of the PSC, $\phi_{A,x,i}$ is the APS term, $\Delta\phi_{O,x,i}$ is the residual phase due to the orbital errors of the satellite, $\Delta\phi_{\theta,x,i}$ is the residual phase due to the look angle errors. For DS pixels, $\Delta\phi_{\theta,x,i}$ is equal to DEM errors, but for PS pixels, it is also contributed by the range difference between the position of the dominant scatterer and the ground patch centre resolved by the pixel (Hooper et al., 2007). $\phi_{N,x,i}$ is a mixed term of other noise such as coregistration errors and thermal noise. $\phi_{D,x,i}$, $\phi_{A,x,i}$, $\Delta\phi_{O,x,i}$ and part of $\Delta\phi_{\theta,x,i}$ are spatially correlated, which can be estimated by calculating the average phase of a PSC and its surrounding PSC (Hooper et al., 2004) or by combining an adaptive band-pass filter and a low-pass filter (Hooper et al., 2007). After subtracting these spatially correlated terms from $\varphi_{x,i}$, the remaining phase except for $\phi_{N,x,i}$ is the spatially uncorrelated part of $\Delta\phi_{\theta,x,i}$, which is approximately linear to the look angle errors (mainly DEM errors) and perpendicular baseline and can be estimated in the least-squares sense. Thus, a measure of the PSC phase stability, the temporal coherence, is defined as follows (Hooper et al., 2007).

$$\gamma_x = \frac{1}{M} \left| \sum_{i=1}^M \exp \left\{ \sqrt{-1(\varphi_{x,i} - \tilde{\varphi}_{x,i} - \Delta\hat{\phi}_{\theta,x,i}^u)} \right\} \right| \quad (2.30)$$

where, γ_x is the temporal coherence of the x th PSC pixel, $\tilde{\varphi}_{x,i}$ is a wrapped estimate of the spatially correlated terms, $\Delta\hat{\phi}_{\theta,x,i}^u$ is an estimate of the spatially uncorrelated part of $\Delta\phi_{\theta,x,i}$, and M is the number of interferograms. The calculation of γ_x is an iterative process, where each iteration will discard low-coherence PSC and recalculate the coherence until it stabilises.

Then, StaMPS selects the final PS based on the temporal coherence in a probabilistic fashion, in which a coherence threshold is determined to maximise the number of real PS while suppressing the fraction of random phase pixels (Hooper et al., 2004). The amplitude dispersion is also considered in this step for a more accurate estimation of PS probability (Hooper et al.,

2007). After the selection of PS, the wrapped interferometric phase of these PS with spatially uncorrelated noise (mainly DEM errors) removed will be unwrapped by a 3D unwrapping method (Hooper and Zebker, 2007) that relies on first unwrapping in time (1D), then estimating the probability density functions in space and using cost-maps (Chen and Zebker, 2001) to optimize spatial unwrapping (2D).

After 3D unwrapping, spatially correlated noise such as APS residuals, orbital residual errors and the spatially correlated part of look angle errors will be filtered from the unwrapped phase using a combination of spatial and temporal filters based on a Delaunay network connecting all PS pixels (Hooper et al., 2007). Finally, the velocity and displacement time series in the LOS will be obtained from the filtered unwrapped phase.

2. SBAS mode

If a multi-primary small baseline interferogram network is available, StaMPS also supports SBAS processing but on the basis of single-look wrapped interferograms, which is in contrast with standard SBAS methods (Berardino et al., 2002) that usually works with multi-looked unwrapped phase. In StaMPS-SBAS, the pixels to be processed are referred to as slowly-decorrelating filtered phase (SDFP) pixels (Hooper, 2008). The SDFP pixels are also initially selected through the amplitude analysis, as in PS mode, but the indicator is the amplitude difference dispersion $D_{\Delta A}$ rather than the amplitude dispersion in PSI.

$$D_{\Delta A} = \sigma_{\Delta A} / \mu_A \quad (2.31)$$

where, $\sigma_{\Delta A}$ is the standard deviation of the amplitude difference between primary and secondary SAR acquisitions at a pixel and μ_A is the mean amplitude value of the pixel. Pixels with $D_{\Delta A} \leq 0.6$ are selected as the SDFP candidates.

SDFP pixels are selected from candidates using the same phase analysis algorithm as PS selection (as described in the PS mode). Then, the wrapped phase of SDFP pixels with spatially uncorrelated errors corrected will be unwrapped in three dimensions and the unwrapped phase will be filtered out of spatially correlated errors as in the PS mode. Finally, the filtered unwrapped phase of each SDFP pixel will be inverted to a time series of phase changes by the least-squares inversion.

This thesis chooses the SBAS mode of StaMPS as the InSAR time series analysis method considering its comprehensive advantages over the StaMPS-PS mode and the standard SBAS.

Compared to the PS mode, StaMPS-SBAS can analyse more coherent pixels in natural terrains and reduce spatial aliasing in the case of high deformation velocity (Hooper, 2008) due to the use of small baseline interferograms. Compared to standard SBAS, the StaMPS-SBAS has advantages in full-resolution processing (single-look without loss of spatial resolution) and more robust 3D phase unwrapping (Hooper et al., 2012).

Chapter 3. Combining multiple satellite observations to model the 2019 Mw 7.5 New Ireland earthquake

This chapter aims to fully capture large transient deformation by combining multiple satellite observations, which overcomes the decorrelation problem of InSAR when observing large magnitude coseismic deformation. The study in this chapter has been published in *Remote Sensing* (<https://doi.org/10.3390/rs11232767>).

The case studied in this chapter is the 2019 Mw 7.5 New Ireland earthquake that occurred in an equatorial area where the dense vegetation and large gradient of coseismic deformation prevent C- or X-band InSAR from acquiring coherent phase measurements. Therefore, multiple remote sensing techniques including the L-band InSAR, the range and azimuth offset tracking of SAR intensities and the optical image offset tracking were employed together to map the co-seismic deformation field and to determine the slip distribution. The surface rupture was clearly and consistently captured by all offset observations, with the ground fault trace striking at an angle of 315° and extending over 10 km. An iterative weighting strategy based on the residual root mean square of inversions using individual datasets was developed to determine the relative weight of each dataset, allowing for the joint inversion of the fault geometry, the refinement of the dip angle and the determination of the best fitting slip distribution. The relationship between the aftershocks and Coulomb failure stress changes was also discussed.

3.1 Introduction

On 14 May 2019 (UTC 12:58:25), an Mw 7.5 earthquake occurred in New Ireland, eastern Papua New Guinea (Figure 3.1). It ruptured the Weitin fault, a strike-slip fault across the south of New Ireland, along the boundary between the South Bismarck and North Bismarck microplates. The epicentre initially estimated by U.S. Geological Survey (USGS) was 4.081°S , 152.569°E , with a focal depth of ~ 10.0 km, indicating shallow strike-slip faulting. The earthquake was followed by 43 aftershocks with magnitude $> \text{Mb } 4.0$ (red dots in Figure 3.1) within five days of the mainshock. Two moderate aftershocks on 14 May, both with a magnitude of Mb 5.0, respectively occurred ~ 40 min and ~ 100 min after the main event and were located ~ 18 km southeast and ~ 70 km northwest of the mainshock. However, the largest aftershock (purple beach ball in Figure 3.1) occurred on 17 May 2019 with a magnitude of Mb 5.9, located ~ 74 km southeast of the main event. The earthquake catalogue from USGS shows that the focal depth of the three aftershocks is 10.0, 12.1 and 21.0 km, respectively.

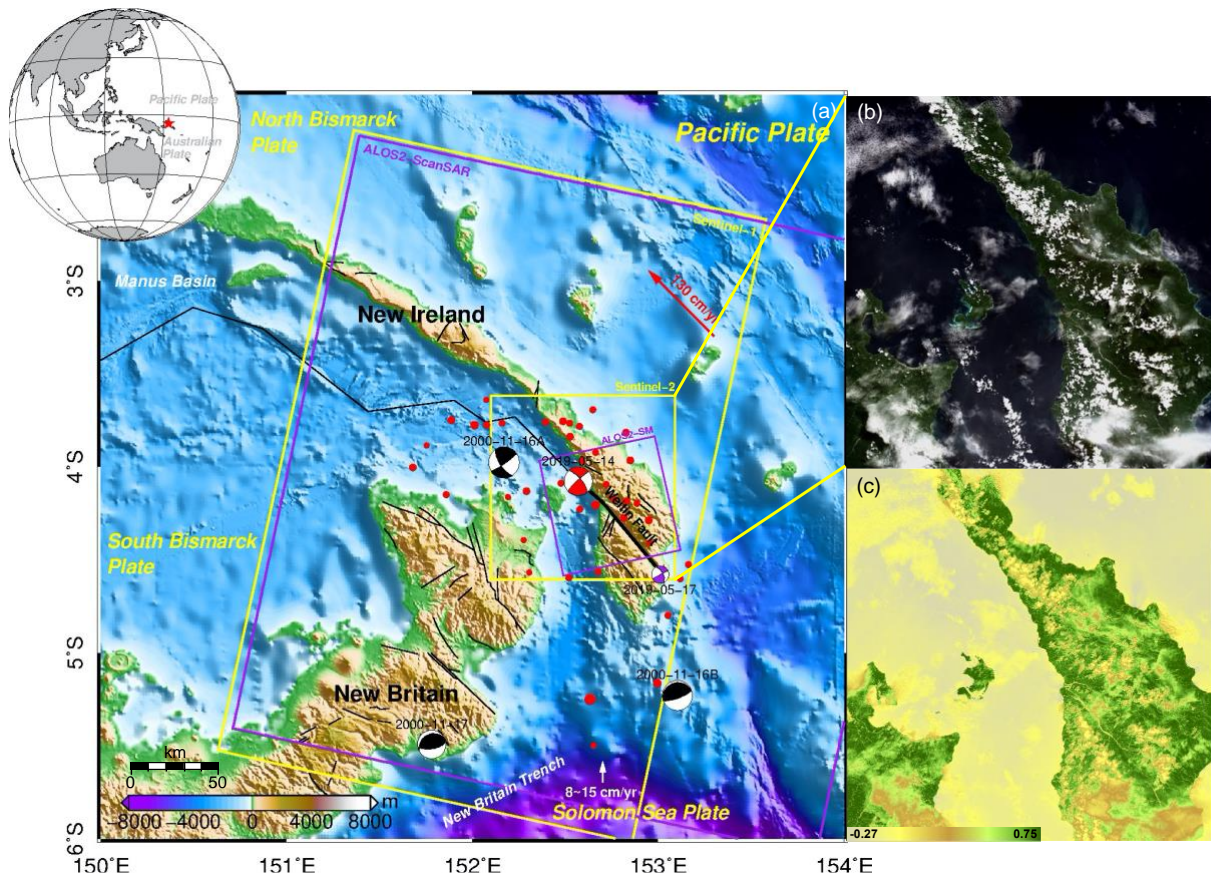


Figure 3.1 Seismotectonic setting of the 2019 New Ireland earthquake. (a) Tectonic background of the study area. The inset global map shows the relative location between New Ireland, the Pacific Plate and the Australian Plate, where the red star denotes the location of this earthquake. The red beach ball represents the focal mechanism of the 2019 New Ireland earthquake from USGS while the purple one represents its largest aftershock. The red dots denote all other aftershocks five days after the main event recorded by USGS. The black beach balls represent three large historical earthquakes in this region that occurred in November 2000. The solid black lines denote the major active faults in the region. The black line above the mainshock is the offshore extension of the Weitin fault. The yellow rectangles outline the spatial coverage of Sentinel-1 (descending track 16) and Sentinel-2 (track 116) frames. The purple rectangles outline the spatial coverage of ALOS-2 ScanSAR (descending track 6) and ALOS-2 strip map (track 108) frames. (b) Natural colour display of Sentinel-2 data imaged on 26 May 2019. (c) Normalized Difference Vegetation Index (NDVI) map calculated from the near-infrared spectrum (band 8) and red range of the spectrum (band 4) of Sentinel-2 image, where large values (from 0.6 to 0.8) indicate temperate or tropical forests.

Papua New Guinea, located in a complex tectonic setting between the Pacific Plate and the Australian Plate, is one of the most seismically active regions in the world. Its eastern areas (Figure 3.1a) accommodate several microplates (e.g., the Solomon Sea, South Bismarck, and North Bismarck microplates) composing part of the edge of the Pacific and Australian plates (Llanes et al., 2009; Holm et al., 2016). As a transform boundary (Baldwin et al., 2012), more than 35 earthquakes with a magnitude greater than Mw 7 occurred since 1970. These include a

well-documented Mw 8.0 earthquake that occurred on 16 November 2000, 45 km to the northwest of the 14 May 2019 event, which was followed by two Mw 7.8 aftershocks on the subduction zone between the Solomon Sea and Pacific plates (Figure 3.1a). Tregoning et al. (2005) used teleseismic data to relocate the aftershocks and concluded that the accumulated strain on the Weitin fault was fully released during the mainshock because no aftershocks were located in the upper 15 km of the Weitin fault. Determining the coseismic slip distribution of the 16 November 2000 event constrained by the teleseismic wave data, Geist and Parsons (2005) modelled the changes in the Coulomb failure stress which they inferred had contributed to the first Mw 7.8 thrust aftershock. However, Park and Mori (2007) carried out inversions using teleseismic P waveforms and showed that the static stress triggering mechanism hardly explains all of the triggered events in the earthquake sequence. To conclude, uncertainties exist due to limited observations for the investigation of the interaction of the faults in New Ireland and subduction trenches (e.g., New Britain trench), especially during large strike-slip earthquakes that occurred on the Weitin fault. Therefore, the 14 May 2019 event, covered for the first time by abundant geodetic observations with a high spatial resolution, provides a great opportunity to study the detailed fault behaviour and potential seismic hazards around New Ireland.

Interferometric Synthetic Aperture Radar (InSAR) has been widely used for tectonic and coseismic studies since the early 1990s (Massonnet et al., 1993; Parks et al., 2012; Hamling et al., 2017). However, their phase measurements may significantly lose coherence in this heavy vegetation area (Figures 3.1b and 3.1c), especially for sensors with short wavelengths such as X- and C- bands, limiting their usage in the tropical region. The decorrelation and unwrapping problems intensify for areas with large displacement gradients. It is, therefore, reasonable to employ multiple remote sensing observations which are feasible over vegetation-covered areas such as the L-band interferometric phase measurements (e.g., from ALOS-2), the C-band SAR pixel offsets (e.g., from Sentinel-1) and the optical image pixel offsets (e.g., from Sentinel-2). SAR pixel offset tracking based on SAR amplitude images as illustrated in Section 2.3, also referred to as incoherent speckle tracking, can provide unambiguous surface displacement in both the Line of Sight (LOS) and azimuth directions by cross-correlating intensities (Michel et al., 1999; De Zan, 2014; Wang and Jónsson, 2015). Optical based offset tracking with a sub-pixel precision can also measure ground deformation regardless of displacement gradient (Leprince et al., 2007) in cloudless areas. Observations from these methods have been individually used for earthquake modelling (Wang et al., 2017; Xu et al., 2018; Socquet et al., 2019), but research combining them all for joint modelling still needs to be explored, given

their different satellite geometries and observation accuracies, as well as the requirement for a proper weighting strategy.

In this study, the observations mentioned above are combined using an iterative weighting strategy for joint earthquake modelling. Firstly, satellite data from Sentinel-1, Sentinel-2 and ALOS-2 PALSAR-2 in both ScanSAR and strip map (SM) modes were collected and processed to map the coseismic deformation field and determine the surface trace of the ruptured fault. With the assumption that the earth crust model is elastic half-space homogeneous (Okada, 1985), finite-fault slips for the earthquake were then jointly inverted from these satellite images. Coulomb failure stress changes were finally calculated and discussed for the uncertainty of the interaction between the Weitin fault and subduction trenches.

3.2 Data and processing strategy

3.2.1 Sentinel-1 data and interferometry

Sentinel is a series of earth observation missions developed and operated by the European Space Agency (ESA) for the Copernicus initiative. The Sentinel missions are operated day and night, providing complete, free and open-access products through the Copernicus Open Access Hub (<https://scihub.copernicus.eu>). As the first of five Sentinel missions, Sentinel-1 performs C-band SAR imaging with a constellation of two satellites, Sentinel-1A and Sentinel-1B, running on the same orbital plane. Since the launch of the first satellite in April 2014, Sentinel-1 can offer repeated wide swath (~250 km) coverage and acquire imagery globally every 6 or 12 days regardless of the weather with the mode of Terrain Observation with Progressive Scans (TOPS) (Torres et al., 2012).

The Sentinel-1 image pair used in this study was captured on 13 May 2019 and 25 May 2019 from descending track 16 and the Sentinel-1 data was mosaicked from two consecutive frames to cover a larger spatial extent. Considering the ruptured fault is a left-lateral northwest-striking fault with long-standing motion (Tregoning et al., 1999), I discarded the usage of the ascending track of Sentinel-1. The GAMMA software (Werner et al., 2000) was used to process SAR images in the Single Look Complex format (level 1). To suppress speckle noise, a 20×4 multi-looking factor was applied in range and azimuth. Compared with traditional InSAR as described in Section 2.2, processing Sentinel-1 TOPS data requires a much more stringent image registration due to the rotation of the antenna during the observation of each burst. The accuracy of coregistration in azimuth should be better than 0.001 of a pixel to avoid phase jumps at the interface between adjacent bursts (Yagüe-Martínez et al., 2016). To achieve such high accuracy,

an iterative amplitude matching procedure was conducted on the SLC after estimating terrain-induced pixel offsets with precise orbits from ESA and a 30 m digital elevation model (DEM) from Shuttle Radar Topography Mission (SRTM) (Farr et al., 2007). Once the azimuth offset correction is smaller than 0.02 pixels (Xu, 2017), a spectral diversity method considering the interferometric phase in the burst overlap areas was used to further reduce coregistration errors.

Upon the completion of high-accuracy coregistration, the conventional two-pass InSAR method was followed. The first step was to simulate the topographic phase with the SRTM DEM, from which the differential interferogram was generated. The second step was to filter the interferogram using adaptive spectral filtering (Goldstein and Werner, 1998) and unwrap it using the Minimum Cost Flow (MCF) method (Chen and Zebker, 2000). After the above processing, however, I found that the low coherence in this region made the unwrapping extremely difficult. The strong decorrelation is mainly caused by the heavy vegetation from tropical rainforests and the large coseismic displacement gradient in the near field. Therefore, Sentinel-1 InSAR in C-band is not suitable for measuring the coseismic deformation of this strong New Ireland earthquake, and other techniques such as SAR pixel offset tracking and other long-wavelength SAR data such as ALOS-2 data should be considered.

Table 3.1 Satellite data used in this chapter

Satellite	Flight direction	Reference Date	Repeat Date	Perpendicular Baseline (m)
Sentinel-1	Descending, right looking	13 May 2019	25 May 2019	1.1
Sentinel-2	Orthogonal looking	11 May 2019	26 May 2019	-
ALOS-2	Descending, right looking	12 May 2019	23 June 2019	114.6
ALOS-2	Ascending, right looking	09 March 2019	01 June 2019	598.9

3.2.2 Sentinel-1 offset tracking

As illustrated in Section 2.3, SAR pixel offset tracking will firstly search for the maximum cross-correlation between primary and secondary image windows after the high-accuracy coregistration, and then it will calculate the offsets between corresponding pixels. Following the offset tracking module in GAMMA software (Wegmüller et al., 2016), I used an SLC offset search window of 300×60 pixels and a cross-correlation function window of 32×32 pixels. The cross-correlation coherence threshold for acceptance of offsets was set as 0.1. After the offset tracking, I further used a median filter (9×9) to reduce the noise. Figure 3.2a shows the Sentinel-1 range offsets, where the red star indicates the epicentral location. Although the offsets are not clean enough and terrain-related residuals still seem to exist, near-field coseismic deformation can be clearly seen. The maximum surface displacement in the range direction

reaches 2 m. Another finding is that the ground trace of the ruptured fault, extending over 10 km, can be easily recognized from the offset map.

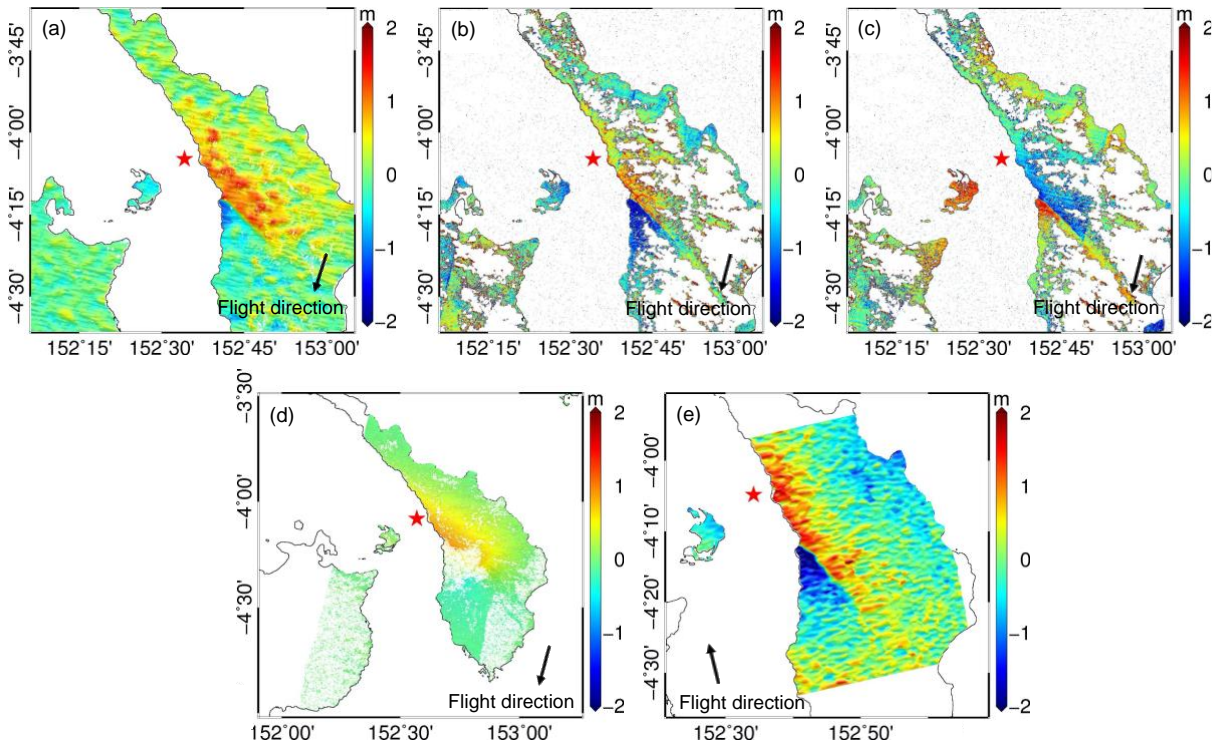


Figure 3.2 Coseismic displacement maps of the 2019 New Ireland earthquake from Sentinel and ALOS-2 data. (a) Observed offsets in the range direction from descending Sentinel-1 satellite track 16. (b) Observed offsets in the north direction from Sentinel-2 satellite track 116. (c) Observed offsets in the east direction from the same Sentinel-2 images. The on-land areas covered by the cloud are masked in (b) and (c). (d) InSAR deformation in the LOS from descending ALOS-2 satellite track 6 (ScanSAR mode). (e) Observed offsets in the azimuth direction from ascending ALOS-2 satellite track 108 (SM mode). The red star denotes the epicentre of this event estimated by USGS.

3.2.3 Sentinel-2 data and offset tracking

Sentinel-2 is the Sentinel mission that aims at providing multi-spectral and high-resolution optical imagery, carrying an optical instrument payload that samples 13 spectral bands: four bands at 10 m, six bands at 20 m and three bands at 60 m spatial resolution (ESA, 2019). With the launch of the first Sentinel-2 satellite in June 2015, the mission can offer systematic global coverage of land surfaces with an orbital swath width of 290 km and a high revisit frequency (e.g., five days at the equator) (Drusch et al., 2012).

The pre- and post-earthquake Sentinel-2 images (11 May 2019 and 26 May 2019) used in the study are relatively cloud-free in the near field. I chose two images in band 8 with a resolution of 10 m and processed them using the COSI-Corr software package (Leprince et al., 2007). I

used a sliding multi-scale window (initial 64×64 and final 32×32 pixels), a step size of four pixels and four robustness iterations to optimize the masking of noise frequencies (Socquet et al., 2019). To further reduce noise, I discarded outliers greater than 5 m, detrended the displacement map with a linear ramp estimated from a spatial subset that excluded the area near the rupture, and denoised the results with a non-local means filter (Buades et al., 2008).

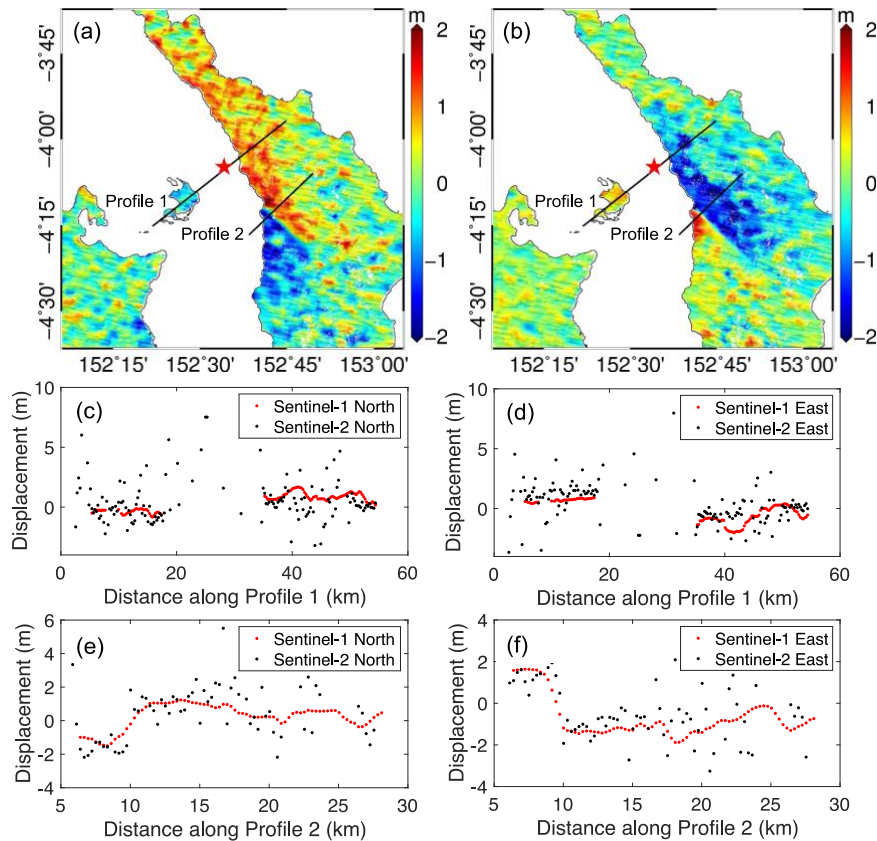


Figure 3.3 Horizontal deformation of the 2019 New Ireland earthquake decomposed from Sentinel-1 offsets. (a) Coseismic deformation map in the north and (b) east. (c) Coseismic displacement in the north from Sentinel-1 and Sentinel-2 offsets along Profile 1 and (e) Profile 2. (d) Coseismic displacement in the east along Profile 1 and (f) Profile 2.

Figures 3.2b and 3.2c show the final displacement map in the north and east direction, respectively, where cloud-covered areas on land are masked. The surface trace of the fault rupture is visible on both maps and is consistent with that displayed in the Sentinel-1 range offset map (Figure 3.2a). To compare Sentinel-1 and Sentinel-2 deformation measurements in the same direction, I converted Sentinel-1 range and azimuth offsets to horizontal displacements with Equation (3.1), where θ and α are the incidence and heading angles of Sentinel-1, respectively. The vertical component is not included in the equation since the fault rupture is mainly controlled by strike-slip motion. As shown in Figures 3.3a and 3.3b, the horizontal deformation map from Sentinel-1 offsets is noisy due to the added azimuth offsets. But the

deformation pattern approximately matches those in the Sentinel-2 deformation maps (Figures 3.2b and 3.2c). I further compared deformation on two profiles (denoted in Figure 3.3a) as shown in Figure 3.3c to 3.3f and found that the dispersion of Sentinel-2 offsets is higher, indicating a lower precision compared to Sentinel-1.

$$\begin{pmatrix} East \\ North \end{pmatrix} = \begin{pmatrix} -\cos\alpha\sin\theta & \sin\alpha\sin\theta \\ \sin\alpha & \cos\alpha \end{pmatrix}^{-1} \begin{pmatrix} Range \\ Azimuth \end{pmatrix} \quad (3.1)$$

3.2.4 ALOS-2 data and interferometry

Inherited from the Advanced Land Observing Satellite (ALOS) in 2014, ALOS-2 carries a Phased Array type L-band Synthetic Aperture Radar-2 (PALSAR-2) sensor to acquire SAR images. PALSAR-2 has three observation modes: spotlight, strip map (SM) and ScanSAR, where the resolution successively decreases from 3 m to 100 m while the observation width increases from 25 km to 350 km. The revisit time also varies from several months to two weeks depending on the observation mode and sensing areas. Compared with the C-band wave, the L-band wave can better penetrate vegetation to obtain ground information due to a longer radar wavelength (Lindsey et al., 2015), which facilitates the maintenance of coherence in rainforest areas.

According to the data availability for the study area, one descending ALOS-2 image pair from track 6 (12 May 2019 to 23 June 2019) in ScanSAR mode and one ascending image pair from track 108 (09 March 2019 to 01 June 2019) in SM mode were collected and processed. The processing for ALOS-2 ScanSAR images follows the conventional InSAR two-pass method after the mosaic of different swaths. I masked out those decorrelation areas with a coherence threshold of 0.4 to conduct phase unwrapping. The unwrapped displacement map, as shown in Figure 3.2d, is difficult to completely interpret the coseismic deformation in the near field because of coherence loss. As for those isolated areas, such as the island to the southwest of the epicentre, phase unwrapping may not work well due to the lack of effective phase linking. Coherent pixels in the map can still be used in slip modelling considering the high precision of SAR interferometry.

3.2.5 ALOS-2 offset tracking

The ALOS-2 SM images covering the seismic region are in an ascending track, so the azimuth observations that are almost parallel with the ruptured fault should be usable. I measured the azimuth offsets with the offset tracking module in GAMMA, where the size of the SLC offset search window was set as 128×128 pixels. The fault trace can also be seen from the ALOS-2

azimuth offsets (Figure 3.2e) although within a smaller spatial extent. However, the offsets seem to be noisier than Sentinel-1 range offsets, especially on the northeast edge, which may be caused by the larger azimuth pixel spacing (3.8 m) in ALOS-2 SM images.

3.3 Geophysical modelling

The UGSS moment tensor solution (USGS, 2019) based on teleseismic waveforms suggests two nodal planes. Investigating the deformation patterns from the above images indicates a left-lateral slip component. Therefore, I used a fault plane dipping to the northeast for the inversion of the detailed fault geometry and its slip distribution. According to Sentinel-1 (Figure 3.2a), Sentinel-2 (Figures 3.2b and 3.2c) and ALOS-2 (Figure 3.2e) offset maps, I estimated a surface trace with a strike angle of 315° , as shown in Figure 3.8, which best separates the direction of deformation.

Before inversion, each dataset was subsampled with different downsampling methods. I masked the island in the southwest of the epicentre to avoid possible unwrapping errors and used the quadtree method (Jónsson et al., 2002) to downsample the ALOS-2 ScanSAR measurements. For the remaining four offset sets, only pixels around the ruptured fault were extracted to retain a high signal-to-noise ratio. I then used the quadtree method to downsample Sentinel-1 and ALOS-2 SM offsets and applied a subsampling scheme depending on the distance to the fault trace to Sentinel-2 measurements. The sampling interval for pixels within 5 km was only 1, then increased to 2 for those pixels from 5 km to 20 km, and finally increased to 4 for those with a distance farther than 20 km.

3.3.1 Inversion method

Assuming an elastic homogeneous half-space with a Poisson ratio of 0.25 (a typical value used in the seismic study, Feng et al., 2010; Wen et al., 2012), a two-step inversion strategy can be used to invert the fault geometry and the slip distribution. The first step is a nonlinear inversion which estimates the fault geometry by assuming a uniform slip on a rectangular fault plane (Feng et al., 2013). The second step is a linear inversion to solve for the finite-fault slip distribution in the least-squares sense. In this study, I fixed the strike angle of the fault based on its surface rupture and then used multipopulation particle swarm optimization (M-PSO) with a hybrid minimization algorithm (Feng and Li, 2010) to search for the other fault geometry parameters, including the dip angle, the width, length and depth of the fault plane, and the upper boundary of the ruptured fault. After the determination of the optimal fault geometry, I discretized the fault plane into rectangular sub-patches ($2 \text{ km} \times 2 \text{ km}$). Since the fault dip angle

from the uniform model may not be optimal for spatial-variable slip distribution (Burgmann et al., 2002; Fukahata and Wright, 2008), I refined the dip angle based on the relationship between weighted model misfits and multiple dip angles. To limit variations in the slip solution, the Laplacian smoothing was applied with a smoothing factor determined from a trade-off curve between slip weighted misfit and roughness (as in Figure 3.4a).

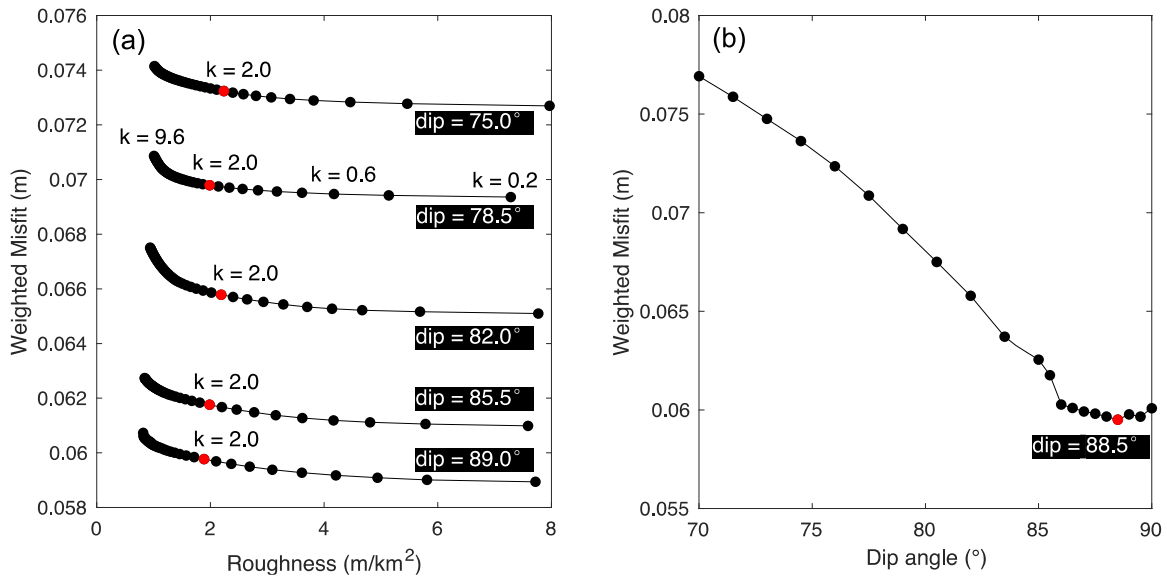


Figure 3.4 Determination of the smoothing factor and dip angle. (a) Trade-off curve between the weighted misfit and roughness of the slip model based on different smoothing factors (k), where the solid red circle indicates the preferred smoothing factor used in the joint inversion. (b) The relationship between the weighted misfit of the slip model and the dip angle of the modelled fault. The dip angle corresponding to the minimum model misfit is marked by a red dot.

3.3.2 Weighting strategy

Following the above inversion strategy, I initially performed individual inversions using each of the five datasets (i.e., ALOS-2 ScanSAR interferometric phases (ALOS2-InSAR), Sentinel-1 range offsets (S1-range), ALOS-2 SM azimuth offsets (ALOS2-azimuth), Sentinel-2 north-south offsets (S2-NS) and Sentinel-2 east-west offsets(S2-EW)). The residuals of individual inversion were used to estimate the initial weights of these data sets in the joint inversion (the smaller the residual, the greater the weight) and the weight ratio is 1:0.35:0.16:0.06:0.06. I then used M-PSO to obtain an optimal fault geometry with a length of 68 km, a width of 16 km, a dip angle of 89° and a strike angle of 315°.

Then, the fault plane was fixed to be 100 km \times 20 km and the joint linear inversion was performed. The Laplacian smoothing factor was determined as 2.0 where the fault model fitted observations well and exerted a relatively small roughness regardless of the setting of dip angles

(Figure 3.4a). I further refined the dip angle to be 88.5° which corresponds to a least model misfit (Figure 3.4b). To better balance the contributions of multiple datasets, the weight ratio was iteratively updated using the residual root-mean-square (RMS) of each dataset. The weight of ALOS2-InSAR was always set as 1. For S1-range, ALOS2-azimuth, S2-NS and S2-EW, the square of the residual RMS reciprocal was calculated respectively, and its ratio to that of ALOS2-InSAR (called the residual RMS ratio) was set as the weight in the next iteration. As shown in Figure 3.5, after three iterations of joint inversion, the data weight ratio and residual RMS ratio of each dataset stabilised, and the final weight ratio was 1:0.14:0.07:0.04:0.05.

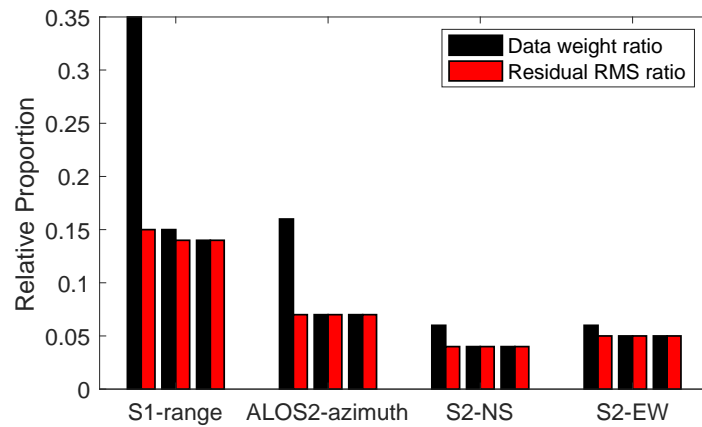


Figure 3.5 Iterative weighting of S1-range, ALOS2-azimuth, S2-NS and S2-EW. Black bars are the weight ratio of the four datasets to ALOS-2 ScanSAR (weight 1). Red bars are the residual RMS ratio defined as the ratio of the square of the residual RMS reciprocal to ALOS2-InSAR. Three groups of bars for each dataset correspond to three iterations of joint inversion.

3.4 Results

Figure 3.6 shows the inverted slip distribution on the fault plane from the joint inversion and individual inversion. It can be found that compared to the slip distribution from joint inversion (Figure 3.6a), the slip distribution inverted from ALOS-2 ScanSAR data only (Figure 3.6b) can hardly illustrate the onshore surface rupture (12~24 km along strike) while that inverted from Sentinel-1 (Figure 3.6c), ALOS-2 SM (Figure 3.6d) and Sentinel-2 (Figure 3.6e) offsets seems to overestimate the length of the offshore surface rupture. The checkerboard test is further used to examine the resolution of these slip solutions. I firstly generated synthetic ground observations based on checkerboard-like slip distributions (Figure 3.7a) and then inverted the slip solution from these synthetic observations using the same inversion method. Results show that the joint inversion (Figure 3.7b) retrieved the fault slip slightly better than ALOS-2 ScanSAR-only (Figure 3.7c) in the onshore part (0~31 km along strike) and performs much better than the other three datasets (Figures 3.7d to 3.7f) especially in the offshore part (>31 km along strike). However, the down-dip slip (>10 km along the dip) of the offshore region is to

some extent underestimated and smeared since no deformation can be captured offshore by satellite remote sensing.

The results from joint inversion which offers a comprehensive geophysical interpretation suggest that the earthquake is mainly controlled by a left-lateral strike-slip component. The maximum strike-slip and dip-slip are 6.07 m and 0.49 m, respectively, with a rake angle of 4.6° . This preferred model indicates the fault ruptures to the surface with a length beyond 50 km and a maximum surface slip of over 5 m. The main slip area extends 18 km along the down-dip and the peak sliding patches with a slip of 6.10 m locates at a depth of about 10 km, where the rupture propagates mostly along the strike direction. The estimated geodetic moment is 1.03×10^{20} N·m, corresponding to a magnitude of Mw 7.31.

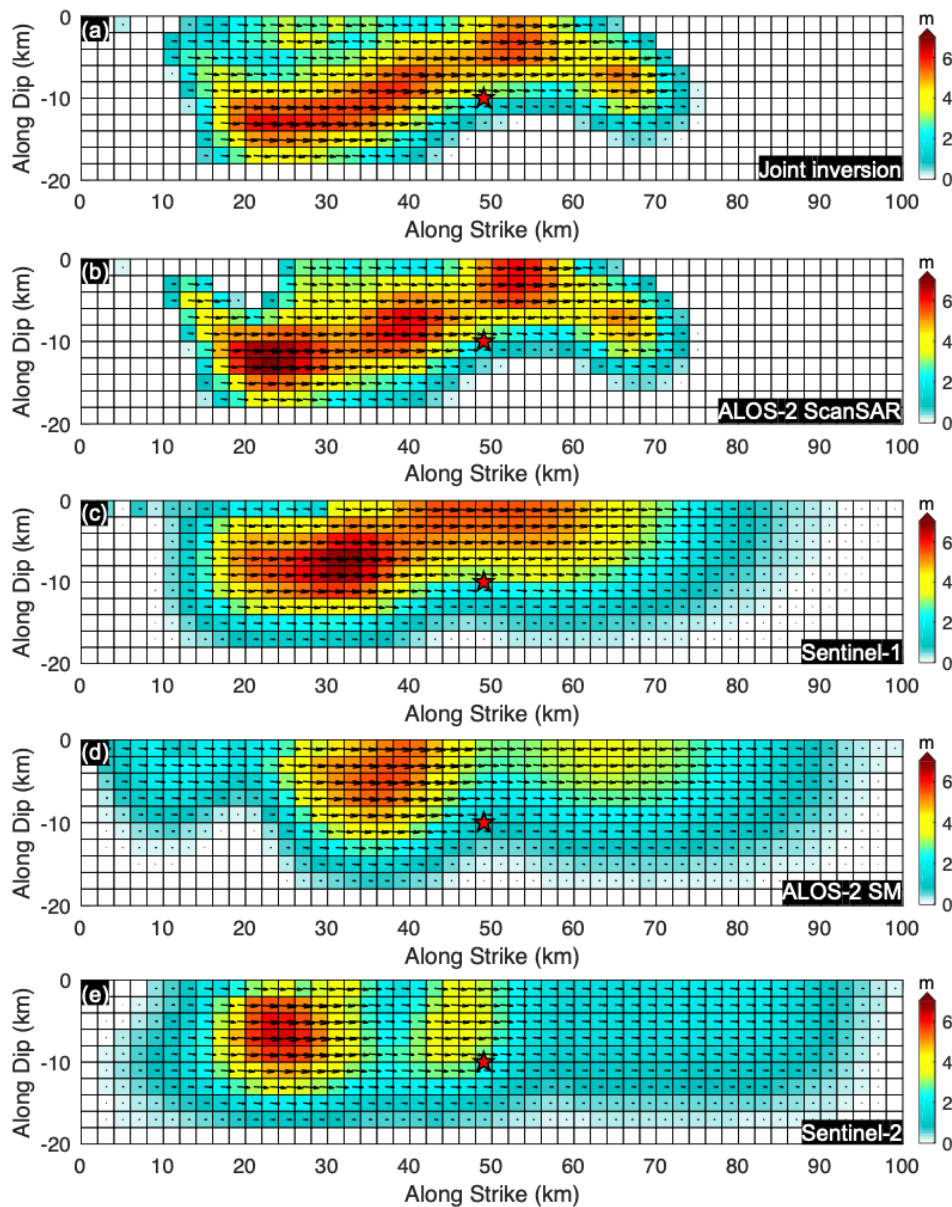


Figure 3.6 Slip distribution on the fault plane from joint and individual inversions. (a) The slip distribution from joint inversion using the five datasets. (b) to (e) are the slip distribution from individual

inversion of ALOS-2 ScanSAR interferometric phases, Sentinel-1 range offsets, ALOS-2 SM azimuth offsets and Sentinel-2 offsets, respectively. The black arrows on the fault patches denote the slip direction. The upper boundary of the fault model corresponds to the surface trace shown in Figure 3.8 and the strike direction is from southeast to northwest. The star denotes the source location from USGS.

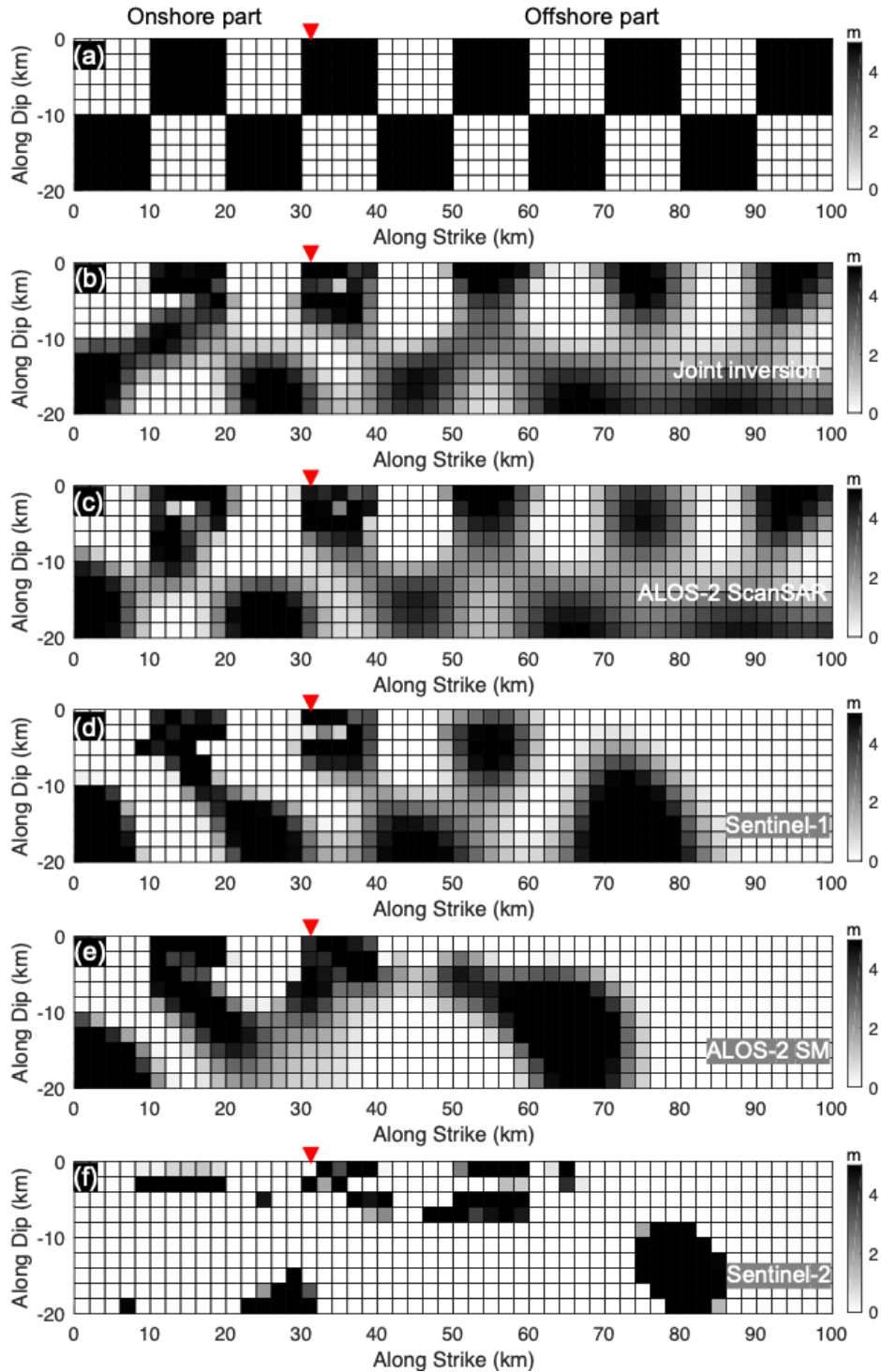


Figure 3.7 Results of checkerboard tests. (a) The synthetic slip distribution. (b) to (f) are the slip solution inverted from the synthetic ground deformation. The red downward-pointing triangles denote the location of the intersection of the fault surface trace and coastline.

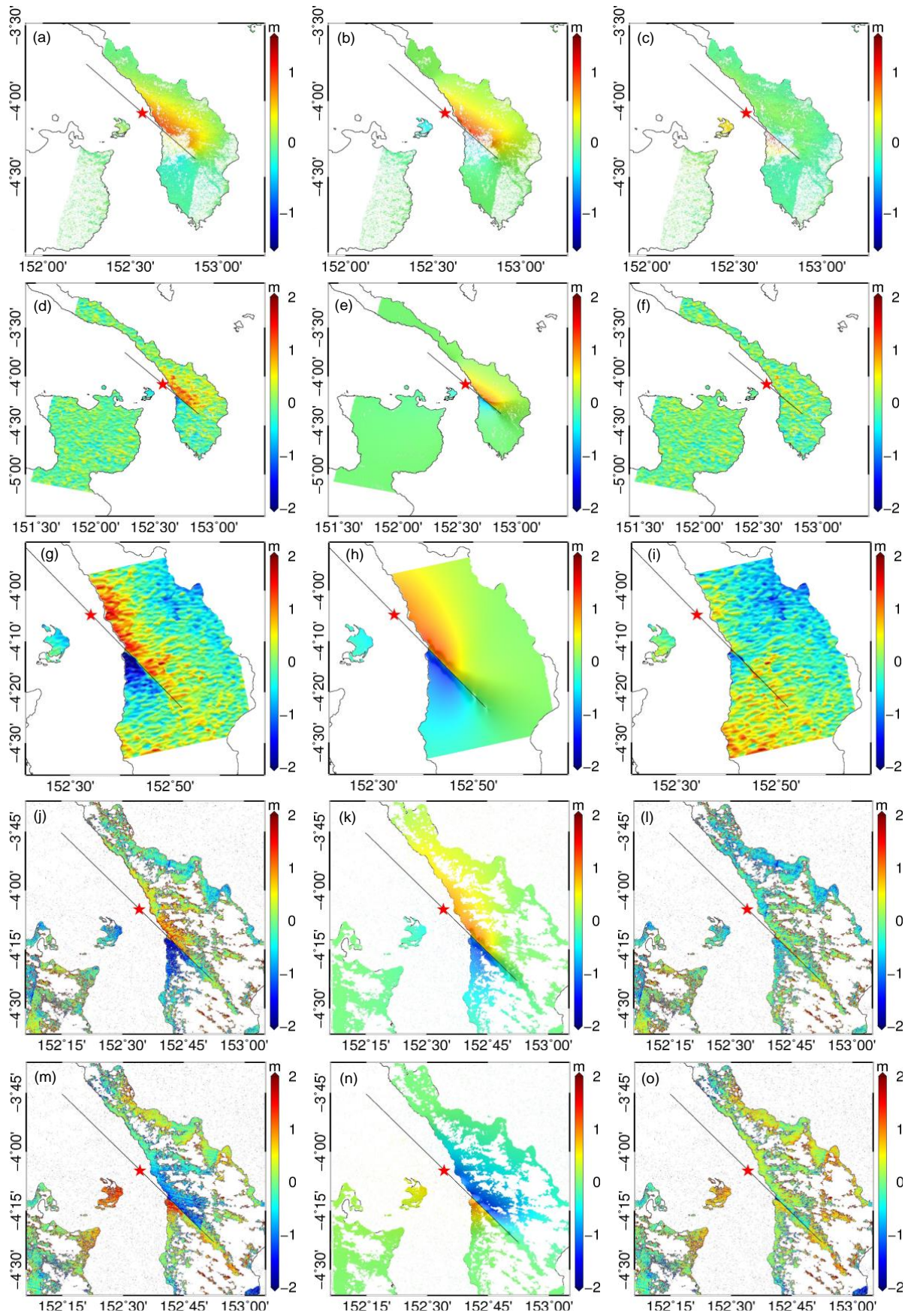


Figure 3.8 Coseismic satellite observations (left), predictions from slip models (middle) and residuals between them (right). (a), (d), (g), (j) and (m) are deformation maps from ALOS-2 ScanSAR interferometry, Sentinel-1 range offsets, ALOS-2 SM azimuth offsets, Sentinel-2 NS and EW offsets,

respectively. The solid black line denotes the surface trace of the ruptured fault, estimated jointly from SAR (Sentinel-1 and ALOS-2) and optical satellite (Sentinel-2) offset maps.

The predicted displacements from the slip model well fit the observations. The RMS of the misfits is respectively 8.7 cm, 23.8 cm, 33.8 cm, 45.6 cm and 41.2 cm for ALOS-2 ScanSAR interferometric phases, Sentinel-1 range offsets, ALOS-2 SM azimuth offsets, Sentinel-2 north-south (NS) offsets and Sentinel-2 east-west (EW) offsets. I further calculated the model predictions on the ground within each data set and compared them with original observations. As shown in Figure 3.8, the deforming pattern of models basically follows that of five data sets, and the residuals in the Sentinel-1 range offset map have the most uniform distribution although not the smoothest. In the residual map of InSAR data from ALOS-2 ScanSAR (Figure 3.8c), there are two asperities on the west side of the fault trace, possibly caused by unwrapping errors in the original data. But the causes of unwrapping errors are different. The island asperity is caused by pixel isolation while the other one is caused by decorrelation. The relatively large residuals of ALOS-2 SM and Sentinel-2 (Figure 3.8i, 8l and 8o) are predictable because their data quality is limited by resolution. Another reason for relatively large residuals in the edges of these images is that only the near-field observations are used in the joint inversion. Moreover, the atmospheric artefacts and early post-seismic deformation may also contribute to the residuals.

3.5 Discussion

Due to heavy vegetation in the study area, the C-band SAR interferometry hardly contributes to the mapping of the coseismic deformation field. The L-band ALOS-2 SAR images generate better interferograms but still suffer coherence loss in areas along the ruptured fault. Such decorrelation may be caused by heavy vegetation or a large deformation gradient. SAR and optical offset fields that can be calculated from Sentinel-1 and Sentinel-2 data are free from coherence loss. Despite the lower precision, offset maps can provide enough near-field data constraints for slip inversion. Moreover, the surface trace of the ruptured fault is consistently displayed in these offset maps, which fixes the strike direction of the fault model. This study has demonstrated the possibility of combining them for a joint inversion, which is beneficial in areas with limited InSAR measurability. I also attempted to jointly use satellite radar interferograms both in descending and ascending, but the coseismic deformation projected in the LOS of ascending ALOS-2/Sentinel-1 interferograms is limited because the direction of the fault rupture is almost perpendicular to the ascending LOS. In addition, there are no ascending ALOS-2 ScanSAR images available spanning the coseismic period.

For the joint inversion with multiple datasets, the determination of the weight of each dataset imposes a large impact on the slip solution. If the data quality is ignored and each data set is weighed equally, a slip distribution with different motion patterns would be generated even with the same fault model and smoothing factor. The relative weight ratio estimated in this study shows that the contributions of SAR and optical offsets are lower than 25%. Although this study combines multiple satellite observations, most data points are still distributed on one side of the fault, which makes the model constraint unbalanced. The checkerboard test also verified that these satellite data hardly provide good constraints for the offshore slip. This is probably the reason for the geodetic moment magnitude being lower than M_w 7.5.

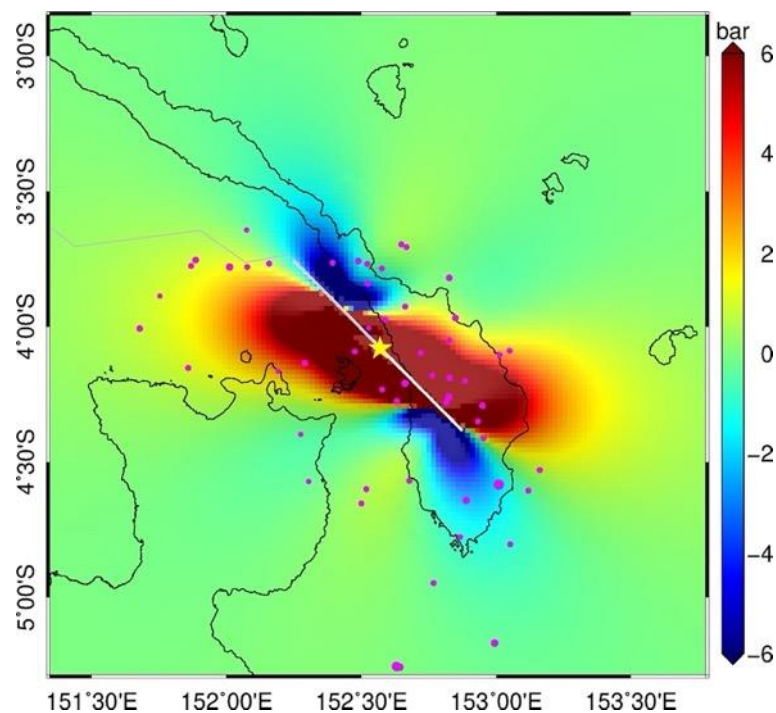


Figure 3.9 Static Coulomb failure stress changes due to the 2019 New Ireland earthquake. The yellow star denotes the epicentre. The solid white line is the surface trace of the fault model used in this study. The solid grey line is the offshore extension of the Weitin fault. The magenta dots represent the aftershocks ($M > 3.0$) three months after the main event recorded by USGS.

The slip distribution results indicate a lengthy rupture on the surface. To evaluate the effect of such fault rupture on the surrounding seismogenic environment, I calculated the Coulomb failure stress (CFS) changes resulting from this event. The CFS changes representing the transfer of stress have been widely used to characterize the evolution of seismicity and quantify the triggering effect of medium/large earthquakes (e.g., Lin and Stein, 2004; Toda et al., 2005; Xu et al., 2010; Yu et al., 2018a). The CFS was estimated on an optimally oriented fault at a depth of 10 km with a friction coefficient of 0.4. The shear modulus is assumed as 33 GPa for

a Poisson's ratio of 0.25. The aftershocks ($M > 3.0$) three months after the main event were collected from USGS and superposed on the map of CFS changes (Figure 3.9). Although the number of recorded aftershocks (55) is few, most of the aftershocks ($\sim 70\%$) are located in the area with increased CFS. The map also shows that the 2019 New Ireland earthquake increases CFS by more than 5.0 bars along the strike of the ruptured fault, except for the northwest and southeast edges of the faults.

The 16 November 2000 Mw 8.0 event shares the same fault structure and initiates from a similar location to this event. Also, their aftershocks do not delimit a linear zone of seismicity as expected for near-vertical strike-slip events (Tregoning et al., 2005). But the aftershocks of the 2000 Mw 8.0 event are clustered to the east of the Weitin fault while that of this event are more scattered around the fault. The shallow rupture of the 2000 Mw 8.0 event may have reactivated many older subduction fractures in the upper plate (Tregoning et al., 2005), which can explain the static stress changes triggering the two 2000 Mw 7.8 thrust earthquakes (Park and Mori, 2007). But in this event, no strong subduction-related activities to the south of the Weitin fault are triggered. I could not deny that the seismicity history repeats on the Weitin fault with a similar rupture mechanism, but the triggering effect of this event is more limited along plate boundaries and associated structures compared to the 2000 earthquake sequence, which reflects the uncertainty of the interaction between the Weitin fault and the subduction trenches.

3.6 Summary

This chapter provides a solution to fully capture large transient deformation caused by geohazards such as earthquakes. The solution overcomes the decorrelation problem of InSAR when observing large-gradient deformation by combining multiple satellite observations including L-band interferometric phases, SAR pixel offsets and optical image offsets. The case used to verify this solution is a large earthquake that occurred in New Ireland, Papua New Guinea in 2019. Therefore, ALOS-2 ScanSAR interferometric phases, ALOS-2 SM azimuth offsets, Sentinel-1 range offsets and Sentinel-2 offsets were processed and combined to map the coseismic deformation field of this earthquake.

These satellite observations were further jointly used in the earthquake modelling to invert the slip distribution. Firstly, the surface traces of the ruptured fault were obtained from SAR (Sentinel-1 and ALOS-2 SM) and optical (Sentinel-2) offset fields, which agree well with each other. Then, an iterative weighting method based on the residual RMS of each dataset was proposed and used to better balance the contributions of multiple data sets, with the Laplacian

smoothing factor as 2.0 and the fault dip angle as 88.5° being successively determined along with the best fitting slip model. The preferred slip distribution suggests a nearly pure left-lateral strike-slip motion (maximum 6.10 m) on the Weitin fault and a surface rupture length of ~ 50 km. It was also found that most aftershocks were located in the area with increased Coulomb failure stress while no strong subduction-related activities to the south of the Weitin fault were triggered by this earthquake.

Chapter 4. Combining InSAR and seismic noise measurements to monitor a landslide in Villa de la Independencia (Bolivia)

This chapter aims to capture both the long-term surface deformation and subsurface information by combining InSAR and geophysical measurements, which highlights the feasibility of the combination in revealing landslide geometry in three dimensions and the power of InSAR time series in tracing landslide motion in detail. The study in this chapter has been published in *Landslides* (<https://doi.org/10.1007/s10346-021-01659-9>).

The case study is a complex landslide involving a town of around 6,000 inhabitants in Villa de la Independencia (Bolivia), where extensive damages to buildings have been observed. To investigate the spatial-temporal characteristics of the landslide motion, Sentinel-1 data from October 2014 to December 2019 were processed using the InSAR time series technique. A new geometric inversion method was proposed to determine the best-fit sliding direction and inclination of the landslide. The landslide movements over time were further analysed by projecting the InSAR time series to the sliding direction, and their acceleration possibly triggered by increased precipitation was observed. Although InSAR enables such a detailed investigation of surface landslide movements, it cannot provide information about subsurface structures. Therefore, seismic noise measurements were collected to analyse the properties of slip surfaces of the landslide and estimate the overall landslide volume. This study reveals the potential of integrating InSAR and seismic noise techniques to understand the landslide mechanism from ground to subsurface.

4.1 Introduction

As introduced in Section 1.1, landslides can result in fatalities and monetary losses across numerous mountainous regions worldwide. Therefore, long-term landslide monitoring is necessary to track the development of mass activities and potentially predict when the landslide occurs (Utili et al., 2015; Del Soldato et al., 2018b; Strozzi et al., 2018; Lacroix et al., 2019). The movement of landslides generally behaves on a small spatial scale but may follow fractured surfaces due to the internal subdivision of landslide mass (Frattini et al., 2018), leading to multiple sliding directions on a single landslide body. Such spatiotemporal features make it difficult for conventional pointwise landslide monitoring sensors to provide continuous measurements with sufficient spatial coverage and resolution. Furthermore, the proper location of such sensors is difficult to choose for newly detected landslides when considering multiple failure surfaces (Barla and Antolini, 2016), and the installation and maintenance of the sensors are labour-intensive and expensive.

To overcome this, numerous researchers have sought to utilise the spaceborne InSAR measurement which can map an entire landslide body continuously at a high spatial resolution (Hilley et al., 2004; Calabro et al., 2010; Tomás et al., 2014; Raspini et al., 2019; Dai et al., 2020; Solari et al., 2020) and enables the investigation of the spatiotemporal features of multi-surface failures (Dai et al., 2016; Hu et al., 2018; Intrieri et al., 2020). Since InSAR can only measure surface landslide movements without the subsurface information (e.g., landslide depth), researchers have proposed strong assumptions such as spatially uniform landslide rheology and a priori vertical variation of velocity to retrieve the depth of landslides (Booth et al., 2013; Delbridge et al., 2016). However, these assumptions likely do not apply to compound landslides with spatially variable or unknown rheology (Booth et al., 2013). Another strategy to unravel the subsurface structure of landslides is to combine surface deformation with various ground sensors or field surveys, where available. For example, Crosta et al. (2014a) jointly used borehole, GPS, optical targets and InSAR data to comprehensively analyse the movements, depth and volume of the La Saxe rockslide (Courmayeur, Italy). Carlà et al. (2019) combined InSAR and GPS displacements with a borehole survey to retrieve both deformation fields and stratigraphic information of the Bosmatto landslide (Gressoney St. Jean, Italy). Crippa et al. (2020) reconstructed the morpho-structures and basal shear zones of the Mt. Mater landslide (Valle Spluga, Italy) by integrating InSAR measurements with field evidence (e.g., persistent scarps).

Knowledge of the landslide depth may also be retrieved from geophysical techniques (Pazzi et al., 2019), and among these, seismic noise measurements can be implemented with a high spatial density. For example, Pazzi et al. (2017) used the Horizontal to Vertical Spectral Ratio (H/V) technique (Nakamura, 1989) to identify the depths of slip surfaces on the basis of substantial changes in the seismic impedance between landslide mass and unweathered material. Therefore, combining InSAR and a dense network of seismic stations can effectively reveal detailed landslide sliding geometry and in principle can enable an accurate estimation of the landslide volume.

In this study, in order to characterise the landslide motion with high resolution and long-term observations, I used a combination of 5-year Sentinel-1 images, with a temporal baseline of 6 to 24 days from 2014 to 2019, and a dense seismic noise network, with 120 observation stations carried out between August and September 2017 (dry season). A geometric inversion method combining InSAR descending and ascending measurements to determine the best-fit sliding

geometry of the landslide body was proposed. The landslide geometry was further investigated by 120 seismic noise measurements in terms of slip interface depth, and, to the best of my knowledge, such dense seismic noise measurements were employed for the first time together with InSAR to investigate a landslide. The temporal evolution of the landslide has also been traced, and a comparative analysis of InSAR deformation and accumulated precipitation time series has been performed to reveal the impact of rainfall on the landslide.

4.2 Study area

Bolivia is a country highly vulnerable to landslides with roughly one third of its territory located in the Andes and subjected to complex hydrogeological conditions. With the rapid growing population and the expanding settlement areas on unstable slopes since the early twentieth century, Bolivia now suffers from destructive landslides almost every year (Roberts et al., 2014), leading to severe human and economic losses. In Bolivia, landslides are most frequent in the late rainy season (January to March) and usually occur after several weeks of continuous wet periods, indicating a clear hydro-meteorological controlling mechanism (Roberts, 2016). This mechanism mainly originates from orographically enhanced precipitation which drives the increase of hillslope erosion in steep terrain consisting of high-relief V-shaped valleys. One of such examples is Villa de la Independencia (Figure 4.1), the capital of Ayopaya Province, in the Cochabamba Department. Although there has been no written record of landslide occurrences in the town, inhabitants report that the first movement dates back thirty years. In addition, the observed cracks and damage on edifices and structures (Figures 4.1d to 4.1j) indicate that the landslide motion in the town deserves attention. However, the town lacks an up-to-date systematic monitoring of the slope stability, resulting in a lack of understanding of the landslide dynamic and the safety condition of the population.

From a geological point of view, the town is settled on an ancient alluvial terrace formed by the dissection of the River Palca and surrounded by large river deposits, where the presence of erosion landforms in furrows and gullies reflects strong erosive activity (Figure 4.1). The deposits of terraces (Qd, as pebbles, gravel, sand, silt, and clay) and colluvial-fluvial sediments (Qcf, mainly gravel, sand, silt and clay) rest on the Anzaldo formation (Oan, as siltstones, shales, and greenish-grey to light brown sandstones). On the east side of the landslide area outcrops are the Capinota formation (Ocp, dark grey shales with horizons of light brown sandstones at the top), while on the west side outcrops are the Amutara formation (Oam, as quartzitic sandstones and grey sandstones and grey sandstones with shales and siltstones) (Raventós et al., 2017). The rock and soil properties are summarised in Table 4.1, while the location of the

samples is shown in Figure 4.1b. The soil exhibits a texture that varies from "fine grain" to "very fine grain". Figure 4.1c shows the stratigraphy as inferred from three boreholes performed in the landslide body whose locations are indicated in Figure 4.1b. The average annual rainfall in the municipality recorded by Servicio Nacional de Meteorología e Hidrología (SENAMHI) of Bolivia is 789.3 mm, where the precipitation reaches an average of 189.4 mm in the dry season (April to October) and of 599.9 mm in the wet season (November to March).

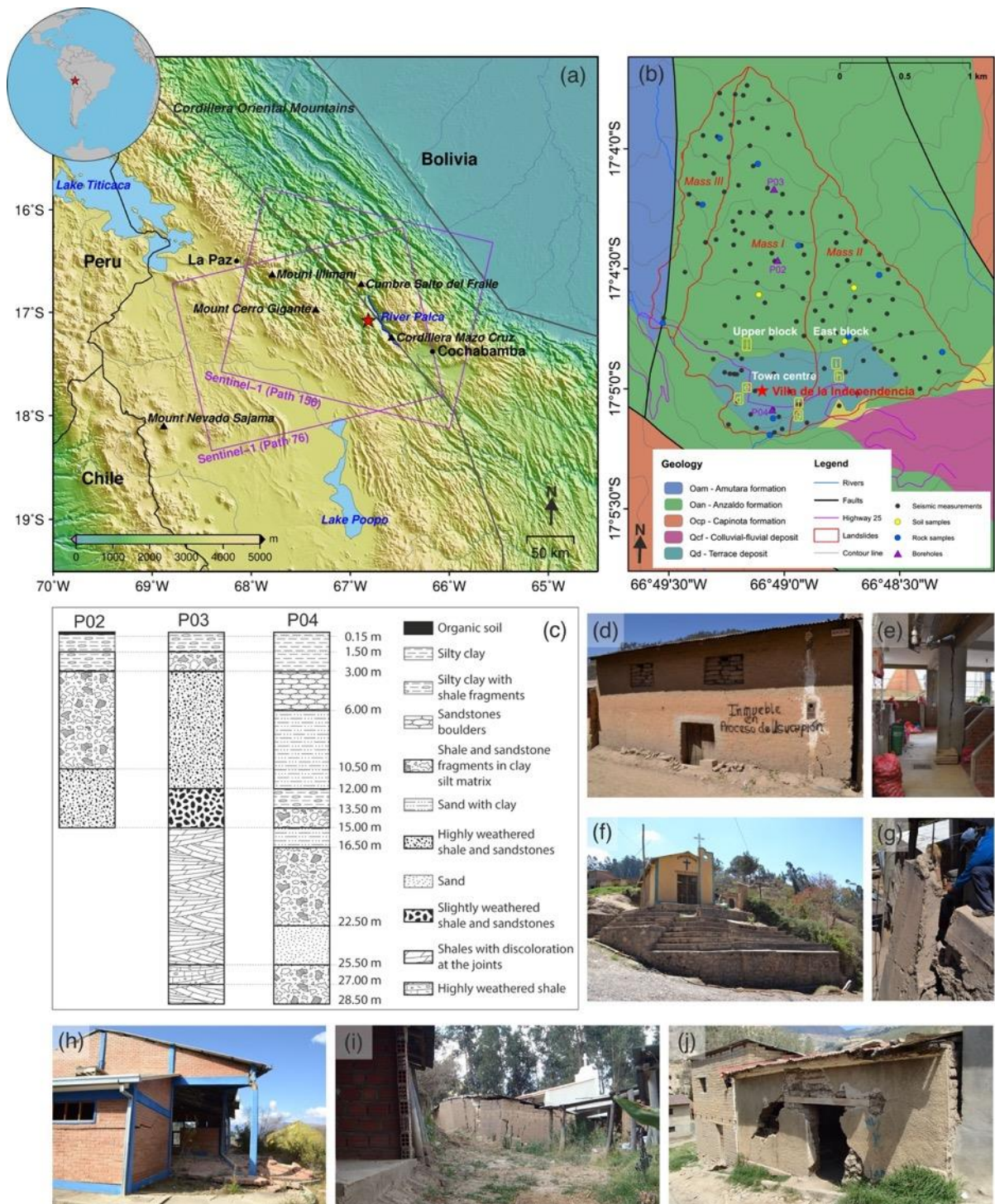


Figure 4.1 Location, geological setting and field photos of Villa de la Independencia, Bolivia. (a) Location of the study area (red star) and the coverage of satellite radar imagery. The purple rectangles

outline the spatial coverage of Sentinel-1 frames of paths 156 (descending track) and 76 (ascending track). The solid blue line represents the River Palca close to the town. The solid grey lines indicate the silhouette of the Cordillera Oriental Mountains. (b) Geological map of the study area (by Julio Torres Navarro, August 2017, as the internal and unpublished output of the project “Proyecto Integral de Estudios de Movimientos en Masa PIEMM”) with 100-metre contour lines (in grey). The landslide boundaries are in red, the seismic noise measurements are black dots, the soil samples are yellow dots, the rock samples are blue dots, and the boreholes are purple triangles. (c) The stratigraphy of the three boreholes. (d) to (j) are seven photos took at the locations indicated by yellow rounded rectangles in (b), showing the damage on edifices and structures. All the photos were taken during the 2017 field survey (between the last days of August and the first days of September).

Table 4.1 Properties of rock and soil samples whose locations are shown in Figure 4.1b.

Rock samples	ID	Rock Type	Texture	Hardness (Mohs)	γ_d (kN/m³)	
	RS01	Mudstone low metamorphic	Very fine grain	3	23.04	
	RS02	Sandstone medium metamorphic	Fine grain	3	24.41	
	RS03	Limonite high metamorphic	Fine grain	3	23.44	
	RS04	Mudstone medium metamorphic	Very fine grain	3	23.66	
	RS05	Mudstone low metamorphic	Very fine grain	3	25.53	
	RS06	Slate	Very fine grain	3	24.87	
	RS07	Mudstone medium metamorphic	Fine grain	3	25.59	
	RS08	Mudstone low metamorphic	Very fine grain	3	23.52	
	RS09	Limonite high metamorphic	Fine grain	3	22.75	
	RS10	-	-	-	25.58	
Soil samples	ID	Soil type	γ_d (kN/m³)	gravel (%)	sand (%)	silt (%)
	SS01	clayey gravel with sand	21.55	45.25	26.62	28.13
	SS02	clayey gravel with sand	20.13	36.36	29.45	34.19
	SS03	silt with sand	-	5.82	10.44	83.75
Note that missing values imply measurements were unable to read at the time of observation. γ_d (kN/m ³): unit weights of samples in the dry condition.						

On a broad scale, the landslide mass includes three sectors (Figure 4.1b): (i) Mass I: the main one affecting the town centre and the upper portion with a length of about 2,700 m and an average width of about 950 m; (ii) Mass II: a second one affecting the eastern portion of the municipality with a length of approximately 1,700 m and a width, in the lower portion, of

approximately 1,100 m (such as the eastern bus station and the cemetery shown in Figure 4.1h and 4.1i); (iii) Mass III: the smallest one affecting the western basin close to the main landslide with a length of approximately 2,000 m and a width, in the lower portion, of approximately 250 m. This work focuses on the investigation of the surface deformations in the town centre and its closest surroundings (i.e., town centre, upper block, and east block as shown in Figure 4.1b) where InSAR can maintain sufficient coherent pixels and the risk for the population is the highest. In addition, since the seismic noise measurement has a larger coverage than the InSAR measurement, the volume of the entire landslide body can also be estimated.

4.3 Data and methodology

4.3.1 InSAR

The SAR images processed are Sentinel-1 Terrain Observation by Progressive Scans (TOPS) (Torres et al., 2012) data in Interferometric Wide (IW) swath mode with a spatial resolution of about 4 m in range and 20 m in azimuth. One hundred and sixty-two Sentinel-1 images in the descending track from 16 October 2014 to 31 December 2019 and 135 images in the ascending track from 3 November 2014 to 25 December 2019 with a minimum temporal baseline of six days were collected. In the process of grouping interferogram pairs, each image was connected with at least three acquisitions. After excluding image pairs with a long temporal baseline (beyond three months), 510 and 503 interferograms respectively for the descending and ascending datasets were obtained (Figure 4.2).

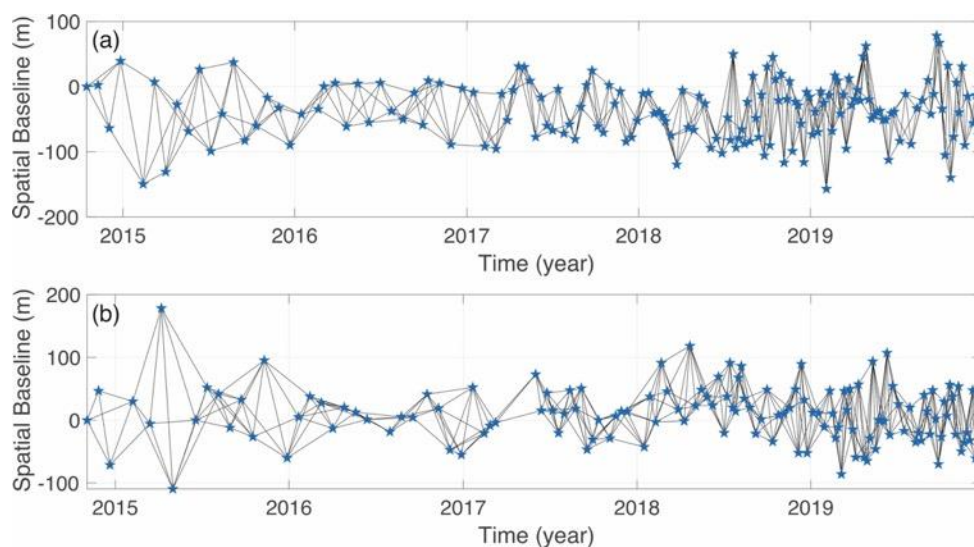


Figure 4.2 Acquisition dates and interferometric pairs of Sentinel-1 imagery in the (a) descending and (b) ascending tracks. Sentinel-1 acquisitions are denoted by blue stars. Y-axis shows the length of perpendicular baselines.

To keep the original spatial resolution of Sentinel-1 and reduce atmospheric disturbance, a single-look Small Baseline Subset (SBAS) InSAR method integrated with tropospheric delay correction to Sentinel-1 images was applied. As shown in the workflow (Figure 4.3), the GAMMA software (Wegmüller et al., 2016) was used to generate interferograms which started with the co-registration of Single Look Complex (SLC) images to a common primary image (2 June 2017 for ascending and 9 April 2017 for descending, chosen as they are in the middle of the time series). After the co-registration, a network of interferograms in full resolution was generated and geocoded based on the resampled SLC images and a 30 m Digital Elevation Model (DEM) from the Shuttle Radar Topography Mission (SRTM) (Farr et al., 2007). The tropospheric delay correction from Generic Atmospheric Correction Online Service (GACOS) for InSAR was then applied to these interferograms (Yu et al., 2017; Yu et al., 2018b; Yu et al., 2018c). It should be noted that the tropospheric effect was generally ignored by previous researchers in the study of local-scale landslides (e.g., Lin et al., 2019; Zhang et al., 2020). However, in steep terrains, the stratified tropospheric delay usually presents seasonal oscillations (Samsonov et al., 2014) which may be misinterpreted as rainfall-induced periodic movements (Dong et al., 2019). After manual inspection of the interferograms corrected by GACOS, it emerged that long-wave and terrain-related tropospheric delays were reduced after the tropospheric correction, so these corrected interferograms were used for time series analysis.

The interferograms with tropospheric correction were imported into the StaMPS software (Hooper et al., 2012) to perform the single-look SBAS analysis. Pixels with an amplitude dispersion index (Ferretti et al., 2001) lower than 0.6 were selected as the “first-round” coherent pixels. The “second-round” coherent pixels were identified based on the characteristics of their phase noise. After correction of spatially uncorrelated noise (mainly DEM error), the wrapped phase was unwrapped with a 3D unwrapping method (Hooper and Zebker, 2007) and the spatially correlated noise, including the residual tropospheric delays, DEM errors, and orbital errors were removed from the unwrapped phase. The velocity and displacement time series in the Line of Sight (LOS) were then estimated from the filtered unwrapped phase in the least-squares sense. The spatial reference value in time series InSAR processing was initially set as the mean phase value in the study area. Then a stable reference area R1 (marked by a black triangle in Figure 4.4) close to the town was selected with which the final displacement time series were re-generated.

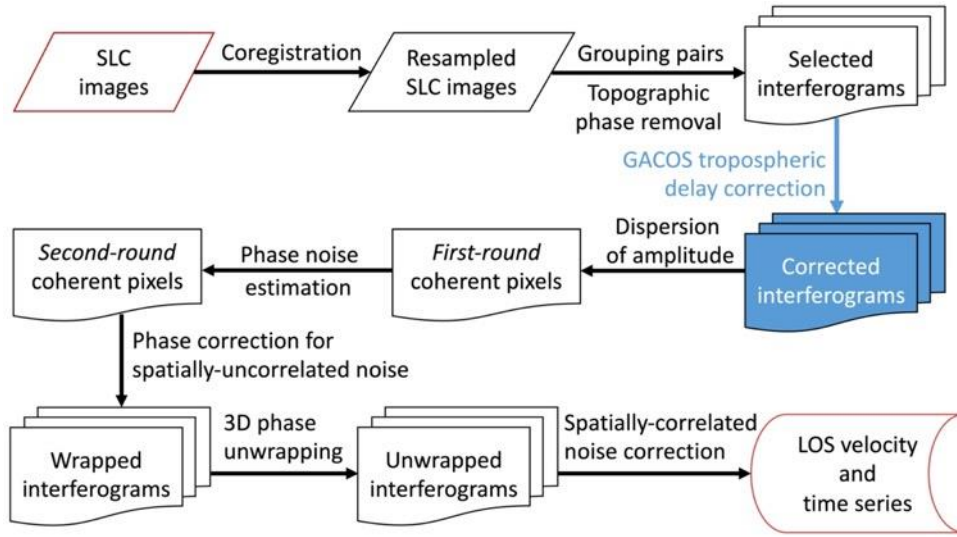


Figure 4.3 Workflow of time series InSAR processing with tropospheric delay correction.

To discuss the relationship between InSAR time series and other external factors (e.g., precipitation and residual atmospheric delays), the wavelet tools including Continuous Wavelet Transform (CWT), cross Wavelet Transform (XWT) and Wavelet Coherence (WTC) (Grinsted et al., 2004) were used. CWT can identify localised intermittent periodicities of a single time series, while XWT and WTC help identify the common power and relative phase between two time series in time-frequency space (Tomás et al., 2016).

4.3.2 Determination of the sliding geometry

A geometric inversion method was designed to determine the best-fit sliding direction (clockwise from the north) and inclination (from horizontal to vertical) of the landslide motion according to the combination of descending- and ascending-track InSAR observations. The method is based on the assumption that the basal failure plane moves approximately but not strictly along the slope surface (Hu et al., 2016) and may have slight deviations from the existing slope geometry.

For a given single landslide sub-block, I assume that it is driven by only one sliding plane with an inclination of β_1 and a sliding direction of β_2 . For each pixel inside this landslide sub-block, a displacement ($D_{sliding}$) along the sliding direction and inclination can be projected to the descending (D_{des}) and ascending (D_{asc}) LOS directions following Equations (4.1) and (4.2).

$$D_{des} = \begin{bmatrix} -\sin\theta_{des}\cos\alpha_{des} \\ \sin\theta_{des}\sin\alpha_{des} \\ \cos\theta_{des} \end{bmatrix}^T \cdot \begin{bmatrix} \cos\beta_1\sin\beta_2 \\ \cos\beta_1\cos\beta_2 \\ -\sin\beta_1 \end{bmatrix} \cdot D_{sliding} \quad (4.1)$$

$$D_{asc} = \begin{bmatrix} -\sin\theta_{asc}\cos\alpha_{asc} \\ \sin\theta_{asc}\sin\alpha_{asc} \\ \cos\theta_{asc} \end{bmatrix}^T \cdot \begin{bmatrix} \cos\beta_1\sin\beta_2 \\ \cos\beta_1\cos\beta_2 \\ -\sin\beta_1 \end{bmatrix} \cdot D_{sliding} \quad (4.2)$$

where, θ_{des} and θ_{asc} are the incidence angles of the descending and ascending SAR satellites, respectively; α_{des} and α_{asc} are the heading angles of the descending and ascending satellites, respectively.

According to Equations (4.1) and (4.2), the ratio (r) between the descending and ascending LOS displacements can be expressed as Equation (4.3), from which $D_{sliding}$ is eliminated. Therefore, the descending-to-ascending ratio is only constrained by the satellite radar and sliding geometries. As a scalar, the ratio represents the relative size of the projection of landslide motion on the descending and ascending LOS, and thereby, reflects the relative sensitivity of the descending and ascending InSAR geometries to landslide motion.

$$r_{predicted} = \frac{\begin{bmatrix} -\sin\theta_{des}\cos\alpha_{des} \\ \sin\theta_{des}\sin\alpha_{des} \\ \cos\theta_{des} \end{bmatrix}^T \cdot \begin{bmatrix} \cos\beta_1\sin\beta_2 \\ \cos\beta_1\cos\beta_2 \\ -\sin\beta_1 \end{bmatrix}}{\begin{bmatrix} -\sin\theta_{asc}\cos\alpha_{asc} \\ \sin\theta_{asc}\sin\alpha_{asc} \\ \cos\theta_{asc} \end{bmatrix}^T \cdot \begin{bmatrix} \cos\beta_1\sin\beta_2 \\ \cos\beta_1\cos\beta_2 \\ -\sin\beta_1 \end{bmatrix}} \quad (4.3)$$

With the descending and ascending InSAR observations available, the ratio ($r_{observed}$) between the observed descending (D_{des}) and ascending (D_{asc}) LOS displacements can be calculated according to Equation (4.4) for each pixel inside the sub-block.

$$r_{observed} = D_{des}/D_{asc} \quad (4.4)$$

Combining Equation (4.3) and (4.4), β_1 and β_2 can be solved in the least-squares sense (Grant and Boyd, 2008, 2013). Since the assumption is that one landslide sub-block has only one sliding surface, pixels inside each sub-block share the same values of β_1 and β_2 . After β_1 and β_2 are estimated, they can be substituted into Equation (4.3) to obtain the model predictions of r and then the relative root mean square (RMS) of the geometric inversion can be calculated by Equation (5) to measure the misfit of the determined sliding geometry.

$$relative\ RMS = \sqrt{\frac{1}{n} \sum_{i=1}^n \left| \frac{r_{predicted} - r_{observed}}{r_{observed}} \right|^2} \quad (4.5)$$

where n is the number of pixels inside the landslide sub-block.

4.3.3 Seismic noise measurements and H/V technique

Seismic noise refers to background noise in seismic data due to relatively persistent ground vibration, mostly consisting of elastic surface waves. Seismic noise measurements can be used to estimate landslide depth by the H/V technique because the slip surface of landslides usually generates shear wave velocity contrasts and polarises seismic noise (Pazzi et al., 2017). The H/V technique analyses the spectral ratio between horizontal and vertical components of motion recorded by a single seismic station and allows the estimation of the fundamental frequency of soft soils (Nakamura, 1989). According to a simplified equation, the frequency of the upper layer is directly proportional to the average shear wave velocity and inversely proportional to four times the layer thickness (Castellaro, 2016). In practice, H/V curves show a number of peaks (n) equal to $(n+1)$ alternating layers of different lithologies or horizontal stratifications in homogeneous layers. As a rule of thumb, a trace recorded on a homogenous soil without a cover layer (a so-called seismic bedrock) has a flat H/V curve, and no seismic wave amplification is expected. According to the SESAME project guideline (SESAME, 2004), a peak has to be taken into account if its amplitude is at least 2. The H/V peak amplitude is proportional to the layers' seismic impedance contrast and can also indicate the presence of seismic velocity reversals when its value is lower than 1 for a wide range of frequencies (Castellaro and Mulargia, 2009). Therefore, knowing the shear velocity (V_s) of the upper layer and its resonant frequency (i.e., an initial constraint is necessary), it is possible to reconstruct the depth (z) of the interface (Pazzi et al., 2017; Del Soldato et al., 2018a).

At the Villa de la Independencia landslide, the seismic noise measurements were designed to cover the entire landslide area (Figure 4.1b) and to obtain alignments across the two main directions to generate vertical cross-sections of H/V (Pazzi et al., 2017). In total 120 measurements were collected by means of four triaxial seismometers of the series Tromino® (a 3-directional, compact, all-in-one, and 24-bit digital tromometer developed by MoHo s.r.l.). Each acquisition ran for 20 min at 256 Hz and was processed using the commercial software Grilla® (provided by MoHo s.r.l.), which applied the guideline for processing ambient vibration data according to the H/V technique and SESAME project standards. To reconstruct the local

seismic stratigraphy model (V_s - z profiles), the H/V curves were constrained in terms of velocity. These velocity values were obtained not only by a direct method (Pazzi et al., 2017) but also from a Multichannel Analysis of Surface Waves (MASW) and a seismic refraction survey carried out along the road that passes through the town (Highway 25, Figure 4.1b). After the H/V data processing, the depth of slip surfaces and the landslide volume were estimated. Furthermore, InSAR and H/V measurements were integrated to reveal the diverse sliding characteristics between landslide sub-blocks during multi-surface fracturing sliding.

4.4 Results

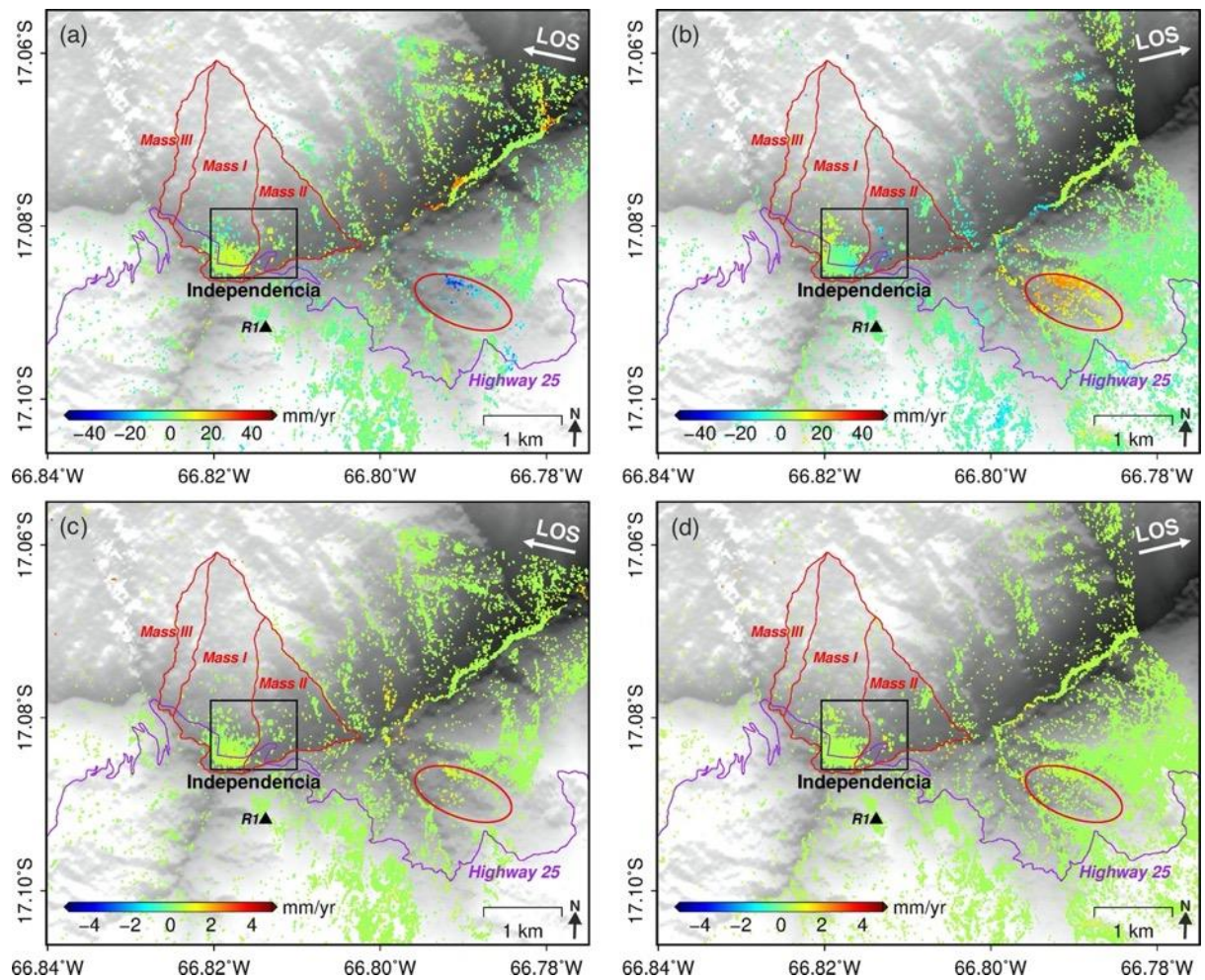


Figure 4.4 Maps of InSAR deformation velocity and its standard deviation. (a) Descending- and (b) ascending-track Sentinel-1 LOS velocity maps. Positive values indicate the surface is moving toward the satellite. The black rectangle covers the location of Independencia (including the town centre, upper block and east block as shown in Figure 4.1b) and the purple line represents Highway 25 that crosses the town. The red oval delimits the approximate extent of a priori unknown deforming area. The black triangle (R1) denotes the location of the reference area. (c) and (d) are the standard deviation maps of descending and ascending LOS velocity, respectively.

The resultant InSAR velocity maps shown in Figures 4.4a and 4.4b reveal considerable deformation (~ 10 mm/yr) in Independencia (enclosed by a black rectangle) which exerts a direct threat to the lives and properties of the residents. Figures 4.4c and 4.4d show 0.4 and 0.5 mm/yr average standard deviations of the estimated InSAR mean velocity respectively for the descending and ascending satellites, revealing the millimetre-level precision of time series InSAR. The sign of the LOS deformation rate in Independencia is opposite between the descending and ascending tracks, implying the movement has a considerable east-west component. A previously unknown deforming area (red oval circle in Figure 4.4) located 2.5 km southeast of Independencia is also identified, with a LOS velocity of ~ 30 mm/yr. Its instability could threaten public transit safety due to the nearby Highway 25 (solid purple line in Figure 4.4). In this section, the focus is on the Independencia landslide and the InSAR deformation maps and seismic H/V measurements covering the landslide as shown in Figure 4.1b will be used to investigate its 3D geometry and the spatiotemporal characteristics of its movements in great detail.

4.4.1 Identification of the fractured sliding surfaces from InSAR

Three sub-blocks were identified in Independencia as shown in Figures 4.1b and 4.5, namely “town centre”, “upper block” and “east block”, according to their overall slope aspects and the field investigation in 2017 that found a ridgeline and a road inside the town (shown in Figures 4.5a and 4.5b) roughly separating the three sub-blocks from each other. The InSAR measurements were then used to analyse the sliding geometry of each sub-block. As shown in Figures 4.5a and 4.5b, the town centre block has more InSAR coherent pixels than the upper and east blocks due to the presence of optimal scatterers (e.g., buildings). To check whether the landslide generally moves along the slope, as is the assumption of the geometric inversion method in Section 4.3.2, firstly a simulated along-slope displacement (100 mm) of each pixel was projected onto the descending and ascending Sentinel-1 LOS directions and was plotted in Figures 4.5c and 4.5d. It can be seen that the observed InSAR cumulative displacement and the simulated displacement are largely consistent, with correlations of 0.71 and 0.70 for the descending and ascending tracks, respectively (Figures 4.5e and 4.5f). The residual discrepancies could be due to the fact that each pixel may not necessarily move with the same magnitude as simulated. But in general, the consistency between observation and simulation verifies the assumption of the geometric inversion method. Note that the purpose of this step is to compare the relative spatial distribution of the simulated and observed displacements and the correlation is calculated from normalised displacements. Therefore, the value of the simulated along-slope displacement is insignificant to the results.

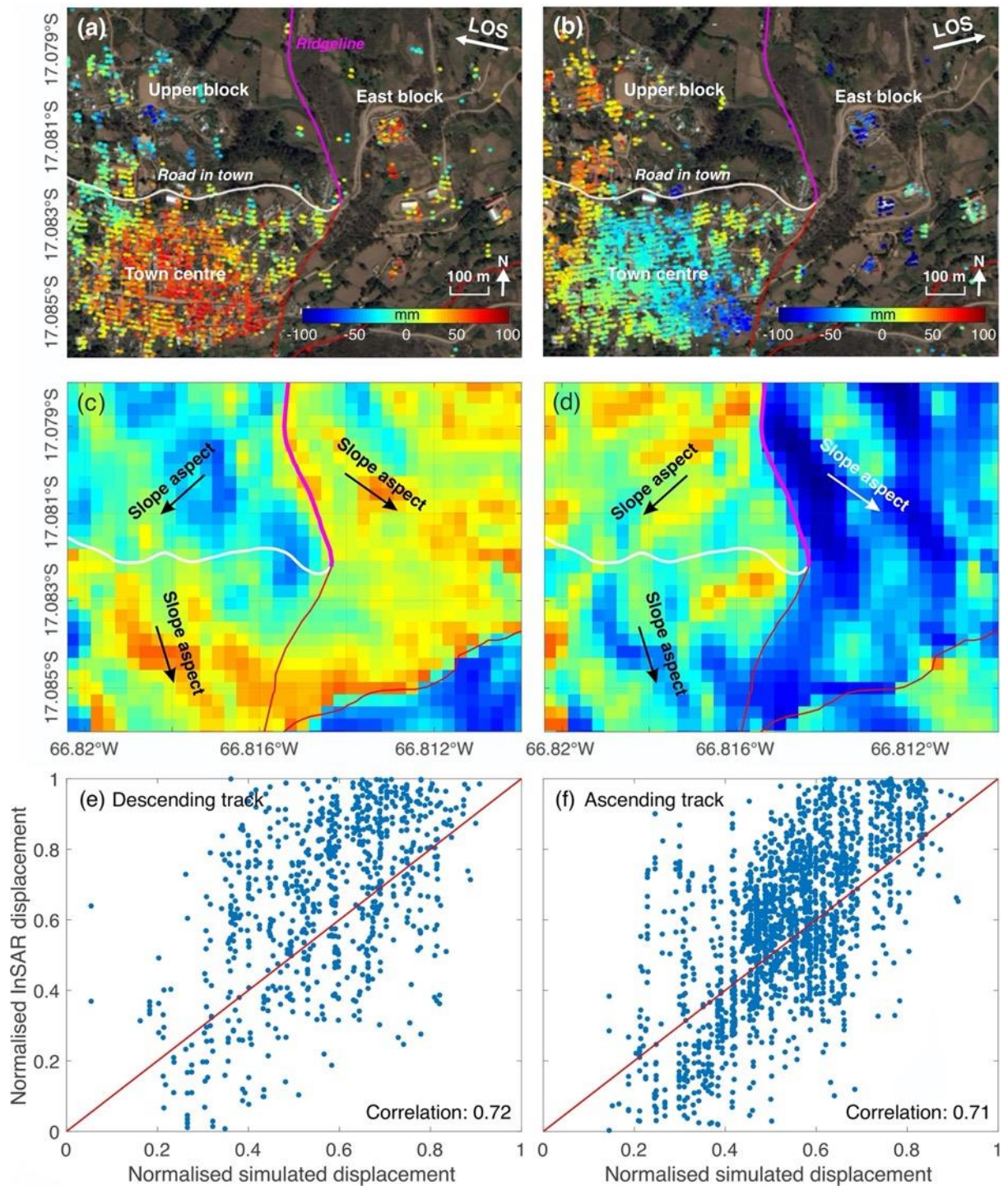


Figure 4.5 Observed and simulated LOS cumulative displacements in Independencia. (a) and (b) are the observed LOS cumulative displacements from October 2014 to December 2019 by descending and ascending Sentinel-1, respectively. (c) and (d) are the simulated descending and ascending LOS displacements, respectively, which are projected from the 100 mm displacement along the slope. The white line represents a road inside the town that roughly separates the town centre and the upper block. The thick magenta line represents a ridgeline separating the upper block and the east block, and the red lines are part of the landslide boundaries shown in Figure 4.1b. (e) and (f) are scatter plots between observed and simulated LOS displacements for the descending and ascending, respectively. Note that the displacements are normalised between 0 and 1.

The InSAR measurements within each sub-block were used to execute the geometric inversion method described in Section 4.3.2, and to determine a uniform geometry for each of the three sub-blocks. Results are shown in Figure 4.6. The basal sliding plane of the upper block has an inclination of about 8° with a sliding direction of about 228° , while that of the flatter town centre has an inclination of about 3° with a sliding direction of about 167° . The inclination of the east block is steeper ($\sim 14^\circ$) than the above two sub-blocks and its sliding direction is about 131° . According to Equation (4.5), the relative RMS of the geometric inversion misfit for the town centre, east block, and upper block is calculated to be 0.35, 0.26, and 0.33, respectively. Despite these misfits that could be caused by InSAR outliers, the inversion results can show that most InSAR pixels in each sub-block share the uniform sliding surface. Therefore, the three sub-blocks move downward along three different planar surfaces, suggesting the type of the landslide in Independencia should be classified as a compound type according to the classification of landslides by Hungr et al. (2014).

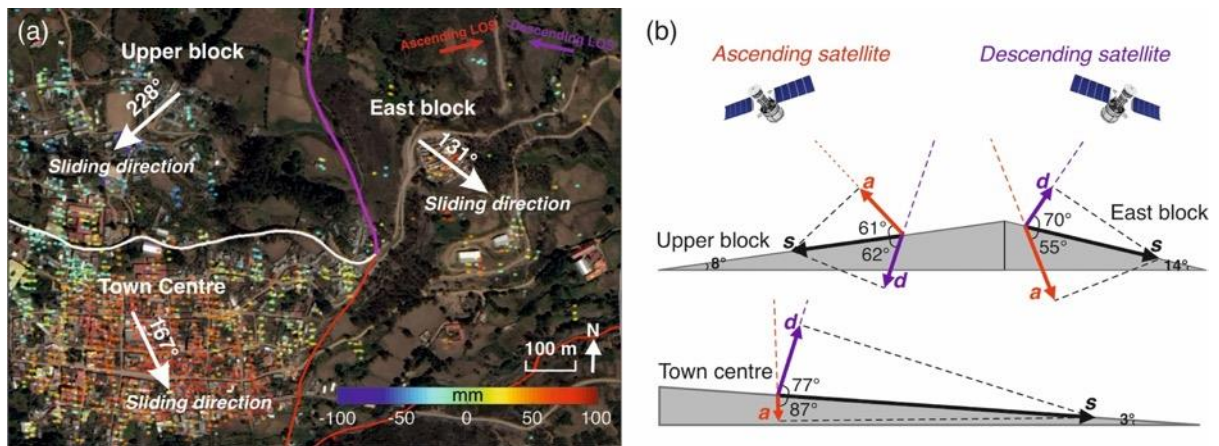


Figure 4.6 Determined sliding geometries of the three landslide sub-blocks. (a) Sliding directions (white arrows) of the three sub-blocks (clockwise from the north). The magenta line represents part of a ridgeline that distinguishes the upper block and the east block, while red lines are part of the landslide boundaries shown in Figure 4.1b. The white line represents the road inside the town. The optical base map is from Google Earth, on which the descending InSAR displacements shown in Figure 4.5a are also superimposed. (b) Sectional views of the determined sliding directions. The black vector \mathbf{s} indicates the sliding displacement $\mathbf{D}_{sliding}$, the purple vector \mathbf{d} represents the descending LOS displacement \mathbf{D}_{des} and the red vector \mathbf{a} represents the ascending LOS displacement \mathbf{D}_{asc} . The angle between the sliding direction and LOS is calculated by $\arccos(\mathbf{D}_{des}/\mathbf{D}_{sliding})$ and $\arccos(\mathbf{D}_{asc}/\mathbf{D}_{sliding})$ according to Equations (4.1) and (4.2).

4.4.2 Sliding interface depth obtained from H/V measurements

Regardless of the seismic shear wave velocity, high-frequency peaks of the H/V curves are associated with the shallower interfaces, while low-frequency peaks with the deeper interfaces (Castellaro, 2016; Pazzi et al., 2017). Figure 4.7 shows the H/V curves of the measurements in the three sub-blocks identified in Section 4.4.1. Three main frequency ranges associated with natural discontinuities can be recognised. On the basis of the geological map of the area (Figure 4.1b) and the results of the three boreholes shown in Figure 4.1c, the highest H/V peak (with a frequency range of 40.0-80.0 Hz) can be related to the shallowest discontinuity between the organic/weathered surface layer (V_s range of 90-200 m/s, V_s mean value 100 m/s) and the unconsolidated soil deposits (i.e., silty clay with or without shale fragments, sandstones boulders, and sand with clay) (V_s range of 150-370 m/s, V_s mean value 250 m/s) at a mean depth (z_0) of approximately 0.2-0.4 m. The second interface is identified at depths (z_1) ranging from 1.5 to 15.0 m (at a frequency of 8.0-40.0 Hz), corresponding to the transition from the unconsolidated soil deposits to the shale and sandstone fragments in clay and silty matrix/highly weathered shale and sandstones (V_s range of 300-900 m/s, V_s mean value 450 m/s). These z_1 peaks are not as high as z_0 , but their amplitudes are significantly higher than 2 and should therefore be considered in accordance with the SESAME project guideline (SESAME, 2004). The third peak is characterised by the frequency range of 2.0-8.0 Hz, identifying the seismic interface between the highly weathered shale and sandstones and the slightly weathered shale and sandstones/unweathered shales (the seismic bedrock) (V_s higher than 1,000 m/s), at a depth (z_2) of approximately 15.0-75.0 m.

From Figure 4.7 it can also be seen that the H/V curves of the three landslide sub-blocks behave at different amplitudes, especially in the frequency range of z_1 and z_2 , implying different seismic impedance contrasts. As the impedance contrast indicates the presence of seismic velocity reversals (Castellaro and Mulargia, 2009) and is possibly affected by an interface on which movement has occurred, the effects of sliding interfaces at different depths can be inferred from H/V amplitudes. Specifically, the H/V curves of the upper block are more similar to the east block rather than the town centre, with a sliding direction of about $(\pm)130^\circ$ relative to the north revealed by InSAR (Figure 4.6a). Compared to them, the H/V curves of the town centre are characterised by the presence of peaks in the frequency range of 2–4 Hz with a higher amplitude. This suggests that in the town centre the z_2 interface between the gravel/consolidated material and the meteorized rock is characterised by a higher seismic impedance contrast, and therefore the town centre is more significantly influenced by this deeper z_2 interface than the other two sub-blocks.

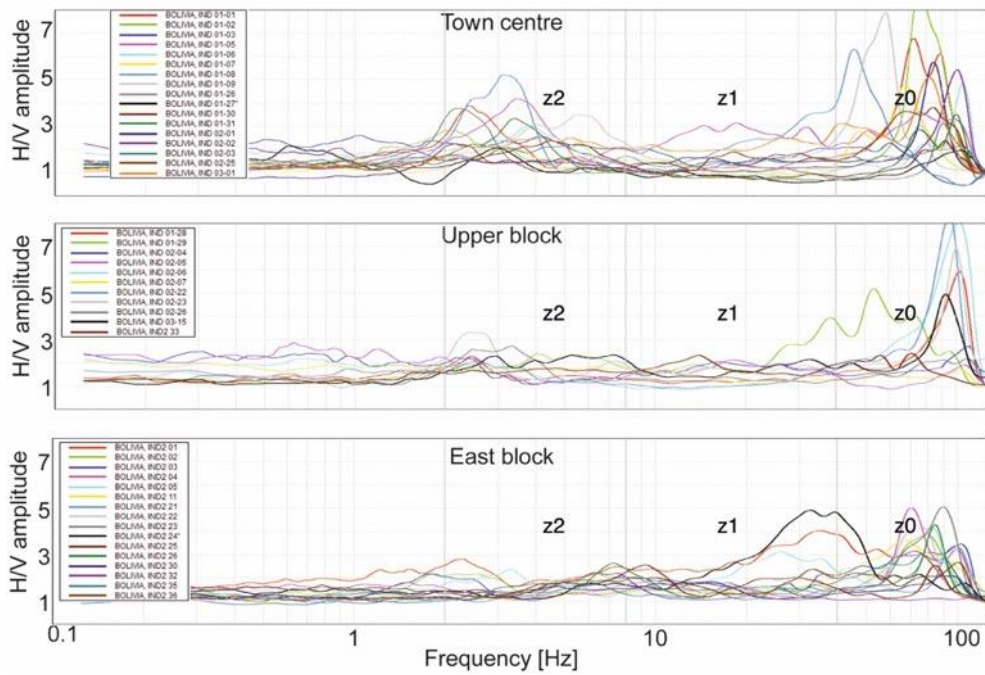


Figure 4.7 A representative selection of H/V curves for the seismic noise measurements carried out in the three landslide sub-blocks (town centre, upper block, and east block).

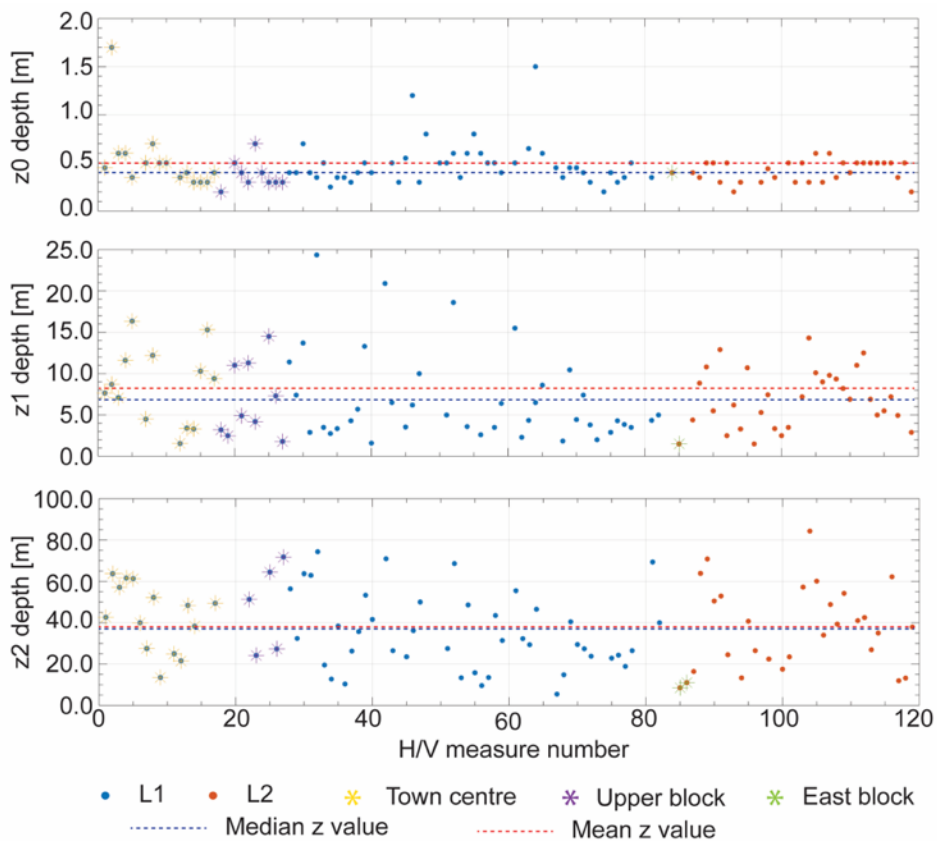


Figure 4.8 Reconstructed z depth values for seismic noise acquisitions located in the town centre (asterisks in yellow), upper block (in purple) and east block (in green). Blue points are all the other measurements carried out in the landslide area that faces to the West (L1) and red points are those in the landslide area that faces to the east (L2).

Considering the nature of the z_0 interface, the landform of the area, and the absence of asphalt in all the streets of the surveyed area (that allowed to carry out H/V measures without amplitude limitations), the identified z_0 surface can generate only shallow sliding involving limited volumes. Therefore, this interface is not significant from a geological point of view. Considering that the maximum depth of the houses' foundations in the whole landslide area is ~ 2 m, it is possible to assess that the z_1 -related slip surface with depths around 5.0 m (see Figure 4.8) is mainly responsible for the buildings' cracks.

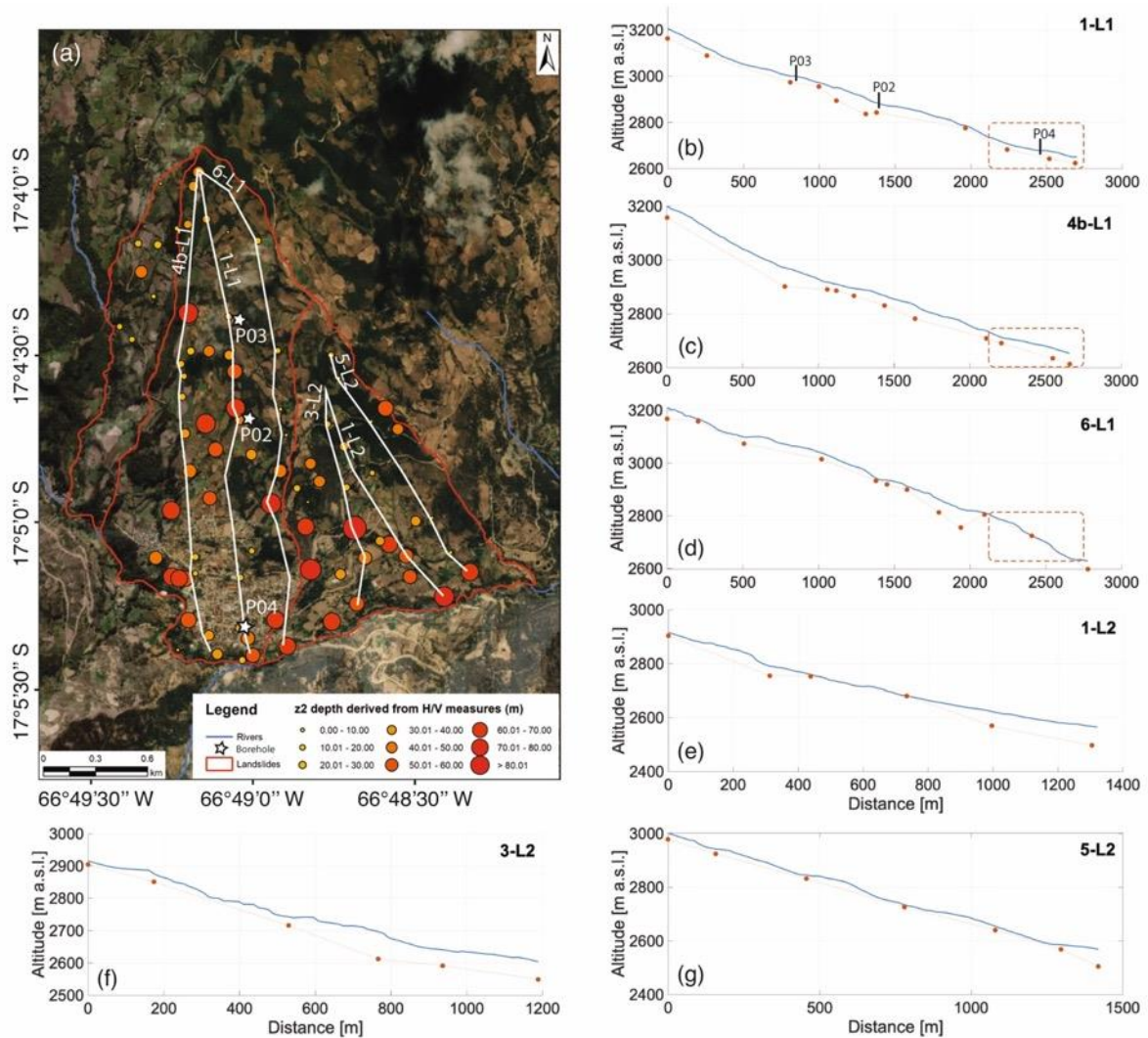


Figure 4.9 Distribution and profiles of z_2 depths. (a) Deeper interface depths (z_2 values) shown as dots of different dimensions. White lines are z_2 profile lines on the ground. (b)-(g) Altitude of ground surface profiles (blue lines) highlighted in (a) and z_2 slip interfaces (red dot-lines) derived from the H/V measurements along the profiles.

Figure 4.8 also shows that the deepest interface z_2 exhibits a larger range. To observe its spatial distribution, the widely varying z_2 values are mapped as dots of different dimensions in Figure 4.9a. It can be seen that in the central landslide body they are randomly distributed, whereas on the east side of the landslide the deeper values are mainly localised near the toe. This is further

confirmed by six slip surface profiles (Figures 4.9b to 4.9g, three in the central landslide and three in the right one) extracted along the slope. Such depth distribution suggests that the eastern part seems to be affected by a rotational movement, while the central one, also considering the slope inclination, is more likely to be controlled by a combination of rotational and translational movements. Figures 4.9b to 4.9d also show that slip surfaces at the toe of the central landslide ($> 2,100$ m from the head) are thin and approximately parallel with the ground surface (as indicated by dot-rectangles), which cross validates the planar motion in the residential areas of the town observed by InSAR (see Section 4.4.1). In conclusion, considering the above slip characteristics and the mixture of Qd and Oan in the landslide area (Figure 4.1b), the landslide type can be determined as a compound slide with sliding at different interfaces (soil/soil, soil/rock) and depths.

4.4.3 Landslide volume estimation

The simplest and most commonly used method to calculate the volume is by multiplying the surface area with the average landslide depth (Jaboyedoff et al., 2020). Calculating first the z2 depth average, the volume of the Villa de la Independencia landslide was estimated as $1.35 \cdot 10^8$ m³. All other methods presented in the literature review (Jaboyedoff et al., 2020) were applied to cross-sections, so they highlighted the need to assume a slip surface mechanism.

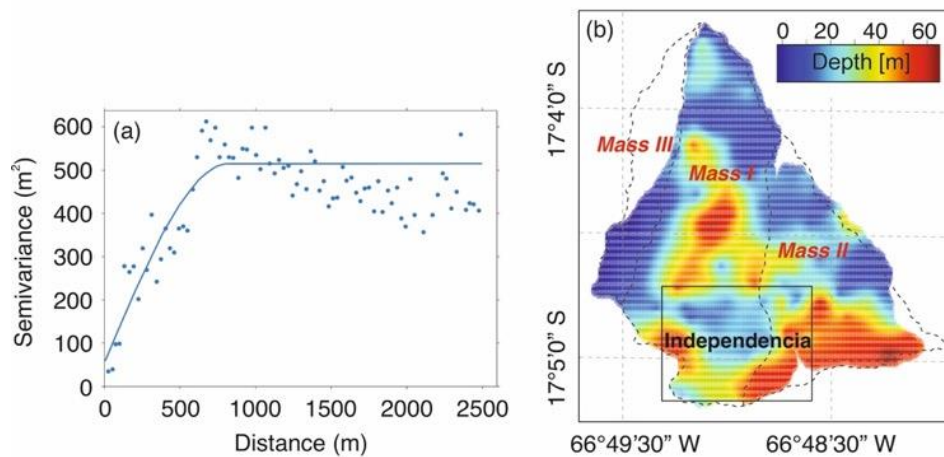


Figure 4.10 Estimation of the sliding surface depth of the entire landslide body. (a) Experimental (points) and theoretical (line) semivariogram of the z2 values. (b) Interpolated z2 sliding surface depths of the entire landslide body. The black dashed lines are the landslide boundaries shown in Figure 4.1b. Note that the distortion of the interpolation boundary is due to the planar visualisation of three-dimensional geometry.

The wide coverage of H/V measurements in the study area allows us to estimate the slip surface depth over the whole landslide area, not just along some cross-sections. Therefore, considering

the deeper interface (z_2), the volume mobilised between the DEM and the interpolated surfaces of z_2 depths was estimated by the tool *Compute2.5 Volume* in CloudCompare2.10.2 software (<http://www.danielgm.net/cc/release/>). The interpolation was made by means of the Rstudio software adopting the Kriging procedure (Bivand et al., 2013). The best-fitting semivariogram (Figure 4.10a) was assessed considering a spherical model for designing the sliding surface depths for the entire area of interest (Figure 4.10b). The volume estimated by the software is $9.18 \cdot 10^7 \text{ m}^3$. This implies that the simplified method that assumes a single sliding plane of average depth would largely overestimate the volume by 46.7%.

4.4.4 Temporal evolution of the landslide

Coherent pixels within the three sub-blocks shown in Figure 4.6a were spatially averaged to generate displacement time series for each of the sub-blocks. The 30-day accumulated precipitation was also produced according to the Global Precipitation Measurement (GPM) daily records (Hou et al., 2014; Huffman et al., 2019) to investigate the relationship between deformation and precipitation. Figures 4.11a and 4.11b show how the deformation time series actively respond to precipitation, with notable displacement acceleration observed during the late rainy seasons (January to March) in both 2018 and 2019, as indicated by blue dot-rectangles.

In the town centre sub-block, the descending and ascending LOS displacements exhibit different sensitivity to the landslide motion. The observed deformation in the ascending track (black dots in Figure 4.11a) shows stronger fluctuations but a weaker response to the increase of precipitation than the descending track. This is because the sliding direction in the town centre is nearly perpendicular to the ascending LOS vector, as shown in Figure 4.6b, resulting in its insensitivity to the displacement on the sliding plane. The insensitivity can be further evidenced by the Sentinel-1 unwrapped interferograms spanning the rainy season from January 2018 to April 2018, where the ascending LOS displacement (Figure 4.11e) is smaller in the town centre compared to the descending one (Figure 4.11d).

The deformation magnitudes along the descending and ascending LOS in the upper block are similar, which is evidenced by their nearly identical decomposition angle on the sliding plane shown in Figure 4.6b. The starting points of the accelerations in the descending and ascending LOS are also close. Compared to the upper block and town centre, the area of the east block is less affected by the increase of precipitation, with a relatively stable LOS deformation time series in both descending and ascending modes during the past five years. However, there were

still oscillations in early 2018 and 2019 marked with blue dot-rectangles in Figure 4.11c which occurred exactly within the time interval of the late rainy season.

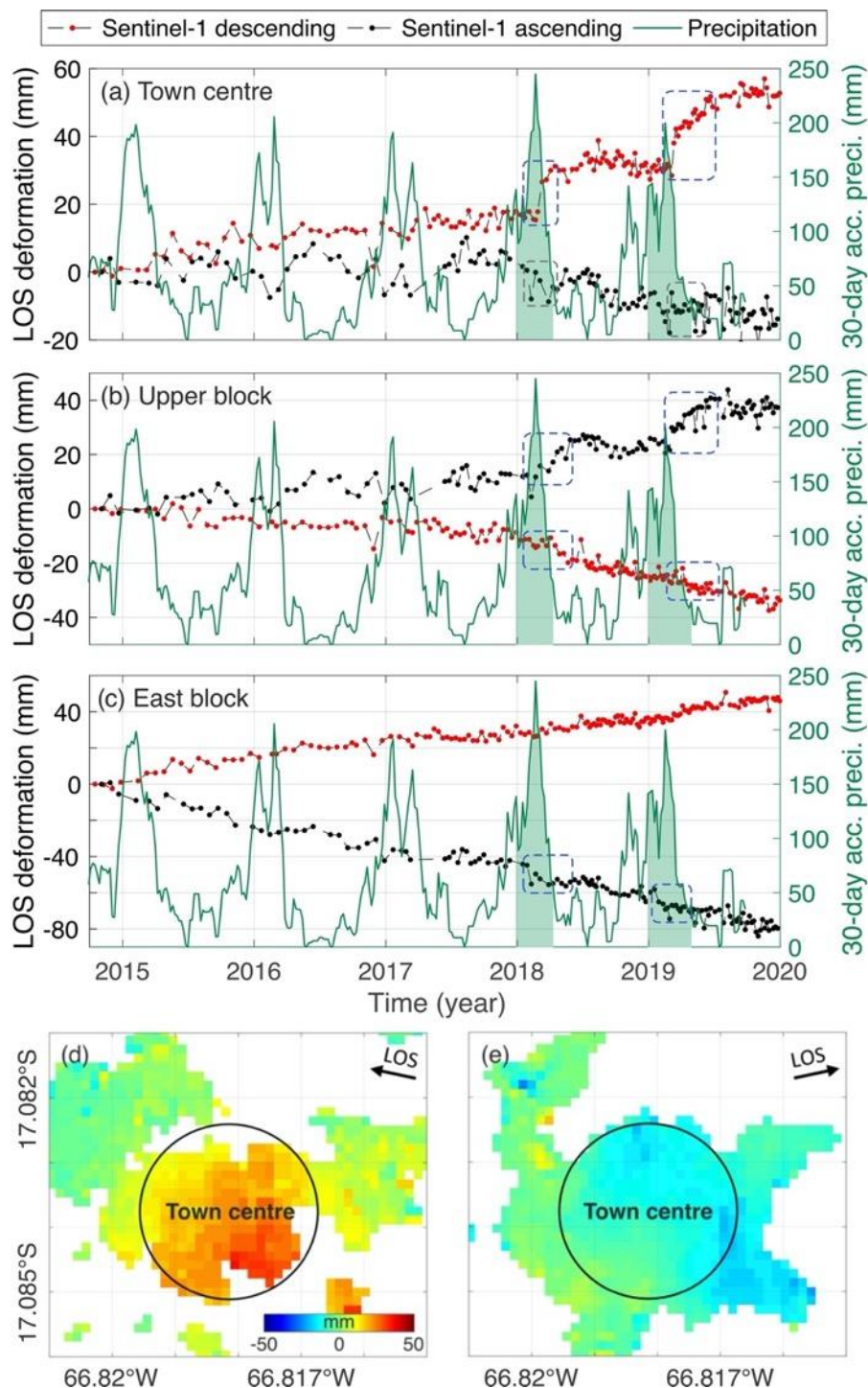


Figure 4.11 InSAR-derived descending- and ascending-track Sentinel-1 time series of (a) town centre, (b) upper block and (c) east block, compared with precipitation data. The red and black dot lines represent displacement time series in the descending and ascending LOS, respectively. The green shading in (a), (b) and (c) corresponds to the late rainy season in 2018 and 2019. The blue dot-rectangles circle the position of the acceleration phase. The parts enclosed by grey dot-rectangles in (a) reveal the insensitivity of descending-track Sentinel-1 observation in the town centre. (d) Sentinel-1 unwrapped interferograms of two descending-track images acquired on 22 January 2018 and 16 April 2018. (e)

Sentinel-1 unwrapped interferograms of two ascending-track images acquired on 16 January 2018 and 22 April 2018. The black circles denote the location of the town centre with high coherence (> 0.6). Note that a positive value in (d) and (e) means the surface is moving towards the satellite radar.

The acceleration of the LOS displacement during early 2018 and 2019 presents a precursor signal of the landslide risk. To observe the acceleration of the landslide motion more intuitively, Sentinel-1 LOS displacements were projected onto the sliding surface using a reverse form of Equation (4.1) and plotted in Figure 4.12. It can be seen that the deformation in the town centre has the largest acceleration compared to the upper and east blocks. Interestingly, the H/V curves shown in Figure 4.7 also reveal their difference by presenting a significantly higher seismic impedance contrast of the deeper z2 interface in the town centre. Therefore, combining InSAR and H/V results, it is possible to assess that the town centre could be more affected by a deeper sliding interface compared to the other two sub-blocks.

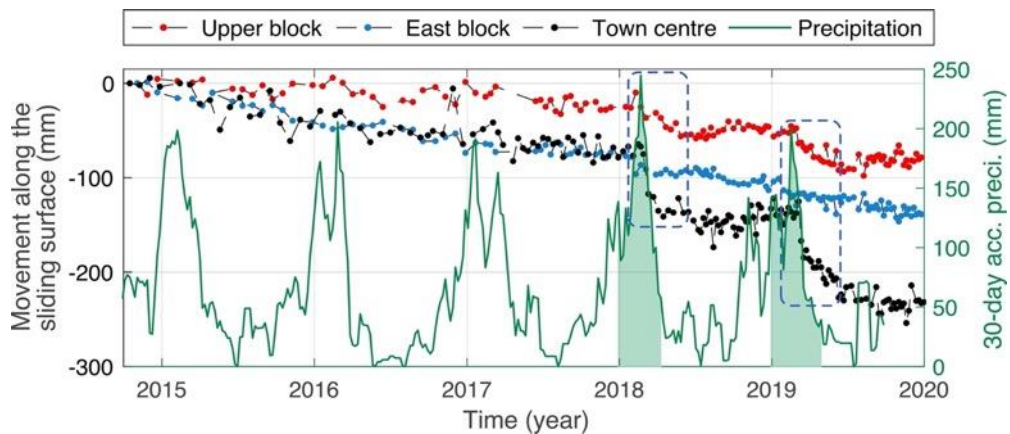


Figure 4.12 Time series InSAR-derived movements along the sliding surface and 30-day accumulated precipitation from GPM. The green shading corresponds to the late rainy season in 2018 and 2019. The blue dot-rectangles circle the two acceleration phases of landslide motion with the same time span.

Despite the fact that there was no increase in rainfall during the 2019 rainy season compared to previous years, the deformation in the study area had been accelerating during this period. The deformation time series projected onto the sliding surface (Figure 4.12) reveal that the acceleration signal in 2019 shared the similar starting time and duration (the late rainy season) as in 2018. Within the period from 2018 to 2019, the displacement presented a seasonally dominated process, especially in the town centre. This leads to the speculation that further accelerations could recur in the future in the case of substantial precipitation during the late rainy season.

4.5 Discussion

The Sentinel-1 data in this study enables us to identify a linear deforming of the landslide before 2018 and then two sudden accelerations during the rainy seasons of 2018 and 2019. It should be noted that the acceleration manifested by the landslide sub-block in the town centre is larger than the acceleration manifested by the other two sub-blocks. On the other hand, the slope aspect in the town centre is nearly parallel to the flight direction of the ascending satellite so that the ascending LOS observations are insensitive to the along-slope displacement. This may result in an underestimation of displacements as only a small portion of the along-slope displacement is observable by the ascending satellite (~5% compared to ~23% by the descending satellite). However, considering the millimetre-level precision of time series InSAR shown in Figures 4.4c and 4.4d, the InSAR-observed acceleration of the landslide movement should be real and worthy of further close monitoring in the future.

4.5.1 Seasonal oscillations in InSAR time series

The displacement time series before 2018 show a stable linear trend but there are also seasonal oscillations in the time series. Two possible causes, precipitation and residual stratified tropospheric delays, may contribute to the oscillations as both of them have a similar seasonal variation. To analyse their relationships and identify the most likely factor, the methods of CWT, XWT and WTC were applied to the detrended time series of the town centre before the 2018 acceleration. Figure 4.13a shows i) the detrended Sentinel-1 descending-track LOS displacement time series, which is more sensitive to the landslide movement than the ascending track as discussed in Section 4.4, ii) the differential Zenith Tropospheric Delays (dZTD, obtained from GACOS as described in Section 4.3.1), and iii) the precipitation. From the CWT results of the InSAR time series (Figure 4.13b), an annual (365 days) cycle with strong power over the entire recording time can be observed. Substantial half-year and 3-month cycle signals can also be identified around 2016 and 2017.

Figures 4.13c and 4.13d show the WTC and XWT relationship between InSAR and dZTD time series, while Figures 4.13e and 4.13f the relationship between InSAR and precipitation. From these figures, it emerges that the annual cycle signal of the InSAR time series is more significantly correlated with the precipitation than dZTD at the 5% significance level (black contour as shown in Figure 4.13f). Figures 4.13e and 4.13f also show that InSAR time series are in-phase with precipitation, presenting significant common power in both annual and half-year cycles. The in-phase relationship is dominated by a phase shift of about 40° as indicated by black arrows in Figure 4.13f. This means the onset of deformation in the town centre is

normally more than a month ahead of the arrival of precipitation peak because the sliding oscillation tends to initiate after the start of the rainy season (Hu et al., 2016) that is before reaching rainwater peak. Here the InSAR times series used for the analysis of seasonal oscillations is before 2018. From Figure 4.12, it can be seen that the landslide motion during this time period showed only a moderate response to precipitation (< 30 mm). But after the precipitation peaks in 2018 and 2019, the two observed accelerations represent strong responses (> 70 mm) to the increased precipitation, which were substantially different from the seasonal oscillations before 2018.

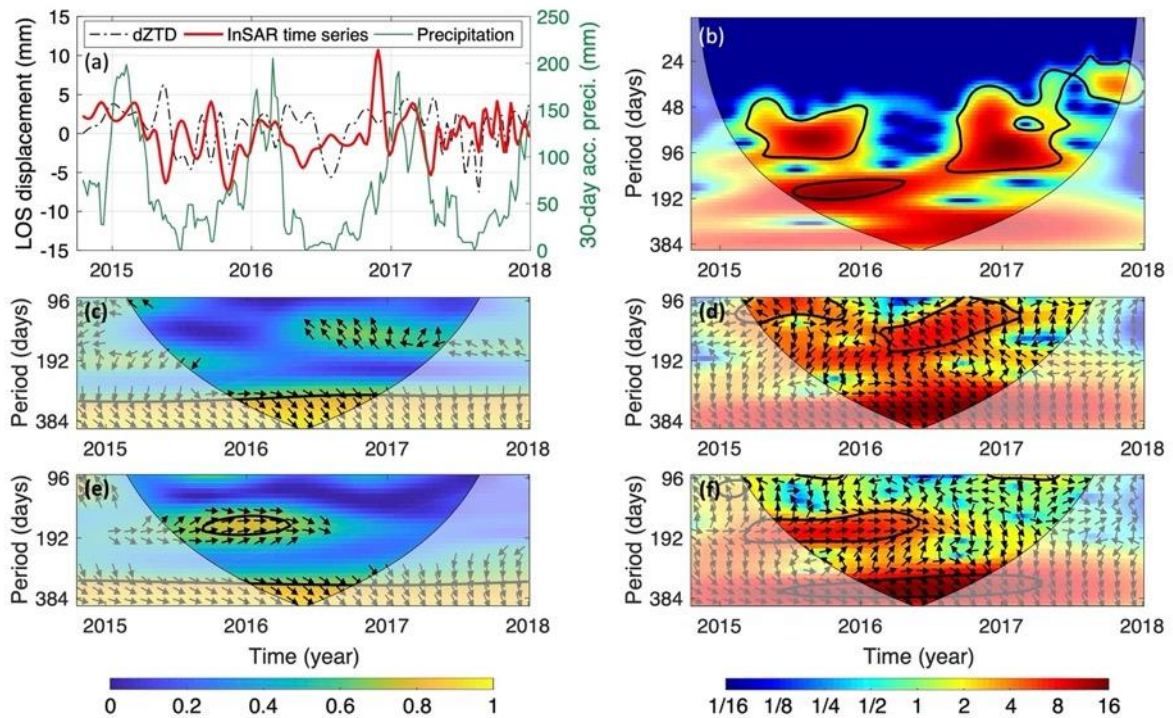


Figure 4.13 Relationship between InSAR time series and differential zenith tropospheric delays (dZTD) and 30-day accumulated precipitation analysed with wavelet tools. (a) Time series of InSAR displacement, dZTD and precipitation. (b) Continuous wavelet power (CWT) of InSAR time series. The black contour designates the 5% significance level against noise. The lighter shadow denotes the cone of influence by potential edge effects. (c) and (d) are wavelet coherence (WTC) and cross wavelet transform (XWT) between InSAR time series and dZTD, respectively. (e) and (f) are WTC and XWT between InSAR time series and precipitation, respectively. The black arrows represent the relative phase shift, with the in-phase pointing right (0°) and the first series leading the second at 90° pointing down.

4.5.2 Instability of the landslide

The ground deformation observed had a dramatic effect on the residential buildings and infrastructures of the town. The examples of the identified damage within the three sub-blocks (Figures 4.1d to 4.1j) indicate that: i) almost all the buildings exhibit sparse cracks, fine and rarely open; ii) the church (Figure 4.1f) and the opposite garage (Figure 4.1g) exhibit big and

spread fractures showing open cracks up to 5 cm wide; iii) the bus station (Figure 4.1h) is completely distorted and partially collapsed with several open fractures; iv) widespread cracking caused by shear stresses induced by the landslide movement is found in several house walls and at the food market (Figure 4.1e).

With InSAR, I further found that the landslide in Villa de la Independencia experienced accelerated deformation since 2018. Due to the increased precipitation in the late rainy season in 2018, more rainwater infiltrated and tended to saturate the landslide body at the base of the slope. This in turn leads to larger porewater pressures and reduces the frictional strength along the failure plane (Hu et al., 2016). Furthermore, the loading by the weight of water on the failure plane can increase the gravitational driving force (Saar and Manga, 2003; Schmidt and Bürgmann, 2003; Crosta et al., 2014b). These two effects lead to the acceleration of the landslide motion. It can be concluded that the landslide is seasonally active and controlled by precipitation, now with a higher risk of failure than before. It is recommended that an early warning system should be installed in this area with, as a minimum, a weather station and a ground total station (or a GPS station) for constant monitoring of precipitation and surface displacements, respectively. Also, any future construction of residential buildings and infrastructure should be outside the areas identified as most subject to surface displacements.

4.6 Summary

This chapter provides a solution to capture both the long-term surface deformation and subsurface information of landslides. The solution combines InSAR time series and seismic noise measurements and thus enables the identification of 3D sliding geometry and the analysis of landslide evolution. The landslide case used to verify this solution was a complex landslide in Villa de la Independencia, Bolivia, where both descending and ascending Sentinel-1 data were collected and processed through the InSAR time series technique. A dense seismic noise observation network with 120 on-site measurements was also established and used to invert the slip surfaces of the landslide.

InSAR observations reveal that the landslide in Independencia is featured by dominant along-slope movements. Three sub-blocks, namely the town centre, upper block, and east block were identified, and their diverse sliding directions were determined by a new InSAR-based geometric inversion method. The seismic noise measurement analysis further reveals the sliding depth of each landslide sub-block and suggests that the town centre sub-block seems to be more affected by a deeper sliding surface (15 to 75 m) compared to the other two sub-blocks. The

combination of InSAR and seismic noise measurements determines the landslide as a compound sliding type with a volume of about $9.18 \cdot 10^7 \text{ m}^3$.

In terms of the temporal evolution of the landslide motion, seasonal precipitation contributes most to the seasonal oscillations in deformation time series. More importantly, the deformation time series from InSAR observations presented periodic accelerations in early 2018 and 2019. The two accelerations, which were greater in the town centre sub-block than in the other two sub-blocks, were found to occur from January to March and lasted for about one month. This was probably due to the sudden increase of precipitation in the late rainy season of 2018 and 2019 compared to previous years as observed by GPM. This leads to speculation that the landslide could be subject to periodic accelerations in the future following periods of heavy rainfalls.

This study showcases the great potential of combining InSAR with seismic noise measurements in characterising landslide motion. InSAR observations are directly related to the deformation on the ground surface while seismic noise measurements can determine the depth of the sliding surface. The combined use of the two techniques allows a full characterisation of landslide kinematics and a better assessment of landslide risks.

Chapter 5. Detection and characterisation of earthquake accelerated landslides in Central Italy with InSAR observations

This chapter aims to automatically identify landslide risk areas after capturing long-term deformation by InSAR. A new InSAR-based automated deforming area detection method was developed and it was applied to identify landslide risk areas in Central Italy after the 2016-2017 earthquake sequence. The application enabled the establishment of an inventory of earthquake accelerated landslides (EALs) in Central Italy for the first time, based on which the landslide conditioning factors and sliding dynamics of these detected EALs will be quantified. This work has been published in *Nature Communications*.

Earthquake-induced landslides often pose a great threat to the safety of human life and property, of which coseismic landslides that are triggered by earthquakes mostly with failures or collapse are subject to transient/short-term seismic effects while EALs respond to long-term seismic effects. The movements of EALs are typically accelerated with increased sliding velocity after earthquakes and the acceleration phenomenon could be maintained for a long time. In other words, the earthquakes trigger EALs to accelerate rather than to fail/collapse, or only to move from immobility (i.e., EALs may also accelerate from moving). EALs are therefore a new type of landslides associated with earthquakes, distinctly different from the extensively studied coseismic landslides, but they have been largely neglected by the emerging research.

Here, I used satellite radar observations to detect and investigate the acceleration and recovery of the EALs in Central Italy. As distinguished from previous studies based on single or discrete landslides, I established a complete EAL inventory and statistically quantified as a whole their spatial clustering features against a set of landslide conditioning factors, their distribution patterns against collapsed coseismic landslides, and their accelerating-to-recovering sliding dynamics. These investigations serve as an important supplement to the complete picture of the landslide inducing mechanism by earthquakes and contribute to a more comprehensive long-term assessment of landslide risk.

5.1 Introduction

Landslides refer to mass wasting on the ground surface, causing severe casualties and economic losses each year either instantaneously from rapid slope failures (Petley, 2012) or accumulatively from slow-to-fast downslope movements of soil and/or rocks (Lacroix et al., 2020). As introduced in Section 1.4, the slope instability of a landslide can be triggered by earthquakes (Marano et al., 2010; Xu et al., 2013), rainfall (Collins and Znidarcic, 2004),

snowmelt (Naudet et al., 2008), volcanic activities (de Vita et al., 2006) and disturbance from anthropogenic activities (Lacroix et al., 2019). Among them, the Earthquake Triggered Landslide (ETL) that occurs immediately following an earthquake (Chigira et al., 2010; Martino et al., 2019) or after a period of time (Fan et al., 2021) accounts for over 60% of landslide casualties between 2002 and 2010 (Lacroix et al., 2015), which is a major concern especially in seismic active regions. This has motivated plentiful studies with a focus on coseismic landslides that collapsed during an earthquake (e.g., Chigira et al., 2010; Fan et al., 2018b; Martino et al., 2019), new post-seismic landslides that were cracked slopes caused by an earthquake and developed into failures by aftershocks or post-seismic rainfalls (e.g., Marc et al., 2015a; Chen et al., 2021), and post-seismic reactivations/remobilizations that were coseismic landslide deposits reactivated or remobilized mostly during rainfall events after earthquakes (e.g., Fan et al., 2018a). However, long-term seismic effects that activated unstable landslides but without causing failures/collapse even after a long period since the earthquake (months to years) are typically ignored due to the minor, if any, ground changes caused compared to collapsed slopes. These landslides respond to coseismic or post-seismic stress disturbances differently from the coseismic landslides and other types of collapsed/cracked post-seismic landslides and are typically activated with considerably increased displacement rates compared to their pre-earthquake levels (hence referred to as Earthquake Accelerated Landslides, EALs). As a result, they may generate continuous damage to the ground or man-made infrastructure above them and develop into catastrophic failures in the future.

Preliminary attempts have located a single EAL (Lacroix et al., 2014; Bontemps et al., 2020) or several neighbouring EALs (Lacroix et al., 2015). For example, Bontemps et al. (2020) used 3-year geodetic and seismic datasets to characterize a slow-moving landslide affected by local earthquakes and seasonal rainfalls and highlighted how small-shaking events had weakened the landslide rigidity. Lacroix et al. (2015) detected nine slow-moving landslides in the Colca valley (Peru) with Pléiades images and reported their accelerations were caused by a regional Mw 6.0 earthquake. However, due to the lack of a complete and consistent EAL inventory after earthquakes, these localized studies only characterized individual EALs and were unable to investigate collectively the landslide behaviours in the perspective of an integral EAL inventory. The spatial-temporal features of EALs such as the spatial pattern of landslide distribution, the different behaviours between EALs and coseismic landslides, and their overall evolution of the sliding velocity were largely unknown. These features may well explain the landslide inducing mechanisms and contribute to hazard early warning or prediction.

In this context, establishing a complete EAL inventory consistently over a sufficiently large spatial extent and a long period becomes superior, based on which various potential landslide conditioning factors (LCFs, e.g., seismic effects, slope, lithology) can be related statistically against the EAL occurrence and different temporal behaviours of EALs before and after the earthquake can be distinguished. However, this poses challenges for traditional field-based landslide investigation which faces difficulties such as labour-intensive, time-consuming and high cost. Remote sensing-based landslide mapping techniques have been proven to be efficient in detecting large-area ground changes, but they can hardly capture very small landslide movements (centimetre level or smaller), even by Very High Resolution (VHR) satellites (Stumpf et al., 2014), despite its high cost for long-term monitoring.

Interferometric Synthetic Aperture Radar (InSAR) has been proven to be able to measure subtle ground displacements such as those induced by interseismic loading (Elliott et al., 2016; Daout et al., 2018), postseismic relaxation (Wen et al., 2012; Pousse-Beltran et al., 2020) and extremely slow-moving landslides (Handwerker et al., 2019; Bekaert et al., 2020; Kang et al., 2021). Landslide inventories over a large area (e.g., Bonì et al., 2020) can be retrieved routinely using high spatial resolution InSAR observations with a short revisit interval (e.g., up to 5 m and 6 to 12 days for Sentinel-1). However, challenges remain in applying InSAR for post-earthquake landslide detection. First, most InSAR-based landslide detection methods employ an empirical velocity threshold (e.g., 2 mm/yr in Lu et al., 2019; 10 mm/yr in Zhang et al., 2020) to define moving pixels which may lack versatility, especially in the absence of prior knowledge of the background deformation level. Second, the threshold-based detection method ignores the spatial correlation and clustering effects among pixels inside a landslide and is prone to be greatly affected by noisy pixels. Third, it is often difficult to distinguish between postseismic deformation and landslide-induced deformation from InSAR time series, especially in areas close to seismogenic faults (e.g., Lacroix et al., 2014).

In this study, I proposed a novel InSAR-based EAL detection method to establish a complete EAL inventory of the 2016-2017 Central Italy earthquake sequence using six years of Sentinel-1 data in both descending and ascending modes from 2014 to 2020. A spatial filter was applied on InSAR-derived velocity maps to reduce the spatially correlated noise and separate postseismic deformation so that localized landslide motion can be retrieved. The algorithms of Minimum Covariance Determinant (MCD) and Density-Based Spatial Clustering of Applications with Noise (DBSCAN) were utilized respectively to adaptively determine slipping pixels and cluster them into landslide bodies. By comparing with the landslides not accelerated

by earthquakes (non-EALs) established with the Italian national landslide inventory (IFFI) created prior to the earthquakes, I investigated 15 landslide conditioning factors (such as topographic, lithology and seismic factors), and quantitatively classified their impacts on landslide acceleration based on the Information Gain (IG) function (Hall and Holmes, 2003). I further investigated the different spatial patterns between EALs and coseismic landslides and the different temporal behaviours of EALs before and after the earthquakes using high temporal resolution InSAR time series. We hope that these investigations could complement a more complete picture of the landslide inducing mechanisms in addition to the extensively studied coseismic landslides and contribute to a more comprehensive long-term assessment of landslide risk.

5.2 Study area and data

5.2.1 Study area

The 2016-2017 earthquake sequence in Italy included four main events that occurred respectively on 24 August 2016 (Mw 6.1), 26 October 2016 (Mw 5.9), 30 October 2016 (Mw 6.6) and 18 January 2017 (Mw 5.5) and struck a wide area of Central Apennines. These four events caused about 300 casualties and severely damaged buildings and transportation routes (Hofer et al., 2018; Martino et al., 2019). The earthquake sequence mainly ruptured the Mt Gorzano-Vettore-Bove (MGVB) fault system in NW-SE trending, with normal fault slipping (Cheloni et al., 2017). According to the geodetic inversion and the relocation of aftershocks, an antithetic NE dipping normal fault near the Norcia area was additionally discovered to be ruptured during the 30 October 2016 event (Walters et al., 2018; Cheloni et al., 2019). The slip state of another inherited west-dipping thrust, the Olevano-Antrodoco-Sibillini (OAS) thrust, was also widely discussed (e.g., Chiaraluce et al., 2017; Pizzi et al., 2017; Chiarabba et al., 2018; Walters et al., 2018) but its role in the rupture geometry and the reactivation mechanism remained unclear (Cheloni et al., 2019). In addition to the coseismic ruptures, postseismic surface deformation in a centimetre scale that followed a logarithmic temporal decay was also observed and the related shallow afterslip was revealed to likely halt the rupture propagation (Pousse-Beltran et al., 2020).

Geologically, in the study area affected by the earthquake sequence, the tectonic stratigraphic evolution includes the NE-trending migration of the imbricate fold-and-thrust Apennines Chain from the Miocene to the Lower Pliocene, and the onset of an extensional tectonic wave associated with normal faulting from the Late Pliocene–Early Pleistocene, exhibiting the characteristic of long term and multi-phase (Bigi et al., 2011; Martino et al., 2019). The ongoing

extension is oriented toward ENE with a velocity of 2 to 4 mm/yr (D'Agostino, 2014; Pousse-Beltran et al., 2020), currently accommodated through normal fault systems (e.g., the MGVB). In terms of the deposits, the sedimentary sequence includes Jurassic–Cenozoic limestones and marls of the Umbria–Marche pelagic basin (Martino et al., 2019), the limestones and dolomites of the Latium-Abruzzi carbonate platform (Pierantoni et al., 2013) and the foreland-deposited flysch of the Upper Miocene Laga Fm. (Falcini et al., 2009).

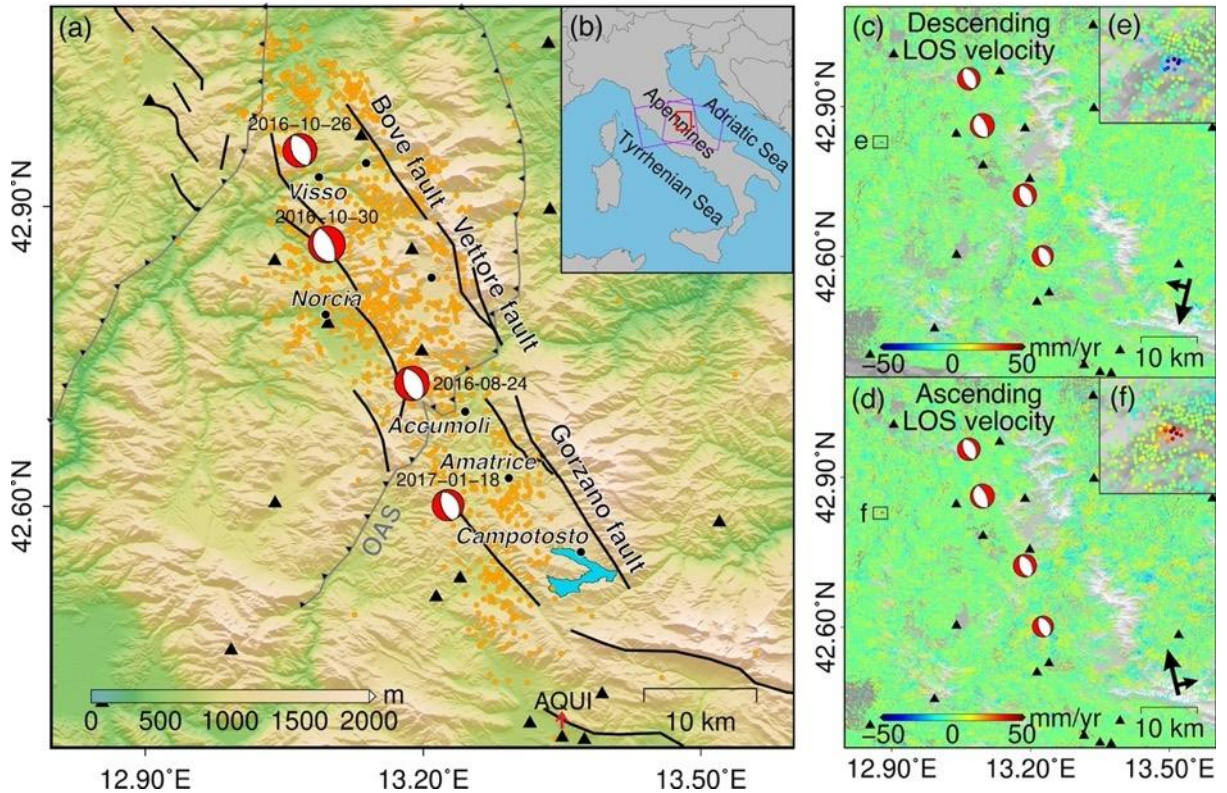


Figure 5.1 Seismotectonic background of the study area and InSAR-derived velocity fields in the Line of Sight (LOS). (a) Seismotectonic background with the four 2016–2017 earthquakes. Solid black lines represent the major active faults while the grey barbed lines indicate the pre-existing compressional faults. The locations and moment tensor solutions of the four main earthquakes in Central Italy from 2016 to 2017 (red beach balls) were obtained from the United States Geological Survey (USGS) (<https://earthquake.usgs.gov>). Orange dots represent aftershocks ($M > 3.0$). Black triangles mark GPS stations, and black solid circles represent cities in Italy. (b) Geographical location of the study area (red rectangle). Purple rectangles indicate the coverage of descending- and ascending-track Sentinel-1 images. (c) and (d) are the filtered post-earthquake descending and ascending LOS velocity fields, with the positive value being toward the ground from the satellite. The inset (e) and (f) are examples of zoom-in views of the InSAR velocity.

5.2.2 InSAR time series

Sentinel-1 Terrain Observation by Progressive Scans (TOPS) (Torres et al., 2012) data in Interferometric Wide (IW) swath mode was used to capture the deformation in the study area.

The Sentinel-1 constellation operated by European Space Agency comprises two polar-orbiting satellites (Sentinel-1A and 1B) performing C-band SAR imaging and offers wide-area monitoring with a minimum 6-day revisit cycle. The spatial resolution of Sentinel-1 acquisitions is about 5 m in range and 20 m in azimuth. I collected 280 Sentinel-1 images in the descending track (Path 22) spanning from 7 October 2014 to 30 August 2020 and 292 images in the ascending track (Path 117) from 13 October 2014 to 30 August 2020. Each SAR image was connected to at least 10 nearest images in time to generate interferometric pairs. Considering that a long temporal baseline could cause strong decorrelation, I excluded interferograms with a temporal baseline greater than three months and finally obtained 1,420 and 1,507 interferometric pairs (Figure 5.2) for the descending and ascending tracks, respectively.

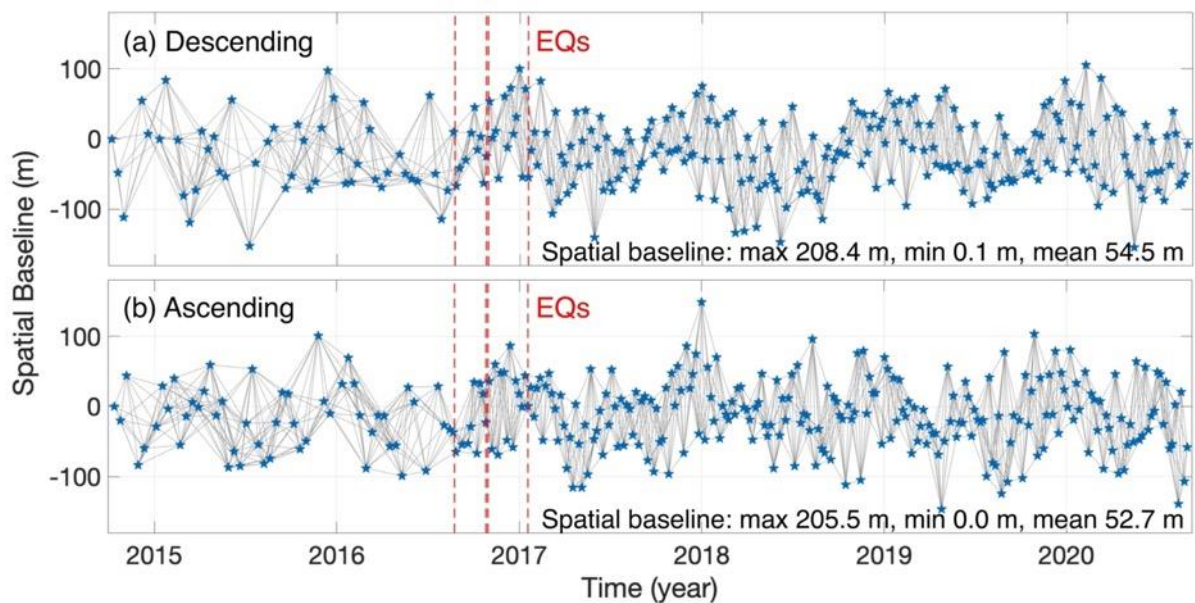


Figure 5.2 Sentinel-1 acquisition dates and generated interferograms in the (a) descending and (b) ascending tracks. Sentinel-1 acquisitions are indicated by blue stars. The grey lines represent Sentinel-1 interferometric pairs used in the time series analysis and Y-axis shows their perpendicular baseline length (m). The red dotted lines indicate the date of earthquakes (EQs).

The time series InSAR processing flow detailed in Song et al. (2021) was used to process the Sentinel-1 data. To generate interferograms, a 30 m Digital Elevation Model (DEM) from the Shuttle Radar Topography Mission (SRTM) (Farr et al., 2007) was used to remove topographic phases and geocode interferograms. Tropospheric delay corrections from Generic Atmospheric Correction Online Service (GACOS) for InSAR (Yu et al., 2017; Yu et al., 2018b; Yu et al., 2018c) were applied to these interferograms to reduce the atmospheric effect. These corrected interferograms were then processed by the Small BAseline Subset (SBAS) mode of the Stanford Method for Persistent Scatterers (StaMPS) software (Hooper et al., 2012) to generate InSAR

time series. During the time series processing, the spatial reference was set as the mean phase value in the study area, and InSAR coherent pixels after the phase correction of spatially uncorrelated noise were resampled to 30 m for 3D unwrapping (Hooper and Zebker, 2007) to improve the processing efficiency. Such SBAS method does not require a pre-defined deformation model to constrain time series and has been proved to be effective in retrieving the coseismic and postseismic displacements (e.g., Pousse-Beltran et al., 2020; Liu et al., 2021).

The resultant InSAR time series was then validated by Global Positioning System (GPS) displacements from 19 stations (black triangles in Figure 5.1) in the Istituto Nazionale di Geofisica e Vulcanologia (INGV) network. GPS time series solutions provided by the Nevada Geodetic Laboratory (NGL) (Blewitt et al., 2018) were projected onto the radar Line of Sight (LOS) direction, following Equation (5.1). In the equation, N , E and U are GPS displacements in the north, east and vertical (up) directions; θ_{inc} is the incidence angle of satellite radar and α_{head} is the heading angle; LOS is the projected displacement along LOS. Then GPS LOS displacement time series were resampled to the SAR acquisition dates. As InSAR observations are relative measurements with a spatial reference, the GPS time series was referenced to AQU1 located in Coppito, Province of L'Aquila, and the InSAR reference point was set to the location of AQU1 (marked in Figure 5.1a). The reason for choosing AQU1 is that it is relatively less affected by the coseismic deformation (< 5 mm) and has recorded the most complete GPS data in the past 10 years without interruption.

$$LOS = \begin{bmatrix} -\sin\theta_{inc}\sin\alpha_{head} \\ \sin\theta_{inc}\cos\alpha_{head} \\ -\cos\theta_{inc} \end{bmatrix}^T \cdot \begin{bmatrix} N \\ E \\ U \end{bmatrix} \quad (5.1)$$

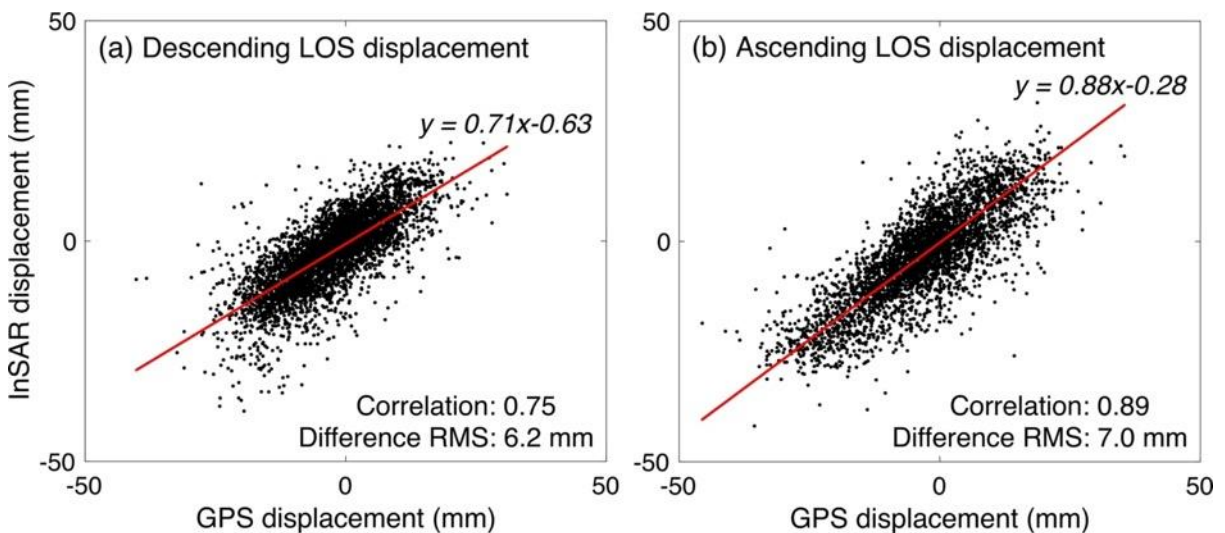


Figure 5.3 Correlation analyses between InSAR and GPS displacements along the LOS in the (a) descending track and (b) ascending track.

The InSAR and GPS displacements were compared for each observation epoch before and after the earthquake sequence. The comparison results (Figures 5.3a and 5.3b) show that the root mean square (RMS) of the difference between GPS and Sentinel-1 InSAR displacements in descending and ascending modes are 6.2 mm and 7.0 mm, respectively. Figures 5.3a and 5.3b also show the linear fit between GPS and InSAR LOS displacements and their Pearson's linear correlations are 0.75 and 0.89 for descending and ascending LOS, respectively. The high correlation with GPS and the small RMS difference implies the reliability of InSAR observations.

5.2.3 IFFI

The Inventario dei Fenomeni Franosi (Inventory of Landslide Phenomena) in Italy (IFFI) project, implemented by Istituto Superiore per la Protezione e la Ricerca Ambientale (ISPRA) and regional environmental protection agencies, provides a basic national database on landslides. The landslide inventory was first published online by ISPRA in 2005. Since then, 620,808 landslide sites (www.progettoiffi.isprambiente.it) have been updated by means of satellite images, airborne photos and field investigation. However, only a few landslides in IFFI remain active, for example, in the Piedmont region of Italy, only ~15% of landslides in IFFI were classified as active by InSAR (Bonì et al., 2018). In addition, different regions differ in the update time of the landslide inventory. The study area spans four regions, of which the Umbria Region has updated the inventory up to 2017 while the Marche, Lazio and Abruzzo Regions only updated up to 2007. In total, 9,509 landslides shown in Figure 5.5a have been documented in the study area, of which 3,615 (38.0% of the inventory) are classified as rotational/translational slides. The second most widely distributed type of landslides is slow earth flow, accounting for 25.7%, followed by shallow landslides (11.3%). Each of the other landslide types, including rapid debris flow (9.5%), rockfalls/topples (9.4%) and complex slides (4.0%), etc., only represents a small percentage of the entire inventory. Note that the types of these landslides in IFFI were determined according to their past failure/moving mechanics and may not be representative of their latest status. In this study, I used IFFI to locate non-EALs with the method described in Section 5.3.1 and compare the spatial characteristics of these non-EALs with EALs to analyse the impact of different LCFs on landslide acceleration. Such comparison focuses on the present seismic-affected activity of landslides and would not be interfered by the original landslide types.

5.2.4 Geo-environmental data

Environmental and earthquake-related data were also collected to statistically perform spatial analysis of geo-environmental factors controlling landslide behaviours. The 30 m SRTM DEM used in InSAR data processing was analysed to quantify topographic factors (e.g., slope, aspect, and curvature). A Sentinel-2 image with almost zero cloud cover (0.2%) on 14 August 2016 was used to calculate the Normalized Difference Vegetation Index (NDVI) (Tucker, 1979) based on the near-infrared spectrum (band 8) and the red range of the spectrum (band 4). I also collected Global Precipitation Measurement (GPM) daily records (Hou et al., 2014; Huffman et al., 2019) from multi-satellite gauging to investigate hydro-climatic factors such as rainfall and snowfall. Regarding the seismic effect, Peak Ground Acceleration (PGA) and Peak Ground Velocity (PGV) of the four 2016-2017 earthquakes in Central Italy were extracted from the USGS ShakeMap products (<https://earthquake.usgs.gov/data/shakemap>). Note that the ground motions of the four earthquakes were accumulated to account for the overall impact of the earthquake sequence.

5.3 Methods

5.3.1 EAL detection method

In this work, InSAR derived velocity fields were used to locate active landslides and then to identify EALs by comparing landslide velocities before and after the earthquake sequence. The EAL detection method includes the following four steps.

Step 1: Generation of pre- and post-earthquake InSAR velocity fields

Based on the InSAR displacement time series processed in Section 5.2.2, I calculated LOS velocity fields respectively for periods before the first event (i.e., pre-earthquake velocity (v_{pre}^{LOS}) from 13 October 2014 to 21 August 2016) and one year after the last event (i.e., post-earthquake velocity (v_{post}^{LOS}) from 24 January 2017 to 25 January 2018). Only one year of the displacement time series after the last event was included to highlight the immediate acceleration effect due to the earthquakes, which may fade away through time as will be discussed in Section 5.4.3, and to avoid possible velocity variations caused by non-seismic inducers (e.g., heavy rainfall) as noticed in Figure 5.9. The velocities during these two periods were obtained by linearly fitting the associated displacement time series (Selvakumaran et al., 2018). Comparing InSAR and co-located GPS derived LOS velocities, I estimated the RMS of their difference in the ascending and descending LOS was approximately 3.1 and 3.0 mm/yr, respectively.

Landslide motion signals may be contaminated by long-wavelength deformation (e.g., post-seismic deformation) or errors (atmospheric, orbital and ocean tide loading errors) on InSAR velocity fields. Therefore, to identify localized landslide motions, I first applied a local spatial filter on the velocity fields to reduce the effects of spatially correlated noise (e.g., residual long-wavelength errors) and postseismic deformation, as shown in Figure 5.4a. Instead of using a fixed global reference point, the local spatial filter referenced the phase of each pixel against the local mean phase averaged within a kernel (i.e., a circular buffering area) surrounding that pixel (Bekaert et al., 2020). The radius of the kernel was fixed to 2 km as suggested by Bekaert et al. (2020) in double-difference phase analysis which minimized the effect of over-filtering on the landslide signals. With this local spatial filter, spatially correlated signals at distances beyond the kernel size can be largely cancelled out.

Step 2: Location of post-earthquake moving pixels

The filtered post-earthquake InSAR velocity fields (Figures 5.1c and 5.1d) were used to locate all moving pixels which may be clustered as active landslides in the follow-on steps. I used the LIBRA software (<https://wis.kuleuven.be/stat/robust/LIBRAfiles/>, Verboven and Hubert, 2005) to statistically identify moving pixels based on the Minimum Covariance Determinant (MCD) method (Rousseeuw, 1984; Hubert and Debruyne, 2010). The inputs of the software were v_{post}^{LOS} of the InSAR pixels and the outputs were the locations of the identified moving pixels. This method does not require an empirical velocity threshold and the moving pixels can be detected adaptively in an automatic way.

Step 3: Clustering moving pixels into landslide bodies

After extracting moving pixels from post-earthquake InSAR velocity fields, I used the Density-Based Spatial Clustering of Applications with Noise (DBSCAN) (Ester et al., 1996; Schubert et al., 2017) algorithm to automatically cluster these pixels into landslide bodies. DBSCAN is a powerful cluster algorithm in statistics but its application in the InSAR field is rare. Unlike the commonly used k-means partitioning algorithm, this algorithm is based on the pixel spatial density without the requirement of a pre-defined number of clusters, which improves the adaptability of clustering. Moreover, the k-means algorithm forcibly clusters all included pixels and is vulnerable to noise, while the DBSCAN algorithm is able to exclude noisy pixels that lack sufficient connected neighbourhoods (Ester et al., 1996).

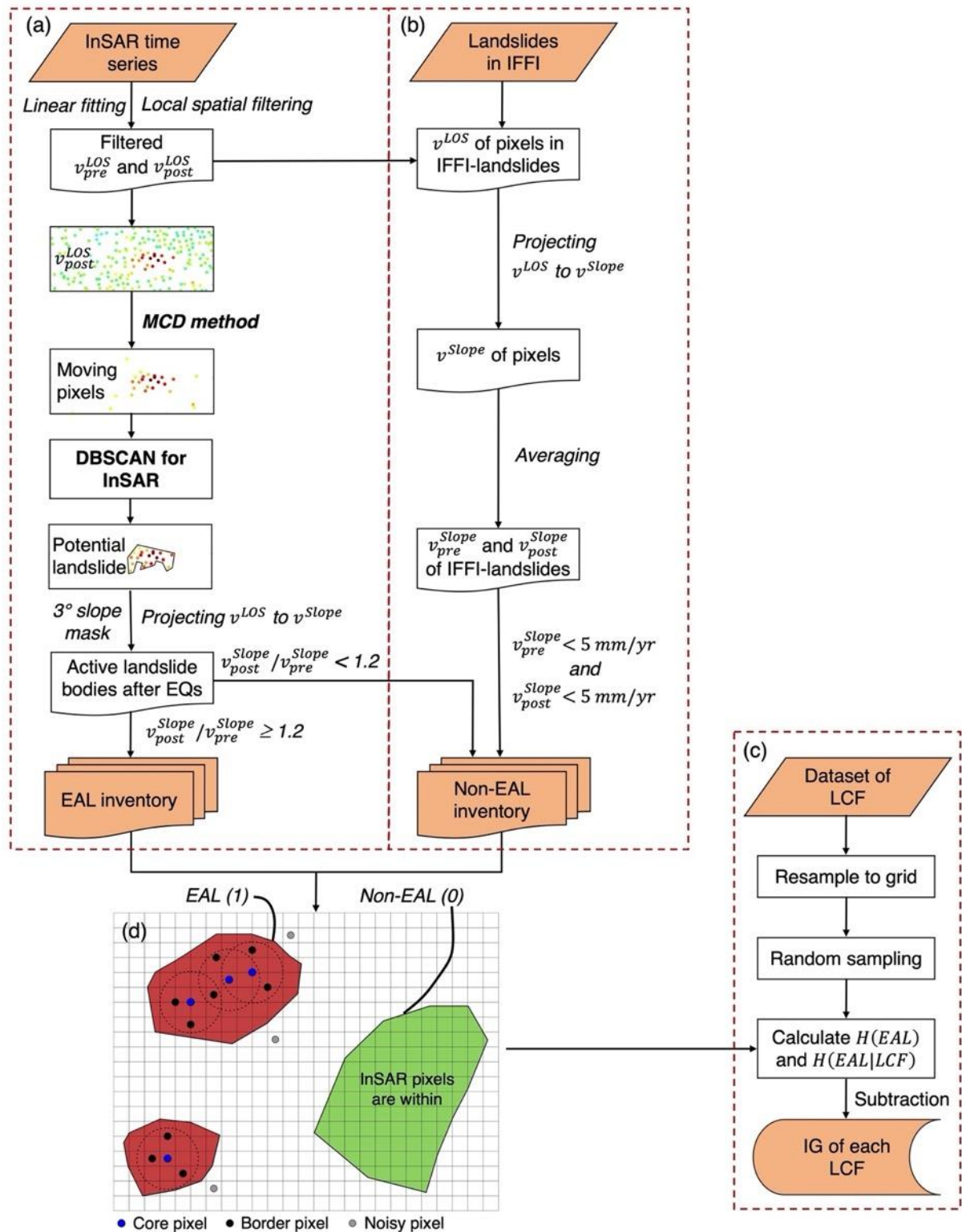


Figure 5.4 Workflow for EAL/non-EAL detection and information gain (IG) methods. (a) Workflow for developing the EAL inventory based on InSAR. (b) Workflow for detecting non-EALs based on InSAR and IFFI. (c) IG method for statistically analysing LCFs. (d) Conceptual diagram of gridding, landslide state definition and three types of pixels (i.e., core, border, and noisy pixels).

DBSCAN defines three types of pixels: core pixels, border pixels and noisy pixels (Figure 5.4d). A core pixel is located inside a cluster that is surrounded by at least a minimum number ($MinPts$)

of moving pixels within a fixed radius (R). These moving pixels are called the neighbourhood moving pixels of the core pixel. In this study, $MinPts$ was set to three to guarantee at least three moving pixels per cluster (Bonì et al., 2018; Crippa et al., 2021), and R was set to 60 m (twice the InSAR pixel spacing) to connect sufficient pixels. A border pixel is the neighbourhood pixel of at least one core pixel, but it has less than $MinPts$ neighbourhood pixels. A noisy pixel is not neighbouring to any core pixel. DBSCAN starts with an arbitrary moving pixel p , 1) if p is a core pixel, all neighbourhood moving pixels of p will be assigned as the same cluster with p and their types (core or border pixel) will be evaluated; 2) repeat step 1) iteratively for all the neighbourhood moving pixels of core and border pixels in the cluster of p until all moving pixels that should be clustered with p are identified; 3) continue to the next moving pixels until all pixels were clustered.

Step 4: Classification of EALs and non-EALs

After clustering all moving pixels into active landslide bodies with DBSCAN, I then masked out those clusters with an average slope of less than 3 degrees, because landslides were unlikely to occur on such flat terrain. Note that since both descending and ascending Sentinel-1 data have been collected, two inventories of post-earthquake active landslides will be generated following the above procedure. Thus, I merged them by uniting overlapping landslide bodies and calculated their pre- and post-earthquake velocities along the slope (v_{pre}^{Slope} and v_{post}^{Slope}) by averaging the along-slope velocities of all pixels inside the landslide body. The along-slope velocity v^{Slope} of each pixel was calculated by projecting the LOS velocity v^{LOS} onto the landslide slope direction, assuming that the landslide movements occurred along the steepest gradient of the slope (Notti et al., 2014; Bonì et al., 2018). The projection can be expressed as Equations (5.2) and (5.3), where s and a are the slope and aspect angles at the location of InSAR pixels, σ and α are the incidence and heading angles of satellite radar, C is the projection coefficient that converts v^{LOS} to v^{Slope} . It should be noted that C is limited to 0.3 when $0 < C < 0.3$ and to -0.3 when $-0.3 < C < 0$ to avoid anomalous exaggeration caused by the projection (Herrera et al., 2013). Besides, for landslides containing both descending- and ascending-mode Sentinel-1 coherent pixels, the along-slope velocities projected from InSAR observations in these two modes are averaged to be representative.

$$C = -\cos(s)\cos(a)\sin(\sigma)\sin(\alpha) + \cos(s)\sin(a)\sin(\sigma)\cos(\alpha) + \sin(s)\cos(\sigma) \quad (5.2)$$

$$v^{Slope} = v^{LOS}/C \quad (5.3)$$

Then, v_{pre}^{Slope} and v_{post}^{Slope} of each candidate landslide were compared to identify the accelerated landslides of interest with sufficient velocity changes ($v_{post}^{Slope} / v_{pre}^{Slope} \geq 1.2$) and an EAL inventory was created. The ratio between v_{pre}^{Slope} and v_{post}^{Slope} is referred to as the landslide acceleration ratio which represents the magnitude of the acceleration caused by the earthquakes. The active landslides that were not accelerated by the earthquake sequence ($v_{post}^{Slope} / v_{pre}^{Slope} < 1.2$) were then classified as non-EALs (Figure 5.4a).

Since InSAR can only detect active landslides, the above procedure is unable to locate non-EALs that are inactive both before and after the earthquake sequence. As shown in Figure 5.4b, IFFI was used to find these inactive non-EALs by 1) locating landslides documented by IFFI on the InSAR velocity maps; 2) projecting v^{LOS} of pixels in IFFI-landslides to v^{Slope} with Equations (5.2) and (5.3); 3) calculating v_{pre}^{Slope} and v_{post}^{Slope} of each IFFI-landslide by averaging v^{Slope} of pixels inside before and after the earthquakes; 4) identifying inactive landslides whose v_{pre}^{Slope} and v_{post}^{Slope} are both smaller than 5 mm/yr as defined by Cigna et al. (2013). These inactive non-EALs and the InSAR-detected active non-EALs, despite differences in activity, are both against EALs with respect to the presence of acceleration phenomena and should be amalgamated for comparison with EALs. The final inventory of non-EALs (1,625 detected by InSAR and 1,120 from IFFI), together with the EAL inventory, enabled the following statistical analysis.

5.3.2 Statistical analysis method

Landslide Conditioning Factors (LCFs) are geo-environmental factors that control landslide occurrence, evolution and potential collapse. Hence, their spatial distribution may play a key role in landslide susceptibility assessment. I used the Information Gain (IG) function to quantitatively rank a set of LCFs linked to EALs in order to statistically investigate the main controlling factors. IG is one of the fastest and simplest attribute ranking methods (Hall and Holmes, 2003) used to select features in a decision tree model (e.g., Lei, 2012; Alhaj et al., 2016). The value of IG represents how much contribution of an LCF can affect the EAL occurrence. As shown in Figure 5.4c, the first step of implementing the IG method is to create a dataset of LCFs. A large set of LCFs including topographic, lithologic, vegetation, hydrologic and seismic factors (Fan et al., 2021) (Table 5.1) was selected. I calculated high-resolution maps for each LCF and resampled them into a 30 m uniform grid as the DEM (i.e., one map per LCF). All the topographic factors were computed in the SAGA GIS software (<http://www.saga-gis.org>)

using the 30 m SRTM DEM. I additionally selected two other types of LCFs to represent the pre-earthquake landslide activity and the size of the landslide body which may also explain the governing mechanisms of EALs. The landslide activity factors included the pre-earthquake velocity (v_{pre}^{Slope}) and the percentage of relatively fast-moving pixels ($v_{pre}^{Slope} > 10$ mm/yr) inside a landslide body.

To calculate the IG of each LCF, the concept of information entropy (Hall and Holmes, 2003), which was used to measure the uncertainty in the classification of the landslide (i.e., whether the landslide is an EAL or non-EAL), should be introduced. I first generated an index map for the study area with the same dimension as the LCF maps with its pixels inside EALs being marked as 1 and pixels inside non-EALs as 0 (Figure 5.4d). Then 1,000,000 pixels on the index map (about 10% of the total) were randomly selected and the information entropy $H(EAL)$ was calculated using Equation (5.4), where $p(i)$ is the percentage of the pixels belonging to landslide class i among the total 1,000,000 pixels ($i = 1$: EAL; $i = 0$: non-EAL) and n represents the number of the class (2 in this case).

Table 5.1 Landslide conditioning/triggering factors used in this study

Type	Landslide conditioning factors	Description
Topographic factors	Elevation	30 m SRTM DEM (Farr et al., 2007)
	Slope	Slope angles derived from the DEM
	Aspect	Orientation of the slope derived from the DEM, clockwise from the north ($0^\circ/360^\circ$)
	Planar curvature	Curvature of the slope, relating to the surface shape (>0 : convex, <0 : concave, 0 : linear)
	Positive openness	Surface convexity, indicating how wide a surface can be viewed from any position (Yokoyama et al., 2002)
	Topographic Position Index (TPI)	Indicating whether the cell position is closer to ridges (>0), valleys (<0) or constant slope (0) (Guisan et al., 1999)
	Morphometric Protection Index (MPI)	Index of how the surrounding relief protects the cell
Lithology	Lithology	Main lithology of the cell
Vegetation	NDVI	Normalized difference vegetation index (Tucker, 1979)
Hydro-climatic factors	Precipitation	Gridded 0.1° GPM records (Hou et al., 2014) during the earthquake sequence, unit: mm
Seismic factors	PGA	Peak ground acceleration, unit: g

	PGV	Peak ground velocity, unit: cm/s
Landslide activity	Pre-earthquake velocity	Landslide velocity before the earthquakes, unit: mm/yr
	Activity proportion	Proportion of pixels that are substantially active (>10 mm/yr) inside the landslide
Landslide size	Landslide area	Unit: m ²

$$H(EAL) = - \sum_{i=1}^n p(i) \log_2 p(i) \quad (5.4)$$

The uncertainty of the landslide class given that the value of an LCF is known was then quantified using the conditional entropy $H(EAL|LCF)$. As shown in Equation (5.5), l represents the value of an LCF, $p(l)$ denotes the percentage of the sampled pixels whose value is l on the LCF map, and $p(i|l)$ represents the percentage of the sampled pixels belonging to landslide class i when its value is l on the LCF map. Thus, with Equation (5.5), I computed the conditional entropy of each LCF.

$$H(EAL|LCF) = - \sum_{l \in LCF} p(l) \sum_{i=1}^n p(i|l) \log_2 p(i|l) \quad (5.5)$$

The IG of an LCF is the difference between the information entropy of the landslide class and the conditional entropy of the LCF, as expressed in Equation (5.6), representing how much the uncertainty of determining a landslide as EAL has been reduced after knowing the LCF. The greater the IG, the stronger the relationship between the LCF and EAL and the more important the LCF is to the EAL occurrence. Following Equations (5.4) to (5.6), the IG of each LCF can be calculated and ranked to find and analyse the main influencing factors of EALs.

$$IG(LCF) = H(EAL) - H(EAL|LCF) \quad (5.6)$$

5.4 Results

In this section, I will first closely investigate the spatial distribution of the detected EALs, and then statistically analyse the spatial correlation between the landslide post-earthquake acceleration and the 15 LCFs collected (Table 5.1) to quantify their impact on the acceleration, by using the IG function. Finally, the temporal characteristics of EAL movements before and after the earthquake sequence will be analysed according to the InSAR time series results.

5.4.1 Spatial distribution of EALs

The InSAR derived EAL inventory reveals a wide-spreading distribution of EALs (Figure 5.5a) around the source of the four earthquakes. A total of 819 EALs was detected in the study area, among which 684 (83.5%, red polygons in Figure 5.5a) were already documented by IFFI and the remaining 135 (16.5%, purple polygons in Figure 5.5a) were newly detected landslides. Not all the landslides in IFFI were detected by InSAR as they were either not moving or not accelerated by the earthquakes according to the criteria in Section 5.3.1. Note that the final boundaries of EALs determined by InSAR may not entirely agree with IFFI due to their different temporal coverages. The newly detected landslides by InSAR are mainly distributed on the southwest side (Lazio Region) of the seismogenic fault, which could be due to the low density of the documented landslides in this area (IFFI only updated to 2007). The distribution may also be due to the hanging wall effect, but this effect is not a decisive factor considering the presence of a number of new EAL clusters in the footwall as well. According to IFFI, 40.3% of the total 819 InSAR-detected EALs are rotational/translational landslides and 17.7% are slow earth flow landslides (Figure 5.5b). These two types of landslides are also dominant in the whole IFFI inventory within the study area. There are 17.0% of EALs whose types are unclear, including four previously undefined landslides in IFFI and 135 newly detected landslides by InSAR. Note that we cannot rule out the possibility that the detected moving slopes are not authentic landslides, but as the vast majority of EALs (83.5%) are IFFI-verified landslides, the portion of false detection is low and will not alter the conclusion.

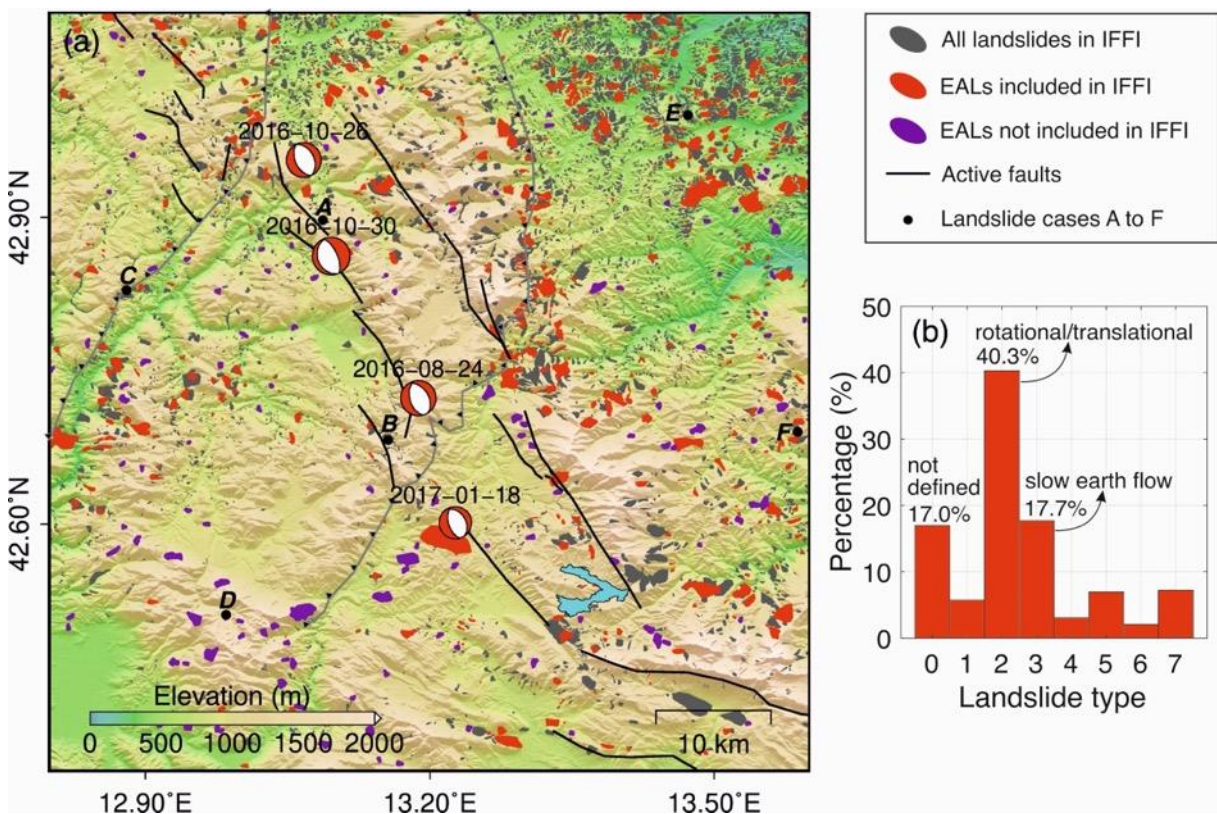


Figure 5.5 InSAR-detected EALs and IFFI documented landslides. (a) Spatial distribution of landslides. Grey polygons are landslides documented by IFFI. Red and purple polygons are respectively EALs already in IFFI and EALs not in IFFI. Black dots indicate the spatial locations of six landslide cases analysed in Section 5.4.3. (b) Proportion of different types of EALs. The codes of landslide types are, 0: not defined, 1: fall/topple, 2: rotational/translational, 3: slow earth flow, 4: rapid debris flow, 5: complex, 6: Deep Seated Gravitational Slope Deformations (DSGSD), 7: shallow landslides.

5.4.2 Conditioning factors of EAL occurrence

The IG values of 15 LCFs were estimated according to Section 5.3.2 and sorted in Figure 5.6a from the largest to smallest. I classified the IG values of these LCFs into three categories: prominent, moderate and negligible IG. Those LCFs with negligible IG contribute little to the determination of EAL occurrence after the earthquake sequence.

Among the LCFs with non-negligible IG, the landslide area (representing the size of the landslide body) exerted the strongest effect (Figure 5.6a), which implies that the uncertainty in determining whether a landslide had been accelerated by the earthquakes will be reduced by 13% (IG=0.13) by knowing the size of the landslide. Comparing the size of EALs and non-EALs (Figure 5.6b), I found that larger landslides were more likely to accelerate after the earthquakes than smaller ones (70.2% non-EALs are smaller than 0.3 km^2 compared to 30.8% for EALs). Note that very small EALs and non-EALs ($< 9 \cdot 10^{-4} \text{ km}^2$) are not detectable in this case and some adjacent small landslides without clear boundaries could be joined together. This is due to the spatial clustering effect of the InSAR-based (30 m spatial resolution) automated landslide detection method and the principle that an EAL or non-EAL need to contain at least three InSAR pixels to ensure measurement reliability. The remarkable effect of landslide size revealed here is consistent with other studies of failed coseismic and post-seismic landslides (Fan et al., 2018a; Chen et al., 2021) which found that the larger coseismic landslides tended to remain active for longer after earthquakes, comparatively more susceptible to remobilisation than the smaller ones. Although EALs and the post-seismic remobilisations in coseismic deposits are two different types of ETLs, they are both attributed to post-seismic effects on landsliding, and the landslide size could be a generic conditioning factor of landslide susceptibility after earthquakes. Moreover, in terms of the landslide nature, larger landslides are typically composed of higher proportions of weak materials which lead to a decrease in frictional strength (Handwerger et al., 2021). Indeed, such a landslide nature may be potentially decisive for landslide activity, as has been observed in other studies. For example, Handwerger et al. (2021) reported the decreasing relationship between landslide size and strength by analysing slow-moving landslides in the northern California Coast Ranges. Bunn et al. (2020)

also found an inverse correlation between landslide size and friction angle, i.e., the shear strength of landslides decreases with the increase of the landslide size. The reduced frictional strength is essential to the acceleration of landslides as the seismic induced stress changes may be already weak at the distances where EALs occur, compared to the strong ground shaking close to the epicentre.

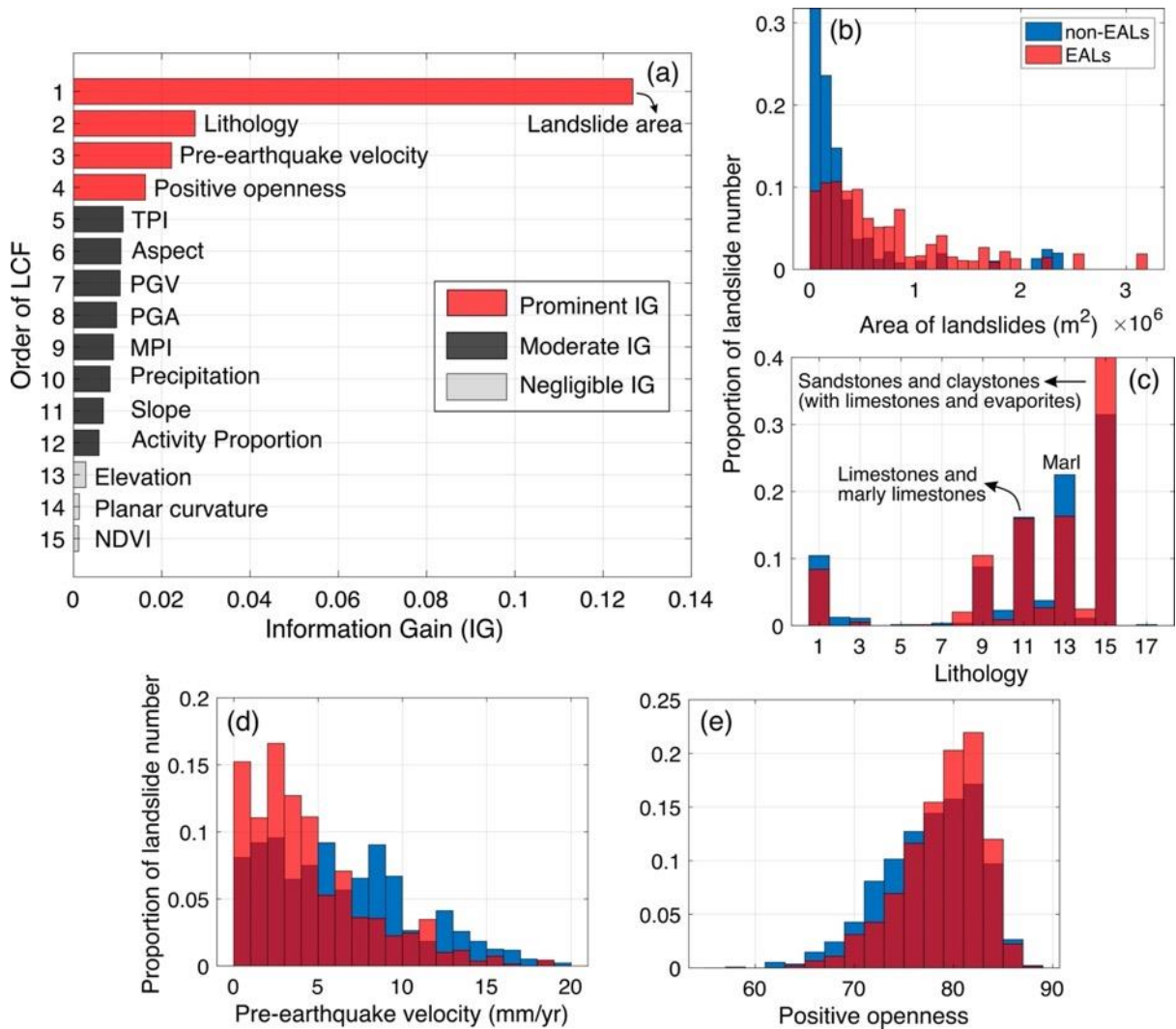


Figure 5.6 IG ranking of 15 collected LCFs and histograms of four prominent LCFs. (a) Ranking and classification (three types: prominent, moderate and negligible) of the 15 LCFs according to their IG values. (b) to (e) are histograms of the four LCFs with prominent IG, i.e., landslide area, lithology, pre-earthquake velocity and positive openness.

The second place in the IG ranking is lithology. As shown in Figure 5.6c, the top three landslide lithologies in the study area are sandstones/claystones (with limestones and evaporites), marl, and limestones/marly limestones. There is a larger proportion of sandstones/claystones type landslides among EALs than non-EALs (40% compared to 32%), suggesting this type of landslide has a weak resistance to the post-earthquake acceleration effect. In contrast, the marl type landslide has a stronger resistance, with its proportion among EALs being smaller than the

proportion among non-EALs by 6%. The third place in the IG ranking is the landslide activity indicator, i.e., the pre-earthquake velocity. Surprisingly, its proportion distribution in Figure 5.6d does not lean towards the high-velocity side which means most EALs are inactive or extremely slow-moving landslides before the earthquakes. Active landslides with velocities greater than 12 mm/yr before the earthquakes seem to be less affected by the earthquakes. One possible explanation is that such landslides are largely dominated by their original driving factors (e.g., gravity), rather than the force induced by earthquakes. Among the topographic factors, the positive openness representing the surface convexity gains the most importance in determining EAL occurrence and Figure 5.6e shows that most EALs are composed of high convexity.

The IG values of PGV and PGA are relatively moderate (~ 0.01) and rank in the middle (7-8) of all LCFs, meaning that the magnitude of ground shaking has made a moderate contribution in determining the occurrence of EALs. To further investigate their relationship, the PGA contours, the earthquake epicentres, and the landslide acceleration ratio ($v_{post}^{Slope} / v_{pre}^{Slope}$, see step 4 in Section 5.3.1) were displayed in Figure 5.7a. Unlike the coseismic landslides (collapsed shortly after the mainshock, black dots in Figure 5.7a, a total of 759 recorded by Martino et al., 2019) which were distributed mostly near the epicentres, EALs had a wide distribution and were not concentrating inside the high PGA area (e.g., inside the purple PGA contour).

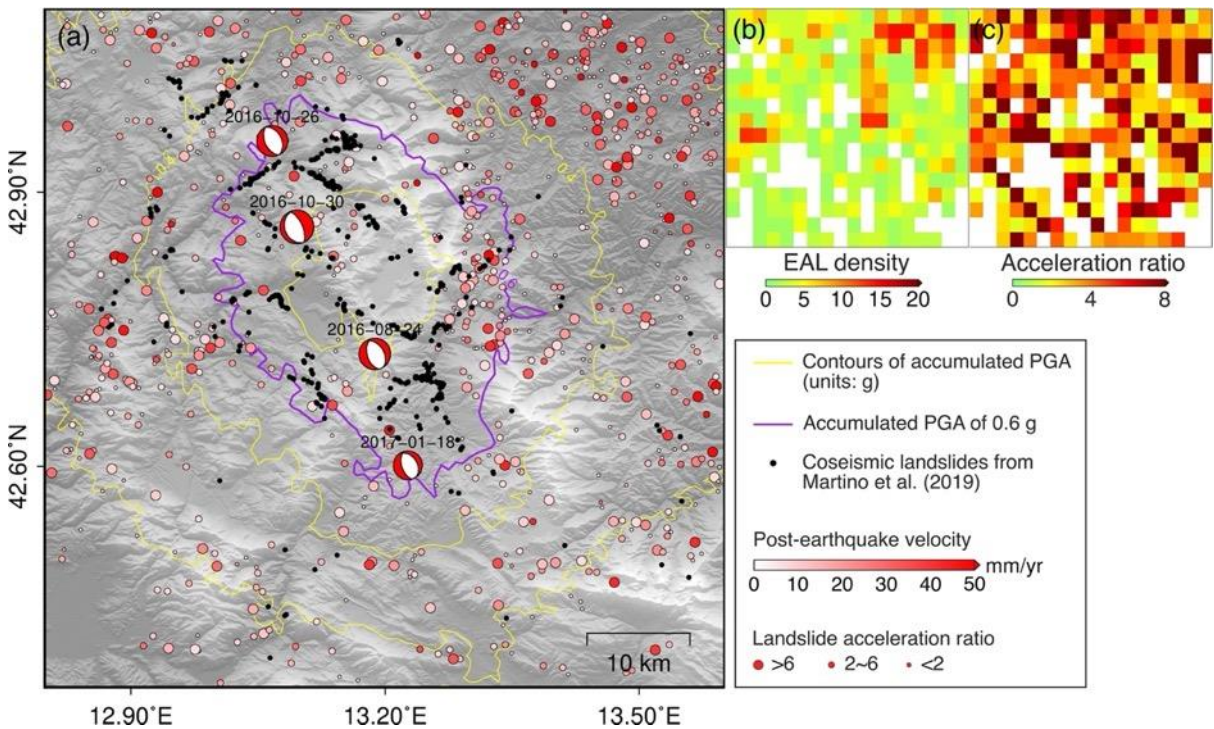


Figure 5.7 Distribution of EAL velocity, EAL density, EAL acceleration and coseismic landslides. (a) Post-earthquake deformation velocity of EALs and the ratio to pre-earthquake velocity. Solid lines

indicate the cumulative PGA contours of the four earthquakes, where the purple contour shows 0.6 g PGA. Black dots are coseismic landslides collected from Martino et al. (2019). (b) Number of EALs on a resampled grid with a cell size of 5×5 km. (c) Average acceleration ratio of EALs on the grid.

A uniform grid map within the study area was further constructed with a cell size of 5×5 km, and for each grid cell, I counted the number of EALs, calculated the average acceleration ratio of EALs and plotted them in Figures 5.7b and 5.7c. More EALs were distributed in the northeast which is consistent with the distribution of landslides in IFFI (Figure 5.5a) but the distribution of the EAL acceleration ratio was almost uniform in space. It is asserted that weak ground shaking far away from the epicentre was enough to cause notable accelerations to the landslide movement and greater ground shaking did not necessarily mean larger potential to accelerate landslides or larger accelerations. On the one hand, most unstable landslides near the epicentre had collapsed during the mainshock, leaving most EALs being identified in the far field. On the other hand, the landslide rigidity could be altered by relatively weak ground shaking and its kinematic behaviour may not be directly related to the magnitude of ground shaking. For example, Bontemps et al. (2020) observed diverse responses of a slow-moving landslide in Peru to a series of small-to-medium earthquakes ($M_l < 4.5$). Lacroix et al. (2014) found the post-seismic motion of a landslide triggered by an M_w 6.0 earthquake 20 km away was even 3 times larger than the coseismic displacement.

The slope and aspect angles are commonly used topographic variables in assessing landslide hazards and have a moderate influence on EAL occurrence according to the IG ranking. From the histogram of slope angles (Figure 5.8a), it can be found that the slope angles of EALs are concentrated between 10 and 20 degrees (strong slope). Note that the plot here describes the probability of slope bins conditional on landslide membership, not the probability of EALs conditional on slope angles (i.e., we can say that more EALs have strong slopes, but not that landslides with strong slope angles are likely to be EALs). The rose diagram of aspect angles (Figure 5.8b) shows that the orientations of EALs are concentrated in the South direction, specifically from SE to SSW directions. In addition, EALs also exhibit an increased proportion in the NNW and NNE directions compared to non-EALs. Most of these directions are roughly parallel to the strike direction of the seismogenic faults (SSE-NNW, solid black line in Figure 5.8b) and perpendicular to the direction of the normal fault slips, suggesting the existence of a directional effect. However, the cause of this effect is inconclusive. Although some previous studies (e.g., Xu et al., 2013; Xu et al., 2014; Fan et al., 2018b) have revealed landslides with a slope aspect parallel to the fault slip direction could be more susceptible to failure during the

earthquake, there are other studies (e.g., Chigira et al., 2010; von Specht et al., 2019) estimating the prevalent landslide orientation to be normal to the fault ruptures. In addition, almost all these studies focus on the coseismic landslides that collapsed during the earthquake. Therefore, at present, we are unable to determine a unified mechanism responsible for the slope aspect effect of EALs.

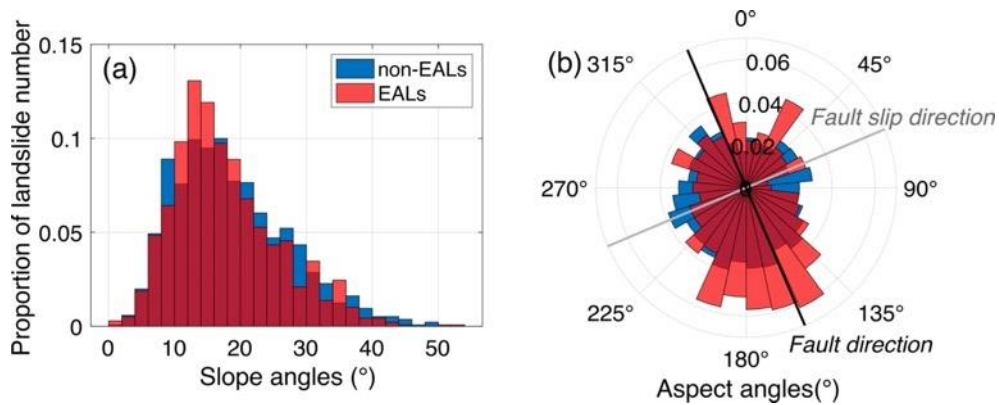


Figure 5.8 Distribution of slope angles, aspect angles of EALs and non-EALs. (a) Distribution of slope angles. The bin width is set as 2 degrees to include enough landslide samples for each bin. (b) Rose diagram of aspect angles.

5.4.3 Post-earthquake dynamics of EALs

InSAR mean deformation velocity fields have enabled the detection and spatial analysis of distributed EALs, in this section, I will investigate further their temporal characteristics, individually or as a whole, using high temporal resolution (6 to 12 days) InSAR deformation time series results. I will also incorporate precipitation and seismic activity datasets to analyse the responding mechanisms of the landslide motion to these triggering factors, particularly the different behaviours before and after the earthquakes.

Figure 5.9 shows the sliding velocities of six example EALs together with the monthly precipitation aggregated from daily GPM records. The six EALs were distributed on both sides of the seismogenic faults (locations shown in Figure 5.5) and away from their respective nearest epicentres by < 10 km (A and B), 10 to 30 km (C and D) and > 30 km (E and F), respectively. The epoch-by-epoch velocity of each EAL was computed by linearly fitting the LOS InSAR displacement time series within a fixed 3-month time window and projected onto the slope direction using Equation (5.3), with their means before and after the earthquakes plotted as dashed lines. Although being the closest to the epicentres, EALs A and B only showed moderate mean post-earthquake velocities and acceleration ratios compared to the other examples. EAL C, 18 km away from the epicentre, exhibited the largest mean post-earthquake velocity (41.6 mm/yr) whilst EAL D (23 km from the epicentre) had the largest acceleration ratio (23.3).

Although far away from the epicentre, EALs E and F were also accelerated substantially after the earthquakes, with an acceleration ratio greater than 3. This behaviour of near- and far-field EALs is consistent with the result analysed from Figure 5.7c.

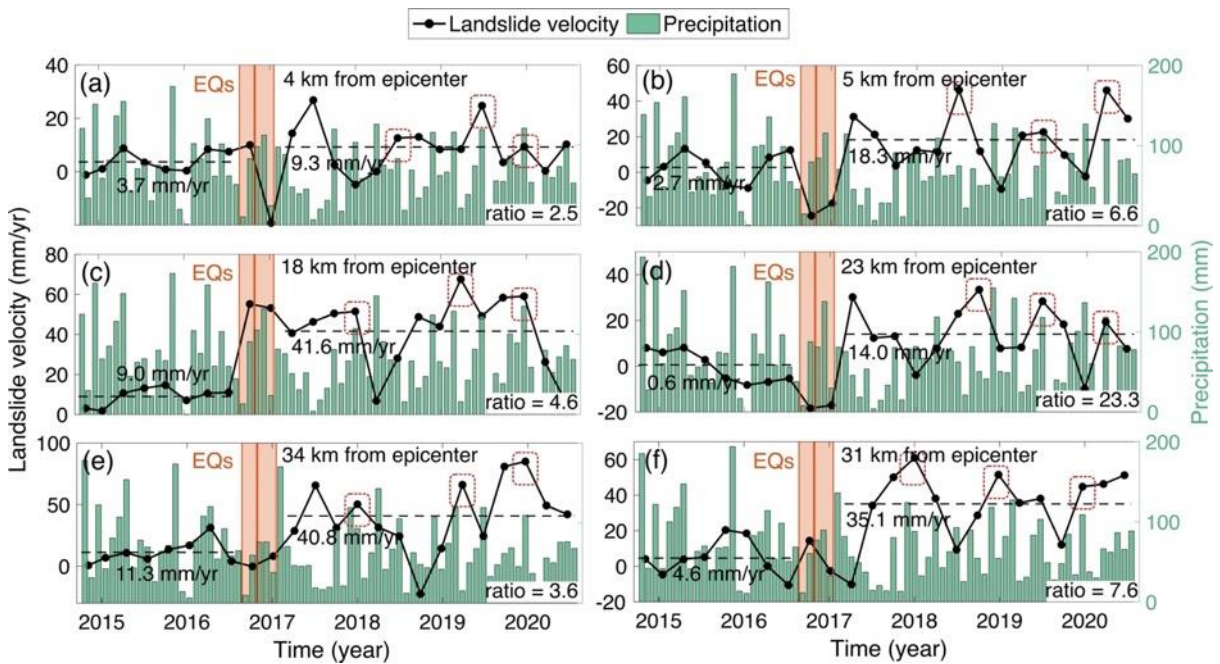


Figure 5.9 Sliding velocity estimated every three months and the monthly precipitation of the six landslide cases. (a) to (f) represent landslides A to F, respectively. Black dashed lines indicate the mean pre- or post-earthquake velocity, and the acceleration ratio is marked at the bottom right of each sub-figure. Red dotted rectangles indicate the velocity peaks after 2018.

Another notable feature shown in Figure 5.9 is that all the six EALs were dominated by stronger seasonal signals after the earthquakes as compared to relatively flat variations before the earthquakes. The variation of the post-earthquake velocity correlated with the precipitation time series and most velocity peaks (red dotted rectangles) were accompanied by local precipitation peaks. We should note that the correspondence is not in a perfect way since the precipitation may not be the only force dominating the activity of these EALs after the earthquakes and other factors (e.g., landslide depth, geomorphological setting and soil properties) could collectively affect the sensitivity of landslides to rainfall/precipitation (Dahal et al., 2008; Bordoni et al., 2015; Zhang et al., 2019a). These complex factors may lead to a delay or heterogeneous response of landslides to the rainfall inputs and therefore the nature of the relation between landslide activity and precipitation is possibly prone to local effects (Marc et al., 2015a). Nevertheless, compared to the pre-earthquake level, the response of velocity to precipitation after the earthquakes is clearly much stronger, implying that the accelerated landslides became more susceptible to precipitation than before. Such changes may be caused by the generation of preferential paths for water infiltration in landslide bodies due to soil damage after the

earthquake (Scheingross et al., 2013; Marc et al., 2015b; Bontemps et al., 2020). The soil damage could be manifested as microfractures (Rojstaczer and Wolf, 1992), which makes it easier for water to penetrate the landslide body and increases the sensitivity of the landslide to precipitation. Thus, the increase in sensitivity enlarges the velocity fluctuation in response to precipitation, which, together with the post-earthquake sliding acceleration, have collectively weakened the stability of EALs.

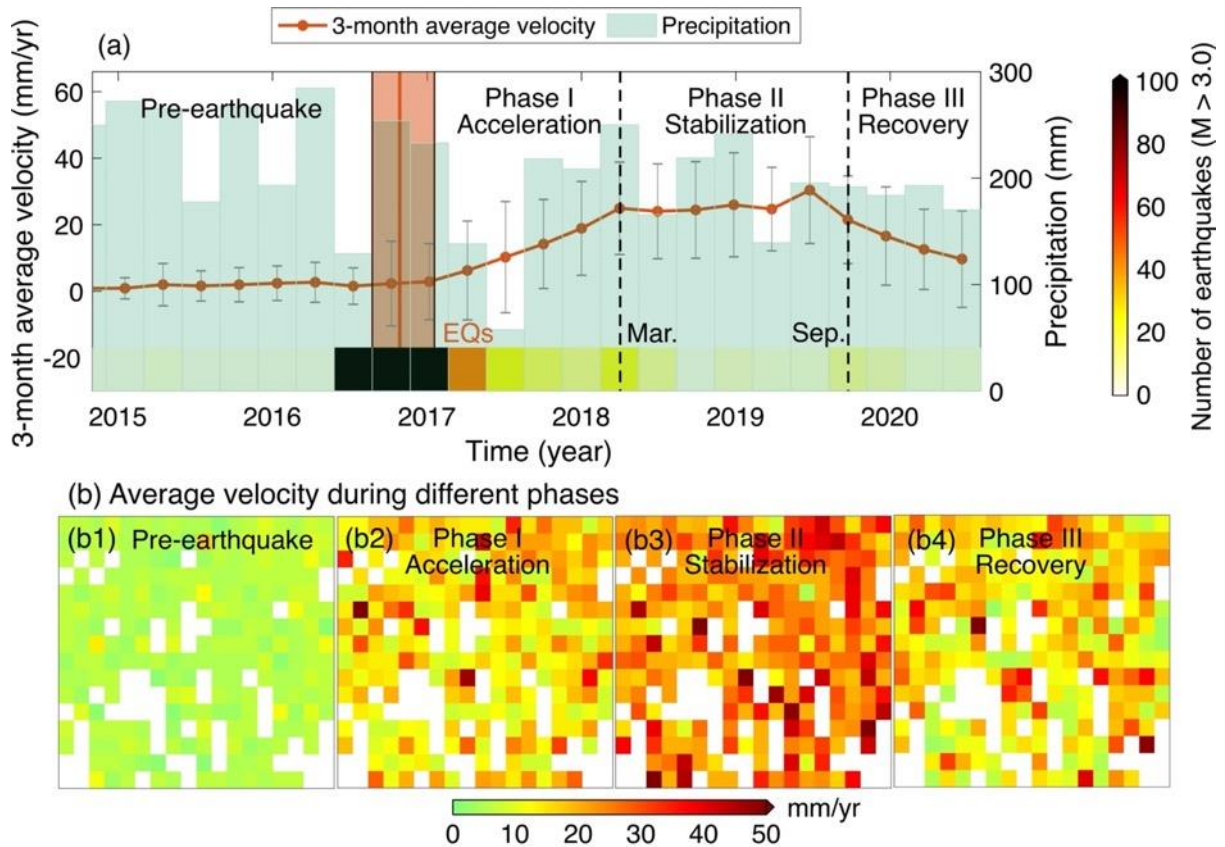


Figure 5.10 Temporal evolution of EALs. (a) Average velocity of EALs and precipitation in the study area estimated every three months. Red shading indicates the coverage period of the 2016-2017 earthquake sequence, and the vertical lines in the shading indicate the specific time of the four earthquakes. The coloured rectangles at the bottom of (a) represent the number of earthquakes ($M > 3.0$) in their time windows. Note that the grey error bars are the standard deviations of all EAL velocities representing the velocity dispersion between EALs rather than a measure of velocity accuracy. (b) Average velocity of EALs on the grid during the phases of (b1) pre-earthquake, (b2) acceleration, (b3) sliding stabilisation and (b4) recovery.

Having the benefit of a complete EAL inventory, it is able to investigate the overall responding mechanism of EALs within the study area, rather than a single EAL as with previous studies. I calculated the 3-month mean velocity of all detected EALs and plotted in Figure 5.10a their averages together with the averaged GPM precipitation in the study area. The 3-month mean

velocity of each EAL was computed in the same way as in Figure 5.9 and then averaged across the whole study area, with the standard deviation calculated (grey error bars in Figure 5.10a). It can be seen that the average velocities before the earthquake sequence were low and their standard deviations were much smaller compared to their post-earthquake counterparts, suggesting a low spatial velocity variability among all EALs. After the earthquakes, the velocity began to increase, with each EAL having its own acceleration ratio, reflected by the large velocity standard deviation among all EALs. According to the change of velocities, I identified three distinct responding phases and plotted in Figures 5.10b2 to 5.10b4 respectively their velocity distributions using the same method as in Figures 5.7b and 5.7c but within the corresponding time periods. The three identified phases were 1) the acceleration phase, from January 2017 to March 2018, during which the average velocity was continuously increasing, implying that most EALs were experiencing substantial accelerations; 2) the stabilisation phase, from March 2018 to September 2019, during which the number of aftershocks was decreasing rapidly and the spatially averaged velocity of EALs became steady, implying a recession of the acceleration effect; 3) the recovery phase, from September 2019, during which the average velocity began to decrease, suggesting the effect of the earthquake was fading away. The fully accelerated velocities were unable to sustain at a high level for long and started to recover (at least partially) ~3 years after the earthquakes.

The phenomenon of landslide recovery was also observed for other earthquakes (e.g., the 1999 Chi-Chi earthquake (Hovius et al., 2011), the 2008 Wenchuan earthquake (Fan et al., 2018a) and the 2015 Gorkha earthquake (Kincey et al., 2021)) although in perspective of landslide rate that represents the potential for new post-seismic landslides or post-seismic reactivations/remobilizations (the other two types of ETLs differing from EALs) to occur, mostly with surface failures. These studies and my work appear to be complementary, and they both shed light, albeit from different perspectives, on the prolonged seismic legacy in landsliding and, more importantly, on the recovery of post-earthquake landslides. This inspires the idea that there may also be similarities in the recovery mechanisms. For the new post-seismic landslide failures or remobilizations, the progressive decay of energy from aftershocks, closure of fractures due to the settlement of shaken rock, re-establishment of plant root networks, and erosive removal of debris and weakened materials will, over time, reduce landslide rates to background levels (Hovius and Meunier, 2012). But for the EALs, due to the slow-moving feature without mass failure or fractures, the plant root networks would not suffer from seismic damage and there would be no significant erosive removal of landslide materials after earthquakes. Therefore, the recession of aftershocks and the closure of earthquake-generated

microfractures could be responsible for the recovery of EALs. Indeed, the number of aftershocks in the phases of stabilization and recovery is significantly reduced as shown in Figure 5.10a. The attribution of the microfracture closure is also justified since the healing process of slow-moving landslides after earthquakes is associated with the re-compaction of the soil as microfractures close and grains re-cement together, which reflects a viscoelastic response of the soil (Bontemps et al., 2020). Such a healing process could be considerably slow. For example, the landslide activity after the 2008 Wenchuan earthquake took 10 years to enter the recovery period and required further 15 years to be completely stable (Chen et al., 2020). For EALs in this Central Italy earthquake sequence, their recovery seems to be faster. Until August 2020 (4 years after the earthquakes), the average velocity has already shown the trend of returning to the pre-earthquake level. However, the spatial variability of the velocity among EALs remains high, suggesting the existence of non-recovering or permanent earthquake-induced effects.

5.5 Discussion

In Section 5.4.2, the different spatial distributions between coseismic landslides and EALs have been observed. In this section, I will evaluate in detail their differences in the perspective of a set of LCFs including seismic, lithological and topographic conditions, which are often regarded as crucial triggering factors.

The first notable difference is their relationship with earthquake-induced ground motions as described by PGA and PGV. Noticing in Section 5.4.2 that EALs and coseismic landslides are distributed in different ground motion areas, I plotted in Figures 5.11a and 5.11b their density scatters against PGA and PGV, in which an opposite correlation is observed between these two types of ETLs. EALs tend to occur in the light-to-moderate ground shaking areas, whilst coseismic landslides tend to appear in areas with strong shaking. One potential explanation is that the ground shaking generated by the mainshocks was large enough to trigger the weak and unstable landslides close to the epicentres so that they had enough energy to collapse in a short period, but the earthquake-induced energy was relatively weak in the far field in which the landslides were only accelerated (relatively moderate) without immediate failures (i.e., becoming EALs). This was also observed by Saroli et al. (2021) who identified a previously unknown paleo-landslide in southern Italy which was triggered by light-to-moderate seismic shaking without a failure but accelerated in motion.

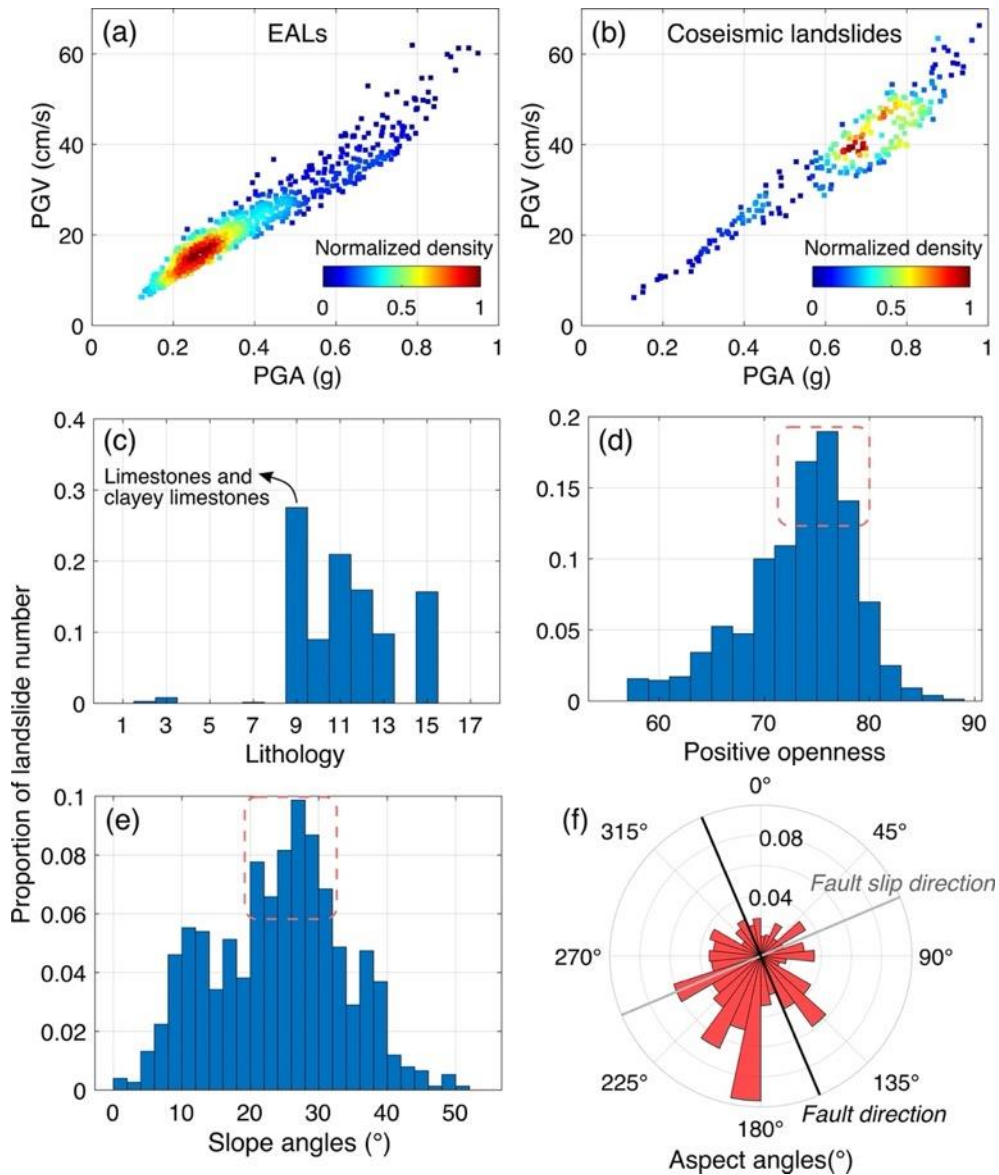


Figure 5.11 Seismic, lithological, and topographic statistics of earthquake-induced landslides. (a) and (b) plot the PGA-PGV density of EALs and coseismic landslides, respectively. (c) to (e) are histograms of lithology, positive openness and slope angles of coseismic landslides. (f) Rose diagram of aspect angles of coseismic landslides.

Another difference between EALs and coseismic landslides is their composition. Figure 5.11c shows that the dominant lithology becomes limestones and clayey limestones (code 9) for coseismic landslides compared to sandstones and claystones (with limestones and evaporites) for EALs (Figure 5.6c). This can be explained by the vulnerability of different lithologies. Since clayey limestones are more fragile than sandstone/claystones in nature (Aksoy et al., 2011; Kim et al., 2012), landslides composed of more clayey limestones are more susceptible to failure during strong seismic ground shaking and develop into coseismic landslides. On the other hand, landslides with finer materials have a longer response time to seismic-induced pore pressure

changes and could be more easily to develop into EALs subject to a delayed but long-lasting post-earthquake effect.

The topographic effect also differs for EALs and coseismic landslides. Comparing Figure 5.6e and Figure 5.11d, it can be seen that the preferential positive openness of coseismic landslides is lower than EALs (75 compared to 80). But their slope angles (Figure 5.11e) tend to be higher than EALs, suggesting that the failure of coseismic landslides relied more on steep slopes rather than EALs. I further visualize the aspect angles of coseismic landslides in Figure 5.11f. Compared to EALs (Figure 5.8b), there are fewer coseismic landslides along the strike direction of the seismogenic faults (i.e., the SSE direction, perpendicular to the direction of the fault slip ruptures). Therefore, in the study area, landslides with an aspect close to the strike of the seismogenic faults are more likely to experience acceleration in motion rather than immediate collapse during the earthquakes.

5.6 Summary

This chapter provides a solution to automatically identify landslide risk areas and statistically characterise landslide motion based on long-term continuous InSAR observations. In this solution, a new InSAR-based landslide detection method was proposed and applied to create the first complete EAL inventory of the 2016-2017 Central Italy earthquake sequence. I first processed six years of Sentinel-1 data in both descending and ascending modes from October 2014 to August 2020 to generate displacement time series. The time series was validated epoch-by-epoch against GPS displacements, showing an RMS difference of about 7 mm. Then pre- and post-earthquake velocity fields were estimated respectively, with a local spatial filter applied to reduce spatially correlated errors and post-seismic effects. Based on the filtered post-earthquake velocity field, I identified moving pixels using the MCD method and then automatically clustered them into landslide bodies using DBSCAN. Finally, among these active landslide candidates, I classified those with sufficient velocity changes before and after the earthquakes (defined as the acceleration ratio) as EALs and those with negligible velocity changes as non-EALs. As InSAR can only detect active landslides, I further identified another set of non-EALs that were inactive both before and after the earthquakes using the IFFI inventory, given that their boundaries would not change significantly during the study period.

Based on the detected EAL and non-EAL inventories, I used the IG method to statistically analyse the spatial correlation between the occurrence of post-earthquake landslide acceleration and 15 commonly used LCFs and thereby investigate the acceleration triggering mechanism.

Results show that the landslide size exerts the most prominent effect in determining the occurrence of EALs, with larger landslides being more likely to accelerate than smaller ones. This conforms to the inverse relationship between landslide size and strength. The other three LCFs with prominent effects are lithology, pre-earthquake velocity and terrain positive openness, with more EALs showing sandstones/claystones lithology, less pre-earthquake activity and higher surface convexity. In addition, PGA/PGV and slope/aspect angles had moderate effects on EALs, where more EALs have a slope of 10 to 20 degrees oriented parallel to the fault and are located in areas with light-to-moderate ground shaking.

Apart from the notable acceleration induced by the earthquakes as discussed above, I also found that after the earthquakes EALs were more responsive to precipitation than before with enlarged seasonal variations coinciding with precipitation. Based on the time series of the 3-month average velocity of EALs, I further identified three post-earthquake velocity evolution phases of EALs, i.e., the acceleration, stabilisation and recovery phases, each with distinctive velocity features. The acceleration phase lasted from January 2017 to March 2018, characterized by a steadily increasing velocity. The stabilisation phase started in March 2018 as the seismic effect faded and the average velocity of EALs was relatively steady. Then the recovery phase started in September 2019 when the overall linear velocity of EALs began to decrease, showing a trend of recovering to the pre-earthquake state.

The differences between EALs and coseismic landslides in respect of seismic-induced ground shaking, lithology and topographic features were also discussed. EALs and coseismic landslides are correlated to seismic ground shaking in an opposite way, where EALs tended to occur in light-to-moderate shaking areas whereas coseismic landslides occurred mostly in strong shaking areas. One explanation is that, as opposed to areas close to the epicentre, the energy resulting from light-to-moderate ground shaking was insufficient to fully make the landslides collapse but instead induced them as EALs. The preferred composition of EALs and coseismic landslides were sandstones/claystones and limestones/clayey limestones, respectively, confirming the fragility of the latter lithology. In terms of topographic features, coseismic landslides had higher slope angles but lower positive openness than EALs. Most EALs had fault-parallel aspect angles whereas coseismic landslides consisted of considerable fault-perpendicular aspect angles, suggesting the different directivity effects of seismic energy propagation on these two types of landslides.

This work opens new perspectives for the study of earthquake-induced landslides. Unlike previous studies focusing on collapsed coseismic landslides, this study revealed the earthquake-induced landslide acceleration over a large spatial scale, by establishing an EAL inventory of large earthquakes for the first time. Such an EAL inventory can help to better analyse the long-term landslide behaviours in response to earthquakes, which complements a more complete picture of earthquake-induced landslide risks (including both coseismic landslide failures and postseismic landslide dynamics). Therefore, this study may have important implications for landslide risk assessment and management in seismically active areas.

Chapter 6. Conclusions

In this thesis, two typical geohazards, earthquakes and landslides, were studied using satellite radar observations. They both occur frequently on a global scale and are interrelated in the sense that landslides can be triggered by earthquakes. To understand their mechanisms and assess their risks, this thesis used advanced SAR/InSAR techniques that can be performed in differential or time series to process satellite radar observations and then study the coseismic slips of earthquakes (transient deformation) and the temporal evolution of slow-moving landslides (long-term deformation). The deformation monitoring and characterisation solutions proposed in this thesis can also be used to investigate other geohazards such as volcano activities, land subsidence and glacial motions.

6.1 Contributions of this thesis

This thesis addressed the following three challenges introduced in Section 1.5 when only using conventional InSAR to characterise the transient or long-term deformation of earthquakes and landslides: (1) the decorrelation problem of InSAR in mapping large transient coseismic deformation, (2) the lack of subsurface information in tracking long-term landslide motion and (3) the dependence on pre-defined velocity thresholds in InSAR-based landslide detection. In addition, one of the gaps in the detection of earthquake-induced landslides, i.e., the detection of earthquake accelerated landslides, was filled in this thesis based on long-term InSAR observations. Therefore, this thesis has the following four contributions.

1. A solution to fully capture large transient coseismic deformation

When using conventional InSAR to map large-gradient coseismic deformation fields, it often suffers from decorrelation due to the intense changes in ground reflection characteristics, which could be worse under heavy vegetation. Such deformation fields are difficult to be fully restored in the near field even using long-wavelength (L-band) SAR images with a small temporal baseline (see Section 3.2.4). Therefore, this thesis introduces multiple remote sensing techniques including InSAR, SAR pixel offset tracking and optical image offset tracking to provide unambiguous surface deformation measurements regardless of the magnitude of displacement gradients.

This thesis presents in Chapter 3 the combination of Sentinel-1, Sentinel-2, ALOS-2 ScanSAR and ALOS-2 SM data to study the coseismic slips of the 2019 Mw 7.5 New Ireland earthquake. The contributions of the study are (1) highlighting the importance of combining multiple

satellite observations to retrieve a complete coseismic deformation field when strong InSAR decorrelation occurs; (2) revealing the effectiveness of combining SAR and optical image offset measurements to determine surface traces of ruptured faults before coseismic modelling; (3) proposing an iterative weighting strategy based on the inversion residual RMS of each dataset to better balance the weights of multiple observations in coseismic modelling; and (4) providing a detailed slip model of this large earthquake and an early seismic risk assessment of its surrounding seismogenic environment.

2. A solution to capture both the long-term surface deformation and subsurface information of landslides.

Spaceborne InSAR is capable of measuring the long-term deformation of the landslide surface at high spatial and temporal resolutions. However, InSAR measurements cannot provide subsurface information such as the depth of sliding interfaces without strong assumptions as introduced in Section 4.1. Geophysical observations such as seismic noise measurements can be used to invert the landslide depth and are easier to carry out with a high spatial density than geotechnical measurements (e.g., borehole survey). Therefore, this thesis combines InSAR and seismic noise measurements to characterise both the long-term surface deformation and subsurface information of landslides.

This thesis presents in Chapter 4 the combination of 5-year InSAR time series and 120 seismic noise measurements to study the landslide motion in Villa de la Independencia, Bolivia, rarely seen in previous studies. The contributions of the study are (1) demonstrating the feasibility of combining a dense network of seismic noise measurements with InSAR to investigate landslides with multi-surface sliding in three dimensions; (2) proposing a new InSAR-based geometric inversion method to determine the sliding geometry of landslides; (3) an accurate estimation of the volume of the Independencia landslide; and (4) a detailed assessment of landslide risk in Independencia by identifying periodic accelerations of landslide movement and their possible triggers.

3. A new InSAR-based automated landslide detection method

After capturing long-term surface deformation by InSAR, how to automatically identify deforming areas with landslide risks over a large spatial scale is another key issue. As introduced in Section 5.1, most InSAR-based landslide detection methods depend on an empirical velocity threshold to define moving pixels, but this may lack generality as the

knowledge of the background deformation level is typically unknown. Also, those threshold-based detection methods ignore the spatial correlation among pixels inside a landslide and are prone to be disturbed by discrete noise pixels. Therefore, this thesis develops an InSAR-based automated landslide detection method with anti-noise capability and without the requirement of an empirical velocity threshold.

This detection method includes two main steps: adaptive identification of moving pixels on InSAR velocity maps using the Minimum Covariance Determinant (MCD) algorithm and automatic spatial clustering of moving pixels into intact landslide bodies using the Density-Based Spatial Clustering of Applications with Noise (DBSCAN) algorithm. These two algorithms have not been jointly used in InSAR and landslide detection fields before. Note that this InSAR-based detection method not only contributes to the landslide study but can also be used to identify other geohazards (e.g., land subsidence), as long as a velocity field is available.

4. First systematic detection and characterisation of earthquake accelerated landslides

Previous studies on earthquake-triggered landslides (ETLs) mainly focused on coseismic landslides that collapse during or within a short period after an earthquake. Earthquake accelerated landslides (EALs) that have not failed but accelerated for a long period since the earthquake are usually ignored due to their insignificant ground changes, but they can generate continuous damage to the ground and may develop into catastrophic failures in the future. Therefore, the detection of EALs is essential for long-term landslide risk assessment.

This thesis presents in Chapter 5 the first systematic detection and characterisation of EALs in Central Italy after the 2016-2017 earthquake sequence using the newly proposed InSAR-based landslide detection and spatiotemporal analysis methods. The contributions of the study are (1) the creation of a complete EAL inventory for the first time; (2) the revelation of prominent conditioning factors of postseismic landslide acceleration; (3) the discovery of three EAL postseismic phases, i.e., the acceleration, stabilisation and recovery phases; (4) the revelation of different seismic response of EALs and coseismic landslides; (5) providing a new perspective for studying a complete picture of earthquake-induced landslide risks.

6.2 Future works

Future works will focus on exploring wider applications of satellite radar observations in the monitoring of geohazards (including earthquakes and landslides) using SAR offset tracking and InSAR time series techniques.

On the basis of SAR offset tracking, this thesis has successfully monitored a fast-moving landslide and two large-magnitude earthquakes as shown in Section 2.3 and Chapter 3. However, these applications are all in a differential sense which means only deformation between two SAR acquisition dates is observed. Future studies will explore the time series technique of SAR offset tracking to perform continuous monitoring on large deformation and then apply it to detect fast-moving landslides on a large spatial scale rather than only investigating a single landslide (e.g, Li et al., 2019).

On the basis of the InSAR time series, this thesis has successfully monitored a complex landslide in Bolivia and detected a large number of landslides induced by the 2016 Central Italy earthquake sequence, as shown in Chapters 4 and 5. Future studies will develop EAL inventories for more strong earthquakes with far-reaching effects, such as the 2008 Mw 7.9 Wenchuan earthquake and the 2015 Mw 7.8 Nepal earthquake. These earthquakes usually have coseismic landslide inventories (e.g., Chigira et al., 2010; Roback et al., 2018) but lack EAL inventories for complete long-term landslide risk assessment. In addition to landslide studies, InSAR time series will also be applied to earthquake studies, such as the investigation of the postseismic deformation of the 2019 New Ireland earthquake. A high-resolution time series analysis of the earthquake cycle will enable a more complete understanding of the earthquake mechanism and a better assessment of the future seismic risk on local faults.

Future works will also include the application of the latest satellite radar observations from future SAR missions such as NISAR. The major SAR data used in this thesis are from Sentinel-1 which is a revolutionary SAR satellite due to its continuous global acquisitions since 2014 and free offer of data. However, Sentinel-1 is limited by its use in vegetated areas or in the case of large deformation as discussed in Chapter 3. L-band SAR is more advantageous in such application scenarios. Therefore, in the next few years, NISAR that will be launched in 2023 and freely provide L-band SAR imagery will open a new perspective for InSAR, and its application in the monitoring of earthquakes and landslides will be promising.

Appendix: List of publications

- Song, C.**, Yu, C., Li, Z., Utili, S., Frattini, P., Crosta, G., Peng, J., 2022. Triggering and recovery of earthquake accelerated landslides in Central Italy revealed by satellite radar observations. *Nature Communications*, 13, 7278. <https://doi.org/10.1038/s41467-022-35035-5>.
- Song, C.**, Yu, C., Li, Z., Pazzi, V., Del Soldato, M., Cruz, A., Utili, S., 2021. Landslide geometry and activity in Villa de la Independencia (Bolivia) revealed by InSAR and seismic noise measurements. *Landslides*, 18, 2721–2737. <https://doi.org/10.1007/s10346-021-01659-9>.
- Song, C.**, Yu, C., Li, Z., Li, Y., Xiao, R., 2019. Coseismic slip distribution of the 2019 Mw 7.5 New Ireland earthquake from the integration of multiple remote sensing techniques. *Remote Sensing*, 11(23), 2767. <https://doi.org/10.3390/rs11232767>.
- Song, C.** and Xu, C., 2018. Loose integration of high-rate GPS and strong motion data considering coloured noise. *Geophysical Journal International*, 215(3), 1530-1539. <https://doi.org/10.1093/gji/ggy357>.
- Wang, S., **Song, C.**, Li, S. S., Li, X., 2022. Resolving co- and early post-seismic slip variations of the 2021 Mw 7.4 Madoi earthquake in east Bayan Har block with a block-wide distributed deformation mode from satellite synthetic aperture radar data. *Earth and Planetary Physics*, 6(1), 108–122. <https://doi.org/10.26464/epp2022007>.
- Yu, C., Li, Z. and **Song, C.**, 2021. Geodetic constraints on recent subduction earthquakes and future seismic hazards in the southwestern coast of Mexico. *Geophysical Research Letters*, 48(13), <https://doi.org/10.1029/2021GL094192>.
- Roger, M., Li, Z., Clarke, P., **Song, C.**, Hu, J.-C., Feng, W., Yi, L., 2020. Joint Inversion of Geodetic Observations and Relative Weighting—The 1999 Mw 7.6 Chi-Chi Earthquake Revisited. *Remote Sensing*, 12, 3125. <https://doi.org/10.3390/rs12193125>.
- Meldebekova, G., Yu, C., Li, Z., **Song, C.**, 2020. Quantifying Ground Subsidence Associated with Aquifer Overexploitation Using Space-Borne Radar Interferometry in Kabul, Afghanistan. *Remote Sensing*. 2020, 12, 2461. <https://doi.org/10.3390/rs12152461>.

References

- Agram, P.S., Simons, M., 2015. A noise model for InSAR time series. *J. Geophys. Res. Solid Earth* 120 (4), 2752-2771. <https://doi.org/10.1002/2014JB011271>.
- Aksoy, C.O., Ozacar, V., Demirel, N., Ozer, S.C., Safak, S., 2011. Determination of instantaneous breaking rate by Geological Strength Index, Block Punch Index and power of impact hammer for various rock mass conditions. *Tunn. Undergr. Space Technol.* 26 (4), 534-540. <https://doi.org/10.1016/j.tust.2011.02.005>.
- Alhaj, T.A., Siraj, M.M., Zainal, A., Elshoush, H.T., Elhaj, F., 2016. Feature selection using information gain for improved structural-based alert correlation. *PLOS ONE* 11 (11), e0166017. <https://doi.org/10.1371/journal.pone.0166017>.
- Aoki, Y., Furuya, M., De Zan, F., Doin, M.-P., Eineder, M., Ohki, M., Wright, T.J., 2021. L-band Synthetic Aperture Radar: Current and future applications to Earth sciences. *Earth, Planets and Space* 73 (1), 56. <https://doi.org/10.1186/s40623-021-01363-x>.
- Askne, J., Nordius, H., 1987. Estimation of tropospheric delay for microwaves from surface weather data. *Radio Sci.* 22 (03), 379-386. <https://doi.org/10.1029/RS022i003p00379>.
- Attema, E.P.W., 1991. The Active Microwave Instrument on-board the ERS-1 satellite. *Proceedings of the IEEE* 79 (6), 791-799. <https://doi.org/10.1109/5.90158>.
- Bacques, G., de Michele, M., Foumelis, M., Raucoules, D., Lemoine, A., Briole, P., 2020. Sentinel optical and SAR data highlights multi-segment faulting during the 2018 Palu-Sulawesi earthquake (Mw 7.5). *Scientific Reports* 10 (1), 9103. <https://doi.org/10.1038/s41598-020-66032-7>.
- Baldwin, S.L., Fitzgerald, P.G., Webb, L.E., 2012. Tectonics of the New Guinea Region. *Annual Review of Earth and Planetary Sciences* 40 (1), 495-520. <https://doi.org/10.1146/annurev-earth-040809-152540>.
- Bamler, R., Eineder, M., 2005. Accuracy of differential shift estimation by correlation and split-bandwidth interferometry for wideband and delta-k SAR systems. *IEEE Geosci. Remote Sens. Lett.* 2 (2), 151-155.
- Bamler, R., Hartl, P., 1998. Synthetic aperture radar interferometry. *Inverse Problems* 14 (4), R1-R54. <https://doi.org/10.1088/0266-5611/14/4/001>.
- Barla, M., Antolini, F., 2016. An integrated methodology for landslides' early warning systems. *Landslides* 13 (2), 215-228. <https://doi.org/10.1007/s10346-015-0563-8>.
- Bekaert, D.P.S., Handwerger, A.L., Agram, P., Kirschbaum, D.B., 2020. InSAR-based detection method for mapping and monitoring slow-moving landslides in remote regions with steep and mountainous terrain: An application to Nepal. *Remote Sens. Environ.* 249, 111983-111983. <https://doi.org/10.1016/j.rse.2020.111983>.
- Bekaert, D.P.S., Hooper, A., Wright, T.J., 2015a. A spatially variable power law tropospheric correction technique for InSAR data. *J. Geophys. Res. Solid Earth* 120 (2), 1345-1356. <https://doi.org/10.1002/2014JB011558>.
- Bekaert, D.P.S., Walters, R.J., Wright, T.J., Hooper, A.J., Parker, D.J., 2015b. Statistical comparison of InSAR tropospheric correction techniques. *Remote Sens. Environ.* 170, 40-47. <https://doi.org/10.1016/j.rse.2015.08.035>.
- Belcher, D.P., 2008. Theoretical limits on SAR imposed by the ionosphere. *IET Radar, Sonar & Navigation* 2 (6), 435-448.
- Berardino, P., Fornaro, G., Lanari, R., Sansosti, E., 2002. A new algorithm for surface deformation monitoring based on small baseline differential SAR interferograms. *IEEE Trans. Geosci. Remote Sens.* 40 (11), 2375-2383. <https://doi.org/10.1109/TGRS.2002.803792>.
- Berg, A., Dammert, P., Eriksson, L.E.B., 2015. X-band interferometric SAR observations of Baltic fast ice. *IEEE Trans. Geosci. Remote Sens.* 53 (3), 1248-1256. <https://doi.org/10.1109/TGRS.2014.2336752>.
- Biggs, J., Wright, T., Lu, Z., Parsons, B., 2007. Multi-interferogram method for measuring interseismic deformation: Denali Fault, Alaska. *Geophys. J. Int.* 170 (3), 1165-1179.
- Biggs, J., Wright, T.J., 2020. How satellite InSAR has grown from opportunistic science to routine monitoring over the last decade. *Nat. Commun.* 11 (1), 3863. <https://doi.org/10.1038/s41467-020-17587-6>.

- Bigi, S., Casero, P., Ciotoli, G., 2011. Seismic interpretation of the Laga basin; constraints on the structural setting and kinematics of the Central Apennines. *J. Geol. Soc.* 168 (1), 179-190. <https://doi.org/10.1144/0016-76492010-084>.
- Bivand, R.S., Pebesma, E., Gómez-Rubio, V., 2013. Hello world: Introducing spatial data. *Applied Spatial Data Analysis with R*, pp. 1-16. New York, NY: Springer New York.
- Blanco-Sánchez, P., Mallorquí, J.J., Duque, S., Monells, D., 2008. The Coherent Pixels Technique (CPT): An advanced DInSAR technique for nonlinear deformation monitoring. *Pure Appl. Geophys.* 165 (6), 1167-1193. <https://doi.org/10.1007/s00024-008-0352-6>.
- Blewitt, G., Hammond, W.C., Kreemer, C., 2018. Harnessing the GPS data explosion for interdisciplinary science. *Eos* 99. <https://doi.org/10.1029/2018EO104623>.
- Bonano, M., Manunta, M., Pepe, A., Paglia, L., Lanari, R., 2013. From previous C-band to new X-band SAR systems: Assessment of the DInSAR mapping improvement for deformation time-series retrieval in urban areas. *IEEE Trans. Geosci. Remote Sens.* 51 (4), 1973-1984. <https://doi.org/10.1109/TGRS.2012.2232933>.
- Bonì, R., Bordoni, M., Colombo, A., Lanteri, L., Meisina, C., 2018. Landslide state of activity maps by combining multi-temporal A-DInSAR (LAMBDA). *Remote Sens. Environ.* 217, 172-190. <https://doi.org/10.1016/j.rse.2018.08.013>.
- Bonì, R., Bordoni, M., Vivaldi, V., Troisi, C., Tararbra, M., Lanteri, L., Zucca, F., Meisina, C., 2020. Assessment of the Sentinel-1 based ground motion data feasibility for large scale landslide monitoring. *Landslides* 17 (10), 2287-2299. <https://doi.org/10.1007/s10346-020-01433-3>.
- Bontemps, N., Lacroix, P., Larose, E., Jara, J., Taïpe, E., 2020. Rain and small earthquakes maintain a slow-moving landslide in a persistent critical state. *Nat. Commun.* 11 (1), 1-10. <https://doi.org/10.1038/s41467-020-14445-3>.
- Boore, D.M., Bommer, J.J., 2005. Processing of strong-motion accelerograms: needs, options and consequences. *Soil Dynam. Earthquake Eng.* 25 (2), 93-115. <https://doi.org/10.1016/j.soildyn.2004.10.007>.
- Booth, A.M., Lamb, M.P., Avouac, J.-P., Delacourt, C., 2013. Landslide velocity, thickness, and rheology from remote sensing: La Clapière landslide, France. *Geophys. Res. Lett.* 40 (16), 4299-4304. <https://doi.org/10.1002/grl.50828>.
- Bordoni, M., Meisina, C., Valentino, R., Lu, N., Bittelli, M., Chersich, S., 2015. Hydrological factors affecting rainfall-induced shallow landslides: From the field monitoring to a simplified slope stability analysis. *Eng. Geol.* 193, 19-37. <https://doi.org/10.1016/j.enggeo.2015.04.006>.
- Buades, A., Coll, B., Morel, J.-M., 2008. Nonlocal image and movie denoising. *International journal of computer vision* 76 (2), 123-139.
- Bunn, M., Leshchinsky, B., Olsen, M.J., 2020. Geologic trends in shear strength properties inferred through three-dimensional back analysis of landslide inventories. *J. Geophys. Res. Earth Surf.* 125 (9), e2019JF005461. <https://doi.org/10.1029/2019JF005461>.
- Burgmann, R., Ayhan, M.E., Fielding, E.J., Wright, T.J., McClusky, S., Aktug, B., Demir, C., Lenk, O., Turkezer, A., 2002. Deformation during the 12 November 1999 Duzce, Turkey, earthquake, from GPS and InSAR data. *Bull. Seismol. Soc. Am.* 92 (1), 161-171.
- Calabro, M., Schmidt, D., Roering, J., 2010. An examination of seasonal deformation at the Portuguese Bend landslide, southern California, using radar interferometry. *J. Geophys. Res. Earth Surf.* 115 (F2), F02020. <https://doi.org/10.1029/2009JF001314>.
- Carlà, T., Tofani, V., Lombardi, L., Raspini, F., Bianchini, S., Bertolo, D., Thuegaz, P., Casagli, N., 2019. Combination of GNSS, satellite InSAR, and GBInSAR remote sensing monitoring to improve the understanding of a large landslide in high alpine environment. *Geomorphology* 335, 62-75. <https://doi.org/10.1016/j.geomorph.2019.03.014>.
- Carnec, C., Massonnet, D., King, C., 1996. Two examples of the use of SAR interferometry on displacement fields of small spatial extent. *Geophys. Res. Lett.* 23 (24), 3579-3582. <https://doi.org/10.1029/96GL03042>.
- Castellaro, S., 2016. The complementarity of H/V and dispersion curves. *Geophysics* 81 (6), T323-T338. <https://doi.org/10.1190/geo2015-0399.1>.
- Castellaro, S., Mulargia, F., 2009. The effect of velocity inversions on H/V. *Pure Appl. Geophys.* 166 (4), 567-592. <https://doi.org/10.1007/s00024-009-0474-5>.
- Chan, Y.K., Koo, V., 2008. An introduction to Synthetic Aperture Radar (SAR). *Progress In Electromagnetics Research B* 2, 27-60. <https://doi.org/10.2528/PIERB07110101>

- Cheloni, D., De Novellis, V., Albano, M., Antonioli, A., Anzidei, M., Atzori, S., Avallone, A., Bignami, C., Bonano, M., Calcaterra, S., Castaldo, R., Casu, F., Cecere, G., De Luca, C., Devoti, R., Di Bucci, D., Esposito, A., Galvani, A., Gambino, P., Giuliani, R., Lanari, R., Manunta, M., Manzo, M., Mattone, M., Montuori, A., Pepe, A., Pepe, S., Pezzo, G., Pietrantonio, G., Polcari, M., Riguzzi, F., Salvi, S., Sepe, V., Serpelloni, E., Solaro, G., Stramondo, S., Tizzani, P., Tolomei, C., Trasatti, E., Valerio, E., Zinno, I., Doglioni, C., 2017. Geodetic model of the 2016 Central Italy earthquake sequence inferred from InSAR and GPS data. *Geophys. Res. Lett.* 44 (13), 6778-6787. <https://doi.org/10.1002/2017GL073580>.
- Cheloni, D., Falcucci, E., Gori, S., 2019. Half-graben rupture geometry of the 30 October 2016 Mw 6.6 Mt. Vettore-Mt. Bove earthquake, Central Italy. *J. Geophys. Res. Solid Earth* 124 (4), 4091-4118. <https://doi.org/10.1029/2018JB015851>.
- Chen, C.W., Zebker, H.A., 2000. Network approaches to two-dimensional phase unwrapping: intractability and two new algorithms. *JOSA A* 17 (3), 401-414. <https://doi.org/10.1364/josaa.17.000401>.
- Chen, C.W., Zebker, H.A., 2001. Two-dimensional phase unwrapping with use of statistical models for cost functions in nonlinear optimization. *J. Opt. Soc. Am. A* 18 (2), 338-351. <https://doi.org/10.1364/JOSAA.18.000338>.
- Chen, J., Dowman, I., Li, S., Li, Z., Madden, M., Mills, J., Paparoditis, N., Rottensteiner, F., Sester, M., Toth, C., Trinder, J., Heipke, C., 2016. Information from imagery: ISPRS scientific vision and research agenda. *Int. J. Photogramm. Remote Sens.* 115, 3-21. <https://doi.org/10.1016/j.isprsjprs.2015.09.008>.
- Chen, M., Tang, C., Wang, X., Xiong, J., Shi, Q., Zhang, X., Li, M., Luo, Y., Tie, Y., Feng, Q., 2021. Temporal and spatial differentiation in the surface recovery of post-seismic landslides in Wenchuan earthquake-affected areas. *Ecological Informatics* 64, 101356. <https://doi.org/10.1016/j.ecoinf.2021.101356>.
- Chen, M., Tang, C., Xiong, J., Shi, Q.Y., Li, N., Gong, L.F., Wang, X.D., Tie, Y., 2020. The long-term evolution of landslide activity near the epicentral area of the 2008 Wenchuan earthquake in China. *Geomorphology* 367, 107317. <https://doi.org/10.1016/j.geomorph.2020.107317>.
- Chen, X., Sun, Q., Hu, J., 2018. Generation of complete SAR geometric distortion maps based on DEM and neighbor gradient algorithm. *Applied Sciences* 8 (11), 2206.
- Chiarabba, C., De Gori, P., Cattaneo, M., Spallarossa, D., Segou, M., 2018. Faults geometry and the role of fluids in the 2016–2017 Central Italy seismic sequence. *Geophys. Res. Lett.* 45 (14), 6963-6971. <https://doi.org/10.1029/2018GL077485>.
- Chiaraluce, L., Di Stefano, R., Tinti, E., Scognamiglio, L., Michele, M., Casarotti, E., Cattaneo, M., De Gori, P., Chiarabba, C., Monachesi, G., Lombardi, A., Valoroso, L., Latorre, D., Marzorati, S., 2017. The 2016 Central Italy seismic sequence: A first look at the mainshocks, aftershocks, and source models. *Seismol. Res. Lett.* 88 (3), 757-771. <https://doi.org/10.1785/0220160221>.
- Chigira, M., Wu, X., Inokuchi, T., Wang, G., 2010. Landslides induced by the 2008 Wenchuan earthquake, Sichuan, China. *Geomorphology* 118 (3), 225-238. <https://doi.org/10.1016/j.geomorph.2010.01.003>.
- Cigna, F., Bianchini, S., Casagli, N., 2013. How to assess landslide activity and intensity with Persistent Scatterer Interferometry (PSI): the PSI-based matrix approach. *Landslides* 10 (3), 267-283. <https://doi.org/10.1007/s10346-012-0335-7>.
- Colesanti, C., Ferretti, A., Novali, F., Prati, C., Rocca, F., 2003. SAR monitoring of progressive and seasonal ground deformation using the permanent scatterers technique. *IEEE Trans. Geosci. Remote Sens.* 41 (7), 1685-1701. <https://doi.org/10.1109/TGRS.2003.813278>.
- Colesanti, C., Wasowski, J., 2006. Investigating landslides with space-borne Synthetic Aperture Radar (SAR) interferometry. *Eng. Geol.* 88 (3), 173-199. <https://doi.org/10.1016/j.enggeo.2006.09.013>.
- Collins, B.D., Znidarcic, D., 2004. Stability analyses of rainfall induced landslides. *J. Geotech. Geoenviron. Eng.* 130 (4), 362-372. [https://doi.org/10.1061/\(ASCE\)1090-0241\(2004\)130:4\(362\)](https://doi.org/10.1061/(ASCE)1090-0241(2004)130:4(362)).
- Costantini, M., 1998. A novel phase unwrapping method based on network programming. *IEEE Trans. Geosci. Remote Sens.* 36 (3), 813-821. <https://doi.org/10.1109/36.673674>.
- Crippa, C., Franzosi, F., Zonca, M., Manconi, A., Crosta, G.B., Dei Cas, L., Agliardi, F., 2020. Unraveling spatial and temporal heterogeneities of very slow rock-slope deformations with targeted DInSAR analyses. *Remote Sens.* 12 (8), 1329. <https://doi.org/10.3390/rs12081329>.
- Crippa, C., Valbuzzi, E., Frattini, P., Crosta, G.B., Spreafico, M.C., Agliardi, F., 2021. Semi-automated regional classification of the style of activity of slow rock-slope deformations using

- PS InSAR and SqueeSAR velocity data. *Landslides* 18, 2445–2463.
<https://doi.org/10.1007/s10346-021-01654-0>.
- Crosetto, M., Monserrat, O., Cuevas-González, M., Devanthery, N., Crippa, B., 2016. Persistent scatterer interferometry: A review. *Int. J. Photogramm. Remote Sens.* 115, 78-89.
- Crosta, G., Di Prisco, C., Frattini, P., Frigerio, G., Castellanza, R., Agliardi, F., 2014a. Chasing a complete understanding of the triggering mechanisms of a large rapidly evolving rockslide. *Landslides* 11 (5), 747-764. <https://doi.org/10.1007/s10346-013-0433-1>.
- Crosta, G.B., Uti, S., De Blasio, F.V., Castellanza, R., 2014b. Reassessing rock mass properties and slope instability triggering conditions in Valles Marineris, Mars. *Earth Planet. Sci. Lett.* 388, 329-342. <https://doi.org/10.1016/j.epsl.2013.11.053>.
- Culshaw, M., 2018. Geohazards. In P.T. Bobrowsky, & B. Marker (Eds.), *Encyclopedia of Engineering Geology*, pp. 381-389. Cham: Springer International Publishing.
- D'Agostino, N., 2014. Complete seismic release of tectonic strain and earthquake recurrence in the Apennines (Italy). *Geophys. Res. Lett.* 41 (4), 1155-1162.
<https://doi.org/10.1002/2014GL059230>.
- Dahal, R.K., Hasegawa, S., Nonomura, A., Yamanaka, M., Dhakal, S., Paudyal, P., 2008. Predictive modelling of rainfall-induced landslide hazard in the Lesser Himalaya of Nepal based on weights-of-evidence. *Geomorphology* 102 (3), 496-510.
<https://doi.org/10.1016/j.geomorph.2008.05.041>.
- Dai, K., Li, Z., Tomás, R., Liu, G., Yu, B., Wang, X., Cheng, H., Chen, J., Stockamp, J., 2016. Monitoring activity at the Daguangbao mega-landslide (China) using Sentinel-1 TOPS time series interferometry. *Remote Sens. Environ.* 186, 501-513.
<https://doi.org/10.1016/j.rse.2016.09.009>.
- Dai, K., Li, Z., Xu, Q., Bürgmann, R., Milledge, D.G., Tomás, R., Fan, X., Zhao, C., Liu, X., Peng, J., Zhang, Q., Wang, Z., Qu, T., He, C., Li, D., Liu, J., 2020. Entering the era of earth observation-based landslide warning systems: a novel and exciting framework. *IEEE Geosc Rem Sen M* 8 (1), 136-153. <https://doi.org/10.1109/MGRS.2019.2954395>.
- Dall, J., 2007. InSAR elevation bias caused by penetration into uniform volumes. *IEEE Trans. Geosci. Remote Sens.* 45 (7), 2319-2324. <https://doi.org/10.1109/TGRS.2007.896613>.
- Daniell, J.E., Schaefer, A.M., Wenzel, F., Tsang, H.H., 2017. The global role of earthquake fatalities in decision-making: earthquakes versus other causes of fatalities. In: *Proceedings of the 16th World Conference on Earthquake Engineering*, Santiago, Chile, pp. 1-12.
- Daout, S., Doin, M.-P., Peltzer, G., Lasserre, C., Socquet, A., Volat, M., Sudhaus, H., 2018. Strain partitioning and present-day fault kinematics in NW Tibet from Envisat SAR interferometry. *J. Geophys. Res. Solid Earth* 123 (3), 2462-2483. <https://doi.org/10.1002/2017JB015020>.
- de Vita, S., Sansivero, F., Orsi, G., Marotta, E., 2006. Cyclical slope instability and volcanism related to volcano-tectonism in resurgent calderas: The Ischia island (Italy) case study. *Eng. Geol.* 86 (2), 148-165. <https://doi.org/10.1016/j.enggeo.2006.02.013>.
- De Zan, F., 2014. Accuracy of incoherent speckle tracking for circular Gaussian signals. *IEEE Geosci. Remote Sens. Lett.* 11 (1), 264-267.
- Dehls, J.F., Larsen, Y., Marinkovic, P., Lauknes, T.R., Stødle, D., Moldestad, D.A., 2019. InSAR.No: A national InSAR deformation mapping/monitoring service in Norway -- from concept to operations. In: *IGARSS 2019 - 2019 IEEE International Geoscience and Remote Sensing Symposium*, pp. 5461-5464.
- Del Soldato, M., Pazzi, V., Segoni, S., De Vita, P., Tofani, V., Moretti, S., 2018a. Spatial modeling of pyroclastic cover deposit thickness (depth to bedrock) in peri-volcanic areas of Campania (southern Italy). *Earth Surface Processes and Landforms* 43 (9), 1757-1767.
<https://doi.org/10.1002/esp.4350>.
- Del Soldato, M., Riquelme, A., Bianchini, S., Tomàs, R., Di Martire, D., De Vita, P., Moretti, S., Calcaterra, D., 2018b. Multisource data integration to investigate one century of evolution for the Agnone landslide (Molise, southern Italy). *Landslides* 15 (11), 2113-2128.
<https://doi.org/10.1007/s10346-018-1015-z>.
- Delbridge, B.G., Bürgmann, R., Fielding, E., Hensley, S., Schulz, W.H., 2016. Three-dimensional surface deformation derived from airborne interferometric UAVSAR: Application to the Slumgullion Landslide. *J. Geophys. Res. Solid Earth* 121 (5), 3951-3977.
<https://doi.org/10.1002/2015jb012559>.

- Deledalle, C., Denis, L., Tupin, F., 2011. NL-InSAR: Nonlocal interferogram estimation. *IEEE Trans. Geosci. Remote Sens.* 49 (4), 1441-1452. <https://doi.org/10.1109/TGRS.2010.2076376>.
- Domingues, A., Custódio, S., Cesca, S., 2012. Waveform inversion of small-to-moderate earthquakes located offshore southwest Iberia. *Geophys. J. Int.* 192 (1), 248-259. <https://doi.org/10.1093/gji/ggs010>.
- Dong, J., Zhang, L., Liao, M., Gong, J., 2019. Improved correction of seasonal tropospheric delay in InSAR observations for landslide deformation monitoring. *Remote Sens. Environ.* 233, 111370. <https://doi.org/10.1016/j.rse.2019.111370>.
- Dong, J., Zhang, L., Tang, M., Liao, M., Xu, Q., Gong, J., Ao, M., 2018. Mapping landslide surface displacements with time series SAR interferometry by combining persistent and distributed scatterers: A case study of Jiayu landslide in Danba, China. *Remote Sens. Environ.* 205, 180-198.
- Drusch, M., Del Bello, U., Carlier, S., Colin, O., Fernandez, V., Gascon, F., Hoersch, B., Isola, C., Laberinti, P., Martimort, P., 2012. Sentinel-2: ESA's optical high-resolution mission for GMES operational services. *Remote Sens. Environ.* 120, 25-36.
- Elliott, J.L., Freymueller, J.T., Rabus, B., 2007. Coseismic deformation of the 2002 Denali fault earthquake: Contributions from synthetic aperture radar range offsets. *J. Geophys. Res. Solid Earth* 112 (B6).
- Elliott, J.R., Walters, R.J., Wright, T.J., 2016. The role of space-based observation in understanding and responding to active tectonics and earthquakes. *Nat. Commun.* 7 (1), 13844. <https://doi.org/10.1038/ncomms13844>.
- ESA, 2019. Sentinel Online: Sentinel-2 overview, <https://sentinel.esa.int/web/sentinel/missions/sentinel-2/overview>. Accessed on 30 June 2019.
- Ester, M., Kriegel, H.-P., Sander, J., Xu, X., 1996. A density-based algorithm for discovering clusters in large spatial databases with noise. In: *Proc. 2nd Int. Conf. Knowledge Discovery and Data Mining (KDD '96)*, Portland, Oregon, pp. 226–231.
- Falcini, F., Marini, M., Milli, S., Moscatelli, M., 2009. An inverse problem to infer paleoflow conditions from turbidites. *J. Geophys. Res. Oceans* 114 (C10). <https://doi.org/10.1029/2009JC005294>.
- Fan, X., Domènech, G., Scaringi, G., Huang, R., Xu, Q., Hales, T.C., Dai, L., Yang, Q., Francis, O., 2018a. Spatio-temporal evolution of mass wasting after the 2008 Mw 7.9 Wenchuan earthquake revealed by a detailed multi-temporal inventory. *Landslides* 15 (12), 2325-2341. <https://doi.org/10.1007/s10346-018-1054-5>.
- Fan, X., Scaringi, G., Xu, Q., Zhan, W., Dai, L., Li, Y., Pei, X., Yang, Q., Huang, R., 2018b. Coseismic landslides triggered by the 8th August 2017 Ms 7.0 Jiuzhaigou earthquake (Sichuan, China): factors controlling their spatial distribution and implications for the seismogenic blind fault identification. *Landslides* 15 (5), 967-983. <https://doi.org/10.1007/s10346-018-0960-x>.
- Fan, X., Yunus, A.P., Scaringi, G., Catani, F., Siva Subramanian, S., Xu, Q., Huang, R., 2021. Rapidly evolving controls of landslides after a strong earthquake and implications for hazard assessments. *Geophys. Res. Lett.* 48 (1). <https://doi.org/10.1029/2020GL090509>.
- Farina, P., Colombo, D., Fumagalli, A., Marks, F., Moretti, S., 2006. Permanent Scatterers for landslide investigations: outcomes from the ESA-SLAM project. *Eng. Geol.* 88 (3), 200-217. <https://doi.org/10.1016/j.enggeo.2006.09.007>.
- Farr, T.G., Rosen, P.A., Caro, E., Crippen, R., Duren, R., Hensley, S., Kobrick, M., Paller, M., Rodriguez, E., Roth, L., 2007. The shuttle radar topography mission. *Rev. Geophys.* 45 (2), RG2004. <https://doi.org/10.1029/2005RG000183>.
- Fattahi, H., Amelung, F., 2013. DEM error correction in InSAR time series. *IEEE Trans. Geosci. Remote Sens.* 51 (7), 4249-4259. <https://doi.org/10.1109/TGRS.2012.2227761>.
- Fattahi, H., Amelung, F., 2014. InSAR uncertainty due to orbital errors. *Geophys. J. Int.* 199 (1), 549-560. <https://doi.org/10.1093/gji/ggu276>.
- Feng, G., Hetland, E.A., Ding, X., Li, Z., Zhang, L., 2010. Coseismic fault slip of the 2008 Mw 7.9 Wenchuan earthquake estimated from InSAR and GPS measurements. *Geophys. Res. Lett.* 37 (1). <https://doi.org/10.1029/2009GL041213>.
- Feng, W., Li, Z., 2010. A novel hybrid PSO/simplex algorithm for determining earthquake source parameters using InSAR observations. *Prog. Geophys.* 25 (4), 1189-1196. <https://doi.org/10.3969/j.issn.1004-2903.2010.04.007>.

- Feng, W., Li, Z., Elliott, J.R., Fukushima, Y., Hoey, T., Singleton, A., Cook, R., Xu, Z., 2013. The 2011 MW 6.8 Burma earthquake: fault constraints provided by multiple SAR techniques. *Geophys. J. Int.* 195 (1), 650-660. <https://doi.org/10.1093/gji/ggt254>.
- Ferretti, A., Fumagalli, A., Novali, F., Prati, C., Rocca, F., Rucci, A., 2011. A new algorithm for processing interferometric data-stacks: SqueeSAR. *IEEE Trans. Geosci. Remote Sens.* 49 (9), 3460-3470. <https://doi.org/10.1109/Tgrs.2011.2124465>.
- Ferretti, A., Monti-Guarnieri, A., Prati, C., Rocca, F., Massonet, D., 2007. InSAR principles: guidelines for SAR interferometry processing and interpretation, Part A. *ESA Publications*, ESTEC, Noordwijk, Netherlands.
- Ferretti, A., Prati, C., Rocca, F., 2000. Nonlinear subsidence rate estimation using permanent scatterers in differential SAR interferometry. *IEEE Trans. Geosci. Remote Sens.* 38 (5), 2202-2212. <https://doi.org/10.1109/36.868878>.
- Ferretti, A., Prati, C., Rocca, F., 2001. Permanent scatterers in SAR interferometry. *IEEE Trans. Geosci. Remote Sens.* 39 (1), 8-20. <https://doi.org/10.1109/36.898661>.
- Fialko, Y., Simons, M., Agnew, D., 2001. The complete (3-D) surface displacement field in the epicentral area of the 1999 MW7.1 Hector Mine Earthquake, California, from space geodetic observations. *Geophys. Res. Lett.* 28 (16), 3063-3066. <https://doi.org/10.1029/2001GL013174>.
- Frattini, P., Crosta, G.B., Rossini, M., Allievi, J., 2018. Activity and kinematic behaviour of deep-seated landslides from PS-InSAR displacement rate measurements. *Landslides* 15 (6), 1053-1070. <https://doi.org/10.1007/s10346-017-0940-6>.
- Froude, M.J., Petley, D.N., 2018. Global fatal landslide occurrence from 2004 to 2016. *Nat. Hazards Earth Syst. Sci.* 18 (8), 2161-2181. <https://doi.org/10.5194/nhess-18-2161-2018>.
- Fruneau, B., Achache, J., Delacourt, C., 1996. Observation and modelling of the Saint-Étienne-de-Tinée landslide using SAR interferometry. *Tectonophysics* 265 (3), 181-190. [https://doi.org/10.1016/S0040-1951\(96\)00047-9](https://doi.org/10.1016/S0040-1951(96)00047-9).
- Fukahata, Y., Wright, T.J., 2008. A non-linear geodetic data inversion using ABIC for slip distribution on a fault with an unknown dip angle. *Geophys. J. Int.* 173 (2), 353-364.
- Funning, G.J., Garcia, A., 2018. A systematic study of earthquake detectability using Sentinel-1 Interferometric Wide-Swath data. *Geophys. J. Int.* 216 (1), 332-349. <https://doi.org/10.1093/gji/ggy426>.
- Funning, G.J., Parsons, B., Wright, T.J., Jackson, J.A., Fielding, E.J., 2005. Surface displacements and source parameters of the 2003 Bam (Iran) earthquake from Envisat advanced synthetic aperture radar imagery. *J. Geophys. Res. Solid Earth* 110 (B9). <https://doi.org/10.1029/2004JB003338>.
- Gabriel, A.K., Goldstein, R.M., Zebker, H.A., 1989. Mapping small elevation changes over large areas: Differential radar interferometry. *J. Geophys. Res. Solid Earth* 94 (B7), 9183-9191. <https://doi.org/10.1029/JB094iB07p09183>.
- Geist, E.L., Parsons, T., 2005. Triggering of tsunamigenic aftershocks from large strike-slip earthquakes: Analysis of the November 2000 New Ireland earthquake sequence. *Geochemistry, Geophysics, Geosystems* 6 (10).
- Ghorbanzadeh, O., Blaschke, T., Gholamnia, K., Meena, S.R., Tiede, D., Aryal, J., 2019. Evaluation of different machine learning methods and deep-learning convolutional neural networks for landslide detection. *Remote Sens.* 11 (2), 196. <https://doi.org/10.3390/rs11020196>.
- Gili, J.A., Corominas, J., Rius, J., 2000. Using Global Positioning System techniques in landslide monitoring. *Eng. Geol.* 55 (3), 167-192. [https://doi.org/10.1016/S0013-7952\(99\)00127-1](https://doi.org/10.1016/S0013-7952(99)00127-1).
- Glennie, C.L., Hinojosa-Corona, A., Nissen, E., Kusari, A., Oskin, M.E., Arrowsmith, J.R., Borsa, A., 2014. Optimization of legacy lidar data sets for measuring near-field earthquake displacements. *Geophys. Res. Lett.* 41 (10), 3494-3501. <https://doi.org/10.1002/2014GL059919>.
- Goldberg, D.E., Melgar, D., Sahakian, V.J., Thomas, A.M., Xu, X., Crowell, B.W., Geng, J., 2020. Complex rupture of an immature fault zone: A simultaneous kinematic model of the 2019 Ridgecrest, CA earthquakes. *Geophys. Res. Lett.* 47 (3), e2019GL086382. <https://doi.org/10.1029/2019GL086382>.
- Goldstein, R.M., Werner, C.L., 1998. Radar interferogram filtering for geophysical applications. *Geophys. Res. Lett.* 25 (21), 4035-4038. <https://doi.org/10.1029/1998gl1900033>.
- Goldstein, R.M., Zebker, H.A., Werner, C.L., 1988. Satellite radar interferometry: Two-dimensional phase unwrapping. *Radio Sci.* 23 (4), 713-720. <https://doi.org/10.1029/RS023i004p00713>.

- Gomba, G., González, F.R., Zan, F.D., 2017. Ionospheric phase screen compensation for the Sentinel-1 TOPS and ALOS-2 ScanSAR modes. *IEEE Trans. Geosci. Remote Sens.* 55 (1), 223-235. <https://doi.org/10.1109/TGRS.2016.2604461>.
- Gomba, G., Parizzi, A., Zan, F.D., Eineder, M., Bamler, R., 2016. Toward operational compensation of ionospheric effects in SAR interferograms: The split-spectrum method. *IEEE Trans. Geosci. Remote Sens.* 54 (3), 1446-1461. <https://doi.org/10.1109/TGRS.2015.2481079>.
- Grant, M.C., Boyd, S.P., 2008. Graph implementations for nonsmooth convex programs. In: *Recent advances in learning and control*, London, pp. 95-110.
- Grant, M.C., Boyd, S.P., 2013. CVX: Matlab software for disciplined convex programming, version 2.0 beta, <http://cvxr.com/cvx>.
- Grinsted, A., Moore, J.C., Jevrejeva, S., 2004. Application of the cross wavelet transform and wavelet coherence to geophysical time series. *Nonlinear Processes in Geophysics* 11 (6), 561-566.
- Guisan, A., Weiss, S.B., Weiss, A.D., 1999. GLM versus CCA spatial modeling of plant species distribution. *Plant Ecology* 143 (1), 107-122. 10.1023/A:1009841519580.
- Guzzetti, F., Peruccacci, S., Rossi, M., Stark, C.P., 2007. Rainfall thresholds for the initiation of landslides in central and southern Europe. *Meteorol. Atmos. Phys.* 98 (3), 239-267. <https://doi.org/10.1007/s00703-007-0262-7>.
- Haddad, D.E., Akçiz, S.O., Arrowsmith, J.R., Rhodes, D.D., Oldow, J.S., Zielke, O., Toké, N.A., Haddad, A.G., Mauer, J., Shilpakar, P., 2012. Applications of airborne and terrestrial laser scanning to paleoseismology. *Geosphere* 8 (4), 771-786. <https://doi.org/10.1130/ges00701.1>.
- Hall, M.A., Holmes, G., 2003. Benchmarking attribute selection techniques for discrete class data mining. *IEEE Trans. Knowl. Data Eng.* 15 (6), 1437-1447. <https://doi.org/10.1109/TKDE.2003.1245283>.
- Hamling, I.J., Hreinsdóttir, S., Clark, K., Elliott, J., Liang, C., Fielding, E., Litchfield, N., Villamor, P., Wallace, L., Wright, T.J., 2017. Complex multifault rupture during the 2016 Mw 7.8 Kaikōura earthquake, New Zealand. *Science* 356 (6334), eaam7194. <https://doi.org/10.1126/science.aam7194>.
- Handwerger, A.L., Booth, A.M., Huang, M.H., Fielding, E.J., 2021. Inferring the subsurface geometry and strength of slow-moving landslides using 3-D velocity measurements from the NASA/JPL UAVSAR. *J. Geophys. Res. Earth Surf.* 126 (3), 1-21. <https://doi.org/10.1029/2020JF005898>.
- Handwerger, A.L., Fielding, E.J., Huang, M.-H., Bennett, G.L., Liang, C., Schulz, W.H., 2019. Widespread initiation, reactivation, and acceleration of landslides in the northern California Coast Ranges due to extreme rainfall. *J. Geophys. Res. Earth Surf.* 124 (7), 1782-1797. <https://doi.org/10.1029/2019JF005035>.
- Hanssen, R.F., 2001. Radar interferometry: data interpretation and error analysis. Boston, MA: Kluwer Academic.
- Herrera, G., Gutiérrez, F., García-Davalillo, J.C., Guerrero, J., Notti, D., Galve, J.P., Fernández-Merodo, J.A., Cooksley, G., 2013. Multi-sensor advanced DInSAR monitoring of very slow landslides: The Tena Valley case study (Central Spanish Pyrenees). *Remote Sens. Environ.* 128, 31-43. <https://doi.org/10.1016/j.rse.2012.09.020>.
- Highland, L., Bobrowsky, P.T., 2008. The landslide handbook: a guide to understanding landslides. Reston, Virginia, US Geological Survey Circular.
- Hilley, G.E., Bürgmann, R., Ferretti, A., Novali, F., Rocca, F., 2004. Dynamics of slow-moving landslides from permanent scatterer analysis. *Science* 304 (5679), 1952-1955. <https://doi.org/10.1126/science.1098821>.
- Hofer, L., Zampieri, P., Zanini, M.A., Faleschini, F., Pellegrino, C., 2018. Seismic damage survey and empirical fragility curves for churches after the August 24, 2016 Central Italy earthquake. *Soil Dynam. Earthquake Eng.* 111, 98-109. <https://doi.org/10.1016/j.soildyn.2018.02.013>.
- Holm, R.J., Rosenbaum, G., Richards, S.W., 2016. Post 8 Ma reconstruction of Papua New Guinea and Solomon Islands: Microplate tectonics in a convergent plate boundary setting. *Earth-Science Reviews* 156, 66-81.
- Hooper, A., 2008. A multi-temporal InSAR method incorporating both persistent scatterer and small baseline approaches. *Geophys. Res. Lett.* 35 (16). <https://doi.org/10.1029/2008GL034654>.
- Hooper, A., Bekaert, D., Spaans, K., Arkan, M., 2012. Recent advances in SAR interferometry time series analysis for measuring crustal deformation. *Tectonophysics* 514, 1-13. <https://doi.org/10.1016/j.tecto.2011.10.013>.

- Hooper, A., Segall, P., Zebker, H., 2007. Persistent scatterer InSAR for crustal deformation analysis, with application to Volcán Alcedo, Galápagos. *J. Geophys. Res.* 112 (B07407), 19.
- Hooper, A., Zebker, H., Segall, P., Kampes, B., 2004. A new method for measuring deformation on volcanoes and other natural terrains using InSAR persistent scatterers. *Geophys. Res. Lett.* 31 (23). <https://doi.org/10.1029/2004GL021737>.
- Hooper, A., Zebker, H.A., 2007. Phase unwrapping in three dimensions with application to InSAR time series. *JOSA A* 24 (9), 2737-2747. <https://doi.org/10.1364/JOSAA.24.002737>.
- Hou, A.Y., Kakar, R.K., Neeck, S., Azarbarzin, A.A., Kummerow, C.D., Kojima, M., Oki, R., Nakamura, K., Iguchi, T., 2014. The global precipitation measurement mission. *Bull. Am. Meteorol. Soc.* 95 (5), 701-722. <https://doi.org/10.1175/Bams-D-13-00164.1>.
- Hovanesian, S.A., 1980. Introduction to synthetic array and imaging radars.
- Hovius, N., Meunier, P., 2012. Earthquake ground motion and patterns of seismically induced landsliding. In J.C. John, & S. Douglas (Eds.), *Landslides: Types, Mechanisms and Modeling*: Cambridge University Press.
- Hovius, N., Meunier, P., Lin, C.-W., Chen, H., Chen, Y.-G., Dadson, S., Horng, M.-J., Lines, M., 2011. Prolonged seismically induced erosion and the mass balance of a large earthquake. *Earth Planet. Sci. Lett.* 304 (3), 347-355. <https://doi.org/10.1016/j.epsl.2011.02.005>.
- Hu, X., Lu, Z., Pierson, T.C., Kramer, R., George, D.L., 2018. Combining InSAR and GPS to determine transient movement and thickness of a seasonally active low-gradient translational landslide. *Geophys. Res. Lett.* 45 (3), 1453-1462. <https://doi.org/10.1002/2017GL076623>.
- Hu, X., Wang, T., Liao, M., 2014. Measuring coseismic displacements with point-like targets offset tracking. *IEEE Geosci. Remote Sens. Lett.* 11 (1), 283-287.
- Hu, X., Wang, T., Pierson, T.C., Lu, Z., Kim, J., Cecere, T.H., 2016. Detecting seasonal landslide movement within the Cascade landslide complex (Washington) using time-series SAR imagery. *Remote Sens. Environ.* 187, 49-61. <https://doi.org/10.1016/j.rse.2016.10.006>.
- Huang, F., Yao, C., Liu, W., Li, Y., Liu, X., 2018. Landslide susceptibility assessment in the Nantian area of China: a comparison of frequency ratio model and support vector machine. *Geomatics, Natural Hazards and Risk* 9 (1), 919-938. <https://doi.org/10.1080/19475705.2018.1482963>.
- Hubert, M., Debruyne, M., 2010. Minimum covariance determinant. *Wiley Interdiscip. Rev. Comput. Stat.* 2 (1), 36-43. <https://doi.org/10.1002/wics.61>.
- Huffman, G.J., Stocker, E.F., Bolvin, D.T., Nelkin, E.J., Tan, J., 2019. GPM IMERG Early Precipitation L3 1 day 0.1 degree x 0.1 degree V06, Edited by Andrey Savtchenko, Greenbelt, MD, Goddard Earth Sciences Data and Information Services Center (GES DISC). Accessed: 20 January 2021. <https://doi.org/10.5067/GPM/IMERGDE/DAY/06>
- Hungr, O., Leroueil, S., Picarelli, L., 2014. The Varnes classification of landslide types, an update. *Landslides* 11 (2), 167-194. <https://doi.org/10.1007/s10346-013-0436-y>.
- Intrieri, E., Frodella, W., Raspini, F., Bardi, F., Tofani, V., 2020. Using satellite interferometry to infer landslide sliding surface depth and geometry. *Remote Sens.* 12 (9), 1462. <https://doi.org/10.3390/rs12091462>.
- Intrieri, E., Raspini, F., Fumagalli, A., Lu, P., Del Conte, S., Farina, P., Allievi, J., Ferretti, A., Casagli, N., 2018. The Maoxian landslide as seen from space: detecting precursors of failure with Sentinel-1 data. *Landslides* 15 (1), 123-133. <https://doi.org/10.1007/s10346-017-0915-7>.
- Jaboyedoff, M., Carrea, D., Derron, M.-H., Oppikofer, T., Penna, I.M., Rudaz, B., 2020. A review of methods used to estimate initial landslide failure surface depths and volumes. *Eng. Geol.* 267, 105478. <https://doi.org/10.1016/j.enggeo.2020.105478>.
- Jakowski, N., Mayer, C., Hoque, M.M., Wilken, V., 2011. Total electron content models and their use in ionosphere monitoring. *Radio Sci.* 46 (6). <https://doi.org/10.1029/2010RS004620>.
- Jolivet, R., Agram, P.S., Lin, N.Y., Simons, M., Doin, M.-P., Peltzer, G., Li, Z., 2014. Improving InSAR geodesy using Global Atmospheric Models. *J. Geophys. Res. Solid Earth* 119 (3), 2324-2341. <https://doi.org/10.1002/2013JB010588>.
- Jolivet, R., Lasserre, C., Doin, M.-P., Guillaso, S., Peltzer, G., Dailu, R., Sun, J., Shen, Z.-K., Xu, X., 2012. Shallow creep on the Haiyuan Fault (Gansu, China) revealed by SAR Interferometry. *J. Geophys. Res. Solid Earth* 117 (B6). <https://doi.org/10.1029/2011JB008732>.
- Jónsson, S., Zebker, H., Segall, P., Amelung, F., 2002. Fault slip distribution of the 1999 M w 7.1 Hector Mine, California, earthquake, estimated from satellite radar and GPS measurements. *Bull. Seismol. Soc. Am.* 92 (4), 1377-1389.

- Jordan, R.L., 1980. The Seasat - A synthetic aperture radar system. *IEEE Journal of Oceanic Engineering* 5 (2), 154-164. <https://doi.org/10.1109/JOE.1980.1145451>.
- Just, D., Bamler, R., 1994. Phase statistics of interferograms with applications to synthetic aperture radar. *Appl. Opt.* 33 (20), 4361-4368. <https://doi.org/10.1364/AO.33.004361>.
- Kang, Y., Lu, Z., Zhao, C., Xu, Y., Kim, J.-w., Gallegos, A.J., 2021. InSAR monitoring of creeping landslides in mountainous regions: A case study in Eldorado National Forest, California. *Remote Sens. Environ.* 258, 112400. <https://doi.org/10.1016/j.rse.2021.112400>.
- Keefer, D.K., 2002. Investigating landslides caused by earthquakes – A historical review. *Surv. Geophys.* 23 (6), 473-510. <https://doi.org/10.1023/A:1021274710840>.
- Kim, J., Kim, M., Kim, P., Nor, S., Park, C., Jo, Y., Park, S., 2012. The mechanical properties of limestones distributed in Jecheon. *Tunn. Undergr. Space* 22 (5), 354-364. <http://doi.org/10.7474/TUS.2012.22.5.354>.
- Kincey, M.E., Rosser, N.J., Robinson, T.R., Densmore, A.L., Shrestha, R., Pujara, D.S., Oven, K.J., Williams, J.G., Swirad, Z.M., 2021. Evolution of Coseismic and Post-seismic Landsliding After the 2015 Mw 7.8 Gorkha Earthquake, Nepal. *J. Geophys. Res. Earth Surf.* 126 (3), e2020JF005803. <https://doi.org/10.1029/2020JF005803>.
- Kohlhase, A.O., Feigl, K.L., Massonnet, D., 2003. Applying differential InSAR to orbital dynamics: a new approach for estimating ERS trajectories. *J. Geodesy* 77 (9), 493-502. <https://doi.org/10.1007/s00190-003-0336-3>.
- Lacroix, P., Berthier, E., Maquerhua, E.T., 2015. Earthquake-driven acceleration of slow-moving landslides in the Colca valley, Peru, detected from Pléiades images. *Remote Sens. Environ.* 165, 148-158. <https://doi.org/10.1016/j.rse.2015.05.010>.
- Lacroix, P., Dehecq, A., Taïpe, E., 2019. Irrigation-triggered landslides in a Peruvian desert caused by modern intensive farming. *Nat. Geosci.*, 1-5. <https://doi.org/10.1038/s41561-019-0500-x>.
- Lacroix, P., Handwerker, A.L., Bièvre, G., 2020. Life and death of slow-moving landslides. *Nat. Rev. Earth Environ.* 1 (8), 404-419. <https://doi.org/10.1038/s43017-020-0072-8>.
- Lacroix, P., Perfettini, H., Taïpe, E., Guillier, B., 2014. Coseismic and postseismic motion of a landslide: Observations, modeling, and analogy with tectonic faults. *Geophys. Res. Lett.* 41 (19), 6676-6680. <https://doi.org/10.1002/2014GL061170>.
- Lanari, R., Casu, F., Manzo, M., Zeni, G., Berardino, P., Manunta, M., Pepe, A., 2007. An overview of the Small BAseline Subset Algorithm: a DInSAR technique for surface deformation analysis. *Pure Appl. Geophys.* 164 (4), 637-661. <https://doi.org/10.1007/s00024-007-0192-9>.
- Lanari, R., Mora, O., Manunta, M., Mallorqui, J.J., Berardino, P., Sansosti, E., 2004. A small-baseline approach for investigating deformations on full-resolution differential SAR interferograms. *IEEE Trans. Geosci. Remote Sens.* 42 (7), 1377-1386. <https://doi.org/10.1109/TGRS.2004.828196>.
- Lei, S., 2012. A feature selection method based on information gain and genetic algorithm. In: *2012 Int. Conf. Comput. Sci. Electr. Eng.* 2, pp. 355-358.
- Leprince, S., Barbot, S., Ayoub, F., Avouac, J.-P., 2007. Automatic and precise orthorectification, coregistration, and subpixel correlation of satellite images, application to ground deformation measurements. *IEEE Trans. Geosci. Remote Sens.* 45 (6), 1529-1558.
- Li, F.K., Goldstein, R.M., 1990. Studies of multibaseline spaceborne interferometric synthetic aperture radars. *IEEE Trans. Geosci. Remote Sens.* 28 (1), 88-97. <https://doi.org/10.1109/36.45749>.
- Li, M., Zhang, L., Shi, X., Liao, M., Yang, M., 2019. Monitoring active motion of the Guobu landslide near the Laxiwa Hydropower Station in China by time-series point-like targets offset tracking. *Remote Sens. Environ.* 221, 80-93. <https://doi.org/10.1016/j.rse.2018.11.006>.
- Li, Y., Huang, J., Jiang, S.-H., Huang, F., Chang, Z., 2017. A web-based GPS system for displacement monitoring and failure mechanism analysis of reservoir landslide. *Scientific Reports* 7 (1), 17171. <https://doi.org/10.1038/s41598-017-17507-7>.
- Li, Z., Muller, J.-P., Cross, P., Fielding, E.J., 2005. Interferometric synthetic aperture radar (InSAR) atmospheric correction: GPS, Moderate Resolution Imaging Spectroradiometer (MODIS), and InSAR integration. *J. Geophys. Res. Solid Earth* 110 (B3). <https://doi.org/10.1029/2004JB003446>.
- Lin, C.H., Liu, D., Liu, G., 2019. Landslide detection in La Paz City (Bolivia) based on time series analysis of InSAR data. *Int. J. Remote Sens.* 40 (17), 6775-6795. <https://doi.org/10.1080/01431161.2019.1594434>.

- Lin, J., Stein, R.S., 2004. Stress triggering in thrust and subduction earthquakes and stress interaction between the southern San Andreas and nearby thrust and strike-slip faults. *J. Geophys. Res. Solid Earth* 109 (B2). <https://doi.org/10.1029/2003JB002607>.
- Lin, Y.-n.N., Simons, M., Hetland, E.A., Muse, P., DiCaprio, C., 2010. A multiscale approach to estimating topographically correlated propagation delays in radar interferograms. *Geochemistry, Geophysics, Geosystems* 11 (9). <https://doi.org/10.1029/2010GC003228>.
- Lindsey, E.O., Natsuaki, R., Xu, X., Shimada, M., Hashimoto, M., Melgar, D., Sandwell, D.T., 2015. Line-of-sight displacement from ALOS-2 interferometry: Mw 7.8 Gorkha Earthquake and Mw 7.3 aftershock. *Geophys. Res. Lett.* 42 (16), 6655-6661.
- Liu, F., Elliott, J.R., Craig, T.J., Hooper, A., Wright, T.J., 2021. Improving the resolving power of InSAR for earthquakes using time series: A case study in Iran. *Geophys. Res. Lett.* 48 (14), e2021GL093043. <https://doi.org/10.1029/2021GL093043>.
- Liu, X., Zhao, C., Zhang, Q., Lu, Z., Li, Z., 2020. Deformation of the Baige Landslide, Tibet, China, Revealed Through the Integration of Cross-Platform ALOS/PALSAR-1 and ALOS/PALSAR-2 SAR Observations. *Geophys. Res. Lett.* 47 (3), e2019GL086142. <https://doi.org/10.1029/2019GL086142>.
- Llanes, P., Silver, E., Day, S., Hoffman, G., 2009. Interactions between a transform fault and arc volcanism in the Bismarck Sea, Papua New Guinea. *Geochemistry, Geophysics, Geosystems* 10 (6).
- Loew, A., Mauser, W., 2007. Generation of geometrically and radiometrically terrain corrected SAR image products. *Remote Sens. Environ.* 106 (3), 337-349. <https://doi.org/10.1016/j.rse.2006.09.002>.
- Lohman, R.B., Simons, M., 2005. Some thoughts on the use of InSAR data to constrain models of surface deformation: Noise structure and data downsampling. *Geochemistry, Geophysics, Geosystems* 6 (1). <https://doi.org/10.1029/2004GC000841>.
- Lu, P., Bai, S., Tofani, V., Casagli, N., 2019. Landslides detection through optimized hot spot analysis on persistent scatterers and distributed scatterers. *Int. J. Photogramm. Remote Sens.* 156, 147-159. <https://doi.org/10.1016/j.isprsjprs.2019.08.004>.
- Marano, K.D., Wald, D.J., Allen, T.I., 2010. Global earthquake casualties due to secondary effects: a quantitative analysis for improving rapid loss analyses. *Nat. Hazards* 52 (2), 319-328. <https://doi.org/10.1007/s11069-009-9372-5>.
- Marc, O., Hovius, N., Meunier, P., Uchida, T., Hayashi, S., 2015a. Transient changes of landslide rates after earthquakes. *Geology* 43 (10), 883-886. [10.1130/g36961.1](https://doi.org/10.1130/g36961.1).
- Marc, O., Hovius, N., Meunier, P., Uchida, T., Hayashi, S., 2015b. Transient changes of landslide rates after earthquakes. *Geology* 43 (10), 883-886. <https://doi.org/10.1130/G36961.1>.
- Marston, R.A., Butler, W.D., Patch, N.L., 2017. Geomorphic Hazards. *International Encyclopedia of Geography*, pp. 1-8
- Martino, S., Bozzano, F., Caporossi, P., D'Angiò, D., Della Seta, M., Esposito, C., Fantini, A., Fiorucci, M., Giannini, L.M., Iannucci, R., Marmoni, G.M., Mazzanti, P., Missori, C., Moretto, S., Piacentini, D., Rivellino, S., Romeo, R.W., Sarandrea, P., Schilirò, L., Troiani, F., Varone, C., 2019. Impact of landslides on transportation routes during the 2016-2017 Central Italy seismic sequence. *Landslides* 16 (6), 1221-1241. <https://doi.org/10.1007/s10346-019-01162-2>.
- Massonnet, D., Feigl, K.L., 1998. Radar interferometry and its application to changes in the Earth's surface. *Rev. Geophys.* 36 (4), 441-500.
- Massonnet, D., Feigl, K.L., Vadon, H., Rossi, M., 1996. Coseismic deformation field of the M=6.7 Northridge, California Earthquake of January 17, 1994 recorded by two radar satellites using interferometry. *Geophys. Res. Lett.* 23 (9), 969-972. <https://doi.org/10.1029/96GL00729>.
- Massonnet, D., Rossi, M., Carmona, C., Adragna, F., Peltzer, G., Feigl, K., Rabaut, T., 1993. The displacement field of the Landers earthquake mapped by radar interferometry. *Nature* 364 (6433), 138. <https://doi.org/10.1038/364138a0>.
- McCall, G.J., 2012. Natural and man-made hazards: their increasing importance in the end-20th century world. In G.J. McCall, D.J.C. Laming, & S.C. Scott (Eds.), *Geohazards*, pp. 1-4: Springer Science & Business Media.
- Meyer, F.J., 2011. Performance requirements for ionospheric correction of low-frequency SAR data. *IEEE Trans. Geosci. Remote Sens.* 49 (10), 3694-3702. <https://doi.org/10.1109/TGRS.2011.2146786>.

- Meyer, F.J., Nicoll, J.B., 2008. Prediction, detection, and correction of Faraday rotation in full-polarimetric L-band SAR data. *IEEE Trans. Geosci. Remote Sens.* 46 (10), 3076-3086. <https://doi.org/10.1109/TGRS.2008.2003002>.
- Mezaal, M.R., Pradhan, B., Rizeei, H.M., 2018. Improving landslide detection from airborne laser scanning data using optimized Dempster–Shafer. *Remote Sens.* 10 (7), 1029.
- Michel, R., Avouac, J.P., Taboury, J., 1999. Measuring ground displacements from SAR amplitude images: Application to the Landers earthquake. *Geophys. Res. Lett.* 26 (7), 875-878.
- Milliner, C.W.D., Dolan, J.F., Hollingsworth, J., Leprince, S., Ayoub, F., 2016. Comparison of coseismic near-field and off-fault surface deformation patterns of the 1992 Mw 7.3 Landers and 1999 Mw 7.1 Hector Mine earthquakes: Implications for controls on the distribution of surface strain. *Geophys. Res. Lett.* 43 (19), 10,115-110,124. <https://doi.org/10.1002/2016GL069841>.
- Mousavi, S.M., Ellsworth, W.L., Zhu, W., Chuang, L.Y., Beroza, G.C., 2020. Earthquake transformer—an attentive deep-learning model for simultaneous earthquake detection and phase picking. *Nat. Commun.* 11 (1), 3952. <https://doi.org/10.1038/s41467-020-17591-w>.
- Nakamura, Y., 1989. A method for dynamic characteristics estimation of subsurface using microtremor on the ground surface. *Quarterly Report of the Railway Technical Research Institute* 30 (1), 25-33.
- Naudet, V., Lazzari, M., Perrone, A., Loperte, A., Piscitelli, S., Lapenna, V., 2008. Integrated geophysical and geomorphological approach to investigate the snowmelt-triggered landslide of Bosco Piccolo village (Basilicata, southern Italy). *Eng. Geol.* 98 (3), 156-167. <https://doi.org/10.1016/j.enggeo.2008.02.008>.
- Notti, D., Herrera, G., Bianchini, S., Meisina, C., García-Davalillo, J.C., Zucca, F., 2014. A methodology for improving landslide PSI data analysis. *Int. J. Remote Sens.* 35 (6), 2186-2214. <https://doi.org/10.1080/01431161.2014.889864>.
- Okada, Y., 1985. Surface deformation due to shear and tensile faults in a half-space. *Bull. Seismol. Soc. Am.* 75 (4), 1135-1154. <https://doi.org/10.1785/BSSA0750041135>.
- Onn, F., Zebker, H.A., 2006. Correction for interferometric synthetic aperture radar atmospheric phase artifacts using time series of zenith wet delay observations from a GPS network. *J. Geophys. Res. Solid Earth* 111 (B9). <https://doi.org/10.1029/2005JB004012>.
- Osmanoğlu, B., Dixon, T.H., Wdowinski, S., Cabral-Cano, E., Jiang, Y., 2011. Mexico City subsidence observed with persistent scatterer InSAR. *Int. J. Appl. Earth Obs. Geoinf.* 13 (1), 1-12. <https://doi.org/10.1016/j.jag.2010.05.009>.
- Osmanoğlu, B., Sunar, F., Wdowinski, S., Cabral-Cano, E., 2016. Time series analysis of InSAR data: Methods and trends. *Int. J. Photogramm. Remote Sens.* 115, 90-102. <https://doi.org/10.1016/j.isprsjprs.2015.10.003>.
- Pairman, D., McNeill, S., 1997. Efficient calculation in the map domain of SAR layover and shadow masks. In: *IGARSS'97. 1997 IEEE International Geoscience and Remote Sensing Symposium Proceedings. Remote Sensing - A Scientific Vision for Sustainable Development*, 4, pp. 2057-2059 vol.2054.
- Park, S.C., Mori, J., 2007. Triggering of earthquakes during the 2000 Papua New Guinea earthquake sequence. *J. Geophys. Res. Solid Earth* 112 (B3).
- Parks, M.M., Biggs, J., England, P., Mather, T.A., Nomikou, P., Palamartchouk, K., Papanikolaou, X., Paradissis, D., Parsons, B., Pyle, D.M., 2012. Evolution of Santorini Volcano dominated by episodic and rapid fluxes of melt from depth. *Nat. Geosci.* 5 (10), 749.
- Pathier, E., Fielding, E.J., Wright, T.J., Walker, R., Parsons, B.E., Hensley, S., 2006. Displacement field and slip distribution of the 2005 Kashmir earthquake from SAR imagery. *Geophys. Res. Lett.* 33 (20). <https://doi.org/10.1029/2006GL027193>.
- Pazzi, V., Morelli, S., Fanti, R., 2019. A review of the advantages and limitations of geophysical investigations in landslide studies. *Int. J. Geophys.* 2019, 2983087. <https://doi.org/10.1155/2019/2983087>.
- Pazzi, V., Tanteri, L., Biccocchi, G., D'Ambrosio, M., Caselli, A., Fanti, R., 2017. H/V measurements as an effective tool for the reliable detection of landslide slip surfaces: Case studies of Castagnola (La Spezia, Italy) and Roccalbegna (Grosseto, Italy). *Phys. Chem. Earth Parts A/B/C* 98, 136-153. <https://doi.org/10.1016/j.pce.2016.10.014>.
- Pepe, A., Berardino, P., Bonano, M., Euillades, L.D., Lanari, R., Sansosti, E., 2011. SBAS-based satellite orbit correction for the generation of DInSAR time-series: Application to RADARSAT-1

- data. *IEEE Trans. Geosci. Remote Sens.* 49 (12), 5150-5165.
<https://doi.org/10.1109/TGRS.2011.2155069>.
- Pepe, A., Calò, F., 2017. A review of interferometric synthetic aperture RADAR (InSAR) multi-track approaches for the retrieval of Earth's surface displacements. *Applied Sciences* 7 (12), 1264.
- Perissin, D., Wang, T., 2012. Repeat-pass SAR interferometry with partially coherent targets. *IEEE Trans. Geosci. Remote Sens.* 50 (1), 271-280. <https://doi.org/10.1109/TGRS.2011.2160644>.
- Petley, D., 2012. Global patterns of loss of life from landslides. *Geology* 40 (10), 927-930.
<https://doi.org/10.1130/g33217.1>.
- Pierantoni, P., Deiana, G., Galdenzi, S., 2013. Stratigraphic and structural features of the Sibillini Mountains (Umbria-Marche Apennines, Italy). *Ital. J. Geosci.* 132 (3), 497-520.
<https://doi.org/10.3301/ijg.2013.08>.
- Pizzi, A., Di Domenica, A., Gallovič, F., Luzi, L., Puglia, R., 2017. Fault segmentation as constraint to the occurrence of the main shocks of the 2016 Central Italy seismic sequence. *Tectonics* 36 (11), 2370-2387. <https://doi.org/10.1002/2017TC004652>.
- Pousse-Beltran, L., Socquet, A., Benedetti, L., Doin, M.P., Rizza, M., D'Agostino, N., 2020. Localized afterslip at geometrical complexities revealed by InSAR After the 2016 Central Italy seismic sequence. *J. Geophys. Res. Solid Earth* 125 (11). <https://doi.org/10.1029/2019JB019065>.
- Raspini, F., Bianchini, S., Ciampalini, A., Del Soldato, M., Montalti, R., Solari, L., Tofani, V., Casagli, N., 2019. Persistent Scatterers continuous streaming for landslide monitoring and mapping: the case of the Tuscany region (Italy). *Landslides* 16 (10), 2033-2044.
<https://doi.org/10.1007/s10346-019-01249-w>.
- Raucoules, D., Michele, M.d., 2010. Assessing ionospheric influence on L-band SAR data: Implications on coseismic displacement measurements of the 2008 Sichuan earthquake. *IEEE Geosci. Remote Sens. Lett.* 7 (2), 286-290. <https://doi.org/10.1109/LGRS.2009.2033317>.
- Raventós, J., Arroyo, M., Heredia, W., Cruz, A., 2017. Aplicación de la Técnica de Interferometría de Radar de Apertura Sintética (InSAR) en la Detección de Movimientos en Masa en el Municipio de Independencia. In: *IX Simposio Nacional de Taludes y Laderas Inestables* 1, Santander, Spain, pp. 528-532.
- Roback, K., Clark, M.K., West, A.J., Zekkos, D., Li, G., Gallen, S.F., Chamlagain, D., Godt, J.W., 2018. The size, distribution, and mobility of landslides caused by the 2015 Mw7.8 Gorkha earthquake, Nepal. *Geomorphology* 301, 121-138.
<https://doi.org/10.1016/j.geomorph.2017.01.030>.
- Roberts, N.J., 2016. Late Cenozoic geology of La Paz, Bolivia, and its relation to landslide activity. PhD thesis, Simon Fraser University, Canada.
- Roberts, N.J., Rabus, B., Hermanns, R.L., Guzmán, M.-A., Clague, J.J., Minaya, E., 2014. Recent landslide activity in La Paz, Bolivia. *Landslide Science for a Safer Geoenvironment*, pp. 431-437: Springer.
- Rojstaczer, S., Wolf, S., 1992. Permeability changes associated with large earthquakes: An example from Loma Prieta, California. *Geology* 20 (3), 211-214. 10.1130/0091-7613(1992)020<0211:Pcawle>2.3.Co;2.
- Rosen, P.A., Hensley, S., Chen, C., 2010. Measurement and mitigation of the ionosphere in L-band Interferometric SAR data. In: *2010 IEEE Radar Conference*, pp. 1459-1463.
- Rosen, P.A., Hensley, S., Peltzer, G., Simons, M., 2004. Updated repeat orbit interferometry package released. *Eos, Transactions American Geophysical Union* 85 (5), 47-47.
<https://doi.org/10.1029/2004EO050004>.
- Rosi, A., Tofani, V., Tanteri, L., Tacconi Stefanelli, C., Agostini, A., Catani, F., Casagli, N., 2018. The new landslide inventory of Tuscany (Italy) updated with PS-InSAR: geomorphological features and landslide distribution. *Landslides* 15 (1), 5-19. 10.1007/s10346-017-0861-4.
- Rousseeuw, P.J., 1984. Least median of squares regression. *J. Am. Stat. Assoc.* 79 (388), 871-880.
<https://doi.org/10.1080/01621459.1984.10477105>.
- Saar, M.O., Manga, M., 2003. Seismicity induced by seasonal groundwater recharge at Mt. Hood, Oregon. *Earth Planet. Sci. Lett.* 214 (3-4), 605-618. [https://doi.org/10.1016/S0012-821X\(03\)00418-7](https://doi.org/10.1016/S0012-821X(03)00418-7).
- Saastamoinen, J., 1972. Atmospheric correction for the troposphere and stratosphere in radio ranging satellites. *The Use of Artificial Satellites for Geodesy*, pp. 247-251
- Samsonov, S.V., Trishchenko, A.P., Tiampo, K., González, P.J., Zhang, Y., Fernández, J., 2014. Removal of systematic seasonal atmospheric signal from interferometric synthetic aperture radar

- ground deformation time series. *Geophys. Res. Lett.* 41 (17), 6123-6130.
<https://doi.org/10.1002/2014gl061307>.
- Sansosti, E., Lanari, R., Fornaro, G., Franceschetti, G., Tesauro, M., Puglisi, G., Coltelli, M., 1999. Digital elevation model generation using ascending and descending ERS-1/ERS-2 tandem data. *Int. J. Remote Sens.* 20 (8), 1527-1547. <https://doi.org/10.1080/014311699212597>.
- Saroli, M., Albano, M., Atzori, S., Moro, M., Tolomei, C., Bignami, C., Stramondo, S., 2021. Analysis of a large seismically induced mass movement after the December 2018 Etna volcano (southern Italy) seismic swarm. *Remote Sens. Environ.* 263, 112524.
<https://doi.org/10.1016/j.rse.2021.112524>.
- Scaioni, M., Feng, T., Lu, P., Qiao, G., Tong, X., Li, R., Barazzetti, L., Previtali, M., Roncella, R., 2015. Close-range photogrammetric techniques for deformation measurement: Applications to landslides. In M. Scaioni (Ed.), *Modern Technologies for Landslide Monitoring and Prediction*, pp. 13-41. Berlin, Heidelberg: Springer Berlin Heidelberg.
- Scanvic, J.Y., Rouzeau, O., Carnec, C., 1993. Evaluation du potentiel des donnees SAR pour la cartographie du risque de mouvements de terrain. In: *Proc. Int. Symp. on: From optic to radar — SPOT and ERS-1 applications*, Paris, France, pp. 301.
- Scheingross, J.S., Minchew, B.M., Mackey, B.H., Simons, M., Lamb, M.P., Hensley, S., 2013. Fault-zone controls on the spatial distribution of slow-moving landslides. *GSA Bull.* 125 (3-4), 473–489. <https://doi.org/10.1130/B30719.1>.
- Schlögel, R., Doubre, C., Malet, J.-P., Masson, F., 2015. Landslide deformation monitoring with ALOS/PALSAR imagery: A D-InSAR geomorphological interpretation method. *Geomorphology* 231, 314-330. <https://doi.org/10.1016/j.geomorph.2014.11.031>.
- Schmidt, D.A., Bürgmann, R., 2003. Time-dependent land uplift and subsidence in the Santa Clara valley, California, from a large interferometric synthetic aperture radar data set. *J. Geophys. Res. Solid Earth* 108(B9) (B9), 2416. <https://doi.org/10.1029/2002JB002267>.
- Schubert, E., Sander, J., Ester, M., Kriegel, H.P., Xu, X., 2017. DBSCAN revisited, revisited: why and how you should (still) use DBSCAN. *ACM Trans. Database Syst.* 42 (3), Article 19.
<https://doi.org/10.1145/3068335>.
- Segall, P., Davis, J.L., 1997. GPS applications for geodynamics and earthquake studies. *Annual Review of Earth and Planetary Sciences* 25 (1), 301-336.
<https://doi.org/10.1146/annurev.earth.25.1.301>.
- Selvakumaran, S., Plank, S., Geiß, C., Rossi, C., Middleton, C., 2018. Remote monitoring to predict bridge scour failure using Interferometric Synthetic Aperture Radar (InSAR) stacking techniques. *Int. J. Appl. Earth Obs. Geoinf.* 73, 463-470. <https://doi.org/10.1016/j.jag.2018.07.004>.
- Sentinel Online, 2021. Forthcoming availability of the Copernicus Sentinel-1A and -1B reprocessed precise orbital products, <https://sentinel.esa.int/web/sentinel/-/forthcoming-availability-of-the-copernicus-sentinel-1a-and-1b-reprocessed-precise-orbital-products>. Accessed on 21 December 2021.
- SESAME, 2004. Guidelines for the implementation of the H/V spectral ratio technique on ambient vibrations: Measurements, processing and interpretation. European Commission–EVG1-CT-2000-00026 SESAME. released on December 2004.
- Seymour, M.S., Cumming, I.G., 1994. Maximum likelihood estimation for SAR interferometry. In: *Proceedings of IGARSS '94 - 1994 IEEE International Geoscience and Remote Sensing Symposium*, 4, pp. 2272-2275 vol.2274.
- Sica, F., Bretzke, S., Pulella, A., Bueso-Bello, J.L., Martone, M., Prats-Iraola, P., González-Bonilla, M.J., Schmitt, M., Rizzoli, P., 2020. InSAR decorrelation at X-band from the joint TanDEM-X/PAZ constellation. *IEEE Geosci. Remote Sens. Lett.*, 1-5.
<https://doi.org/10.1109/LGRS.2020.3014809>.
- Skolnik, M.I., 1962. Introduction to radar. Radar handbook 2.
- Smith, E.K., Weintraub, S., 1953. The constants in the equation for atmospheric refractive index at radio frequencies. *Proceedings of the IRE* 41 (8), 1035-1037.
<https://doi.org/10.1109/JRPROC.1953.274297>.
- Socquet, A., Hollingsworth, J., Pathier, E., Bouchon, M., 2019. Evidence of supershear during the 2018 magnitude 7.5 Palu earthquake from space geodesy. *Nat. Geosci.*, 1.
- Solari, L., Del Soldato, M., Raspini, F., Barra, A., Bianchini, S., Confuorto, P., Casagli, N., Crosetto, M., 2020. Review of satellite interferometry for landslide detection in Italy. *Remote Sens.* 12 (8), 1351. <https://doi.org/10.3390/rs12081351>.

- Song, C., Yu, C., Li, Z., Pazzi, V., Del Soldato, M., Cruz, A., Utili, S., 2021. Landslide geometry and activity in Villa de la Independencia (Bolivia) revealed by InSAR and seismic noise measurements. *Landslides* 18, 2721–2737. <https://doi.org/10.1007/s10346-021-01659-9>.
- Sreejith, K.M., Sunil, P.S., Agrawal, R., Saji, A.P., Ramesh, D.S., Rajawat, A.S., 2016. Coseismic and early postseismic deformation due to the 25 April 2015, Mw 7.8 Gorkha, Nepal, earthquake from InSAR and GPS measurements. *Geophys. Res. Lett.* 43 (7), 3160-3168. <https://doi.org/10.1002/2016GL067907>.
- Strozzi, T., Klimeš, J., Frey, H., Caduff, R., Huggel, C., Wegmüller, U., Rapre, A.C., 2018. Satellite SAR interferometry for the improved assessment of the state of activity of landslides: A case study from the Cordilleras of Peru. *Remote Sens. Environ.* 217, 111-125. <https://doi.org/10.1016/j.rse.2018.08.014>.
- Stumpf, A., Malet, J.P., Allemand, P., Ulrich, P., 2014. Surface reconstruction and landslide displacement measurements with Pléiades satellite images. *Int. J. Photogramm. Remote Sens.* 95, 1-12. <https://doi.org/10.1016/j.isprsjprs.2014.05.008>.
- Toda, S., Stein, R.S., Richards-Dinger, K., Bozkurt, S.B., 2005. Forecasting the evolution of seismicity in southern California: Animations built on earthquake stress transfer. *J. Geophys. Res. Solid Earth* 110 (B5). <https://doi.org/10.1029/2004JB003415>.
- Tomás, R., Li, Z., Liu, P., Singleton, A., Hoey, T., Cheng, X., 2014. Spatiotemporal characteristics of the Huangtupo landslide in the Three Gorges region (China) constrained by radar interferometry. *Geophys. J. Int.* 197 (1), 213-232. <https://doi.org/10.1093/gji/ggu017>.
- Tomás, R., Li, Z., Lopez-Sanchez, J.M., Liu, P., Singleton, A., 2016. Using wavelet tools to analyse seasonal variations from InSAR time-series data: a case study of the Huangtupo landslide. *Landslides* 13 (3), 437-450. <https://doi.org/10.1007/s10346-015-0589-y>.
- Tomiyasu, K., 1978. Tutorial review of synthetic-aperture radar (SAR) with applications to imaging of the ocean surface. *Proceedings of the IEEE* 66 (5), 563-583. <https://doi.org/10.1109/PROC.1978.10961>.
- Torres, R., Snoeij, P., Geudtner, D., Bibby, D., Davidson, M., Attema, E., Potin, P., Rommen, B., Floury, N., Brown, M., 2012. GMES Sentinel-1 mission. *Remote Sens. Environ.* 120, 9-24. <https://doi.org/10.1016/j.rse.2011.05.028>.
- Touzi, R., Lopes, A., Bruniquel, J., Vachon, P.W., 1999. Coherence estimation for SAR imagery. *IEEE Trans. Geosci. Remote Sens.* 37 (1), 135-149. <https://doi.org/10.1109/36.739146>.
- Trajkovic, S., Kisi, O., Markus, M., Tabari, H., Gocic, M., Shamshirband, S., 2016. Hydrological hazards in a changing environment: early warning, forecasting, and impact assessment. *Advances in Meteorology* 2016, 2752091. <https://doi.org/10.1155/2016/2752091>.
- Tregoning, P., Jackson, R.J., McQueen, H., Lambeck, K., Stevens, C., Little, R.P., Curley, R., Rosa, R., 1999. Motion of the South Bismarck Plate, Papua New Guinea. *Geophys. Res. Lett.* 26 (23), 3517-3520.
- Tregoning, P., Sambridge, M., McQueen, H., Toulmin, S., Nicholson, T., 2005. Tectonic interpretation of aftershock relocations in eastern Papua New Guinea using teleseismic data and the arrival pattern method. *Geophys. J. Int.* 160 (3), 1103-1111.
- Tribolet, J., 1977. A new phase unwrapping algorithm. *IEEE Transactions on Acoustics, Speech, and Signal Processing* 25 (2), 170-177. <https://doi.org/10.1109/TASSP.1977.1162923>.
- Tucker, C.J., 1979. Red and photographic infrared linear combinations for monitoring vegetation. *Remote Sens. Environ.* 8 (2), 127-150. [https://doi.org/10.1016/0034-4257\(79\)90013-0](https://doi.org/10.1016/0034-4257(79)90013-0).
- USGS, 2019. M 7.6 - 48 km NE of Kokopo, Papua New Guinea, <https://earthquake.usgs.gov/earthquakes/eventpage/us70003kyy/executive>. Accessed on 30 June 2019.
- Utili, S., Castellanza, R., Galli, A., Sentenac, P., 2015. Novel approach for health monitoring of earthen embankments. *J. Geotech. Geoenviron. Eng.* 141 (3), 04014111. [https://doi.org/10.1061/\(ASCE\)GT.1943-5606.0001215](https://doi.org/10.1061/(ASCE)GT.1943-5606.0001215).
- Verboven, S., Hubert, M., 2005. LIBRA: a MATLAB library for robust analysis. *Chemometrics and Intelligent Laboratory Systems* 75 (2), 127-136. <https://doi.org/10.1016/j.chemolab.2004.06.003>.
- Vigny, C., Simons, W.J.F., Abu, S., Bamphenyu, R., Satirapod, C., Choosakul, N., Subarya, C., Socquet, A., Omar, K., Abidin, H.Z., Ambrosius, B.A.C., 2005. Insight into the 2004 Sumatra–Andaman earthquake from GPS measurements in southeast Asia. *Nature* 436 (7048), 201-206. <https://doi.org/10.1038/nature03937>.

- von Specht, S., Ozturk, U., Veh, G., Cotton, F., Korup, O., 2019. Effects of finite source rupture on landslide triggering: the 2016 Mw 7.1 Kumamoto earthquake. *Solid Earth* 10 (2), 463-486. <https://doi.org/10.5194/se-10-463-2019>.
- Walters, R.J., Gregory, L.C., Wedmore, L.N.J., Craig, T.J., McCaffrey, K., Wilkinson, M., Chen, J., Li, Z., Elliott, J.R., Goodall, H., Iezzi, F., Livio, F., Michetti, A.M., Roberts, G., Vittori, E., 2018. Dual control of fault intersections on stop-start rupture in the 2016 Central Italy seismic sequence. *Earth Planet. Sci. Lett.* 500, 1-14. <https://doi.org/10.1016/j.epsl.2018.07.043>.
- Wang, C., Ding, X., Shan, X., Zhang, L., Jiang, M., 2012. Slip distribution of the 2011 Tohoku earthquake derived from joint inversion of GPS, InSAR and seafloor GPS/acoustic measurements. *J. Asian Earth Sci.* 57, 128-136. <https://doi.org/10.1016/j.jseaes.2012.06.019>.
- Wang, S., Xu, C., Wen, Y., Yin, Z., Jiang, G., Fang, L., 2017. Slip model for the 25 November 2016 Mw 6.6 Aketao earthquake, western China, revealed by Sentinel-1 and ALOS-2 observations. *Remote Sens.* 9 (4), 325. <https://doi.org/10.3390/rs9040325>.
- Wang, T., Jónsson, S., 2015. Improved SAR amplitude image offset measurements for deriving three-dimensional coseismic displacements. *IEEE Journal of Selected Topics in Applied Earth Observations and Remote Sensing* 8 (7), 3271-3278.
- Wang, Z., Li, Z., Mills, J., 2018. A new approach to selecting coherent pixels for ground-based SAR deformation monitoring. *Int. J. Photogramm. Remote Sens.* 144, 412-422. <https://doi.org/10.1016/j.isprsjprs.2018.08.008>.
- Wegmüller, U., Werner, C., Strozzi, T., Wiesmann, A., Frey, O., Santoro, M., 2016. Sentinel-1 support in the GAMMA software. *Procedia Comput. Sci.* 100, 1305-1312. <https://doi.org/10.1016/j.procs.2016.09.246>.
- Wempen, J.M., McCarter, M.K., 2017. Comparison of L-band and X-band differential interferometric synthetic aperture radar for mine subsidence monitoring in central Utah. *International Journal of Mining Science and Technology* 27 (1), 159-163. <https://doi.org/10.1016/j.ijmst.2016.11.012>.
- Wen, Y., Li, Z., Xu, C., Ryder, I., Bürgmann, R., 2012. Postseismic motion after the 2001 MW 7.8 Kokoxili earthquake in Tibet observed by InSAR time series. *J. Geophys. Res. Solid Earth* 117 (B8). <https://doi.org/10.1029/2011JB009043>.
- Werner, C., Wegmüller, U., Strozzi, T., Wiesmann, A., 2003. Interferometric point target analysis for deformation mapping. In: *IGARSS 2003. 2003 IEEE International Geoscience and Remote Sensing Symposium. Proceedings (IEEE Cat. No.03CH37477)*, 7, pp. 4362-4364 vol.4367.
- Werner, C., Wegmüller, U., Strozzi, T., Wiesmann, A., 2000. Gamma SAR and interferometric processing software. In: *Proceedings of the 2000 ERS-Envisat Symposium, Gothenburg, Sweden*, 1620, pp. 1620.
- Wicks, C.W., Dzurisin, D., Ingebritsen, S., Thatcher, W., Lu, Z., Iverson, J., 2002. Magmatic activity beneath the quiescent Three Sisters volcanic center, central Oregon Cascade Range, USA. *Geophys. Res. Lett.* 29 (7), 26-21-26-24. <https://doi.org/10.1029/2001GL014205>.
- Wright, T., Parsons, B., Fielding, E., 2001. Measurement of interseismic strain accumulation across the North Anatolian Fault by satellite radar interferometry. *Geophys. Res. Lett.* 28 (10), 2117-2120. <https://doi.org/10.1029/2000GL012850>.
- Xiao, R., Yu, C., Li, Z., He, X., 2021. Statistical assessment metrics for InSAR atmospheric correction: Applications to generic atmospheric correction online service for InSAR (GACOS) in Eastern China. *Int. J. Appl. Earth Obs. Geoinf.* 96, 102289. <https://doi.org/10.1016/j.jag.2020.102289>.
- Xu, C., Wang, J., Li, Z., Drummond, J., 2010. Applying the Coulomb failure function with an optimally oriented plane to the 2008 Mw 7.9 Wenchuan earthquake triggering. *Tectonophysics* 491 (1-4), 119-126.
- Xu, C., Xu, X., Shyu, J.B.H., Zheng, W., Min, W., 2014. Landslides triggered by the 22 July 2013 Minxian–Zhangxian, China, Mw 5.9 earthquake: Inventory compiling and spatial distribution analysis. *J. Asian Earth Sci.* 92, 125-142. <https://doi.org/10.1016/j.jseaes.2014.06.014>.
- Xu, C., Xu, X., Yu, G., 2013. Landslides triggered by slipping-fault-generated earthquake on a plateau: an example of the 14 April 2010, Ms 7.1, Yushu, China earthquake. *Landslides* 10 (4), 421-431. <https://doi.org/10.1007/s10346-012-0340-x>.
- Xu, W., 2017. Finite-fault slip model of the 2016 Mw 7.5 Chiloé earthquake, southern Chile, estimated from Sentinel-1 data. *Geophys. Res. Lett.* 44 (10), 4774-4780. <https://doi.org/10.1002/2017GL073560>.

- Xu, W., Feng, G., Meng, L., Zhang, A., Ampuero, J.P., Bürgmann, R., Fang, L., 2018. Transpressional rupture cascade of the 2016 Mw 7.8 Kaikoura earthquake, New Zealand. *J. Geophys. Res. Solid Earth* 123 (3), 2396-2409.
- Yagüe-Martínez, N., Prats-Iraola, P., Gonzalez, F.R., Brcic, R., Shau, R., Geudtner, D., Eineder, M., Bamler, R., 2016. Interferometric processing of Sentinel-1 TOPS data. *IEEE Trans. Geosci. Remote Sens.* 54 (4), 2220-2234. <https://doi.org/10.1109/TGRS.2015.2497902>.
- Yamagiwa, S., Miyazaki, S.i., Hirahara, K., Fukahata, Y., 2015. Afterslip and viscoelastic relaxation following the 2011 Tohoku-oki earthquake (Mw9.0) inferred from inland GPS and seafloor GPS/Acoustic data. *Geophys. Res. Lett.* 42 (1), 66-73. <https://doi.org/10.1002/2014GL061735>.
- Yokoyama, R., Shirasawa, M., Pike, R., 2002. Visualizing topography by openness: A new application of image processing to digital elevation models. *Photogrammetric Engineering and Remote Sensing* 68, 257-265.
- Yu, C., 2019. Generic interferometric synthetic aperture radar atmospheric correction model and its application to co- and post-seismic motions. PhD thesis, Newcastle University, United Kingdom.
- Yu, C., Li, Z., Chen, J., Hu, J.-C., 2018a. Small magnitude co-seismic deformation of the 2017 Mw 6.4 Nyingchi earthquake revealed by InSAR measurements with atmospheric correction. *Remote Sens.* 10 (5), 684.
- Yu, C., Li, Z., Penna, N.T., 2018b. Interferometric synthetic aperture radar atmospheric correction using a GPS-based iterative tropospheric decomposition model. *Remote Sens. Environ.* 204, 109-121. <https://doi.org/10.1016/j.rse.2017.10.038>.
- Yu, C., Li, Z., Penna, N.T., Crippa, P., 2018c. Generic atmospheric correction model for Interferometric Synthetic Aperture Radar observations. *J. Geophys. Res. Solid Earth* 123 (10), 9202-9222. <https://doi.org/10.1029/2017jb015305>.
- Yu, C., Penna, N.T., Li, Z., 2017. Generation of real-time mode high-resolution water vapor fields from GPS observations. *J. Geophys. Res. Atmos.* 122 (3), 2008-2025. <https://doi.org/10.1002/2016JD025753>.
- Yu, H., Lan, Y., Yuan, Z., Xu, J., Lee, H., 2019. Phase unwrapping in InSAR: A review. *IEEE Geosc Rem Sen M* 7 (1), 40-58. <https://doi.org/10.1109/MGRS.2018.2873644>.
- Zebker, H.A., Villasenor, J., 1992. Decorrelation in interferometric radar echoes. *IEEE Trans. Geosci. Remote Sens.* 30 (5), 950-959. <https://doi.org/10.1109/36.175330>.
- Zhang, K., Wang, S., Bao, H., Zhao, X., 2019a. Characteristics and influencing factors of rainfall-induced landslide and debris flow hazards in Shaanxi Province, China. *Nat. Hazards Earth Syst. Sci.* 19 (1), 93-105. 10.5194/nhess-19-93-2019.
- Zhang, Y., Heresh, F., Falk, A., 2019b. Small baseline InSAR time series analysis: Unwrapping error correction and noise reduction. *Comput. Geosci.*, 104331.
- Zhang, Y., Meng, X., Dijkstra, T., Jordan, C., Chen, G., Zeng, R., Novellino, A., 2020. Forecasting the magnitude of potential landslides based on InSAR techniques. *Remote Sens. Environ.* 241, 111738. <https://doi.org/10.1016/j.rse.2020.111738>.
- Zheng, D., Da, F., 2011. A novel algorithm for branch cut phase unwrapping. *Optics and Lasers in Engineering* 49 (5), 609-617. <https://doi.org/10.1016/j.optlaseng.2011.01.017>.